

# **MEMS Electrolytic Inchworms for Movable Neural Probe Applications**

Thesis by

**Luca Giacchino**

In Partial Fulfillment of the Requirements

for the Degree of

Doctor of Philosophy



California Institute of Technology

Pasadena, California

2011

© 2011

Luca Giacchino

All Rights Reserved

# Acknowledgements

This thesis is the product of five years of work at the Caltech Micromachining Lab. During this time, I had the pleasure to work with many talented people, and I would like to express my gratitude to them all.

First, I would like to thank my advisor, professor Yu-Chong Tai. His brilliant ideas and insightful advice guided me all along. The opportunity to share his knowledge and experience has been truly invaluable.

Thanks to all my colleagues in the Caltech Micromachining Lab over these years, for the friendship, exchange of ideas, and help in keeping the lab running: Ray Huang, Chun-Hui Lin, Mandheerej Nandra, Changlin Pang, Damien Rodger, Angela Tooker, Scott Miserendino, Siyang Zheng, Po-Jui Chen, Jason Shi, Nick Lo, Wen Li, Quoc Quach, Mike Liu, Justin Kim, Penvipha Satsanarukkit, Bo Lu, Wendian Shi, Yu Zhao, Han-Chien Chang, Charles DeBoer, Dongyang Kang, Zhao Liu, John Chen, Jogson Hu, Roger Kuo, Agnes Tong, Christine Garske, and Trevor Roper. Particular appreciation goes to Changlin Pang, for the extensive cleanroom training during my first and second year in the lab. Thanks to the colleagues, visitors, and summer students that helped me with my project: Roger Kuo, Jogson Hu, Tony Wu, Dolawat Wanichwatphibun, and Andrew Mo. Special thanks also to Christine Garske for the great management of the lab, and to Trevor Roper for all the assistance and timely repairs on the equipment.

I would like to thank professors Richard A. Andersen and Joel W. Burdick for their collaboration on the project. Thanks also to professors Changhuei Yang, Azita Emami, and Julia A. Kornfield for the help in reviewing this thesis.

My deep gratitude goes to the National Institute of Health (NIH) for providing the funds that made this work possible.

Most importantly, I would like to thank my wife Juliana, whom I met and married during my years as a graduate student. Her love and support helped me overcome any difficulty along the way. I would also like thank my parents, Anna Maria Murdaca and Bartolomeo Giacchino, for their love and guidance throughout my life.



# **Abstract**

## **MEMS Electrolytic Inchworms for Movable Neural Probe Applications**

Thesis by

**Luca Giacchino**

Doctor of Philosophy in Electrical Engineering

California Institute of Technology

Over decades of cortical neural prosthesis, it was found that “movable” neural probes are important to track neurons for long-term, reliable prostheses. This is challenging because the ideal movable probes require low voltage, small power, bidirectional/latchable movement, and large total traveling distance. The device should also be small enough to entirely fit under the skull after implantation. Many different devices have been demonstrated to move neural probes, but none of them satisfies all the actuation and size requirements.

This thesis presents our work on actuators for movable neural probes that combine MEMS technology with an electrolytic actuation mechanism. Each inchworm is based on two electrolytic balloon actuators. The actuators rely on gas generation by electrolysis inside a sealed balloon, which causes its expansion. When electrolysis is stopped, gas recombination and permeation across the balloon membrane cause the

balloon to relax. Electrolytic actuation, although slow, has several advantages: low power, low voltage, and ability to provide large force and displacement. The balloons have been characterized and their behavior mathematically modeled. Innovative salt-shell-based and hydrogel-based processes have been developed to fabricate the balloons and to allow their replenishment by osmosis.

Two balloons are combined into a bidirectional inchworm mechanism. Large traveling distance can be obtained in multiple cycles, the only constraint being the probe length. Displacement of a silicon probe and of a commercial metal probe have been demonstrated in both directions, with a displacement per cycle between 0.5  $\mu\text{m}$  and 75  $\mu\text{m}$ . The voltage required to drive electrolysis is typically around 3.5 V, with peak power per balloon around 100  $\mu\text{W}$ . The devices were tested in air, water, and saline.

Closed-loop control of the inchworm may be needed for accurate positioning of the probe, and monitoring of the pressure inside the balloons represents a possible source of feedback from the inchworm. Parylene-membrane pressure sensors that are suitable for integration inside balloon actuators have been demonstrated.

# TABLE OF CONTENTS

---

CHAPTER 1. INTRODUCTION TO MOVABLE NEURAL PROBES.....	1
<b>1.1 Neural Recording and Stimulation .....</b>	<b>1</b>
1.1.1 Neural Recordings .....	1
1.1.2 Single-unit Recordings.....	2
1.1.3 Neural Stimulation .....	4
<b>1.2 Brain Tissue Mechanics .....</b>	<b>4</b>
<b>1.3 Neural Probes .....</b>	<b>5</b>
1.3.1 Microwires .....	6
1.3.2 MEMS Probes.....	7
1.3.3 Inflammatory Response .....	9
<b>1.4 Movable Neural Probes.....</b>	<b>11</b>
1.4.1 Motivation.....	11
1.4.2 Hand-operated Devices.....	12
1.4.3 Motorized Devices.....	15
1.4.4 Commercial Electrode Manipulators .....	19
1.4.5 Microactuated Devices.....	21
<b>1.5 Current Challenges and Actuator Requirements.....</b>	<b>24</b>

<b>1.6 Electrolytic Inchworms for Movable Neural Probes .....</b>	<b>27</b>
1.6.1 Electrolytic Inchworm Design .....	27
1.6.2 Overview of the Chapters .....	30
 <b>CHAPTER 2. ELECTROLYTIC BALLOON ACTUATORS .....</b>	<b>31</b>
 <b>2.1 Balloon Actuator Principle .....</b>	<b>31</b>
 <b>2.2 Electrolysis as an Actuation Method .....</b>	<b>33</b>
2.2.1 Water Electrolysis .....	33
2.2.2 Electrolysis-based Actuation .....	34
2.2.3 Comparison with Other Actuation Methods .....	35
2.2.4 Electrolysis-based Microdevices .....	42
 <b>2.3 Balloon Design .....</b>	<b>44</b>
 <b>2.4 Balloon Modeling .....</b>	<b>45</b>
2.4.1 Model .....	45
2.4.2 Sensitivity to Initial Conditions .....	53
2.4.3 Refined Model .....	54
 <b>2.5 Balloon Test Setup .....</b>	<b>58</b>
2.5.1 Experimental Setup for Testing of the Balloons .....	58
2.5.2 Balloon Pressure and LVDT Reading .....	59
 <b>2.6 Parylene Balloons .....</b>	<b>60</b>

2.6.1 Silicon Frame Fabrication.....	60
2.6.2 Balloon Fabrication.....	61
2.6.3 Results.....	65
<b>2.7 Balloon Discs .....</b>	<b>68</b>
<b>2.8 Silicone Balloons .....</b>	<b>73</b>
2.8.1 Silicone .....	74
2.8.2 Fabrication .....	74
2.8.3 Results.....	76
<b>2.9 Osmosis and Water Replenishment.....</b>	<b>78</b>
<b>2.10 Further Characterization and Optimization .....</b>	<b>80</b>
 CHAPTER 3. MONOLITHIC NEURAL PROBE ACTUATORS .....	 83
<b>3.1 Design .....</b>	<b>83</b>
3.1.1 Single-balloon Design.....	83
3.1.2 Dual-balloon Design .....	84
<b>3.2 Fabrication .....</b>	<b>86</b>
3.2.1 Silicon Frame Fabrication.....	87
3.2.2 Balloon Fabrication.....	88
<b>3.3 Results.....</b>	<b>90</b>
<b>3.4 Dealing with Permeation.....</b>	<b>92</b>

CHAPTER 4. FIRST-GENERATION INCHWORMS.....	95
<b>4.1 From Monolithic to Inchworm.....</b>	<b>95</b>
<b>4.2 Design .....</b>	<b>96</b>
<b>4.3 Simulations.....</b>	<b>99</b>
<b>4.4 Fabrication.....</b>	<b>100</b>
<b>4.5 Results.....</b>	<b>104</b>
 CHAPTER 5. FIRST-GENERATION INCHWORMS.....	 107
<b>5.1 From First to Second Generation .....</b>	<b>107</b>
<b>5.2 Design .....</b>	<b>108</b>
5.2.1 Frame Design.....	108
5.2.2 Balloon Disc Design .....	112
<b>5.3 Fabrication.....</b>	<b>113</b>
5.3.1 Frame and Ruler Probe .....	113
5.3.2 Balloon and Clamping Discs .....	114
5.3.3 Disc Assembly .....	116
5.3.4 MgSO <sub>4</sub> -based Balloon Process .....	120
5.3.5 Clamping Balloon Release.....	124
<b>5.4 MgSO<sub>4</sub>-based Inchworm Results .....</b>	<b>126</b>

<b>5.5 Hydrogel-based Process .....</b>	<b>129</b>
<b>5.6 Hydrogel-based Inchworm Results.....</b>	<b>132</b>
5.6.1 Results in Air .....	132
5.6.2 Results in Water .....	135
5.6.3 Results in Saline.....	138
5.6.4 DVRT Measurements .....	139
5.6.5 Reliability and Failure Modes.....	141
<b>5.7 Inchworm Array.....</b>	<b>143</b>
<b>5.8 Comments on Feedback Sensors.....</b>	<b>146</b>
 <b>CHAPTER 6. BALLOON PRESSURE SENSORS .....</b>	 <b>149</b>
<b>6.1 Introduction .....</b>	<b>149</b>
6.1.1 Motivation.....	149
6.1.2 MEMS Pressure Sensors.....	150
<b>6.2 Design .....</b>	<b>150</b>
6.2.1 Membrane and Cavity.....	151
6.2.2 Simulations .....	152
6.2.3 Strain Gauges .....	155
<b>6.3 Fabrication .....</b>	<b>156</b>
<b>6.4 Results.....</b>	<b>159</b>

6.4.1 Pressure Response.....	159
6.4.2 Membrane Permeability .....	160
<b>6.5 Modified Design .....</b>	<b>163</b>
6.5.1 Simulations .....	164
6.5.2 Process Integration.....	167
 CHAPTER 7. CONCLUSION .....	 169
7.1 Conclusions .....	169
7.2 Future Work .....	174
 APPENDIX A. MEMS TECHNOLOGY .....	 175
A.1 Bulk and Surface Micromachining.....	175
A.2 Patterning.....	176
A.3 Deposition .....	177
A.4 Etching.....	178
A.5 Parylene .....	179



APPENDIX B. THERMODYNAMICS AND ELECTROCHEMISTRY .....	183
<b>B.1 Thermodynamics .....</b>	<b>183</b>
B.1.1 Energy and Thermodynamic Potentials .....	183
B.1.2 Chemical and Electrochemical Potential.....	187
B.1.3 Mixtures and Activity.....	189
B.1.4 Chemical Reactions.....	192
B.1.5 Ideal Gases .....	194
B.1.6 Permeation.....	195
B.1.7 Osmosis .....	199
<b>B.2 Electrochemistry .....</b>	<b>201</b>
B.2.1 Electrochemical Cells.....	201
B.2.2 Electrode-electrolyte Interface .....	202
B.2.3 Cell and Electrode Potentials .....	205
B.2.4 Overpotential.....	207
B.2.5 Reaction Kinetics .....	208
B.2.6 Mass Transfer.....	211
B.2.7 Equivalent Electrical Model.....	213
REFERENCES.....	219



# LIST OF FIGURES

---

Figure 1-1. Examples of MEMS electrode arrays. a) Michigan array. b) Utah array. c) Caltech silicon probes.....	9
Figure 1-2. Microdrive demonstrated by Jackson and Fetz [37]. .....	13
Figure 1-3. Hand-operated microdrives based on a screw mechanism. a) Microdrive by Vos et al. [38]. b) Microdrive by Swadlow et al. [39]. .....	14
Figure 1-4. Motorized microdrive by Fee and Leonardo [44]. The microdrive uses miniature brushless DC motors connected to a screw mechanism to move the electrodes. a) Schematics of the device. b) Picture of the complete assembly. ....	16
Figure 1-5. Assembly for an electrode array with hydraulic positioning [45]. a) Full schematics of the device. b) Close-up on the fluid and piston system inside each channel in the electrode housing. c) Picture of the assembled device. ....	17
Figure 1-6. Microdrive based on piezoelectric microactuators [46-47]. a) Picture of the four piezoelectric actuators. b) Drawing of the entire assembly. c) Picture of the device being mounted into a cranial chamber. ....	18
Figure 1-7. Electrode manipulator by Eckhorn and Thomas [57]. a) Cross-section of the manipulation mechanism for each electrode. b) Motorized array of electrodes. ....	20
Figure 1-8. Commercial Eckhorn-type system by Thomas Recording.....	21
Figure 1-9. Electrostatic microactuator by Muthuswamy et al. [62]. a) Drawing of the actuation principle (not to scale). b) Picture of the fabricated system, with close-up on the probe tip.....	22

Figure 1-10. Thermal microactuator by Muthuswamy et al. [62]. Only the top half of the system is shown. The picture is taken during actuation. ....	23
Figure 1-11. Electrostatic microactuator by IMEC [64]. a) Drawing of the actuator structure. b) Actuation principle. c) SEM picture of the fabricated structure. d) Device packaged with a glass cap.....	24
Figure 1-12. a) Schematics of the inchworm. b) Inchworm actuation principle. The first row illustrates forward displacement (downward in the figure), while the second row illustrates backward displacement (upward in the figure).....	29
Figure 2-1. Balloon actuation cycle.....	32
Figure 2-2. Piston system used to compare gas-heating, water-vaporization, and electrolytic actuation. ....	37
Figure 2-4. Electrolysis-actuated pumps. a) Pump for spray application [74]. b) Pump based on surface roughness gradient [75].....	43
Figure 2-5. Geometry and results of the ellipsoidal balloon simulation.....	45
Figure 2-6. Experimental setup for testing of the balloon actuators.....	58
Figure 2-7. Fabrication steps for balloons with parylene wall. Steps 1-5 are to fabricate the supporting silicon structure. Steps 6-10 are to fabricate the balloon. ....	64
Figure 2-8. a) Silicon frame. Different geometries are fabricated, and a number on the structure is used to identify them. b) Parylene balloon after photoresist release. ....	64
Figure 2-9. Expansion and relaxation of a parylene balloon. The experimental data is fitted with the balloon model. ....	66

Figure 2-10. a) 3D models of silicon discs: a1) without handle, a2) with handle. b) Fabrication steps for the silicon discs (the cross-section does not show the holes in the disc).....	69
Figure 2-11. Fabrication of a balloon using silicon discs. ....	70
Figure 2-12. Device after disc assembly and photoresist dispensing, viewed from different angles.....	71
Figure 2-13. Expansion and relaxation of a parylene balloon with silicon discs. The experimental data is fitted with the balloon model. ....	73
Figure 2-14. Balloon with silicone wall and silicon discs. ....	76
Figure 2-15. Expansion and relaxation of a balloon with PDMS walls and silicon discs. Electrolysis is stopped at the dashed line.....	77
Figure 3-1. Monolithic movable probes with single-balloon actuator [83]. a) Device after releasing the sacrificial photoresist. A parylene balloon surrounds the spring. b) Balloon filled with electrolyte. Electrolysis is being run, and a gas bubble inside the balloon is visible. ....	84
Figure 3-2. a) Silicon structure of the dual-balloon device before balloon fabrication [26]. b) Close-up of the neural probe tip, with electrode openings. c) Close-up of one of the springs, with the platinum electrode for electrolysis on the surface. ....	85
Figure 3-3. Dual-balloon device after balloon fabrication. a) Two balloons with approximately the same volume. b) Two balloons with different volume. ....	86
Figure 3-4. Fabrication of the silicon frame. ....	88
Figure 3-5. Balloon fabrication steps (dual-balloon device). ....	89

Figure 3-6. Experimental results for the actuation of a dual-balloon monolithic device. The two sets of plots are part of the same test, and they are separated only for ease of visualization. The applied voltage is at the top, and the resulting displacement is at the bottom.....	91
Figure 4-1. 3D model of the inchworm actuator. a) Silicon frame only, without balloons. b) Silicon frame with balloons. ....	97
Figure 4-2. Inchworm actuation principle. The steps for forward and backward movement are illustrated.....	98
Figure 4-3. Finite-element simulations of the spring mechanism. The colors show the Von Mises stress, to highlight the stress concentrations point. a) The force is applied on the side of the spring. b) The force is applied in-line with the spring.....	100
Figure 4-4. Fabrication steps for the inchworm. The process is divided into two parts: frame fabrication and balloon fabrication.....	103
Figure 4-5. Fabricated first-generation inchworm devices. a) Silicon frame. Frames with different dimensions were fabricated, and the number on the frame identifies them. b) Close-up of the spring. c) Close-up of the electrodes. d) Frame with sacrificial photoresist. Due to photoresist reflow, the shape tends to become spherical. e) Frame with parylene balloons, after release of the sacrificial photoresist. ....	104
Figure 5-1. Second-generation frame design: a) frame only, b) complete device.....	109
Figure 5-2. Inchworm actuation principle. ....	111
Figure 5-3. a) Effect of the lateral anchors on the lateral expansion of the balloon. b) T-trenches around the edge of the disc to create the lateral anchors. ....	112

Figure 5-4. Frame fabrication steps. ....	114
Figure 5-5. a) Fabricated silicon frame. b) Fabricated ruler probe. ....	114
Figure 5-6. a) Fabrication steps for the discs (both balloon discs and clamping discs). b) Fabricated discs. ....	115
Figure 5-7. a) Assembly of the balloon discs. b) Assembly of the clamping discs. c) Frame with assembled discs (case of balloons with one disc). ....	117
Figure 5-8. Assembly of discs with tweezers mounted on a xyz micrometer stage. The assembly is performed under a stereoscope. ....	118
Figure 5-9. a) Frame with assembled balloon discs (case of balloons with two discs). b) Frame with assembled balloon and clamping discs (case of balloons with one disc). ....	118
Figure 5-10. Fabrication steps for balloons with one disc. ....	119
Figure 5-11. Fabrication steps for balloons with two discs. ....	119
Figure 5-12. Device at different stages of balloon fabrication. The balloons filled with water are shown in Figure 5-14b. ....	120
Figure 5-13. Release of the front side of the clamping balloon by laser ablation. A close-up of the ablated section is shown. ....	125
Figure 5-14. a) Inchworm with dry balloons ( $\text{MgSO}_4$ crystals are visible inside). b) Inchworm with balloons full of water (filled by osmosis). c) Inchworm with ruler probe. d) Close-up of the clamping mechanism and ruler probe. ....	125
Figure 5-15. a) Balloons overfilled after being immersed in water for 2.5 days (the clamping balloon was not released in this device prior to immersion in water). b) Gas bubble covering the electrodes. ....	128

Figure 5-16. a) Balloon with hazy surface. b) Balloon with clear surface. ....	130
Figure 5-17. a) Complete inchworm system. A commercial metal probe is mounted on top of a silicon ruler probe. b1-b3) Close-ups of the probe, with frames showing the probe displacement (experiment run in air). b1) Initial position of the probe. b2) Probe after 4 cycles of forward displacement (cumulative displacement: about 100 $\mu\text{m}$ ). b3) Probe after 1 cycle of backward displacement from b2 position (displacement: about 75 $\mu\text{m}$ ).....	132
Figure 5-18. a) Connection of the cable to the inchworm by conductive epoxy. b-c) Inchworm with connected and insulated cable b) in air and c) in water.....	135
Figure 5-19. Inchworm during an actuation cycle in water. Because the displacements are small compared to the overall size of the device, they are not very visible, and they are highlighted by marker lines. a1) The device is at rest. a2) The same device, with the probe clamped and the displacing balloon expanded. b) Close-ups of the clamping balloon and the probe: b1) unclamped probe, b2) clamped probe. ....	136
Figure 5-20. Bubbles forming on the surface of the balloons after the inchworm is actuated for several cycles. The bubbles are due to gas permeating through the balloon wall. a) Case of smooth balloon surface: only few large bubbles form. b) Case of hazy balloon surface: many small bubbles form, due to the many nucleation points available.....	137
Figure 5-21. Inchworm displacement versus charge supplied to the displacing balloon.....	141



Figure 5-22. Some delamination of parylene from the platinum traces after a few months in deionized water. ....	143
Figure 5-23. a) Array bottom plate. b) Array top plate. c) Assembly of the array (only one inchworm shown for visual convenience). d) Complete array, with three inchworms and probes in their guides. ....	145
Figure 5-24. Fabricated array components. a) Top plate. b) Bottom plate. ....	145
Figure 6-1. Top-view of two fabricated devices with different dimensions. The cavity under the silicon can be clearly seen (dark grey) together with the hole array for $\text{XeF}_2$ etching (black dots over the cavity). The cavity is surrounded by the etch stops and anchors (black). The Wheatstone bridge arrangement of the strain gauges is also shown. ....	152
Figure 6-2. a) Distribution of the normal strain the y direction (it is the same for the x direction, due to symmetry). Blue areas correspond to tensile strain, red areas to compressive strain, with the color intensity proportional to the absolute value of the strain. b) Strain distribution along a cross-section passing through the center of the membrane, i.e., along the dashed line in a). The membrane deformation is not to-scale, and it is exaggerated for better visualization. ....	153
Figure 6-3. Behavior of the strain gauge resistance R when the pressure P on the membrane increases and the membrane deforms. ....	156
Figure 6-4. Process flow for the fabrication of the pressure sensors. ....	157
Figure 6-5. Surface scan of a $200\text{ }\mu\text{m} \times 200\text{ }\mu\text{m}$ sensor. The image was obtained with a scanning laser confocal microscope by Keyence Corporation. The	

dimples (due to filled etched holes) and grooves (due to the anchors and etch stops) are about 2 $\mu\text{m}$ deep. ....	159
Figure 6-6. Pressure response of the 200 $\mu\text{m} \times 200 \mu\text{m}$ sensor. $V/V_s$ is the ratio of the bridge output and supply voltages. The data point at atmospheric pressure (origin of the plot) is taken as a reference for the data, to eliminate the bridge offset. The data points are fitted to a quadratic function. ....	160
Figure 6-7. Effect of permeation of $\text{N}_2$ through parylene on pressure response of the 200 $\mu\text{m} \times 200 \mu\text{m}$ sensor. $V/V_s$ is the ratio of the bridge output voltage and the supply voltage. The initial data point (at atmospheric pressure) is taken as a reference for the data. Only part of the relaxation after pressure release is shown. ....	162
Figure 6-8. Pressure sensor with rectangular cavity. The geometrical parameters varied in the simulation are shown. ....	165
Figure 6-9. Maximum deflection (i.e., deflection at the center of the membrane) and strain gauge relative resistance change as a function of pressure for three different sets of geometric parameters. ....	166
Figure 6-10. Modified pressure sensor fabrication process. ....	168
Figure A-1. a) Common types of parylene. b) Parylene deposition process. Images courtesy of Specialty Coating Systems. ....	180
Figure B-1. Schematics of a simplified gas permeation case. ....	198
Figure B-2. Electrical double layer at the electrode-electrolyte interface. ....	203
Figure B-3. Electronic energy levels at the electrode-electrolyte interface. ....	204

Figure B-4. Electrical model of the electrochemical system, from one electrode the bulk of the solution. ....	214
--	-----



# LIST OF TABLES

---

Table 1-1: Requirements of an ideal actuator for movable neural probes.....	25
Table 1-2: Performance comparison of current MEMS movable probes.....	27
Table 2-1: Comparison of actuation mechanisms for microdevices.....	36
Table 5-1: Feature and technology comparison of the first and second generation of inchworms.....	109
Table 7-1 (next page): Comparison of actuator requirements and the demonstrated performance of hydrogel-based second-generation inchworms. ....	172
Table A-1: Selected properties of parylene (from Specialty Coating Systems). ....	181
Table A-2: Parylene barrier properties compared to other common polymers (source: Specialty Coating Systems) .....	182



# CHAPTER 1

---

## Introduction to Movable Neural Probes

Moving neural probes is the primary application for which our actuators were designed. This chapter starts with an overview of the field of neural recordings and stimulation. The recording of signals from the brain and the stimulation of brain activity have numerous applications in neuroscience and medicine, and the literature and research on the subject are extensive. Our review focuses on the current technology to fabricate neural probes and, in particular, the actuators to make them movable. This is followed by a discussion of the technological challenges presently faced by movable neural probes and of the requirements of an ideal actuator. Finally, the MEMS electrolytic inchworm design we propose for moving neural probes is introduced.

### 1.1 Neural Recording and Stimulation

#### 1.1.1 Neural Recordings

Several techniques have been developed to record signals from the brain. The recordings generally rely on electrodes, which are able to detect the perturbations of the electrical potential caused by neuronal activity. There are three main techniques, listed here in order of spatial resolution:

- electroencephalography (EEG),
- intracranial electroencephalography (iEEG), or electrocorticography (EcoG),
- single-unit recordings.

EEG recordings are obtained by placing electrodes on the scalp. The recordings can assist, for example, in the diagnosis of neurological disorders. The technique is minimally invasive; however, it has poor spatial resolution, and it suffers from attenuation by the meninges and the skull. ECoG is more invasive, as the electrodes are placed directly on the surface of the brain. The spatial resolution is still limited, but the signal attenuation is greatly reduced. Single-unit recordings have the ability to isolate signals coming from individual neurons. This technique has high spatial resolution (at single cell level), but it requires the use of electrodes inserted directly into the brain tissue. It is, therefore, clear that there is a tradeoff between invasivity and spatial resolution.

### **1.1.2 Single-unit Recordings**

Single-unit recordings obtained with implanted electrodes are extracellular recordings, because the electrodes are outside the membrane of the neurons. The electrodes detect the perturbation of the extracellular potential due to the generation or propagation of action potentials in the cells. The electrodes employed for single-unit recordings are described in Section 1.3.

For clean recordings, the electrodes must be positioned in proximity of one or more neurons. The electrodes must be within 50-100  $\mu\text{m}$  from a neuron to attain sufficient signal-to-noise ratio, and the neuron soma is the main contributor to the recorded signal [1]. An electrode often does not record only from a single cell; instead it senses the contributions of several neighboring neurons. The signal from each cell can be isolated with data processing, by exploiting, for example, the differences in the shape and pattern of action potentials originating from different cells.



Bundles or arrays of electrodes are used to record multiple single units simultaneously, making it possible to find correlations between the activities of neighboring neurons. By analyzing the signals from several adjacent electrodes, more complex algorithms can also be developed for the isolation of individual cells.

Single-unit and multiple single-unit recordings are an invaluable tool for neuroscience research, as they cast a light on the inner workings of the brain at the cellular level. These recordings recently found application in neural prosthetics, i.e., devices that exploit a connection between the nervous system and man-made machines, in order to restore sensory or motor function. This kind of connection is also called brain-machine or brain-computer interface. Several reviews of the field are available in literature [2-6]. For neural prosthetic applications, the signals recorded from the motor cortical neurons are analyzed to extract information about an intended movement [7-8]. The information is then used to control, for example, a prosthetic limb or a cursor on a screen. Sensory feedback can be provided by regular sensation (if not impaired) or by the prosthetic device itself. For instance, in some systems currently under development, the sensory information is supplied to the central nervous system by neural stimulation.

The time span of the recordings varies from short-term, lasting a few hours or days (acute recordings), to long-term, lasting more than a week (chronic recordings). For successful neural prosthetics, chronic recordings are needed, as the subject has to be trained for months or years to take advantage of the newly implanted brain-machine interface.

In chronic recordings, the electrodes are left inside the brain tissue for long periods of time, from several days to a few years. It is observed that the signal from an

implanted electrode degrades over time, until it is eventually lost. This is attributed to the relative movement between the electrode and the tissue (due to movements of the animal and to natural drift of the tissue) and to the formation of scar tissue around the electrode (Section 1.3.3). In general, movements of the animal can cause abrupt changes in signal quality, while tissue drift and scar tissue formation cause more gradual signal degradation. Movable electrodes are proposed as a possible solution to signal degradation (Section 1.4).

### **1.1.3 Neural Stimulation**

Electrodes are also employed for electrical stimulation of neuronal activity [9]. Stimulation is accomplished by an ionic current that depolarizes the neuron membrane. The current is generated by charge-injection, exploiting capacitive or faradaic mechanisms at the electrode surface. Neuronal stimulation is used for the treatment of some conditions, such as Parkinson's disease (using deep-brain stimulation), and for sensory prostheses, such as cochlear and retinal implants.

## **1.2 Brain Tissue Mechanics**

The mechanical properties of the brain tissue are important for the design of neural probes and of surgical tools, especially automated ones. This is particularly true for movable neural probes, where a suitable actuator must be designed to displace a probe inside the tissue. A fundamental design parameter for the actuator is the force necessary for a probe to penetrate the brain tissue. This force is strongly dependent on the probe geometry and surface material.

Several studies have been conducted on animal and human brain tissue, both in-vitro and in-vivo. Some studies use the experimental data to develop a viscoelastic model of the brain tissue [10-11]. Other studies focus on brain penetration. In one study, stainless-steel spheres with 2.5 mm diameter were used for in-vivo penetration of human brain tissue [12]. An average force of 8 g (0.08 N) was measured during penetration. In another study, the penetration of swine brain tissue was examined [10]. A 10-mm diameter indenter was used, and a force of 0.1 N was measured for 2 mm penetration. These results reveal the order of magnitude of the forces involved, but they are not directly applicable to the case of neural probes, because the diameter of the tools employed in these studies is much larger than the diameter of common neural probes. Moreover, probe tips typically have a wedge or pointed shape to make penetration easier.

### **1.3 Neural Probes**

Extracellular single-unit recordings are obtained by metal electrodes inserted in the brain. The theory behind metal electrodes and their electrical performance was presented by Robinson [13]. Important characteristics of metal electrodes are material, surface area, impedance, shape, and other mechanical properties.

The electrode material must be compatible with the tissue, in order to minimize the electrode degradation and the inflammatory response. The surface area determines the recording range of the electrode. In general, a larger area corresponds to a larger recording volume (i.e., the volume of tissue whose neural activity is sensed by the probe). Smaller electrodes are better suited for isolating the signal of a single cell. The impedance is determined by the material and surface area of the electrode. The electrode behaves like a capacitor inside the brain fluid, due to the formation of an electrical

double-layer. A larger surface area implies a larger capacitor, which has smaller impedance at any given frequency.

The mechanical properties of the electrode are essential in determining the insertion method. Some electrodes are strong enough to penetrate the dura without the need for an incision. Other electrodes are mechanically weak, and they require an incision or the support of an insertion tool. Very thin electrodes are susceptible to buckling during insertion.

Electrodes, unless very sharp and optimally positioned in proximity of a single cell, pick up signal from multiple neurons at the same time. In some cases, it is possible to separate the contributions of different neurons in the compound signal, based on the fact that different neurons generate spikes with different shapes and patterns. Signal processing algorithms are available for this purpose. To improve the separation, electrodes with multiple conductors have been developed. A “stereotrode” [14] is constructed with two conductors, so that each conductor records the signals from a slightly different position. The additional recording site makes it easier to identify the waveforms coming from each neuron in the compound signal. The technique is taken a step further by creating electrodes with four conductors, called “tetrodes” [15].

Electrodes for neural recordings are fabricated with several different technologies. Metal microwires and MEMS probes are the most common examples. The following sections examine these technologies.

### **1.3.1 Microwires**

Microwires are the simplest electrodes for neural recordings [16]. Insulated wires with small diameters (typically from 12 to tens of microns) are cut to expose the

conductive core. Core materials include platinum, iridium, platinum-iridium alloys, nichrome, gold, tungsten, and stainless steel. Insulation materials include parylene C, Teflon, polyimide, and quartz glass. Different techniques have been used to sharpen the tip, in order to reduce the recording sphere. Examples of these techniques include etching or grinding the tip. A tapered tip, for example, can be obtained by immersing one end of the wire into an etchant solution and then gradually pulling it out. The exposed area at the tip can also be modified by accurately trimming the insulating layer with a laser or a SEM electron beam. Moreover, the properties of the tip, such as the impedance, can be tuned by surface modification or coating. For example, platinum black is a popular way of increasing the effective surface area.

As the wires become thinner, it becomes harder to insert them into the tissue, due to the lack of mechanical strength. Guide tubes typically assist with the insertion. Microwires are often arranged into one- and two-dimensional arrays to increase the number of signals in the recording. Arrays with a variety of geometric patterns have been demonstrated. Microwires and microwire arrays are commercially available from companies such as MicroProbes [17] and FHC Inc. [18].

### **1.3.2 MEMS Probes**

Microelectromechanical system (MEMS) technology allows the fabrication of miniaturized devices. A brief introduction to the technology is the subject of appendix A. A review of MEMS technology for neural probe applications is given by HajjHassan et al. [19]. MEMS technology enables accurate and repeatable fabrication of microprobes, and it has the ability to include multiple recording sites on each shank with excellent control over their size and spacing. Commercial MEMS probes are available from some

manufacturers, such as NeuroNexus Technologies [20]. MEMS neural devices can be broadly divided into silicon-based and polymer-based.

A famous example of silicon-based device is the Michigan probes [21]. They are fabricated by ethylene diamine pyrocatechol (EDP) etching of silicon, with a diffused boron etch-stop to determine the shape. Signal processing circuitry is integrated on the devices, and the planar arrays can be stacked into 3D arrays [22] (Figure 1-1a).

Another example of silicon-based device is the Utah probe array [23] (Figure 1-1b). The array is square, and it contains 100 electrodes. The shanks are defined by a dicing saw, followed by silicon etching to sharpen them. The shanks are then coated with metal and insulated by polyimide, leaving the metal exposed only at the tip of each shank. The Utah array is offered by Cyberkinetics [24] as a part of their BrainGate technology.

Silicon probes can also be fabricated by deep reactive ion etching (DRIE). The substrate can be a regular silicon wafer or a silicon-on-insulator (SOI) wafer, where the buried oxide layer acts as an etch stop. DRIE-etched silicon probes with multiple recording sites and integrated parylene-C cable were demonstrated in our group at Caltech [25-27] (Figure 1-1c).

Polymers are widely used as insulation layers for the recording sites and for the interconnection cables. Polymers are also used for the fabrication of flexible electrode arrays [28]. Typically, these devices are not able to penetrate the tissue, and implant sites have to be created beforehand. Parylene-C flexible electrode arrays with platinum recording and stimulation sites have also been demonstrated in our group [29].

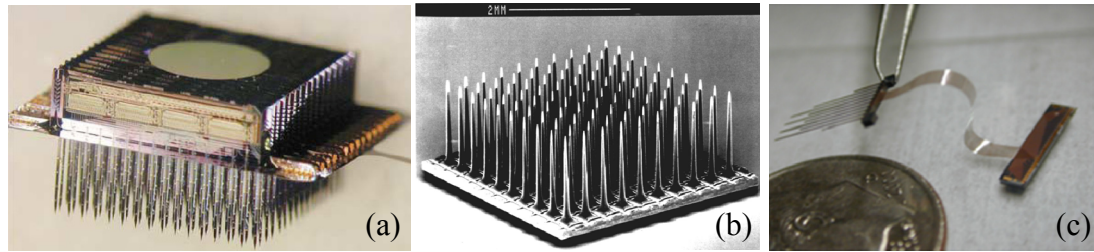


Figure 1-1. Examples of MEMS electrode arrays. a) Michigan array. b) Utah array. c) Caltech silicon probes.

### 1.3.3 Inflammatory Response

Introducing electrodes in the brain causes an inflammatory response. A review of the literature on the subject is given by Polikov et al. [1]. It is important to differentiate between the damage caused by the insertion of the electrodes and the inflammation caused by the long-term presence of the electrodes in the tissue. The insertion is traumatic, due to the rupture of capillaries and processes of glial cells and neurons. An acute healing response similar to that of other tissues ensues, with activation of platelets, clotting factors, and macrophages. Activated microglia participate in the acute response as well. After a few days, the acute response is observed to decrease, leaving the stage for a chronic foreign body reaction.

Activated microglia and reactive astrocytes participate in the foreign body reaction. As reported by Biran et al. [30], the first layer around the electrode is composed of macrophages (the microglia), which try to phagocytose the foreign matter. The microglia are identified by the expression of a particular marker called ED1. Around this first layer are multiple layers of astrocytes. The astrocytes are detected by immunostaining of the glial fibrillary acidic protein (GFAP), which is thought to be

specific to astrocytes. The astrocytes form the glial scar (gliosis), which encapsulates the electrode. The encapsulation becomes more dense and compact with time [31], isolating the electrode from the brain.

Another effect of the electrode insertion and long-term presence is the formation of a “kill-zone” around the electrode, characterized by low neuronal density. Reduction in neuronal density within 100  $\mu\text{m}$  of the electrode was reported [30]. The kill-zone is attributed to the insertion damage or to the presence glial scar, which pushes the neurons away from the electrode and inhibits neuronal growth in order to re-establish the blood-brain barrier.

Studies of the response triggered by different implant materials are available in literature. For example, the response to silicon devices [31-32] and to platinum electrodes [33] has been studied. The study of the glial scar is typically done by immunostaining, which requires the removal of the electrode from the brain. In [34], impedance measurements are used to study the encapsulation of the electrodes over time, without removing them from the tissue.

The encapsulation causes degradation or even loss of signal from electrodes that have been implanted for long times (days or weeks). To counteract this trend, two approaches are usually followed. The first approach is to deliver a drug locally or to coat or treat the electrode surface, in an attempt to reduce the foreign body response or to stimulate neuronal growth. For example, a silica sol-gel porous coating was demonstrated [35]. The second approach is to move the electrodes after implantation, which is the subject of the next section.



## 1.4 Movable Neural Probes

### 1.4.1 Motivation

The ability to adjust the position of a probe after implantation is very desirable to maximize and maintain the quality of the recorded signal. Movable neural probes assist with the initial positioning and make signal recovery possible after degradation or loss, thus extending the lifetime of the implants without the need for a new surgical procedure.

When an array of fixed electrodes is implanted, its position is chosen to maximize the fraction of electrodes that are able record signals with satisfactory signal-to-noise ratio. This task may be particularly challenging during surgery, due to the low spontaneous neuron firing rate when the animal is under anesthesia. After the implantation is complete, only a fraction of the electrodes are correctly positioned to collect useful data, limiting the yield of the array. In an array of individually movable electrodes, the position of each electrode can be tuned in order to maximize the fraction of usable electrodes. Even though arrays of movable electrodes cannot usually be made as compact as fixed arrays, the larger number of high-quality signals attainable by moving the electrodes may compensate for the lower electrode count.

The quality of chronic single-unit recordings degrades over time, due to the relative movement between the electrodes and the tissue and to the formation of scar tissue around the electrodes. Movable electrodes enable the experimenter to compensate for probe or tissue movements, in order to maintain the electrodes in proximity of the cells. The electrodes can be moved to track the same neuron, if possible, or to approach different cells. Even when the signal from an electrode is still acceptable, the experimenter may decide to reposition it to record from cells at different depths. This

flexibility is important for multiple single-unit studies to find correlates between the activities of different neurons.

Movement of the electrodes is also thought to break through the scar tissue. Study of the glial encapsulation around movable electrodes showed lower levels of GFAP expression at the tip of the electrode after it was moved [36], indicating a reduced presence of astrocytes. Jackson and Fetz report in [37] that moving an electrode after it has been in the same position for several days or weeks produces large changes in the detected signal at the first movement, while the changes are not as large for subsequent movements. This suggests that scar tissue around the electrode is broken at the first movement. By moving the electrodes, clean recordings were obtained for more than 22 months. Similarly, Vos et al. [38] could not maintain a neuronal signal for two consecutive days, but by moving the electrodes either up or down the signal was regained. Swadlow et al. [39] report recording for more than 4 years in one case by using a microdrive.

Several examples of movable electrodes are found in the literature. The microdrives that are used to move the electrodes can be divided into two main categories: hand-operated and motorized. Microactuated devices can be considered as a sub-category of the motorized ones. The different kinds of microdrives are examined in the following sections.

### **1.4.2 Hand-operated Devices**

In the simplest hand-operated microdrives, the electrodes are moved with forceps, as demonstrated by Jackson and Fetz [37] (Figure 1-2). The device uses 12 Teflon-insulated tungsten microwires with 50  $\mu\text{m}$  diameter. The wires move inside polyamide

guide tubes with an internal diameter of 225  $\mu\text{m}$ . The array is  $6 \times 2$ , with an inter-electrode separation of 600  $\mu\text{m}$ . The tubes are filled with an antibiotic ointment, and they are sealed at both ends with Silastic (the wires can slide freely through Silastic). The assembly is then housed in a titanium casing that is attached with screws to the skull. The wires above the guide tubes are grasped by forceps to move them up and down.

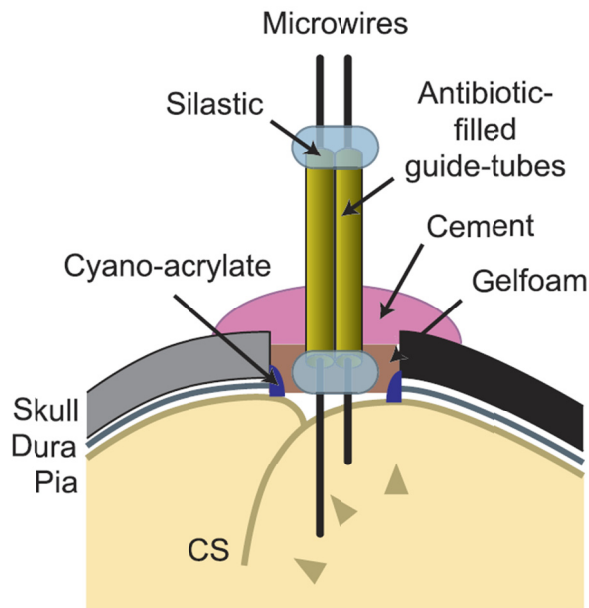


Figure 1-2. Microdrive demonstrated by Jackson and Fetz [37].

Very commonly, hand-operated microdrives are based on screws that move the electrodes along the vertical direction when turned [38-43]. The position accuracy is typically limited to tens of microns. An example of screw-based device is reported by Vos et al. [38] (Figure 1-3a). The electrodes are arranged in a  $2 \times 3$  matrix with 0.6 mm inter-electrode spacing. Each electrode is secured to a shuttle, which is threaded with a screw. When the screw is turned, the shuttle moves in the vertical direction. Each screw

moves against a counteracting spring. The microdrive is designed to host high-impedance sharp tungsten electrodes ( $1\text{ }\mu\text{m}$  tip, with parylene or epoxylite insulation). The base plate is  $19\text{ mm} \times 23\text{ mm}$ , the total height of the device is  $16\text{ mm}$ , and its weight is  $14\text{ g}$ .

Another example of screw-based microdrive is presented by Swadlow et al. [39] (Figure 1-3b). The system is designed for flexible platinum-tungsten microwires with a diameter as small as  $40\text{ }\mu\text{m}$ . The microwires are moved inside stainless steel guide tubes. To prevent the buckling of the microwire when it is pushed by the screw, the extremity of the wire is enclosed in a polyimide tubing that slides over the guide tube. The electrode is connected by a side-arm to a shuttle, which is moved by a screw. The shuttle is placed in a grooved cylinder below and in-line with the screw. This design allows the device to be light (each microdrive weighs  $60\text{ mg}$ ) and compact (each microdrive has a  $1\text{ mm}$  diameter, so they can be spaced by  $1.3\text{ mm}$ ). The linear motion range is  $3\text{--}6\text{ mm}$ .

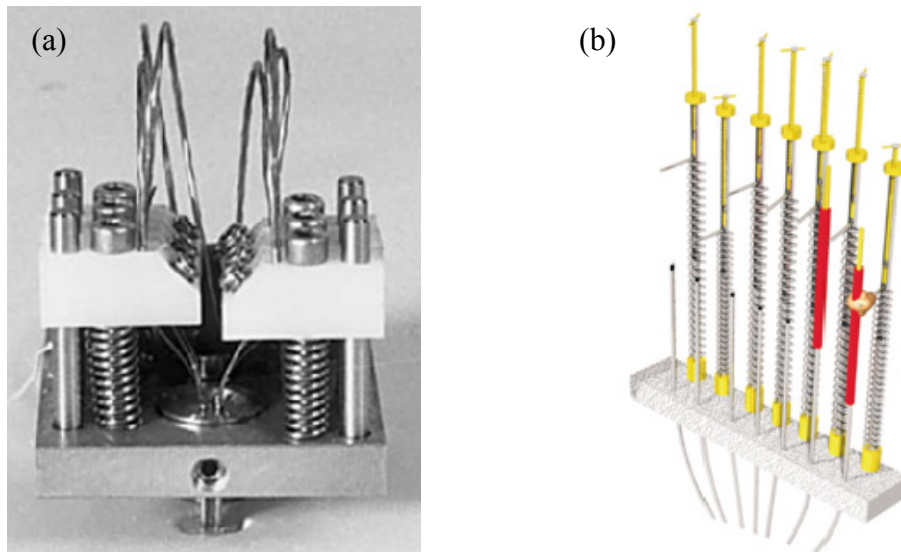


Figure 1-3. Hand-operated microdrives based on a screw mechanism. a) Microdrive by Vos et al. [38]. b) Microdrive by Swadlow et al. [39].

Venkatachalam et al. [40] demonstrated a hexagonal array of guide-tubes for dual-wire electrodes (stereotrodes). Parylene-coated tungsten wire with 25  $\mu\text{m}$  diameter is used in the device. The electrodes are 450  $\mu\text{m}$  apart, and they can protrude 3 mm into the brain. The headstage is 5.8 mm in diameter, and it weighs 1.4 g.

Lansink et al. [41] designed a microdrive to independently position 14 tetrodes (fabricated with 13  $\mu\text{m}$  nichrome microwires). The screws are arranged radially around the headstage. The tetrodes are guided through cannulae to two distinct bundles, in order to record signals from two separated areas simultaneously. The height of the device is 5.6 mm, with a maximum diameter of 4.1 mm at the top.

### **1.4.3 Motorized Devices**

Motorized microdrives have been demonstrated using a number of actuation mechanisms, such as brushless DC motors [44], hydraulic actuation [45], and piezoelectric actuation. Compared to hand-operated devices, the motorized ones provide better positional accuracy (down to about 1  $\mu\text{m}$  or less).

Fee and Leonardo [44] started from the design of Venkatachalam et al. [40] and connected miniature brushless DC motors to the screws (Figure 1-4). The DC motors are 1.9 mm in diameter and they weight 100 mg. The motors contain a planetary gear system that increases the available torque (300  $\mu\text{Nm}$ ). Parylene-coated tungsten wires (from Microprobe, Inc.) are placed in a hexagonal array. The assembly is 6 mm in diameter, 17 mm high, it weighs 1.5 g, and it is able to produce 3.5 mm of vertical displacement.

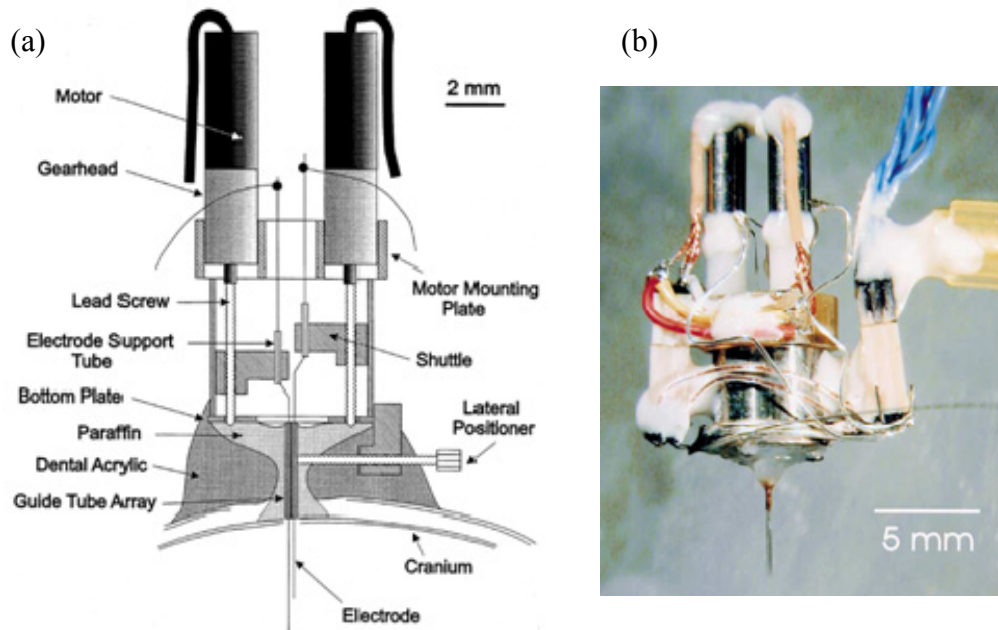


Figure 1-4. Motorized microdrive by Fee and Leonardo [44]. The microdrive uses miniature brushless DC motors connected to a screw mechanism to move the electrodes. a) Schematics of the device. b) Picture of the complete assembly.

Sato et al. [45] demonstrated a microdrive based on hydraulic actuation (Figure 1-5). The electrodes are parylene-coated tungsten wires (30  $\mu\text{m}$  diameter), and each one of them is connected to a stainless steel guide. Each guide is placed inside a channel in the housing, where it acts like a piston. Fluid is pumped into the channel at the back of the guide, pushing the guide and the attached electrode down. The top part of the assembly comprises a routing mechanism, which selects the electrode the fluid should be delivered to, allowing the external hydraulic system to be shared by the electrodes. The channels are sealed when they are not selected, thus maintaining the last set electrode position. Interestingly, the fluid is conductive, and it also provides electrical connection to the electrodes. The signal travels through the electrode, the guide, the fluid, and it is then

passed to a connector. The microdrive hosts 22 electrodes with 350  $\mu\text{m}$  spacing. The assembly is cylindrical, it is 23.5 mm in diameter and 37 mm in height, it weighs 15 g, and it has a vertical movement range of 4 mm.

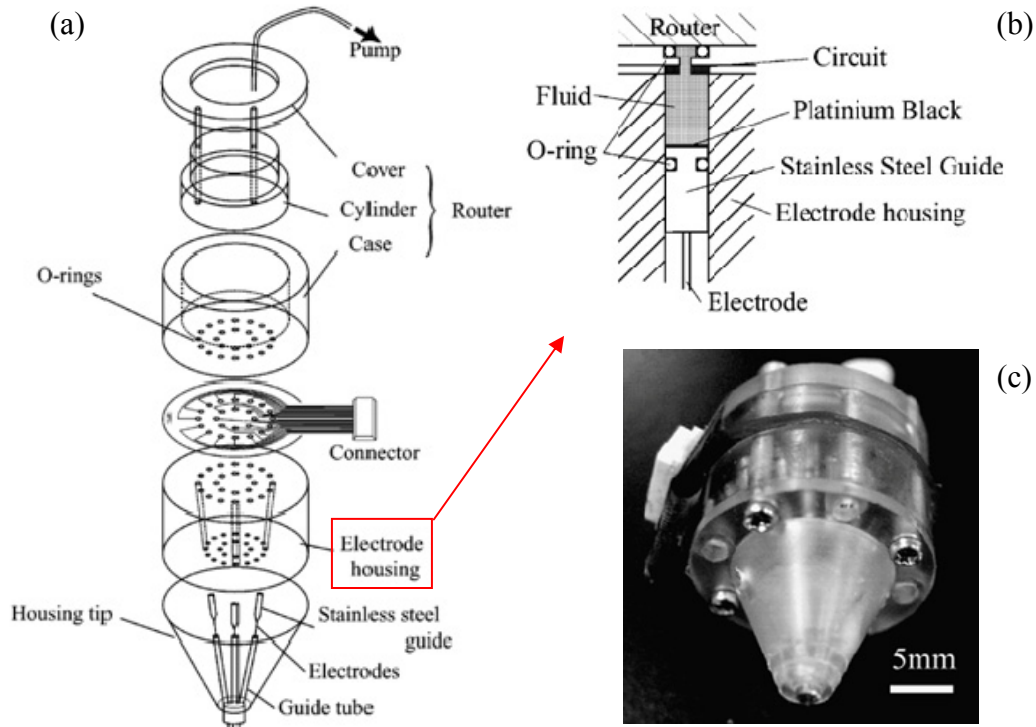


Figure 1-5. Assembly for an electrode array with hydraulic positioning [45]. a) Full schematics of the device. b) Close-up on the fluid and piston system inside each channel in the electrode housing. c) Picture of the assembled device.

A group of researchers at the California Institute of Technology demonstrated a miniature robot for neural recording [46-47]. The device (Figure 1-6) uses 4 custom-made piezoelectric linear microactuators (3 mm in diameter, 22.5 mm in length). The actuators are able to generate displacement with sub-micron accuracy over a 5 mm range, with a maximum force of 30 mN. The electrodes used in this device are glass-coated Pt-Ir

wires (125  $\mu\text{m}$  diameter) sharpened at the tip. An algorithm was also developed to automate the detection of action potentials and the isolation of cells [48-49]. The algorithm starts with a search phase, during which the electrodes are moved in search of action potentials. When action potentials are found, an isolation phase fine-tunes the electrode position in order to maximize the signal quality. If, during the recordings, the signal-to-noise ratio decays below a certain threshold, the algorithm repositions the electrodes automatically to regain the lost signal quality. An improved version of the microdrive, still based on piezoelectric actuators, was developed by the same group [50-51].

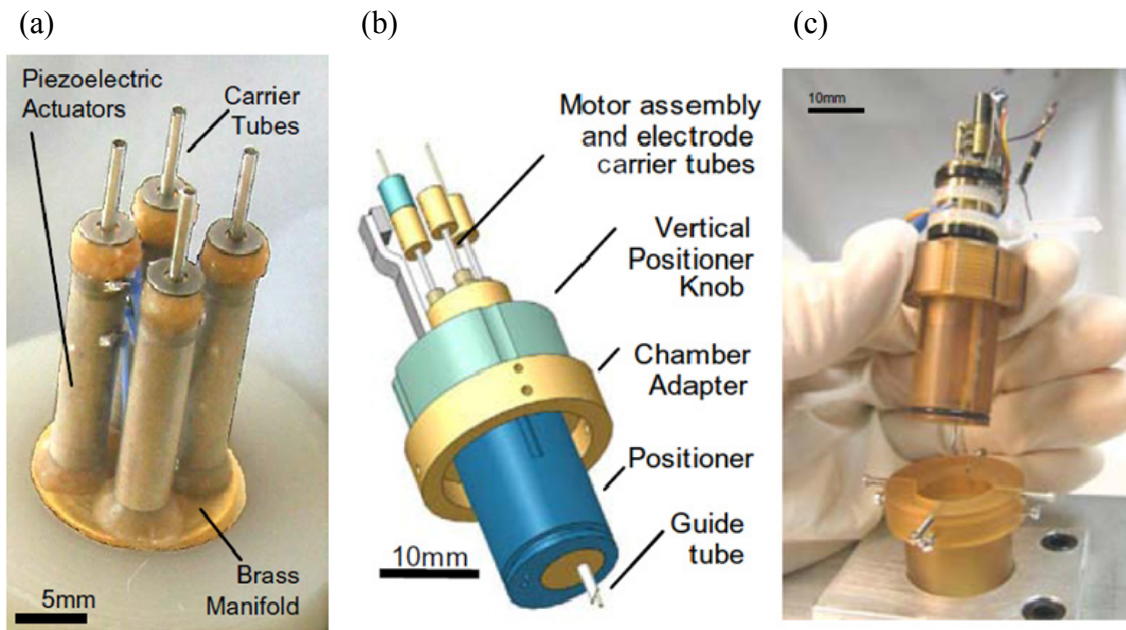


Figure 1-6. Microdrive based on piezoelectric microactuators [46-47]. a) Picture of the four piezoelectric actuators. b) Drawing of the entire assembly. c) Picture of the device being mounted into a cranial chamber.



#### 1.4.4 Commercial Electrode Manipulators

Electrode manipulators are available commercially from several manufacturers, such as Thomas Recording GmbH [52], David Kopf Instruments [53], Alpha Omega Ltd [54], Nan Instruments Ltd [55], FHC Inc. [18], and Narishige [56].

Thomas Recording offers different kinds of manipulators. One is based on the work of Eckhorn and Thomas [57], which improves on the Reitboeck manipulator [58]. The system is designed for thin-shaft probes. A serious limitation of thin-shaft electrodes is buckling when they are pushed into the tissue. This is particularly problematic when the dura or pia are to be penetrated, and the maximum penetration depth is typically limited to a few millimeters. The mechanism proposed by Eckhorn and Thomas is illustrated in Figure 1-7a. The probe is mounted inside a stretched flexible rubber tube, which prevents buckling and transfers force to the probe. At the insertion point, the probe is guided by a capillary clamped to the rubber tube. At the top, the rubber tube is connected to a pulling string that keeps it stretched. By modifying the pulling force of the string, the stretching of the rubber tube changes, causing a large force to be exerted on the probe in the insertion direction. Figure 1-7b shows an array of movable electrodes built around this mechanism. Each pulling string is wound around a drum. The drum is connected to the shaft of a DC micromotor with gear reduction. The motor controls the tensioning of the pulling string, indirectly controlling the position of the probe. The motors are equipped with position sensors, with which a probe position accuracy of 0.27  $\mu\text{m}$  is attainable.

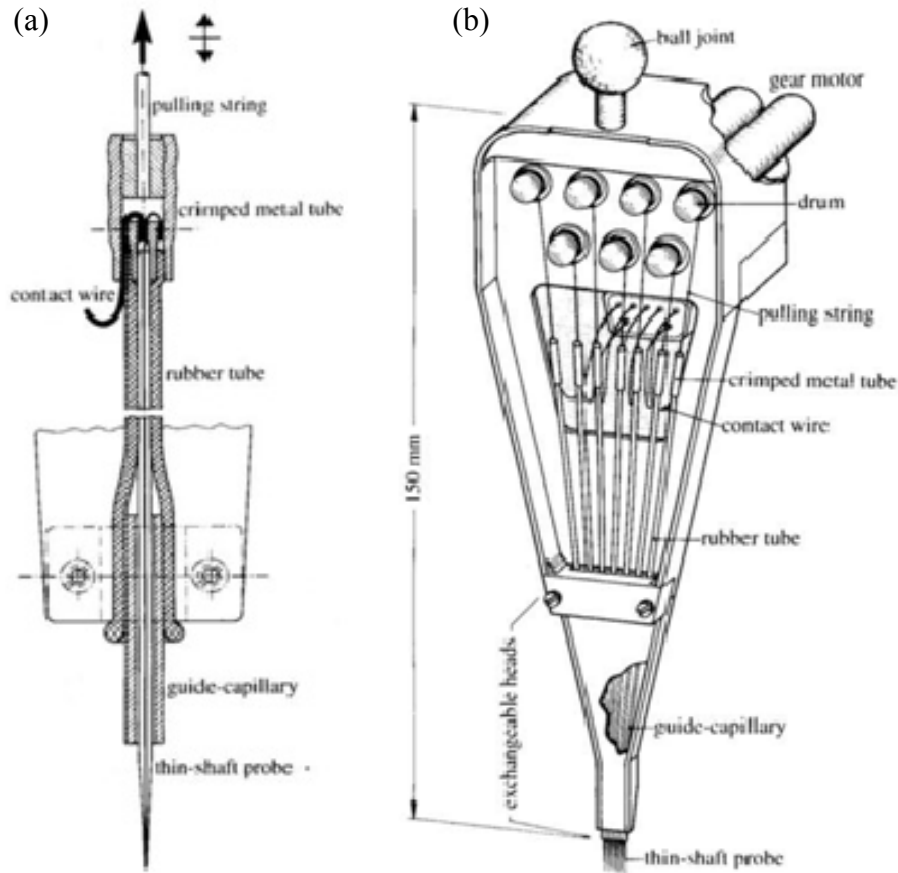


Figure 1-7. Electrode manipulator by Eckhorn and Thomas [57]. a) Cross-section of the manipulation mechanism for each electrode. b) Motorized array of electrodes.

Thomas Recording offers a commercial version of the Eckhorn microdrive in several configurations and up to 16 electrodes. One such device is shown in Figure 1-8. The head is exchangeable, allowing different electrode spacing and arrangements. The system provides 1  $\mu\text{m}$  position accuracy over a range of 20 mm, with controllable speed. This system has been used for numerous recordings, for example in [59-60].

David Kopf Instruments offers hydraulic and direct-drive micropositioners with travel distances up to 50 mm. Hydraulic couplers between the electrodes and the stepping

motors help reduce the vibrations. Recordings were successfully performed using this device, for example in [61].

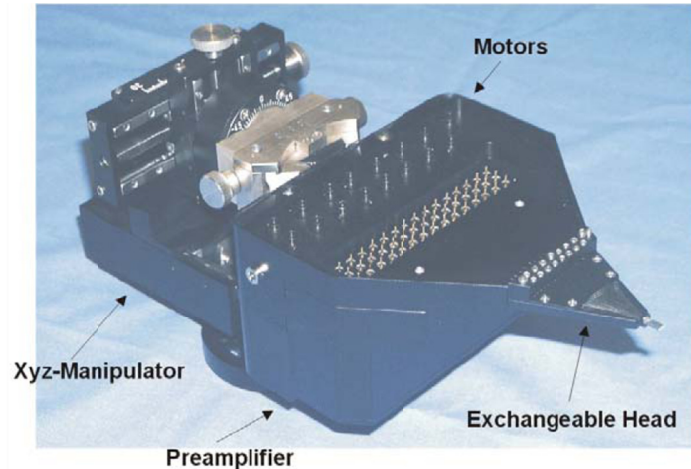


Figure 1-8. Commercial Eckhorn-type system by Thomas Recording.

### 1.4.5 Microactuated Devices

Electrode microactuation mechanisms fabricated by MEMS technology have been demonstrated based on electrostatic [62] and thermal actuation [63].

Two devices, one electrostatically actuated and one thermally actuated, have been demonstrated by Muthuswamy et al., both fabricated using the Sandia's Ultraplanar Multi-level MEMS Technology (SUMMiT V) process by Sandia National Labs. SUMMiT V is a surface micromachining process that uses five polysilicon layers with sacrificial silicon dioxide layers.

The electrostatic device (Figure 1-9) is based on two comb-drives connected to gears. To transfer the movement, teeth on the gears are matched to teeth on the polysilicon probe. The device produces bidirectional translation with about 1  $\mu\text{m}$

accuracy over a 5 mm range. The probe is fabricated together with the actuator, and it consists of a polysilicon slab 50  $\mu\text{m}$  wide and 4  $\mu\text{m}$  thick. The comb-drives are actuated by a voltage of 90 V, with current in the nA range. The force produced is in the  $\mu\text{N}$  range. The system is found to be very sensitive to the alignment of the gears.

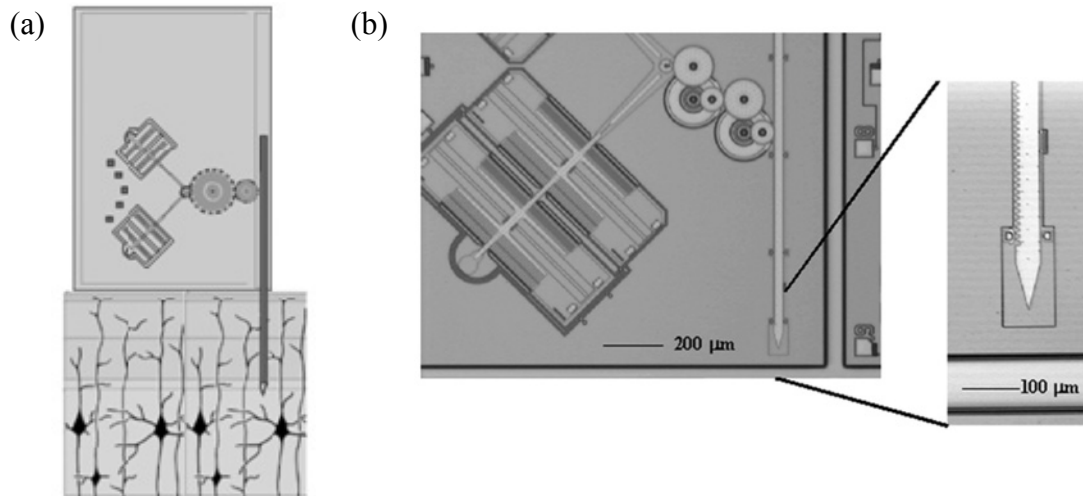


Figure 1-9. Electrostatic microactuator by Muthuswamy et al. [62]. a) Drawing of the actuation principle (not to scale). b) Picture of the fabricated system, with close-up on the probe tip.

The thermally-actuated device is based on angled sets of silicon beams. When current flows through the beams, they heat up and expand, producing in-plane displacement. The system is composed of two almost identical sections like the one shown in Figure 1-10. One section moves the probe forward; the other moves it backward. Each section has two clamps at the sides, which are engaged to keep the probe in position, and released when the probe is moved. A shuttle above the probe generates displacement along the probe axis. The displacement is transferred to the probe by a

ratcheting mechanism. The system produces displacement with  $8.8\text{ }\mu\text{m}$  steps over a range of 2 mm. To disengage the clamps, 10 V and 35 mA are needed. The clamps must be held in the disengaged position while pulses of 10 V and 18 mA are applied to the shuttle to ratchet over one tooth.

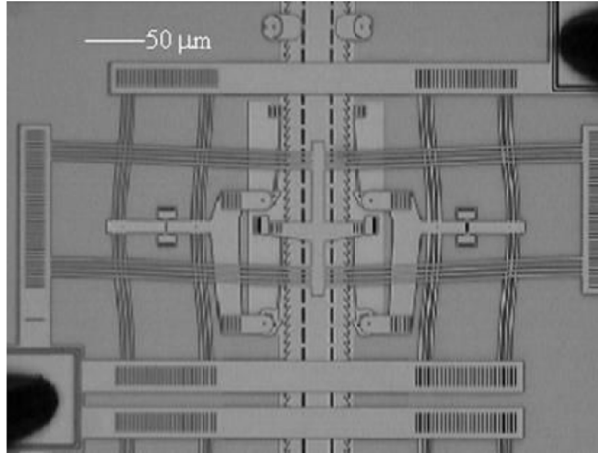


Figure 1-10. Thermal microactuator by Muthuswamy et al. [62]. Only the top half of the system is shown. The picture is taken during actuation.

Another electrostatic MEMS device that can be applied to neural probes has been presented by IMEC [64] (Figure 1-11). The device is fabricated with a SOI Multi-User MEMS Process (SOIMUMPs). In one design, the device is operated at 12 V, with an output force of  $400\text{ }\mu\text{N}$ , a range of  $100\text{ }\mu\text{m}$ , and a step size of 130 nm. The device is packaged with a glass cap.

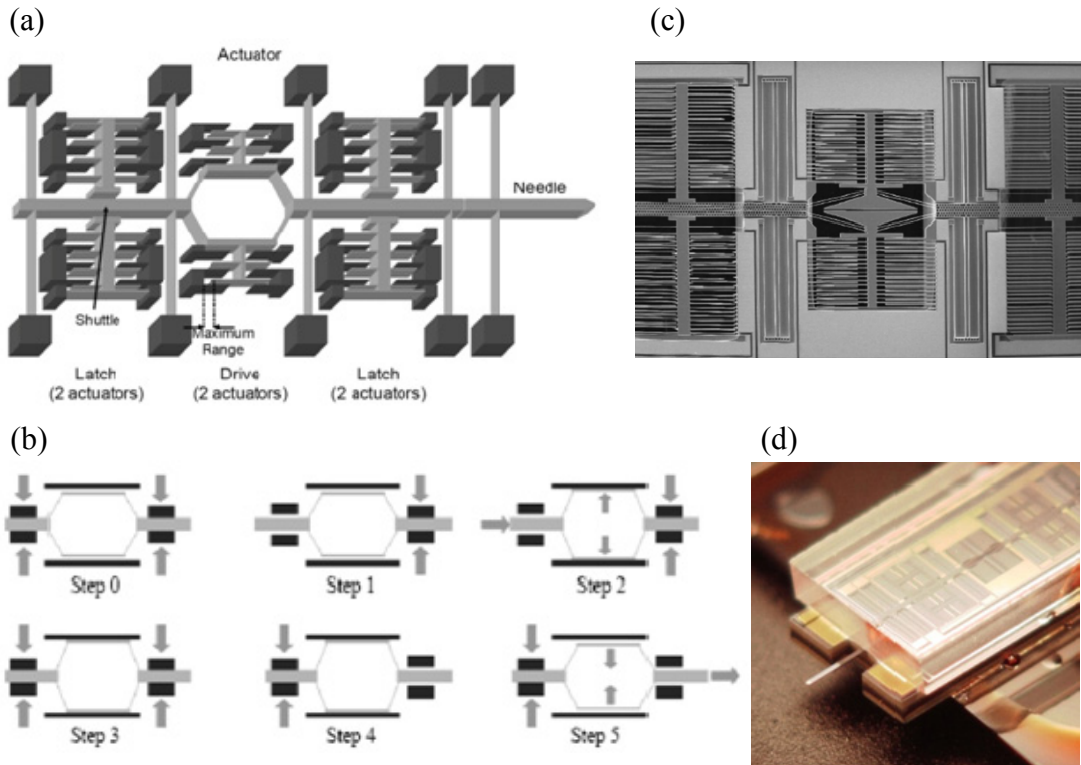


Figure 1-11. Electrostatic microactuator by IMEC [64]. a) Drawing of the actuator structure. b) Actuation principle. c) SEM picture of the fabricated structure. d) Device packaged with a glass cap.

## 1.5 Current Challenges and Actuator Requirements

The previous review of the literature on movable neural probes reveals some of the challenges currently posed by this kind of devices. To evaluate the performance of the reviewed devices, the requirements of an ideal actuator are illustrated in Table 1-1.

First of all, it is desirable for the actuator to fit entirely under the skull. This allows the skull to be completely resealed after implantation, reducing the risk of infections. To meet this requirement, a device must be at most a few millimeters per side and it must not require manual operation. Many motorized actuators are too bulky to fit

under the skull, and the device is left protruding from the head after the implantation surgery. Even though the devices are carefully sealed on the skull, the risk of infections is higher than when the skull is fully resealed. Moreover, difficulties arise in the case of animal testing, as the protruding device may cause injury if touched by the animal, either voluntarily or accidentally. Some of the largest manipulators even require head fixation. As a consequence, the animal has to be restrained for the duration of the recordings, impeding the study of subjects moving and behaving freely. It would be advantageous to also integrate telemetry circuitry on the devices, to eliminate the need for wires across the skull and scalp.

MEMS devices offer a solution to the size problem, but meeting all the other actuation requirements is not trivial. Table 1-2 lists the specifications and performance of the MEMS devices presented in Section 1.4.5. The red underlined items represent the parameters we are mostly concerned about.

Table 1-1: Requirements of an ideal actuator for movable neural probes.

Parameter	Desired/acceptable properties	Motivation/comments
Size requirements		
Dimensions	Small, a few millimeters per side	The device should fit entirely under the skull.
Supply requirements		
Voltage	Low, not higher than a few volts	Voltage higher than a few volts causes electrolysis of the brain fluid if not properly insulated.
Power/heating	Low, with temperature rise less than 1 °C	Heating damage to the surrounding tissue must be prevented. A low-power device could be wirelessly powered, with no cables through the skull.

Mechanical requirements		
Displacement	Large (relative to the size of the device), from hundreds of microns to millimeters	The probe movement range must be sufficient to track neurons and maintain signal quality in long-term implants.
Positioning accuracy	In the micron range	The probe position should be tunable in fine increments.
Force	In the millinewton range	The device must provide enough force for the probe to penetrate the tissue.
Speed	Not a requirement	Slow speed is acceptable, because position adjustments are not frequent and need not be fast. Slow speed may also help prevent tissue damage.
Latchability	Latchable without power	The probe should stay in the last set position when power is turned off. This minimizes power consumption, as probes are typically left in the same position for long times.
Biocompatibility requirements		
Materials	Biocompatible	The inflammatory reaction must be minimized for long-term implantation.
By-products	Biocompatible	If the actuation mechanism produces any by-product during operation, these must not be toxic.
Desirable features		
Choice of probes	Flexible choice	The actuator should be able to handle different kinds of probes, so that the best probe for a specific application can be selected without modifying the actuator.



Table 1-2: Performance comparison of current MEMS movable probes.

	Electrostatic microdrive [62]	Thermal microdrive [63]	Electrostatic microdrive [64]
<b>Displacement range</b>	5 mm (2 mm after insulation)	5 mm (2 mm after insulation)	<u>100 <math>\mu\text{m}</math></u>
<b>Force</b>	<u><math>\mu\text{N}</math></u>	Hundreds of $\mu\text{N}$	400 $\mu\text{N}$
<b>Minimum step</b>	1 $\mu\text{m}$	8.8 $\mu\text{m}$	130 nm
<b>Voltage</b>	<u>90 V</u>	10 V	<u>12 V</u>
<b>Current</b>	nA	<u>18-35 mA</u>	-
<b>Other</b>	<u>4 <math>\mu\text{m}</math> thick probe</u> (obtained with same process as actuator)	-	Devices with different specifications were demonstrated

## 1.6 Electrolytic Inchworms for Movable Neural Probes

### 1.6.1 Electrolytic Inchworm Design

In order to meet the requirements for movable neural probe actuators specified in Table 1-1, we propose a new kind of actuator, a MEMS electrolytic inchworm. The actuator combines MEMS technology, which allows the fabrication of miniaturized devices, with electrolysis-based actuation, which is able to provide large force and displacement while operating at low voltage and low power.

Each inchworm is based on two electrolytic balloon actuators. Each balloon is filled with an electrolyte, and it encloses two electrodes. When electrolysis is run, generation of gas causes the balloon to expand. When electrolysis is stopped, the balloon

relaxes (i.e., shrinks) back to the initial condition, due to gas recombination and permeation through the balloon wall.

The operation principle of the inchworm is schematically illustrated in Figure 1-12. One balloon is used to clamp the probe (“clamping balloon”), the other to provide the displacement (“displacing balloon”). By expanding and shrinking the two balloons in specific sequences, the probe is moved forward or backward. For forward displacement, the probe is first clamped, and then the inchworm is moved by expanding the displacing balloon. For backward displacement, the inchworm is first moved by expanding the displacing balloon, and then the probe is clamped. The probe is moved backward during the relaxation of the displacing balloon.

The electrolytic inchworm design is very convenient for several reasons. First, being an inchworm, it can achieve large displacement in multiple cycles. The maximum displacement is limited only by the length of the probe being moved. Second, the inchworm does not have any mechanical latch or ratchet that imposes a fixed or minimum step size. The displacement per step is determined by the expansion of the displacing balloon, and variable displacement per step is possible. The minimum displacement per step is only determined by the accuracy with which the displacing balloon can be actuated. Third, the actuator design and fabrication are decoupled from the probe’s, and different kinds of probes can be moved by the inchworm. Small modifications may be required to adapt the inchworm to a specific probe, in particular in the clamping section, but the core of the inchworm does not change. Fourth, the electrolytic actuation provides the large force and displacement necessary when moving

neural probes, while operating at low power and low voltage, thus preventing damage to the tissue.

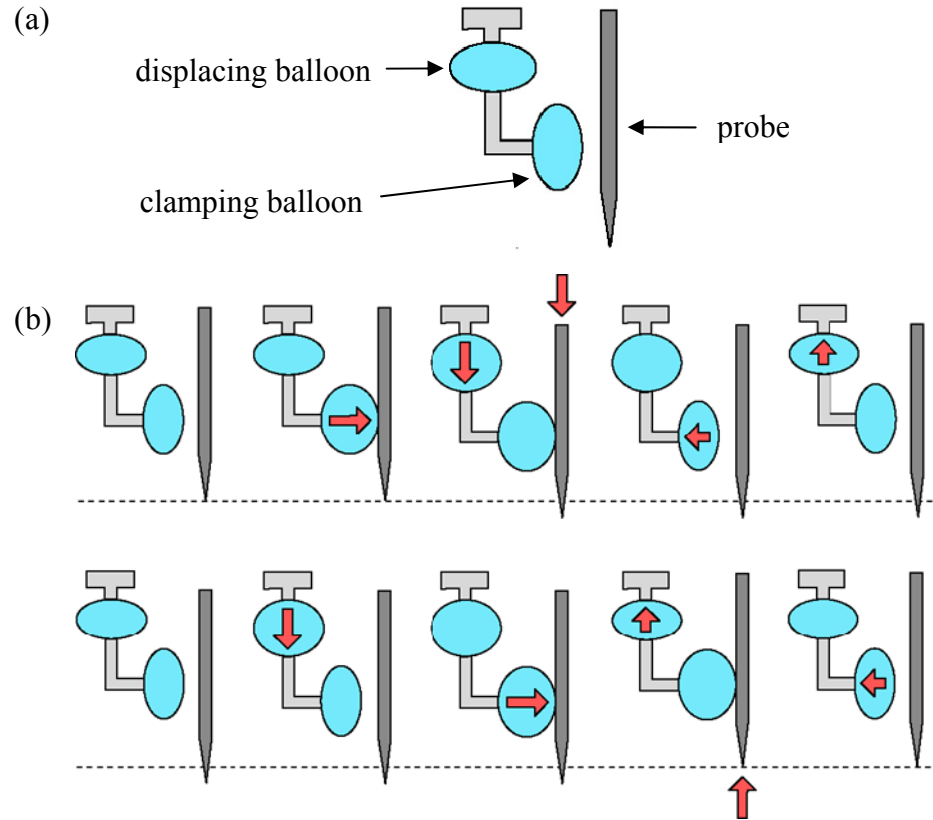


Figure 1-12. a) Schematics of the inchworm. b) Inchworm actuation principle. The first row illustrates forward displacement (downward in the figure), while the second row illustrates backward displacement (upward in the figure).

In the literature, there are many examples of MEMS inchworms. These devices are usually based on more common actuation principles, such as piezoelectric, electrostatic, or thermoelastic. The devices illustrated in Section 1.4.5 are examples of MEMS inchworms specifically designed for movable neural probe applications, and they are either electrostatically or thermally actuated. At the moment of writing, and to the

best of our knowledge, there are no examples of electrolytically-actuated inchworms in literature.

### **1.6.2 Overview of the Chapters**

The balloon actuators are the building blocks of the inchworms, and they are described in detail in Chapter 2. The balloons were first employed in monolithic devices, in which the actuators and the neural probe are on the same devices, as described in Chapter 3. Due to the shortcomings of the monolithic devices, the electrolytic inchworms were developed. The inchworms evolved through two generations. The first generation is the subject of Chapter 4. The performance and reliability issues of the first generation led to the development of a second generation of inchworms, which is examined in Chapter 5. Accurate control of the probe position may require the implementation of feedback mechanisms on the inchworms. Pressure sensors to be integrated into the balloons for feedback purposes are illustrated in Chapter 6.

## CHAPTER 2

---

# Electrolytic Balloon Actuators

This chapter describes the electrolytic balloon actuators that are the building blocks of the inchworms. An overview of water electrolysis as an actuation mechanism is provided, in which electrolysis is compared to other common actuation mechanisms for microfabricated devices, followed by a few examples of electrolysis-based MEMS devices found in literature. The design, fabrication, testing, and modeling of the electrolytic balloon actuators are then examined in detail.

## 2.1 Balloon Actuator Principle

The inchworms we propose in this thesis are based on balloon actuators, which are a convenient method to harness the actuation potential of electrolysis [65]. Figure 2-1 illustrates the phases of one balloon actuation cycle. The device consists of a sealed balloon filled with an electrolyte. The balloon wall is made of a flexible material (polyethylene or silicone in our devices), and it encloses two electrodes to drive electrolysis (made of platinum in our devices). When electrolysis is run inside the balloon, the generated gas produces a pressure increase, causing the balloon to expand. When electrolysis is stopped, two concurrent phenomena cause the relaxation of the balloon. First, oxygen and hydrogen recombine back into water. For the reaction to proceed at a noticeable rate, it must be catalyzed (for example, by the platinum of the electrodes). Second, oxygen and hydrogen permeate through the balloon membrane and escape from the balloon. Both recombination and permeation cause the pressure inside the balloon to

decrease, until the balloon returns to the initial condition. Because of permeation, a net loss of water occurs. However, if the device is operating in water (or body fluid), the balloon can be replenished by osmosis, thus compensating for the water lost by permeation.

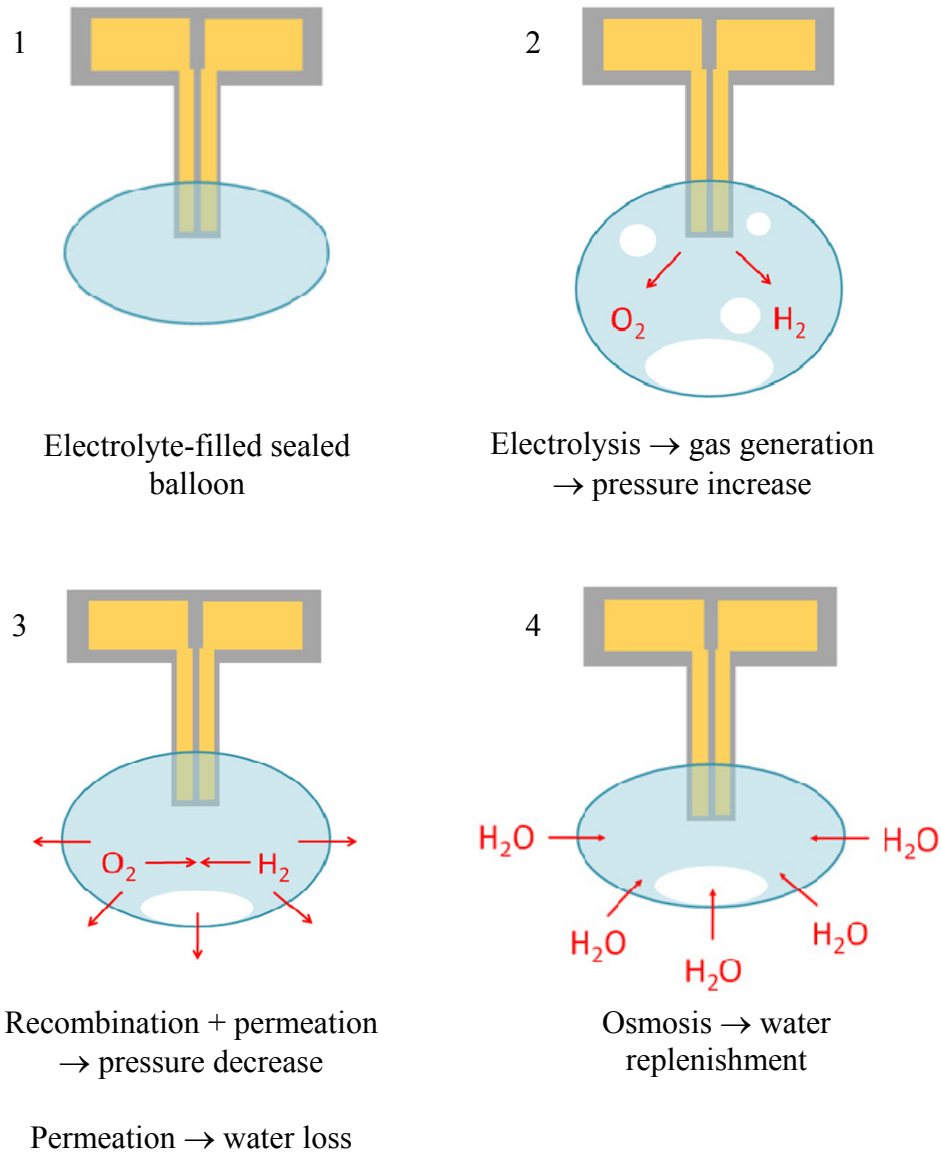


Figure 2-1. Balloon actuation cycle.

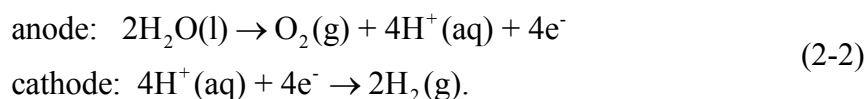
## 2.2 Electrolysis as an Actuation Method

### 2.2.1 Water Electrolysis

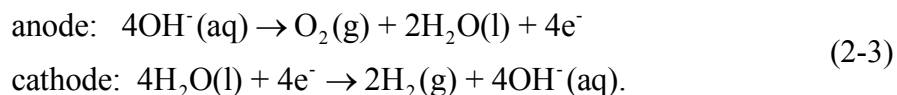
Water electrolysis is the electrochemical process of separating water into its components, hydrogen and oxygen. The overall reaction is



The half-reactions depend on whether the environment is acidic or alkaline. In the acidic form, protons are the charge carriers



In the alkaline form, hydroxyl ions are the charge carriers



The cell standard potential can be calculated from Equation (B-54) to be -1.23 V. The value of  $\Delta G$  for the reaction is positive, which means that the reaction is not spontaneous, and electrical energy must be consumed to drive electrolysis. As for any electrochemical reaction, an overpotential must be applied to have the reaction proceed at a certain speed, and a potential of a few volts is typically used.

It is common to use platinum electrodes for water electrolysis, due to their catalytic action and their chemical stability. Numerous studies have been conducted to find the reaction path at both electrodes, investigate the role of adsorption, and identify

the intermediate products [66]. It was found that the overpotential is mostly due to the oxygen-generating electrode. Water electrolysis is used industrially for hydrogen production, for which it is very important to maximize the efficiency of the process. Electrodes with special nanostructure can increase the surface area [67] and thus reduce the overpotential needed for a certain reaction speed.

The recombination reaction of hydrogen and oxygen to form water is thermodynamically favorable, but it proceeds extremely slowly at room temperature, unless catalyzed. The reaction is exploited in fuel cells, in which the energy released by the reaction is converted into electrical energy. The recombination of hydrogen and oxygen is catalyzed at the surface of electrodes made of platinum group metals (PGMs), i.e., ruthenium, rhodium, palladium, osmium, iridium, and platinum [68-69]. PGMs are transition metals that are close to platinum in the periodic table, and they have similar chemical properties.

### 2.2.2 Electrolysis-based Actuation

The large increase in volume or pressure obtained by converting water into its components gases can be used as an actuation mechanism [70]. One mole of water in standard conditions ( $T = 25\text{ }^{\circ}\text{C}$ ,  $p = 1\text{ atm}$ ) has a volume of 18 cc. The molar volume of water is denoted by  $v_{\text{H}_2\text{O}}$ . If the water is completely converted into the component gases, we obtain one mole of hydrogen and half a mole of oxygen. The volume  $V$  of the resulting gas mixture in the same standard conditions can be computed by Equation (B-39)

$$V = \left( n_{\text{H}_2} + \frac{1}{2} n_{\text{O}_2} \right) \frac{RT}{p} = \frac{3}{2} \frac{RT}{p} = 36700\text{ cc} \quad (2-4)$$



where  $n$  indicates the number of moles of each gas, and  $R$  is the gas constant. The result shows a 2000-fold increase in volume as a consequence of the liquid-gas conversion at constant pressure and temperature. Instead of exploiting the volume increase, we can constrain the gas in the same volume of the liquid water and exploit the pressure increase. The pressure of the gas mixture is

$$p = \left( n_{\text{H}_2} + \frac{1}{2} n_{\text{O}_2} \right) \frac{RT}{v_{\text{H}_2\text{O}}} = 207 \text{ MPa.} \quad (2-5)$$

The result shows a 2000-fold pressure increase at constant volume and temperature. This large increase in volume or pressure can be harnessed for actuation purposes to produce large displacement or large force. A combination of the two techniques can achieve the desired balance of displacement and force.

In addition to the great potential in the mechanical domain, electrolysis has also desirable properties in the electrical domain. Electrolysis runs at low voltage (a few volts), and small currents ( $\ll 1$  mA) are sufficient for actuation of microdevices. The ability to provide large force and displacement while operating at low voltage and low power is the most desirable characteristic of electrolytic actuation.

### 2.2.3 Comparison with Other Actuation Methods

Table 2-1 compares the typical performance of actuation mechanisms used in microdevices. In this table, the voltage is considered high when it is above a few volts, and the current when it is above a few hundred microamperes. The heat dissipation is large if it causes a temperature increase higher than a few degrees Celsius. The force is large if it is at least in the millinewton range, and the displacement is large if it is over

100  $\mu\text{m}$ . Electrostatic actuation, for example, is very popular in microdevices, but it usually requires high voltage (tens of volts), and it is not able to deliver large force or displacement. Thermal actuation is another very common method, because it is able to provide large displacement and force, but it requires a large amount of power, with consequent large heat dissipation.

Table 2-1: Comparison of actuation mechanisms for microdevices.

Actuation Type	Power Supply	Heat Dissipation	Force	Displacement
<b>Electrolysis</b>	Low current Low voltage	Low	Large	Large
<b>Shape-memory alloy</b>	High current High power	High	Large	Large
<b>Piezoelectric</b>	High voltage	Medium	Large	Small
<b>Electromagnetic</b>	High current	High	Medium	Med/Large
<b>Electrostatic</b>	High voltage	Low	Small	Small
<b>Thermo-mechanic</b>	High current High power	Medium/High	Large	Small
<b>Thermo-pneumatic</b>	Low voltage Low/Med current	Medium/High	Large	Large
<b>Electro-osmotic</b>	High voltage	Medium	Large	Small

An in-depth comparison can be made between electrolytic and thermo-pneumatic actuation. Two kinds of thermo-pneumatic actuation are considered: actuation by heating of a gas and actuation by vaporization of water. Bubble generation by electrolysis and boiling are compared in [71-72].

The comparison is made here using the system in Figure 2-2. The system is analogous to a balloon actuator in which the load and the elastic stretching of the balloon wall are neglected. The piston applies a pressure  $p = 1$  atm on the system. This choice of  $p$  is convenient because it is a standard condition, and values for the physical quantities involved are available at this pressure. Initially, the system has volume  $V_0$  and temperature  $T_0$ . After actuation, the system has volume  $V$  and temperature  $T$ . The system is assumed to have no thermal losses to the environment. The actuation process requires a certain amount of energy  $e$ , which partly goes to increase the internal energy of the system by  $\Delta U$  and partly to perform work  $w = p(V - V_0)$ . We, therefore, have the following energy-conservation relation

$$e = \Delta U + w = \Delta U + p(V - V_0). \quad (2-6)$$

For each actuation mechanism, we calculate the efficiency  $\varepsilon$ , defined as the ratio of the work done and the energy supplied to the system

$$\varepsilon = \frac{w}{e} = \frac{w}{\Delta U + w}. \quad (2-7)$$

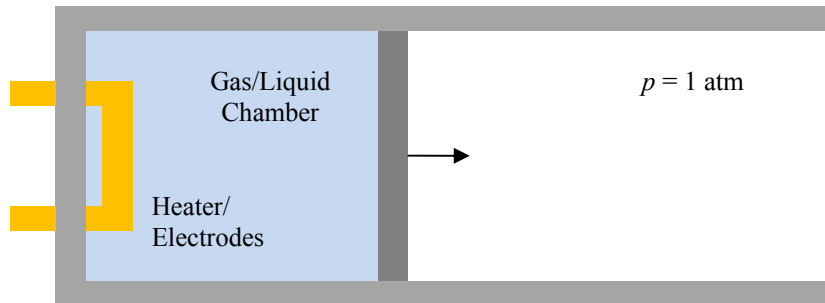


Figure 2-2. Piston system used to compare gas-heating, water-vaporization, and electrolytic actuation.

The case of gas heating is the simplest to analyze. The chamber is assumed filled with  $n$  moles of an ideal gas. Energy is supplied to the gas as heat. To increase the volume to  $V$ , the temperature must be raised by

$$p(V - V_0) = nR(T - T_0) \Rightarrow T - T_0 = \frac{p(V - V_0)}{nR}. \quad (2-8)$$

This corresponds to an increase in internal energy, using Equation (B-38) and assuming a monoatomic gas,

$$\Delta U_{\text{gas}} = \frac{3}{2} nR(T - T_0) = \frac{3}{2} p(V - V_0). \quad (2-9)$$

The efficiency is given by

$$\epsilon_{\text{gas}} = \frac{w}{e} = \frac{w}{\Delta U + w} = \frac{2}{5} = 40\%. \quad (2-10)$$

In the case of a diatomic gas (like  $\text{O}_2$  or  $\text{H}_2$ ), the efficiency changes to  $2/7 = 28.6\%$ .

In the case of water vaporization, the chamber is filled with liquid water at room temperature  $T_0 = 25^\circ\text{C}$ . The amount water (number of moles  $n$ ) in the chamber is such that it generates a volume  $V$  of vapor when completely vaporized at temperature  $T_{\text{vap}}$  and pressure  $p = 1$  atm. The vapor phase is treated like an ideal gas. The amount of water is calculated as

$$pV = nRT_{\text{vap}} \Rightarrow n = \frac{pV}{RT_{\text{vap}}}. \quad (2-11)$$

This corresponds to an initial volume  $V_0 = nv_{\text{H}_2\text{O}}$ , where  $v_{\text{H}_2\text{O}}$  is the molar volume of water. In order to push the piston, the temperature  $T_{\text{vap}}$  of the vapor must be such that the pressure of the vapor is 1 atm. This condition requires  $T_{\text{vap}} = 100\text{ }^\circ\text{C}$ . Energy is supplied to the water as heat. The heat is used first to raise the temperature of the liquid from  $T_0$  to  $T_{\text{vap}}$  and then to vaporize the liquid by providing the heat of vaporization. The energy to be provided is given by

$$e_{\text{vap}} = c_{\text{H}_2\text{O}}n(T_{\text{vap}} - T_0) + n\Delta H_{\text{vap}} = \frac{pV}{RT_{\text{vap}}} \left[ c_{\text{H}_2\text{O}}(T_{\text{vap}} - T_0) + \Delta H_{\text{vap}} \right] \quad (2-12)$$

where  $c_{\text{H}_2\text{O}}$  is the molar heat capacity of water, assumed constant over the temperature range, and  $\Delta H_{\text{vap}}$  is the molar heat of vaporization. Because vaporization causes a very large volume increase, we can assume  $V_0 \ll V$ , so that  $w = pV$ . We obtain a simplified expression for efficiency

$$\varepsilon_{\text{vap}} \approx \frac{1}{\frac{1}{RT_{\text{vap}}} \left[ c_{\text{H}_2\text{O}}(T_{\text{vap}} - T_0) + \Delta H_{\text{vap}} \right]} = 6.7\%. \quad (2-13)$$

This calculation assumes that the amount of liquid water is such that it is completely vaporized. If the initial amount of liquid water is larger, the efficiency of the system decreases. In fact, the whole volume of water must be heated to  $100\text{ }^\circ\text{C}$ , even if only part of it needs to be vaporized (uniform temperature across the system is assumed).

Similarly to the case of water vaporization, in the case of water electrolysis, the chamber is filled with liquid water at room temperature  $T_0 = 25\text{ }^\circ\text{C}$ . The amount of water (number of moles  $n$ ) in the chamber is such that it generates a volume  $V$  of gas when

completely electrolyzed. The energy supplied is electrical energy. The energy is used to separate water into its components, and it is stored as chemical energy in them. Electrolysis is assumed to run without dissipation to heat due to an overpotential. Therefore, the final temperature is equal to the initial one,  $T = T_0$ . The gas phase is treated like an ideal gas, so the moles of gas needed to create a volume  $V$  at 1 atm is

$$pV = nRT_0 \Rightarrow n = \frac{pV}{RT_0}. \quad (2-14)$$

To create  $n$  moles of oxygen and hydrogen mixture we need to electrolyze  $2/3 n$  moles of water. To transform water into oxygen and hydrogen, we need to provide the negative of the enthalpy of formation

$$e_{\text{el}} = -\frac{2}{3}n\Delta H_f = -\frac{2}{3}\frac{pV}{RT_0}\Delta H_f. \quad (2-15)$$

As explained above, it is justified to assume  $V_0 \ll V$  to simplify the formula for the efficiency

$$\varepsilon_{\text{el}} \approx \frac{1}{\frac{2}{3}\frac{1}{RT_0}\Delta H_f} = 1.3\%. \quad (2-16)$$

From the calculations above, the gas-heating method is found to be the most energy efficient. In the case of water vaporization, energy must be supplied to heat and vaporize the liquid, while, in the case of electrolysis, energy must be supplied to separate water into its components. These additional energy expenditures are not involved in the

gas-heating method, making it more efficient. However, with the gas-heating method, a relative increase in volume requires the same relative increase in temperature (in Kelvin)

$$\frac{V - V_0}{V_0} = \frac{T - T_0}{T_0}. \quad (2-17)$$

For example, for a 10% increase in volume starting from  $T_0 = 25\text{ }^{\circ}\text{C}$ , the temperature must be raised to  $T = 54.8\text{ }^{\circ}\text{C}$ . This kind of temperature increase is not tolerable in an implant device.

Water vaporization is found to be more energy efficient than electrolysis. As pointed out before, this is only true if there is not a large amount of liquid water to heat up. Also, a large temperature increase is needed to vaporize the water, and damage to the surrounding tissue may ensue in implant devices.

The efficiency advantage of gas heating and water vaporization are lost in practice if we introduce heat losses in the system. It is observed experimentally that electrolysis runs at power four orders of magnitude lower than water vaporization [71].

Electrolysis has the advantage of not requiring a temperature increase. Gas molecules are generated by supplying chemical energy, not thermal energy. Moreover, the chemical energy stored in oxygen and hydrogen can in principle be recovered by a fuel-cell mechanism, which would increase the efficiency of the system dramatically. In practice, the conditions are not ideal even for electrolysis, and dissipation to heat generally consumes a considerable part of the energy supplied, due to the overpotential that must be applied to sustain a certain current. However, the heat dissipation rate can be kept low with electrolysis, thus limiting the temperature increase. In fact, electrolysis can

be run over longer periods of time compared to gas heating or water vaporization, where heat must be supplied quickly to overcome heat losses.

Water vaporization and electrolysis also differ in the way the bubbles are removed. Water vapor bubbles are removed by natural condensation. In order for this to be fast, the system must have thermal losses, which reduce the energy efficiency of actuation. Electrogenerated bubbles are made of oxygen and hydrogen, and they are removed by their recombination into water. This reaction proceeds very slowly unless catalyzed (by platinum, for example). Another option for bubble removal, which works with both actuation methods, is to use a permeable membrane and let the gases escape from the device. However, this causes a net loss of water from the system.

## **2.2.4 Electrolysis-based Microdevices**

There are several examples of electrolysis-based microdevices in literature. A microvalve based on electrolytic actuation was demonstrated [73] (Figure 2-3). The channel is controlled by a gate, which has arms that protrude laterally into an electrolysis chamber. Producing gas bubbles on the front or back side of the lateral arms pushes the gate into the open or closed position respectively.

Electrolysis has also been used for several kinds of microfluidic pumps. In [74], electrolysis bubbles push a liquid through a spray nozzle (Figure 2-4a). In [75], a bubble pushes a liquid through a channel (Figure 2-4b). Due to the surface roughness gradient in the channel, the gas bubble shrinks faster on one side than on the other, causing a net flow of liquid in the channel at the end of a cycle. In another pump, a liquid is pushed by an electrolysis-generated bubble, which is finally vented through a hydrophobic



membrane [76]. In another instance, liquid is pumped by the growth of a sequence of bubbles in a channel [77].

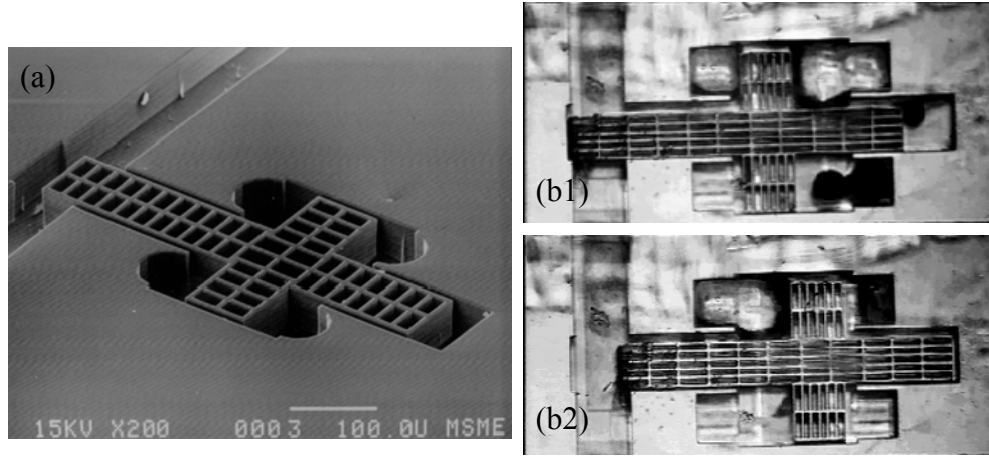


Figure 2-3. Electrolysis-actuated gate valve [73]. a) SEM picture of the device. b1) Gate in closed position. b2) Gate in open position.

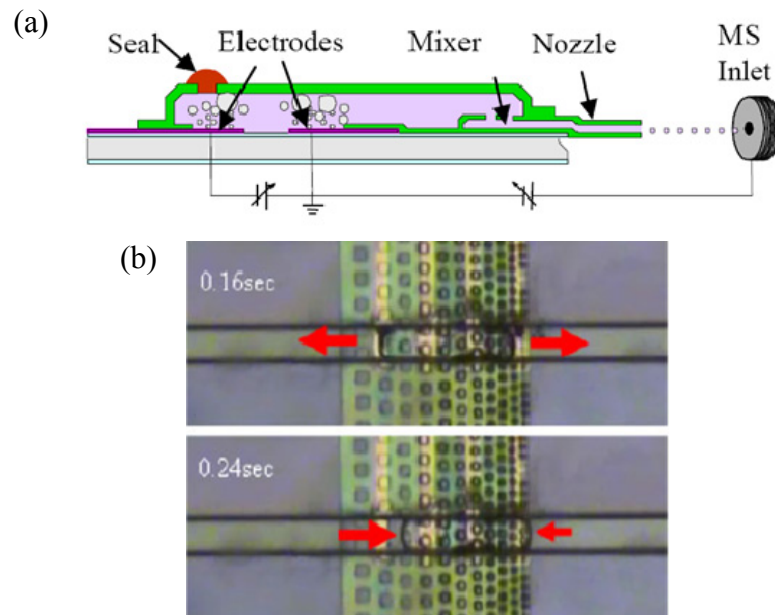


Figure 2-4. Electrolysis-actuated pumps. a) Pump for spray application [74]. b) Pump based on surface roughness gradient [75].

Electrolysis-based diaphragm actuators have been demonstrated in our group [78]. Electrolysis is run inside a sealed microfabricated chamber, and the pressure increase is exploited to deflect a diaphragm on top of the chamber.

## 2.3 Balloon Design

The deformation of the balloons was simulated using a 3D shell model in COMSOL. The balloons are modeled as ellipsoids (Figure 2-5), with spherical balloons being a particular case. The two semiaxes of the ellipsoid perpendicular to the displacement direction are set to 500  $\mu\text{m}$ . The third semiaxis, parallel to the displacement direction, has variable length. The balloon wall is made of 10- $\mu\text{m}$  thick parylene C. A pressure of 10 psi is applied inside the balloon, and the expansion of the balloon along the displacement direction is measured. Figure 2-5 reports the displacement obtained for different lengths of the variable semiaxis. We notice that, for the same internal pressure, more elliptical shapes provide larger displacement in the desired direction, because a larger fraction of the balloon surface, over which the pressure acts, is perpendicular to the displacement direction. Theoretical formulas are available for spherical balloons, i.e., hollow spheres subject to internal pressure [79].

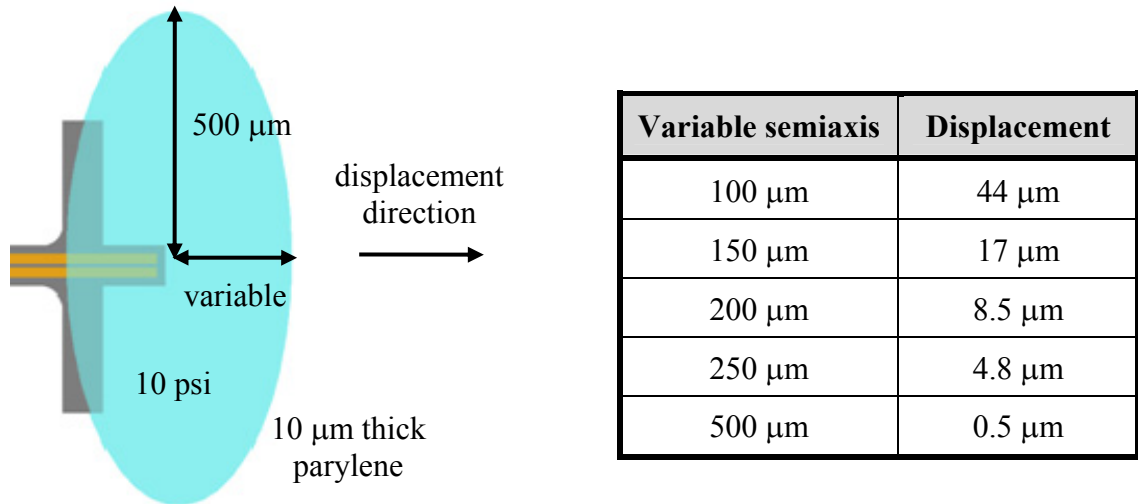


Figure 2-5. Geometry and results of the ellipsoidal balloon simulation.

## 2.4 Balloon Modeling

### 2.4.1 Model

A model for the balloons was developed to understand and predict their behavior. The model takes the current flowing through the electrodes as input. Given a current waveform, the model keeps track of the amount of water, hydrogen, oxygen and nitrogen (permeating into the balloon from the external environment) in the balloon as a function of time. From these amounts, other important quantities are derived, in particular the balloon internal pressure as a function of time.

There are two coexisting phases in the balloon: a liquid phase and a gas phase. By assumption, the liquid phase is composed exclusively of water, while the gas phase is composed exclusively of oxygen, hydrogen, and nitrogen. We ignore the presence of water vapor in the gas phase and the presence of gases in solution in water. The volumes

of the two phases  $V_{\text{gas}}$  and  $V_{\text{liq}}$  vary with time, and they are constrained by the volume of the balloon

$$V = V_{\text{gas}}(t) + V_{\text{liq}}(t). \quad (2-18)$$

The balloon volume  $V$  is known from the geometry of the device and assumed fixed.

The first step is to relate the volumes of the phases to the amounts of the components inside them. The amount of component  $x$  is expressed in moles, and indicated by  $n_x$ . The volume of the liquid phase is simply related to the amount of water present in the balloon through the molar volume of water  $v_{\text{H}_2\text{O}}$

$$V_{\text{liq}}(t) = v_{\text{H}_2\text{O}} \cdot n_{\text{H}_2\text{O}}(t). \quad (2-19)$$

The gas phase is treated like an ideal gas mixture. The partial pressure  $p_x$  of each gas is expressed using (B-40)

$$p_{\text{O}_2}(t) = \frac{n_{\text{O}_2}(t)RT}{V_{\text{gas}}(t)} \quad p_{\text{H}_2}(t) = \frac{n_{\text{H}_2}(t)RT}{V_{\text{gas}}(t)} \quad p_{\text{N}_2}(t) = \frac{n_{\text{N}_2}(t)RT}{V_{\text{gas}}(t)}. \quad (2-20)$$

The total pressure  $p$  in the balloon is assumed uniform across the two phases. The balloon pressure is easily calculated in the gas phase, as it is the sum of the partial pressures of the gases, as stated by Equation (B-41),

$$p(t) = p_{\text{O}_2}(t) + p_{\text{H}_2}(t) + p_{\text{N}_2}(t). \quad (2-21)$$

This completes the relations between the component amounts, the phase volumes, and the pressure in the balloon.

The second step is to model the variations in the amounts of water and gases inside the balloon. There are three phenomena that determine these variations: generation of hydrogen and oxygen by electrolysis (with consumption of water), recombination of hydrogen and oxygen back into water, and permeation of gases and water through the balloon wall. Mass balance equations are written for each component

$$\begin{aligned}
 \frac{dn_{\text{O}_2}(t)}{dt} &= g_{\text{O}_2}(t) - r_{\text{O}_2}(t) - f_{\text{O}_2}(t) \\
 \frac{dn_{\text{H}_2}(t)}{dt} &= g_{\text{H}_2}(t) - r_{\text{H}_2}(t) - f_{\text{H}_2}(t) \\
 \frac{dn_{\text{H}_2\text{O}}(t)}{dt} &= g_{\text{H}_2\text{O}}(t) - r_{\text{H}_2\text{O}}(t) - f_{\text{H}_2\text{O}}(t) \\
 \frac{dn_{\text{N}_2}(t)}{dt} &= -f_{\text{N}_2}(t).
 \end{aligned} \tag{2-22}$$

Each term on the right side of the equations models one of the mechanisms mentioned above. The  $g_x$  terms represent the effect of electrolysis. Electrolysis causes the generation of hydrogen and oxygen while consuming water. Due to the stoichiometry of the reaction, for every two water molecules that are consumed, two molecules of hydrogen and one molecule of oxygen are produced. Each time this reaction occurs, four electrons flow in the system. We normalize all the generation terms with respect to the oxygen term, and we get

$$g_{\text{O}_2}(t) = g(t) \quad g_{\text{H}_2}(t) = 2g(t) \quad g_{\text{H}_2\text{O}}(t) = -2g(t). \tag{2-23}$$

When we consider the electron flow, the generation is related to the current  $i(t)$  by

$$g(t) = \frac{i(t)}{4F}. \quad (2-24)$$

The factor 4 in the denominator represents the fact that 4 electrons are needed to generate one molecule of oxygen. Since  $g(t)$  is measured in mol/s, the Faraday constant  $F$  is needed to match the units.

In the balloon, the electrodes are very close to each other. The small separation implies a short distance for the ionic current to travel, which reduces the ohmic losses in the solution. However, the small separation also causes the generated gases to mix easily immediately after generation. This mixing, in presence of the platinum electrodes, causes some recombination to occur. This type of recombination occurs only when electrolysis is running. We call this phenomenon “early recombination,” to distinguish it from the “regular” recombination that occurs also when electrolysis is not running. The choice of separation distance between the electrodes is therefore dictated by a tradeoff between reducing the ohmic losses and reducing early recombination. As a consequence of early recombination, only a fraction of the generated gases actually leaves the electrodes and contributes to the gas phase in the balloon. This fact is included in the model by modifying Equation (2-24) to

$$g(t) = \varepsilon \frac{i(t)}{4F}. \quad (2-25)$$

The term  $\varepsilon$  is a current-efficiency factor, and it takes values from 0 to 1. It represents the fraction of generated gases that escapes early recombination and thus contributes to the gas phase in the balloon.

The  $r_x$  terms in Equation (2-22) represent the recombination of hydrogen and oxygen back into water. This recombination does not include the early recombination during electrolysis, which is already accounted for by the current-efficiency factor  $\varepsilon$ . The stoichiometry of the reaction  $2\text{H}_2 + \text{O}_2 \leftrightarrow 2\text{H}_2\text{O}$  is again taken into account, and all the terms are normalized with respect to oxygen

$$r_{\text{O}_2}(t) = r(t) \quad r_{\text{H}_2}(t) = 2r(t) \quad r_{\text{H}_2\text{O}}(t) = -2r(t). \quad (2-26)$$

The reaction rate of oxygen and hydrogen at room temperature in absence of a catalyst is extremely slow. Therefore, the recombination reaction should only occur in proximity of the electrodes. During regular balloon operation, the electrodes are always immersed in the liquid phase, implying that recombination occurs between oxygen and hydrogen in solution. Even though we neglected the amount of gases in solution in the accounting of the component amounts, we still consider their recombination, as if the reaction occurred directly in the gas phase. A simple reaction kinetics model can be assumed here

$$r(t) = kC_{\text{H}_2}^2(t)C_{\text{O}_2}(t) \quad (2-27)$$

where  $C$  indicates concentration. This kinetics model has not been experimentally validated, because permeation is found to dominate on recombination in our devices. Experiments can be devised to validate and, if necessary, alter the expression of the reaction kinetics.

The  $f_x$  terms in Equation (2-22) represent the permeation through the balloon wall. The mathematical treatment of permeation is illustrated in Section B.1.6. For gases, the permeation flux is assumed proportional to the partial pressure gradient

$$f_x(t) = c_x \frac{A}{h} \Delta p_x(t). \quad (2-28)$$

In this equation,  $x$  refers to  $O_2$ ,  $H_2$  or  $N_2$ ,  $A$  is the surface area of the balloon,  $h$  is the thickness of the balloon walls,  $c_x$  is the permeability coefficient for gas  $x$ , and  $\Delta p_x$  is the partial pressure gradient between the inside and the outside of the balloon. Gas permeation is assumed to occur over the whole surface area of the balloon, not just the surface area in contact with the gas phase. This is justified by the fact that the two phases are assumed to be in equilibrium at all times, so that the chemical potential of each component is the same in both phases. Even though solubility was neglected when accounting for the composition of each phase (because it has negligible effects on the components' amounts), its effect on permeation is accounted for, as it is for recombination.

The analysis of permeation is extended to water. Permeation of water is assumed proportional to the pressure of its saturated vapor, for which data is available in literature. This is justified by the fact that the chemical potential of a substance is the same in the liquid as in the saturated vapor. As for gases, permeation is assumed to occur over the whole surface area of the balloon, not just from the surface in contact with the liquid phase. Even though the presence of water vapor in the gas phase was neglected in terms of composition, the effect on permeation is accounted for. The vapor pressure of water is affected by the “external” pressure caused by the presence of the other gases. As explained in [80], the vapor pressure of water is related to the external pressure by

$$p_{\text{vap}}(p) = p_{\text{vap}}^0 e^{\frac{v_{\text{H}_2\text{O}} P_e}{RT}} \quad (2-29)$$



where  $p_{\text{vap}}$  is the vapor pressure,  $p_e$  is the pressure caused by the other gases,  $p_{\text{vap}}^0$  is the vapor pressure in absence of other gases, and  $v_{\text{H}_2\text{O}}$  is the molar volume of water. For water, the vapor pressure increases only by 7.6% when  $p_e = 100$  atm. Given that our devices work at pressures of tens of psi at most, the vapor pressure variation is minimal, and it can be neglected in our analysis. Therefore, the permeation of water is taken as constant

$$f_{\text{H}_2\text{O}}(t) = c_{\text{H}_2\text{O}} \frac{A}{h} \quad (2-30)$$

where  $c_{\text{H}_2\text{O}}$  is the water vapor permeability. The unit of  $c_{\text{H}_2\text{O}}$  is different from that of the gas permeability coefficients, due to the lack of dependence on the pressure gradient. The water vapor permeability coefficient available in literature is usually measured between a phase with 0% relative humidity and one with 90% relative humidity. Inside the balloon the humidity is 100% (saturated vapor), while it is usually lower outside when the device is operated in air. If needed, the permeability coefficient can be adjusted for the relative humidity difference between the inside and the outside of the balloon.

The mass balance equations constitute a system of first-order non-linear ordinary differential equations, and initial conditions are needed for their solution. The initial conditions are the amounts of each component inside the balloon at time  $t = 0$ . Equivalently, the initial volume of the gas phase and its composition can be specified as initial conditions. The gas phase is considered to be initially in equilibrium with the external environment, and, therefore, it has the same composition as air. The characteristics of the external environment are also necessary to determine the permeation-driving gradients. It is sufficient to specify the relative humidity and the

partial pressures of  $O_2$ ,  $H_2$ , and  $N_2$  in the environment. The geometry of the balloon is specified by the volume, the surface area and the wall thickness. If a specific shape is assumed for the balloon (spherical, hemispherical, ellipsoidal, cylindrical, and so on), the volume and surface area are related to each other. The source term of the mass balance equation system is represented by the applied current  $i(t)$ .

In summary, there are several parameters in the model. Some of the parameters are known and fixed, while others are varied for data fitting. The fixed parameters are

- balloon geometry: volume  $V$ , surface area  $A$ , and wall thickness  $h$ ;
- external environment: partial pressure of  $O_2$ ,  $H_2$ , and  $N_2$ , and relative humidity;
- other known and fixed conditions: temperature  $T$ .

The fitting parameters are

- electrolysis current efficiency  $\varepsilon$ ,
- recombination kinetic coefficient  $k$ ,
- permeability coefficients for water and gases  $c_{O_2}$ ,  $c_{H_2}$ ,  $c_{N_2}$ , and  $c_{H_2O}$ .

The values of the fitting parameters are influenced by the inexact knowledge of some of the fixed parameters and initial conditions. For example, inexact knowledge of the initial volume of gas in the balloon strongly affects the estimation of the current efficiency (as it is explained in Section 2.4.2).

The values of the fitting parameters are limited to certain ranges. First, the values of the parameters must be physically meaningful. Second, for some parameters there are values available in literature, and those are used as starting points. The permeability coefficients are an example. If values are found in literature, they are varied only if a satisfactory fit is not possible with those values. Significant variations in permeability

are, in fact, possible, because the permeability is sensitive to the material deposition and treatment. Moreover, the apparent discrepancy in permeation rate between the fitting and the literature may not be due to the permeability itself, but to the inexact knowledge of the balloon geometry (surface area and thickness of the balloon wall).

The equations are not solved analytically, but they are implemented numerically using a finite-difference method. The equations are symbolically manipulated with Maple (Waterloo Maple, Inc.), and numerically solved with Matlab (The MathWorks, Inc.).

## 2.4.2 Sensitivity to Initial Conditions

The amount of gas initially in the balloon, mathematically represented by  $V_{\text{gas}}(0)$ , has a strong effect on the balloon behavior. This effect has an intuitive explanation. If the initial volume of the gas phase is very small (i.e., the balloon is almost completely filled with water), the generation of even a small amount of gas causes the pressure to increase significantly. If the initial volume of the gas phase is large, more gas needs to be generated to cause the same pressure increase.

A simplified example well explains the magnitude of the effect. We assume that the current is applied in a very short burst, so that the effect of permeation and recombination is negligible. We also assume that the volume of water consumed is negligible. In this simplified situation, the volume of the gas phase does not vary. The number of gas molecules needed to increase the pressure by a certain amount is proportional to the gas volume. A balloon with  $V_{\text{gas}}(0) = 0.1V$  (i.e.,  $V_{\text{gas}}(0)$  equal to 10% of the total balloon volume) requires ten times more generated gas than a balloon with  $V_{\text{gas}}(0) = 0.01V$  to produce the same pressure increase.

The amount of gas in the balloon is determined by the history of the device, which causes drift in the properties of the balloon with time. The drift can be predicted by the model, but due to inaccuracies in the model and its parameters, the predictions lose their accuracy in the long run.

### 2.4.3 Refined Model

A refined version of the model is needed in some situations, in particular when the balloon expansion is large or the device is operated in water. The balloon model is refined by generalizing the treatment of some phenomena and by relaxing some assumptions. The improved version of the model includes the following:

- expansion of the balloon volume with internal pressure,
- more general modeling of water permeation to include osmosis,
- gas solubility into water.

In this section, we analyze each of these refinements.

The balloon volume is considered fixed in the first version of the model. This assumption is justified if the balloon expansion is negligible compared to its volume at rest. When parylene is used for the balloon wall, this assumption is usually acceptable. However, when silicone is used, the low elastic modulus allows the balloon to expand significantly, and the fixed volume assumption is not accurate. The variation of volume  $V$  with pressure is approximated by a linear relationship

$$V(t) = V_0 \left[ 1 + \beta (p(t) - p_{\text{atm}}) \right] \quad (2-31)$$

where  $p$  is the balloon internal pressure,  $p_{\text{atm}}$  is the external atmospheric pressure,  $V_0$  is the volume at rest (i.e., when the internal pressure is equal to the atmospheric pressure),

and  $\beta$  is a proportionality constant. To be more accurate, a full finite-element simulation of the balloon expansion as a function of pressure should be done. However, the fabrication process produces large variations in the geometric parameters of the balloons, and these variations would strongly affect the results of the simulation. Therefore, the accuracy of the simulation would not be guaranteed to be better than a simple model like the linear approximation above. The dependence of the volume on pressure causes the equations to be much harder to solve. To simplify the solution, the volume-pressure relation above is not inserted directly into the mass balance equations. In each time step of the numerical solution of the mass balance equations, the balloon volume is considered fixed. The solution of the mass balance equations is then used to calculate the current balloon volume, which is updated for the following time step.

The modeling of water permeation is generalized. The objective is to extend the model to the case of a balloon containing an electrolyte solution and operating in water (or in an aqueous solution), where water can permeate in either direction due to osmosis. The permeation of water is assumed proportional to the chemical potential difference between the inside ( $\mu_{\text{H}_2\text{O}_i}$ ) and the outside ( $\mu_{\text{H}_2\text{O}_o}$ ) of the balloon

$$f_{\text{H}_2\text{O}}(t) = c_{\text{H}_2\text{O}} \frac{A}{h} \Delta\mu_{\text{H}_2\text{O}}(t) = c_{\text{H}_2\text{O}} \frac{A}{h} [\mu_{\text{H}_2\text{O}_i}(t) - \mu_{\text{H}_2\text{O}_o}(t)]. \quad (2-32)$$

If an electrolyte (i.e., a solution of some solute in water) is present inside the balloon, the chemical potential of water inside the balloon is calculated using the equations for ideal and non-ideal solutions illustrated in Section B.1.3. The chemical potential of pure water can be taken as a reference, because we are only interested in the chemical potential gradients, and that term would cancel anyway when taking the difference

$$\mu_{\text{H}_2\text{O}_i}(t) = RT \ln \gamma x_{\text{H}_2\text{O}}(t) = RT \ln \gamma \frac{n_{\text{H}_2\text{O}}(t)}{n_{\text{H}_2\text{O}}(t) + i_{\text{vh}} \cdot n_{\text{sol}}(t)}. \quad (2-33)$$

The term  $x_{\text{H}_2\text{O}}$  is the molar fraction of water in the liquid phase, and  $\gamma$  is the activity coefficient, which accounts for the non-ideality of the solution. The term  $n_{\text{sol}}$  represents the moles of solute in solution. The total amount of solute in the balloon is fixed, because no solute is assumed to permeate into or out of the balloon. However, the amount of solute actually in solution may be smaller, due to the solubility limit. The amount  $n_{\text{sol}}$  cannot be higher than the solubility of the solute in water, and it is, therefore, capped at that value, while the excess solute is assumed to precipitate in solid form (with negligible volume). The term  $i_{\text{vh}}$  is the Van't Hoff factor (indicated by the traditional  $i$ , with a subscript to avoid confusion with current), which accounts for the dissociation of the solute molecules in water. The chemical potential of water is affected not only by the composition, but also by the pressure of the other gases in contact with water. However, as explained by Equation (2-29), the effect of pressure is negligible at the typical balloon operational pressure.

The chemical potential of water outside the balloon is calculated in different ways depending on whether the environment is a liquid or air. If the environment is a water solution, Equation (2-33) holds there too. If the environment is air, we consider the relative humidity instead of the molar fraction.

The permeability coefficient of water is calculated from the water vapor permeability given in literature. In literature, the permeation between a phase at 90% relative humidity and one at 0% relative humidity is usually measured. We calculate the difference in chemical potential between these two phases, and we divide the

permeability coefficient by this amount, to find the permeability coefficient per unit of chemical potential gradient. This is used as the coefficient  $c_{\text{H}_2\text{O}}$  in Equation (2-33).

In the first version of the model,  $\text{O}_2$ ,  $\text{H}_2$ , and  $\text{N}_2$  were considered to be present only in the gas phase. However, these gases are soluble in water, and they are present also in the liquid phase. The amount of each substance  $x$  is then split between the two phases

$$n_x(t) = n_{xl}(t) + n_{xg}(t). \quad (2-34)$$

The subscript  $l$  indicates the liquid phase, whereas the subscript  $g$  indicates the gas phase. We assume that Henry's law of absorption holds (Section B.1.3), so that the concentration of each gas in solution is proportional to its partial pressure. We can then write

$$n_{xl}(t) = S_x p_x(t) n_{\text{H}_2\text{O}}(t) \quad (2-35)$$

where  $S_x$  is the solubility coefficient of component  $x$ , expressed in moles of gas per moles of water per unit of partial pressure. Assuming that Henry's law holds at every instant is equivalent to assuming that the gases are always at equilibrium in the two phases. In other words, the equilibrium condition is assumed to be reached very quickly relative to the time scale of the other phenomena in the system. The volume of the liquid phase is considered to be unaffected by the presence of the gases in solution. The main effect of including gas solubility is that more gas is required to generate the same pressure increase, because some of the gas is stored in the liquid phase, where it does not contribute to the pressure.

The presence of water vapor in the gas phase should be included in the model as well. However, the vapor pressure of water at room temperature (or at human body temperature) is much lower than the partial pressure of the gases, and it can be neglected to simplify the equations.

## 2.5 Balloon Test Setup

### 2.5.1 Experimental Setup for Testing of the Balloons

The balloons are connected to a voltage source to drive electrolysis. The applied voltage and the resulting current are monitored by multimeters. The displacement generated by the balloon is measured by a linear variable differential transformer (LVDT), positioned as in Figure 2-6. The LVDT is spring-loaded, and its spring constant has been measured to be  $2.5 \text{ mN}/\mu\text{m}$ . The spring in the LVDT produces a counteracting force that must be overcome by the balloon. Therefore, the measured displacement is lower than it would be in load-free conditions. The voltage, current, and displacement measurements are recorded on a computer with LabView (National Instruments Corp.) and exported to Matlab (The MathWorks, Inc.) for analysis.

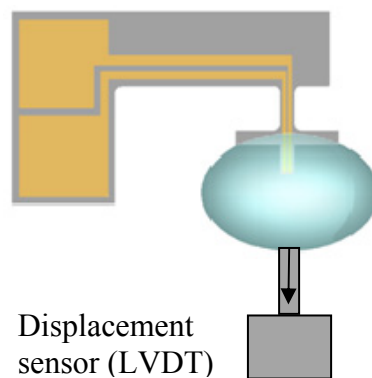


Figure 2-6. Experimental setup for testing of the balloon actuators.



### 2.5.2 Balloon Pressure and LVDT Reading

The solution of the mass balance equations gives the amounts of all the components in the balloon as a function of time. These are the basic values from which all the other significant balloon quantities can be derived, including the total balloon pressure. The total pressure is computed in the gas phase, which is treated as an ideal gas mixture. It follows that the total pressure is the sum of the gases' partial pressures, which are calculated using the ideal gas law

$$p(t) = p_{\text{H}_2\text{O}}(t) + p_{\text{O}_2}(t) + p_{\text{N}_2}(t) = \frac{n_{\text{H}_2\text{O}}(t) + n_{\text{O}_2}(t) + n_{\text{N}_2}(t)}{V - v_{\text{H}_2\text{O}}n_{\text{H}_2\text{O}}(t)} RT. \quad (2-36)$$

The pressure must be converted to an expected LVDT reading for fitting the model to the experimental data. The LVDT is spring-loaded, and the spring is modeled by Hooke's law

$$F = k_{\text{LVDT}}x \quad (2-37)$$

where  $F$  is the force applied on the LVDT, and  $x$  is the displacement. The objective is to find a relation between the balloon internal pressure  $p$  and the force  $F$  applied to the LVDT. A rigorous model would require a finite-element simulation of the balloon, to find how it deforms as a function of the internal pressure when loaded by the LVDT. However, the geometry of the balloon is not known very accurately, due to fabrication variations that are hard to control and measure. Therefore, a simplified approach is followed. The force on the LVDT is assumed proportional to the pressure inside the balloon

$$F = pA_{\text{eq}}. \quad (2-38)$$

The proportionality constant is an “equivalent” area  $A_{\text{eq}}$ . The stress in the balloon wall due to the balloon expansion must be accounted for as well. A simplified model for the wall stress is to think of it as an additional spring pushing against the balloon. This reduces the force available to push against the LVDT spring

$$F = k_{\text{LVDT}}x = pA_{\text{eq}} - k_{\text{stress}}x \quad (2-39)$$

The relation between  $p$  and  $x$  is then

$$x = \frac{A_{\text{eq}}}{k_{\text{LVDT}} + k_{\text{stress}}} p = \alpha p. \quad (2-40)$$

We condense the proportionality term into one constant  $\alpha$ . If  $k_{\text{stress}}$  is negligible compared to  $k_{\text{LVDT}}$ , the equivalent area can be estimated by the contact area between the balloon and the LVDT. Otherwise,  $\alpha$  is left as an additional fitting parameter.

## 2.6 Parylene Balloons

The balloons are built on a silicon frame, which has the form of a cross. The frame serves as a substrate for the platinum electrodes, and it provides two lateral beams which help contain the sacrificial photoresist during balloon fabrication.

### 2.6.1 Silicon Frame Fabrication

The fabrication of the silicon cross is illustrated in Figure 2-7 (steps 1-5). Thin silicon wafers, 200  $\mu\text{m}$  thick, are used for the convenience of etching and release of the

devices. A first layer of parylene C, 0.5  $\mu\text{m}$  thick, is deposited by room-temperature low-pressure chemical vapor deposition (LPCVD). The parylene is then molten at 350  $^{\circ}\text{C}$  in a nitrogen environment, in order to prevent oxidative degradation of the polymer.

A second layer of parylene C, 1  $\mu\text{m}$  thick, is deposited on top of the molten parylene layer. The molten parylene acts as an adhesion layer between silicon and this second parylene layer. Platinum is then deposited by e-beam evaporation, and it is patterned by a liftoff process. No adhesion layer is used between platinum and parylene, because metals commonly used as adhesion layers (like titanium) are easily corroded during electrolysis. The adhesion of platinum to parylene is sufficient for the fabrication of the devices.

Parylene is patterned by reactive ion etching (RIE) in oxygen plasma, using a photoresist mask. The same mask is used for the following deep reactive ion etching (DRIE) step, which defines the shape of the devices and releases them from the wafer. A complete silicon frame is shown in Figure 2-8a.

### **2.6.2 Balloon Fabrication**

The fabrication steps for the balloons are shown in Figure 2-7 (steps 6-10). The devices are first glued to a glass slide for ease of handling during fabrication. The adhesive must be carefully selected, as it must be able to withstand soaking in acetone in a later step (although protected by parylene). Polyurethane adhesives are found to perform much better in this sense than cyanoacrylate or epoxy adhesives.

Sacrificial photoresist (AZ4620) is dispensed on the silicon structure to form a ball. Photoresist (PR) is also dispensed on the pads, so that they can be reopened after the parylene is deposited. The photoresist is applied with a commercial fluid dispenser (EFD

2000XL) equipped with a 33-gauge (180  $\mu\text{m}$ ) needle. The dispenser applies pressure pulses that push the photoresist through the needle. The pressure and duration of each pulse are customizable by the user.

The sacrificial photoresist is hardened by baking. Due to the ball shape, bubbles tend to grow in the photoresist during baking. These gas bubbles are detrimental to the following parylene-coating step, as they easily burst in vacuum. The bubbles are due to solvent evaporation or to air trapped inside the photoresist ball as a consequence of the dispensing process. The problem is particularly noticeable when the device is baked in a convection oven. In the oven, the photoresist is baked starting from the outer layer, causing the surface to harden before the interior is fully baked. The hardened “crust” on the surface impedes the release of air and solvent from the interior of the ball, resulting in trapped bubbles. Baking the device on a hotplate offers a solution to this issue. The glass slide supporting the device is placed on the hotplate, with the device extending outside the edge of the hot surface. In this way, the heat travels along the slide and the silicon structure, reaching the photoresist from inside. Baking the photoresist ball from inside prevents air and solvent from being trapped, as they can diffuse out through the still soft outer layer during baking. To further reduce the formation of bubbles, the photoresist is not applied and baked all at once, but in layers with intermediate baking steps. At each step, only the outer layer of photoresist has to be baked, while the interior is already hardened, thus reducing the thickness through which solvent and air have to diffuse to leave the photoresist.

The baking temperature cannot be raised over 70  $^{\circ}\text{C}$ , in order to limit photoresist reflow, which tends to make the balloon assume a spherical shape. As the finite-element

simulations in Section 2.3 show, the most desirable shape for the balloon is an ellipsoid with the shortest axis along the displacement direction, so that the internal pressure is better exploited to produce displacement and force in that direction.

After baking, the devices are coated with parylene. Due to the conformal nature of the deposition, the balloon is sealed. When the deposition is complete, a hole is opened through the parylene of the balloon with a hot needle (the needle is heated by mounting it on a soldering iron). The parylene over the pads is opened as well with a blade. The device is then immersed in acetone to release the photoresist from the balloon and pads. After the release is complete, acetone is left to evaporate out. The parylene over the pads is then peeled off and cut with a blade. A balloon at this step is shown in Figure 2-8b.

The balloon is filled with electrolyte through the same hole used for releasing the sacrificial photoresist. The device is immersed in an electrolyte solution inside a vacuum chamber. When vacuum is applied, the air inside the balloon expands and it leaves from the hole. When vacuum is broken, the air inside the balloon shrinks, and liquid is pulled into the balloon. The residual amount of air inside the balloon at the end of the process depends on the minimum pressure achieved in the vacuum chamber. There is a fundamental limitation to the minimum pressure, because the electrolyte solution starts boiling when the pressure is low enough (water at 25 °C has a vapor pressure of 23.76 mmHg).

Finally, the hole is sealed with epoxy. Epoxy must be applied as soon as possible after the filling step, to prevent evaporation of the electrolyte. Application of excessive epoxy on the balloon causes its stiffening, which negatively affects the balloon

expansion. To reduce this effect and make the epoxy application easier, the release/fill hole is opened at the base of the balloon, close to the silicon-parylene interface.

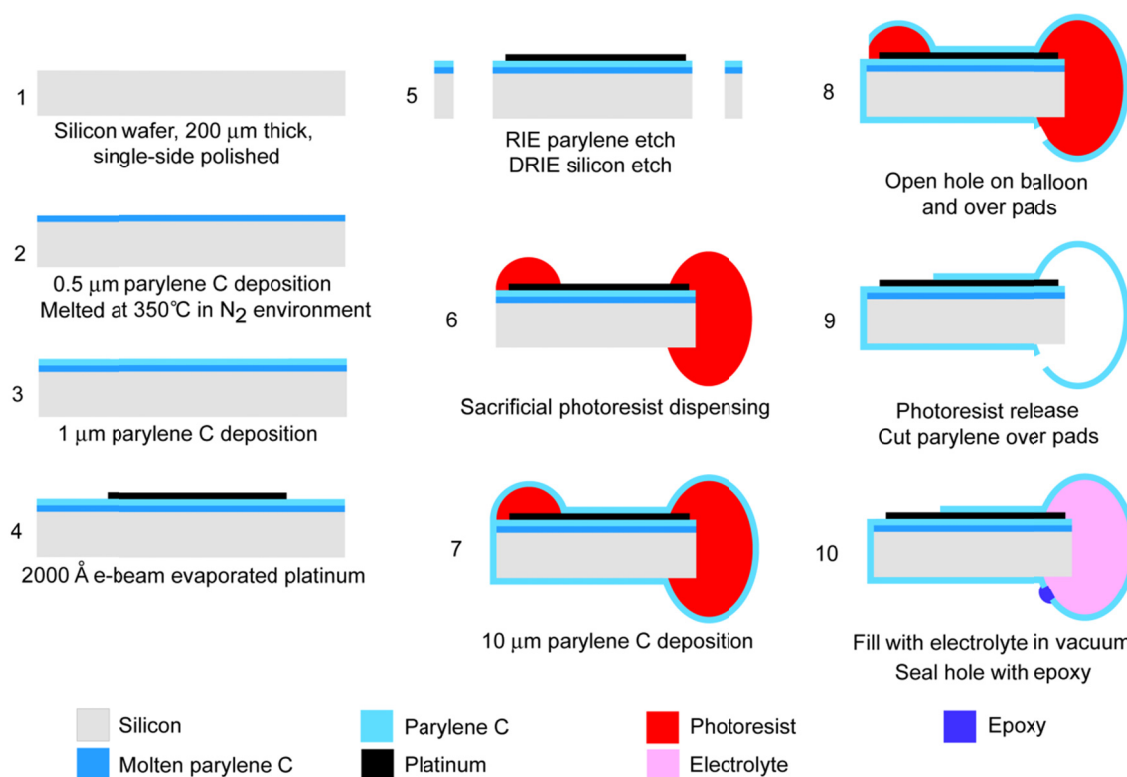


Figure 2-7. Fabrication steps for balloons with parylene wall. Steps 1-5 are to fabricate the supporting silicon frame. Steps 6-10 are to fabricate the balloon.

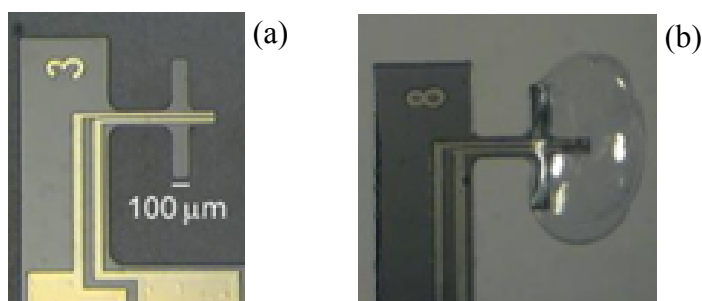


Figure 2-8. a) Silicon frame. Different geometries are fabricated, and a number on the structure is used to identify them. b) Parylene balloon after photoresist release.

### 2.6.3 Results

Parylene balloons were tested using the setup illustrated in Section 2.5.1. Figure 2-9 shows the results of a test in which a balloon is expanded by running electrolysis and then allowed to shrink back by stopping electrolysis. The balloon has a parylene wall that is 10  $\mu\text{m}$  thick, and it is filled with an electrolyte composed of deionized water, acetic acid, and methanol mixed in 95:5:0.1 ratio. Electrolysis is controlled by the applied voltage. The resulting current has large variations in time due to the formation of gas bubbles on the electrodes. The bubbles stick to the electrodes for some time, where they coalesce with other bubbles, until they finally leave the electrode. The presence of the bubbles alters the effective area of the electrode (i.e., the area over which electrolysis can take place), therefore altering the impedance and the resulting current. The random behavior of the bubbles on the electrodes causes variations in the current that are hard to control.

The balloon model introduced in Section 2.4.1 is used to fit the experimental data. The measured current is used as the input for the balloon model, and a set of parameters to fit the model to the experimental data is found. As the displacement plot on Figure 2-9 shows, the model fits the data very closely. The model estimates the efficiency term  $\varepsilon$  to be about 10%. This means that most of the gases recombine at the electrodes immediately after generation, due to the narrow spacing between the electrodes (10  $\mu\text{m}$ ). We also find that permeation dominates over recombination, which can be assumed negligible. In fact, the recombination reaction is catalyzed only at the platinum electrodes, which are small compared to the balloon size.

If the refined model of Section 2.4.3 is applied, a similar fit is obtained. The only difference is the estimated value of the efficiency  $\varepsilon$ . With the refined model, the estimated current efficiency is higher, around 20-30%. The reason is that a part of the generated gases, which is assumed to early recombine at the electrodes in the first version of the model, is assumed to go into solution in water in the refined model.

The balloon is slow, and one cycle takes more than one hour. The expansion speed can be controlled by the electrolysis rate, but the relaxation phase is determined by the permeation rate. The expansion phase shows the convergence of the displacement to a saturation value, as expected. In fact, for a certain applied current, the pressure in the balloon increases until permeation balances the amount of new gas generated. After the balance is reached, additional pressure increase is only possible by increasing the current.

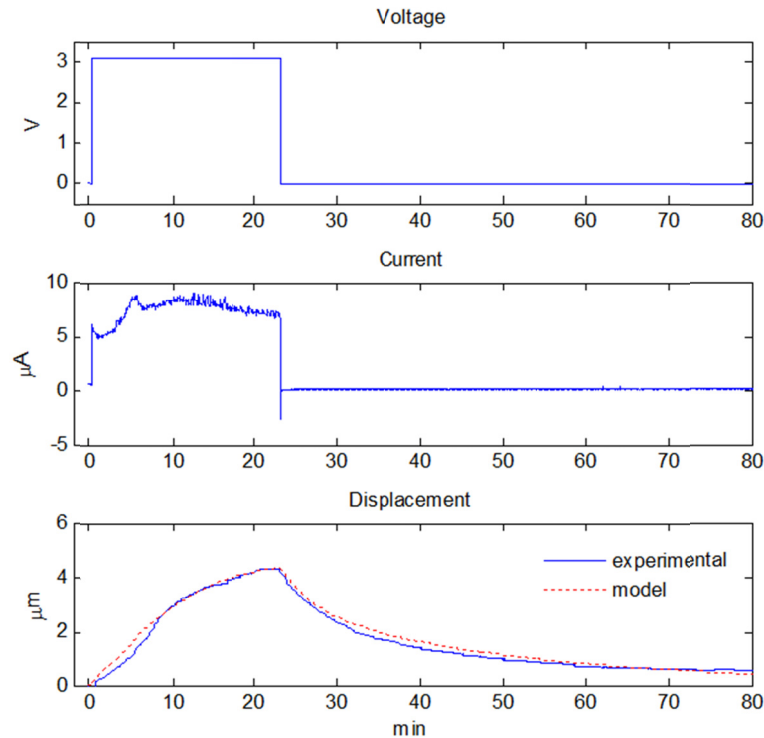


Figure 2-9. Expansion and relaxation of a parylene balloon. The experimental data is fitted with the balloon model.



The most frequent failure mode is the formation of leaks, which compromise the sealing of the balloon and the ability to maintain the internal pressure. There are two main mechanisms of leak formation: failure of the epoxy seal and insufficient adhesion between the balloon wall and the silicon frame.

The need for the epoxy seal is a consequence of the fabrication process, which requires a hole for releasing the sacrificial photoresist and for filling the balloon. The epoxy is cured with the electrolyte already inside the balloon, which may negatively affect its properties and adhesion. Also, the epoxy is placed on the flexible balloon wall, introducing stress concentration points at the edge of the hardened epoxy drop.

The parylene balloon wall has to adhere to the silicon frame to provide good sealing. There are three interfaces involved: the parylene-parylene and platinum-parylene interfaces on the top side of the frame, and the parylene-silicon interface on the other sides of the frame. Adhesion of parylene to silicon on the sidewalls of the frame is improved by the DRIE process, which leaves the silicon surface rough there. The bottom side is rough as well when a single-side polished wafer is used for fabrication. To improve the parylene-parylene adhesion, the parylene on the frame is roughened by oxygen plasma before the parylene deposition for the balloon wall. The adhesion of parylene to platinum was found to be the weakest. We tried to locally melt the parylene layers around platinum to improve the sealing in the area behind the balloon, but the process is difficult to control.

## 2.7 Balloon Discs

The parylene balloons fabricated in Section 2.6.2 have two prominent problems. The first problem is the failure of the seal during operation. The second problem is the scarce control over the final balloon shape. As explained in Section 2.3, the balloon shape is an important factor in determining the displacement obtained for a certain internal pressure. During fabrication, the balloon shape is determined by the shape of the sacrificial photoresist ball, which is difficult to control due to the dispensing process and to the reflow during the baking step. The reflow causes the balloon to harden into an almost spherical shape. To solve these problems, special silicon discs have been developed. Figure 2-10a illustrates the features of the discs.

The discs are to be mounted on the silicon frame (Figure 2-11) by inserting the electrode-supporting silicon beam of the frame into the matching central hole provided on each disc. This hole is made slightly (a few tens of microns) larger than the nominal frame beam dimensions, in order to tolerate fabrication variations. A larger hole makes the insertion easier, but it makes it harder to seal the gap between the disc and frame.

There are two concentric trenches around the edge of the disc. These trenches provide anchoring for the balloon wall, to improve its adhesion and sealing. The discs have a second hole (in addition to the one for mounting on the frame), which is used to release the sacrificial photoresist and to fill the balloon. This hole replaces the one that had to be opened in the parylene wall in the disc-less process of Section 2.6.2. This hole is surrounded by an anchor, to improve the sealing. Discs of different sizes are fabricated, with radiuses from 450  $\mu\text{m}$  to 650  $\mu\text{m}$ , and a notch-coded marker is provided to identify the size. Some discs have a handle, for easier manipulation with tweezers.

The fabrication of the discs is illustrated in Figure 2-10b. A 1.5  $\mu\text{m}$  thick layer of silicon dioxide is grown on thin wafers (200  $\mu\text{m}$  thick) by wet oxidation at 1050  $^{\circ}\text{C}$ . The oxide is then patterned and used as a mask for DRIE. Two kinds of trenches are needed: anchor trenches (for anchors and geometry marker notches) and release trenches (for holes and releasing of the device). The anchor trenches are 5  $\mu\text{m}$  wide, whereas the release trenches are 100  $\mu\text{m}$  wide. The DRIE etching rate is lower in narrower trenches (the so-called RIE lag), making it possible to obtain both types of trenches with a single-mask process. When the release trenches are etched all the way through the wafer (thus releasing the discs from the wafer), the anchor trenches are only about 80-90% through.

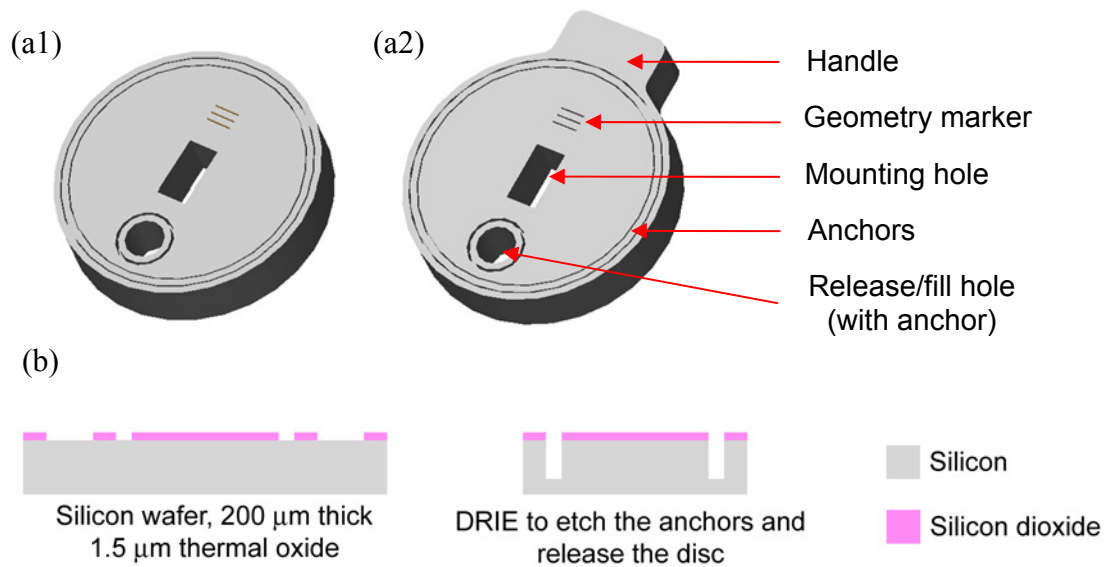


Figure 2-10. a) 3D models of silicon discs: a1) without handle, a2) with handle. b) Fabrication steps for the silicon discs (the cross-section does not show the holes in the disc).

A disc is assembled on the silicon frame by inserting the electrode-supporting silicon beam into the mounting hole of the disc (Figure 2-11). The disc is manipulated with tweezers and glued to the frame by epoxy. Epoxy is applied all around the hole, in order to seal the disc-frame gap on all sides. Sacrificial photoresist is dispensed on the disc. A second disc is placed on the front of the balloon when the photoresist is only partially baked, in order for the disc to stick to the still soft photoresist. The disc put on this side of the balloon does not have any holes. The space between the two discs is then completely filled with photoresist. Figure 2-12 shows pictures of a device after this step. The fabrication then proceeds in the same way as in Section 2.6.2, by baking the photoresist and coating with parylene. The only difference is that the release/fill hole is not opened on the side of the balloon, but within the hole provided for this purpose on the disc.

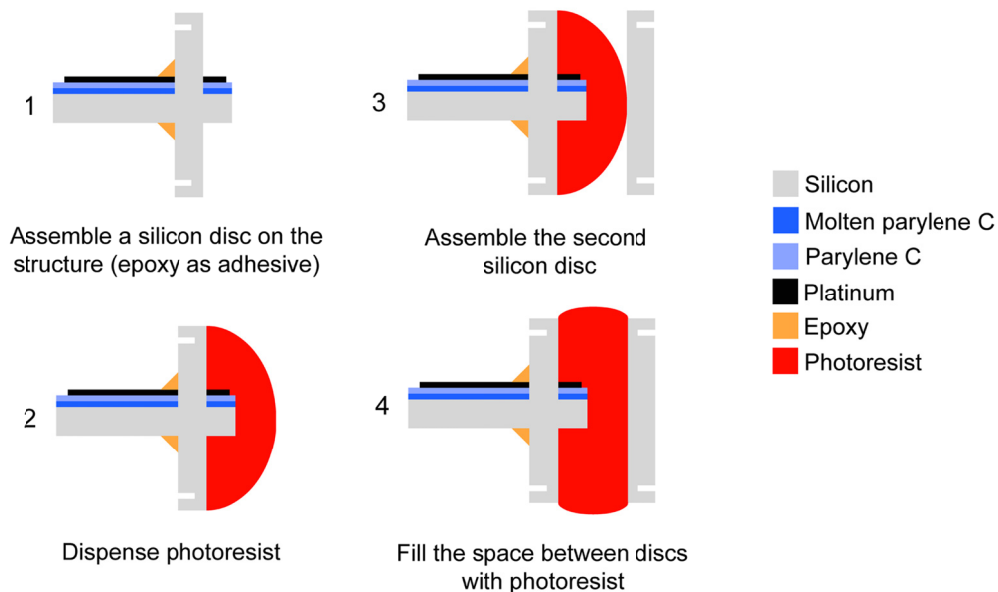


Figure 2-11. Fabrication of a balloon using silicon discs.

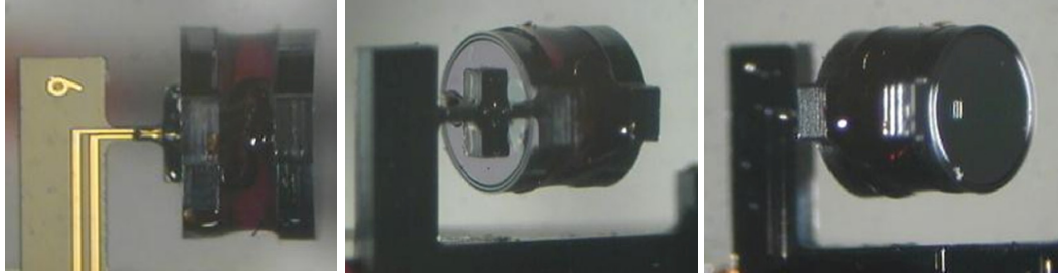


Figure 2-12. Device after disc assembly and photoresist dispensing, viewed from different angles.

The discs have two functions. The first function is to make the balloon shape more controllable and repeatable by providing a surface over which the photoresist is dispensed. Instead of the almost spherical shape obtained without discs, the balloons assume an almost cylindrical shape, which generates larger displacement for the same internal pressure.

The second function of the discs is to improve the balloon sealing. In disc-less balloons, the quality of the sealing is determined by the adhesion between the parylene balloon wall and the silicon frame. When discs are used, there are two interfaces to be sealed: the wall-disc interface and the frame-disc interface. The wall-disc interface is sealed through the anchors fabricated on the disc surface. When the parylene for the balloon wall is deposited, it fills the anchor trenches, producing a good seal. The frame-disc interface is sealed by the epoxy that secures the disc to the frame.

Another sealing improvement is given by the release/fill hole on the disc. In disc-less balloons, the hole is opened in the parylene wall, and then sealed with epoxy. The presence of hard epoxy on the flexible balloon wall causes adhesion issues and stress concentration around the edge of the epoxy drop. With the disc, the quality of the epoxy

seal is improved because it is placed on a hard surface. There is also an anchor trench around the release/fill hole, in order to further prevent the delamination of parylene around the hole.

The anchors are placed on the back side of the disc, and not on the photoresist side, for ease of fabrication. If the anchors were on the photoresist side, there would be the risk of covering them with photoresist during the dispensing process. By having the anchors on the other side, photoresist is conveniently dispensed over the whole surface of the disc. One drawback of this design is that the parylene balloon wall has to wrap around the edge of the disc before reaching the anchors, and stress concentration at the edge may facilitate balloon failure.

Figure 2-13 shows the testing results of a balloon with discs. The parylene is 4  $\mu\text{m}$  thick, reinforced by a layer of PDMS (poly-di-methyl-siloxane), and the discs are 650  $\mu\text{m}$  in radius. The electrolyte inside the balloon is a 0.25 M solution of magnesium sulfate ( $\text{MgSO}_4$ ). The balloon model of Section 2.4.1 is applied to this case as well, and the fit is very good. Comparing this data with the disc-less case of Figure 2-9, we notice that the expansion phase is faster, due to the improved shape of the balloon. As expected, the presence of the disc does not affect the current efficiency  $\varepsilon$ , which has the same value as for the disc-less balloon test of Section 2.6.3. Relaxation of the balloon is faster, due to the thinner parylene wall. This is a further confirmation of the dominant role of permeation during balloon relaxation.

Due to the flat surface of the disc on the front of the balloon, it is easier to convert from the internal pressure to the LVDT reading, because the contact area between the balloon and the LVDT is approximately equal to the area of the disc. The internal

pressure at the maximum displacement in Figure 2-13 is estimated to be 0.22 atm over the external atmospheric pressure. This is much lower than for disc-less balloons, where the pressure is usually estimated to be around a few atm for similar displacement.

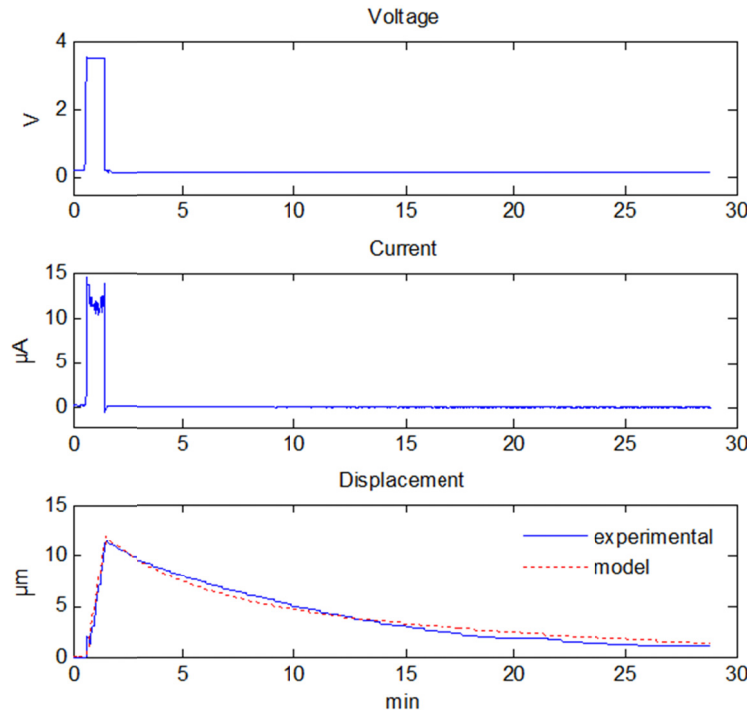


Figure 2-13. Expansion and relaxation of a parylene balloon with silicon discs. The experimental data is fitted with the balloon model.

## 2.8 Silicone Balloons

The balloon relaxation time depends on the permeation rate through the balloon wall. The permeation rate is directly proportional to the permeability of the wall and inversely proportional to its thickness, as stated by Equation (B-45). As confirmed by the previous experiments, the relaxation time can be reduced by using a thinner balloon wall.

However, a very thin wall raises reliability concerns, as leaks may form more easily. The alternative is to use a material with higher permeability.

### **2.8.1 Silicone**

Silicone rubber was chosen for the combination of high permeability and mechanical flexibility. Silicones are polymerized siloxanes, composed of a Si-O backbone, with two organic groups attached to the silicon atom. These side groups confer silicones specific properties. Table A-2 shows that silicone's permeability is orders of magnitude higher than parylene's. The high permeability is attributed to the flexibility of the Si-O chain, which creates free volume and permits fast diffusion [81].

The high permeability causes more gas loss during the balloon expansion phase, raising the amount of gas to be generated to reach a certain pressure. However, this drawback is compensated by the low elastic modulus, which is in the MPa range for silicone rubbers, compared to 2.5-4 GPa for parylene. Due to the lower elastic modulus, the balloon can be operated at lower pressure, to the benefit of reliability and efficiency.

A very common type of silicone is polydimethylsiloxane (PDMS), in which two methyl groups are bonded to the silicon atom. PDMS is popular in microfluidics as a fast way of fabricating microchannels by molding. The permeability of PDMS has been studied in [82]. PDMS is commercially available in many formulations with different cure methods and properties, including medical-grade formulations.

### **2.8.2 Fabrication**

The process to fabricate balloons with silicone wall is analogous to the one for balloons with parylene wall. The parylene deposition is simply replaced by the



application and cure of PDMS (Sylgard 184, Dow Corning, Inc.). Silicone can only be applied to balloons with silicon discs, because they provide anchors. Without the anchors, the adhesion of PDMS to the other materials is poor, easily causing leaks.

In the uncured state, PDMS is a clear viscous liquid. PDMS is deaired in vacuum for 10 minutes, to remove gas bubbles trapped in the uncured PDMS. After the sacrificial photoresist is baked, the PDMS is applied around the balloon with a thin piece of wire held by tweezers. Contrary to parylene, PDMS does not require deposition in vacuum. This eliminates the issues related to gas bubbles trapped in the sacrificial photoresist, which may burst when the device is put in vacuum. The PDMS is cured by baking in oven at 70 °C. The PDMS is applied on the balloon multiple times in order to reach the desired thickness. The intermediate curing of these layers should not be complete, in order to promote adhesion between the layers. Baking for 15-30 minutes is sufficient to harden the silicone enough to allow the painting of another layer. After the last layer, the PDMS is baked for at least a few hours to complete the curing process.

It is important to make sure the silicone is sufficiently thick at the edge of the silicon discs. The silicone is free to flow after painting it, and it tends to be thin at the edge. The disc edge is a stress concentration point, and having only a thin silicone layer there is a reliability concern, because the silicone may break when the balloon is expanded. During fabrication, some layers of silicone are applied only at the disc edge, in order to guarantee sufficient thickness there.

There is a tradeoff to consider when choosing the silicone thickness. Thinner silicone allows faster permeation and, therefore, shorter relaxation times. However, faster permeation also causes more power to be wasted during the expansion phase of the

balloon, as more gas needs to be generated by electrolysis to compensate for the increased loss by permeation. Thin silicone may also fail more easily.

After the silicone is cured, the release/fill hole is opened with a needle, and the photoresist is released (Figure 2-14). The balloon is then filled in vacuum and the hole is sealed.

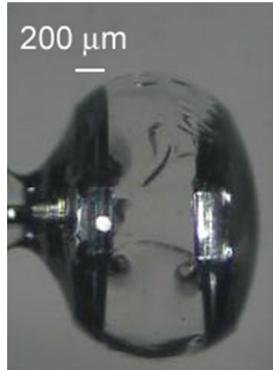


Figure 2-14. Balloon with silicone wall and silicon discs.

### 2.8.3 Results

Silicone balloons were fabricated and tested. Figure 2-15 shows the displacement as a function of time for a silicone balloon, with a wall about 100 μm thick and discs' radius of 500 μm, filled with a saturated solution of  $\text{MgSO}_4$ . The relaxation time is greatly reduced compared to balloons with parylene wall, due to the high permeability of PDMS. One actuation cycle of the balloon can be completed in a few minutes instead of tens of minutes. The refined version of the model (Section 2.4.3) is used to fit the experimental data. Since the spring constant of the LVDT is 2.5 mN/μm, the data shows that the balloon is able to produce force of several tens of mN.

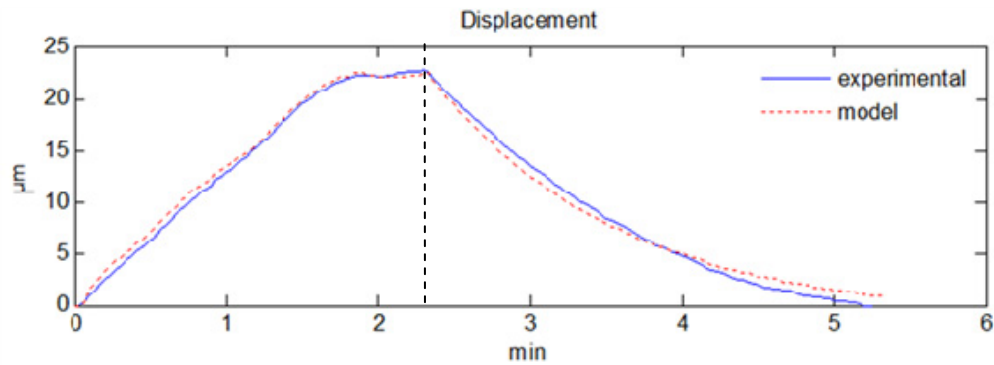


Figure 2-15. Expansion and relaxation of a balloon with PDMS walls and silicon discs. Electrolysis is stopped at the dashed line.

The expansion of the balloon has also been tested in load-free conditions, without the LVDT in front (whose spring applies a load on the balloon, reducing the achievable displacement). In this condition, displacement in excess of 100  $\mu\text{m}$  was demonstrated.

The permeability of silicone is found to be higher when permeation occurs from gas to gas than when it occurs from liquid to gas. The external environment during the experiments is air. Inside the balloon, the gas bubbles are sometimes in contact with the balloon wall, while other times they are surrounded by water. It is observed that the permeation rate strongly increases when a gas bubble is in direct contact with the balloon wall. In one experiment, a gas bubble was generated by electrolysis inside the balloon. The bubble was observed under a stereoscope during the relaxation of the balloon. The bubble was initially surrounded by water. At some point, electrolysis was reactivated, to make the bubble larger. The bubble grew and moved in contact with the balloon wall. A significantly increased relaxation speed was observed as soon as the bubble got in contact

with the balloon wall, indicating a faster permeation rate. These observations were confirmed on several other devices.

## 2.9 Osmosis and Water Replenishment

Permeation causes a net loss of water from the balloon over time, which is a serious concern for the lifetime of the device. In the body, the device operates in a liquid environment (the body fluid). Water from the external environment can be used to replenish the electrolyte inside the balloon by exploiting osmosis through the balloon wall. To generate an osmotic flow from the outside to the inside of the balloon, a chemical potential gradient for water must be established.

Permeation was tested in a balloon with parylene wall, 10  $\mu\text{m}$  thick. In the first test, the balloon was sealed without filling it, leaving air inside. The device was then immersed in deionized water. Water permeates through the parylene wall, it creates a saturated vapor inside the balloon, and it then starts condensing into droplets. The phenomenon is observed, but it is very slow. It takes about a month to fill 10% of the balloon volume. This is not surprising, as the process speed is limited by the nucleation of water droplets inside the balloon. In fact, the chemical potential of water in liquid form and in saturated vapor form is the same, and a gradient across the wall is established only because nucleation removes some water from the saturated vapor.

The same device was then filled with a 0.25 M solution of  $\text{MgSO}_4$ . About one third of the water was left to evaporate before sealing the balloon. The device was then immersed in deionized water. The presence of deionized water outside and of a salt solution inside creates a chemical potential gradient that drives water into the balloon.

After about a month, no significant increase in the amount of water inside the balloon was observed.

The experiment above suggests that the permeability of parylene is not sufficient to establish a significant osmotic flow. Better performance is expected from PDMS, due to its high permeability. A silicone balloon, with a wall thickness of about 100  $\mu\text{m}$ , was filled with a 0.25 M solution of  $\text{MgSO}_4$  and sealed. The device was left in air for half a day, to let all the water permeate out of the balloon. When the balloon was empty, salt crystals were visible on the inner surface of the balloon wall. The device was then immersed in deionized water. After 45 minutes, some water was already visible on the crystals inside the balloon. After 1 day, the balloon was about 25% full. After 10 days, the balloon was 75% full, and after 25 days it was completely full.

The refined balloon model of Section 2.4.3 is applied to the osmosis replenishment experiment above. The model is fitted to the observed data points, and the agreement is good. The model predicts that, in the case of a saturated solution of  $\text{MgSO}_4$  inside the balloon, the time to refill the balloon would only be 2 days. This prediction is confirmed experimentally.

The successful demonstration of water replenishment by osmosis in silicone balloons opens new possibilities for the fabrication of the balloons. The filling in vacuum can be completely replaced by osmosis. For example,  $\text{MgSO}_4$  can be inserted into the balloon before the silicone coating. We tried this approach by embedding  $\text{MgSO}_4$  crystals into the photoresist during the dispensing process. After the photoresist is released in acetone, the crystals are clearly visible inside the balloon. The filling of the balloon by osmosis, however, is slow because the crystals are concentrated inside the balloon. When

the balloon is filled with a solution of  $\text{MgSO}_4$  and allowed to dry, the crystals are evenly distributed on the inner surface of the balloon wall, making osmosis faster from the beginning. This approach is not very advantageous anyway, because a hole in the balloon is still required to release the photoresist.

A more innovative approach that does not require any hole in the balloon was developed for the second-generation inchworms, and it is presented in Chapter 5. The photoresist is replaced by a shell of magnesium sulfate or by a hydrogel, which still provide the mechanical support for the silicone coating, but do not have to be released from the balloon.

## **2.10 Further Characterization and Optimization**

The electrodes used in the balloons are simple rectangular platinum electrodes. Other geometries that may increase the electrolysis efficiency should be studied. For example, the spacing between the electrodes is an important geometric parameter, and, as explained in Section 2.4.1, there is a possible efficiency tradeoff related to it. Close electrodes cause lower ohmic losses in the solution, but they also cause increased recombination of oxygen and hydrogen, because each gas easily gets in contact with the other electrode. Electrodes that are farther apart cause more ohmic losses in the solution, but recombination is reduced. Both ohmic losses and recombination during electrolysis are detrimental to the efficiency of the device. An optimum inter-electrode distance that maximizes the efficiency should be found. Electrode materials other than platinum can also be tried, in order to eliminate the recombination problem. Moreover, surface treatments can be used to increase the effective electrode area and reduce the overpotential.

The balloon relaxation phase is the main limitation to the actuation speed. Relaxation currently relies on permeation of gases more than on recombination. To enhance the role of recombination, the platinum surface area inside the balloon can be increased. In the current device, the only exposed platinum area is represented by the electrodes, which are relatively small compared to the size of the balloon. One possibility is to deposit platinum on the inner surface of the discs, thus providing a large surface that catalyzes the recombination reaction.

The examination of the electrode geometry and material, and more detailed characterization of electrolysis, recombination, and permeation would provide useful information to improve the device. For this purpose, we developed a test chamber to run further tests. The chamber is built with acrylic plastic, using computer numerically controlled (CNC) machining. The chamber is equipped with interchangeable electrodes and a commercial pressure sensor. A film of silicone, parylene, or other material can be inserted on one side of the chamber, by clamping it between two perforated acrylic plates. The chamber behaves like a balloon actuator on a larger scale, which means that the balloon model can be applied to the experiments conducted in this chamber.

Running the experiments in the chamber has several advantages compared to running them directly in the balloons. First, the chamber is more versatile. The chamber is reusable for many experiments, as different sensors and different kinds of electrodes are easily connected to it. Second, the machining of the chamber is much less time-consuming than the microfabrication of the balloons. Third, the geometric parameters of the chamber are known more precisely than those of the microfabricated balloons, because of the larger scale of the chamber and the more controllable fabrication process.

The better knowledge of the parameters enables us to obtain more accurate predictions from the balloon model.



## CHAPTER 3

---

# Monolithic Neural Probe Actuators

The first kind of balloon-based actuator we designed was a monolithic one, in which the neural probe and the actuator are on the same device. The testing of these devices revealed some issues that made the design shift to the inchworm approach. It is interesting to present these devices here to understand the reasons that inspired the inchworm design. This chapter illustrates the design, fabrication, and testing of the monolithic devices. The work on these devices was started by C. Pang [26, 83] and continued by the author.

### 3.1 Design

The devices are an application of the balloon actuators described in Chapter 2. Initially, devices with a single balloon were developed. Then, in order to solve some of the issues of the single-balloon devices, devices with two balloons were designed.

#### 3.1.1 Single-balloon Design

The first version of the device features a single balloon actuator fabricated behind a silicon neural probe [83] (Figure 3-1). The device is based on a silicon frame with two sections: a probe section and a spring section. The probe section is a silicon neural probe, with electrodes for neural recording or stimulation on the top surface. It is long and tapered, to penetrate easily into the brain tissue. The spring section is located behind the probe. The spring is needed to provide a path for the metal traces that lead to the neural

probe electrodes. At the same time, the spring is mechanically flexible to allow the displacement of the probe. A balloon actuator is fabricated to enclose the spring. The top surface of the spring supports the platinum electrodes that drive electrolysis inside the balloon. When electrolysis is run, the pressure inside the balloon causes the expansion of the spring, with consequent forward displacement of the neural probe. Relaxation of the balloon must be prevented or compensated for, in order to keep the probe in a specific position.

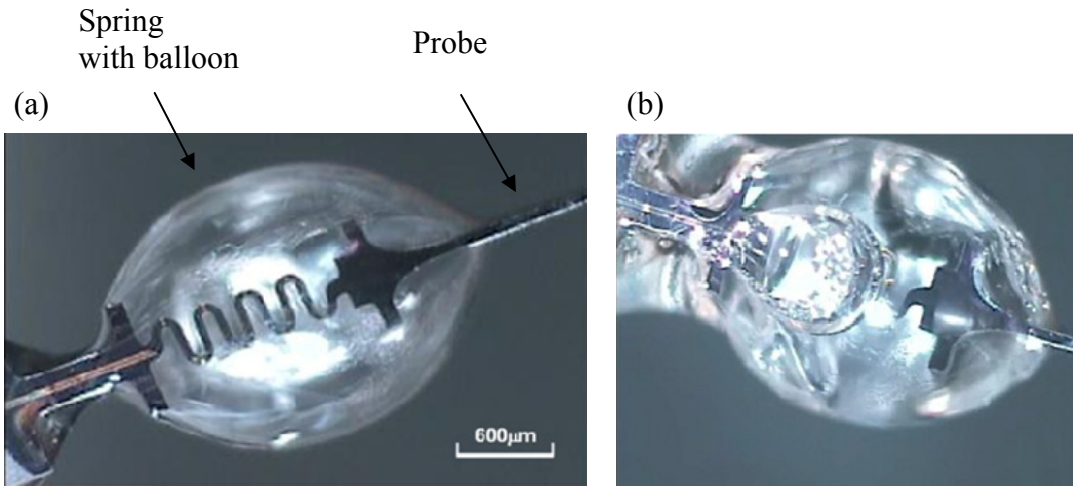


Figure 3-1. Monolithic movable probes with single-balloon actuator [83]. a) Device after releasing the sacrificial photoresist. A parylene balloon surrounds the spring. b) Balloon filled with electrolyte. Electrolysis is being run, and a gas bubble inside the balloon is visible.

### 3.1.2 Dual-balloon Design

In the single-balloon version, the oxygen and hydrogen generated by electrolysis are in the same chamber. The catalytic effect of the platinum electrodes causes the gases to recombine back into water. In order to keep the probe in a certain position,

recombination must be compensated for by continuously running electrolysis in the device. To reduce the power consumption, it is desirable to minimize the recombination.

In order to reduce the recombination, a dual-balloon approach was devised [26]. The silicon spring is split in two parts (Figure 3-2). Each spring supports only one of the two electrodes used for electrolysis. Two balloons are fabricated, one on each spring (Figure 3-3). To close the electrochemical circuit, the two balloons are connected by a small channel or a salt-bridge fabricated on the silicon slab in between the two springs. When electrolysis is run, oxygen is generated in one balloon, while hydrogen is generated in the other. The two gases are physically separated, thus limiting their recombination. However, gas separation is not perfect, as interdiffusion occurs through the channel that connects the two balloons.

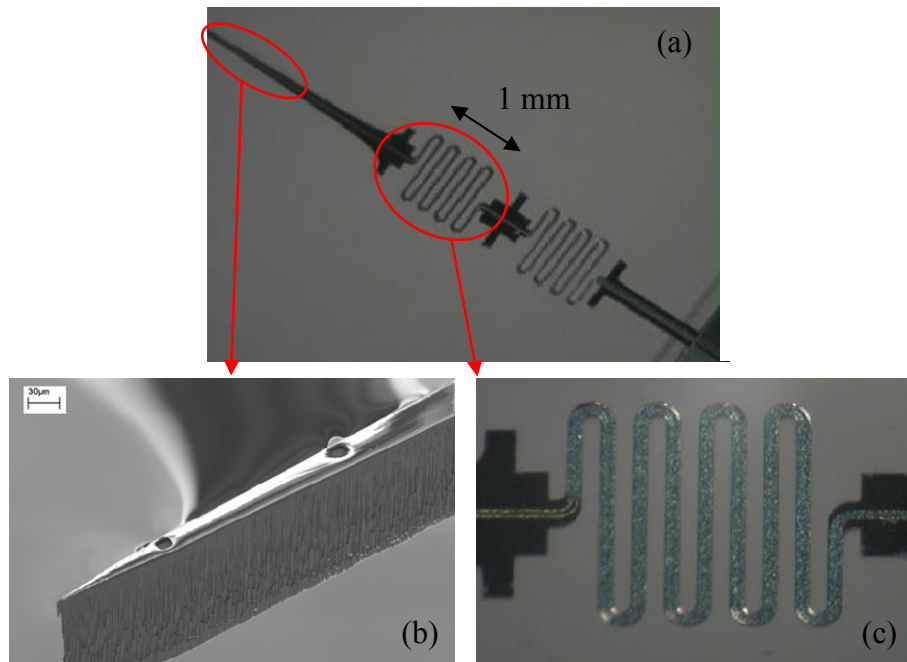


Figure 3-2. a) Silicon structure of the dual-balloon device before balloon fabrication [26]. b) Close-up of the neural probe tip, with electrode openings. c) Close-up of one of the springs, with the platinum electrode for electrolysis on the surface.

Due to the stoichiometry of the water electrolysis reaction, the amount of hydrogen generated is twice as large as the amount of oxygen. If the two balloons have the same volume, the gas generation difference causes a pressure gradient to develop between the two balloons. The pressure gradient produces a flow in the connecting channel, making gas intermix faster than when just diffusion occurs. To reduce the pressure imbalance, we can fabricate a hydrogen balloon whose volume is larger than that of the oxygen balloon (Figure 3-3b).

To further prevent intermixing between the two balloons, we also tried to put a solid electrolyte (Nafion) in the connecting channel of some devices, but the devices resulted non-functional.

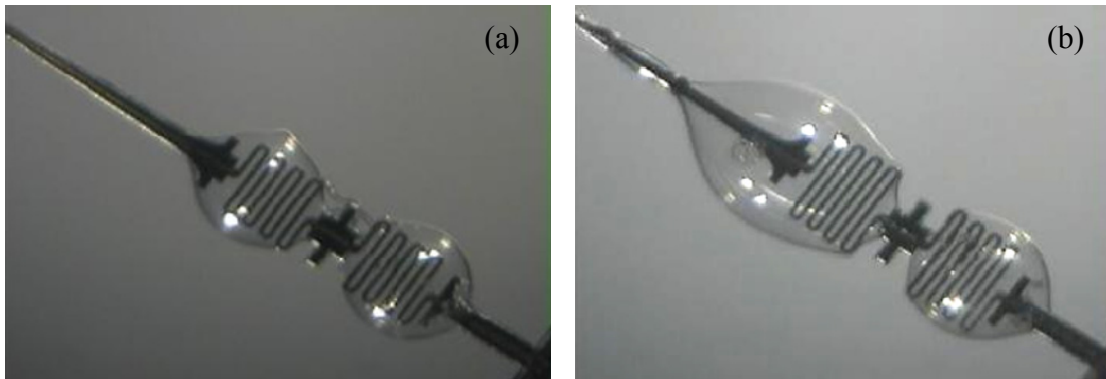


Figure 3-3. Dual-balloon device after balloon fabrication. a) Two balloons with approximately the same volume. b) Two balloons with different volume.

## 3.2 Fabrication

The fabrication of the devices consists of two phases: the fabrication of the silicon frame and the fabrication of the balloons on the frame.

### 3.2.1 Silicon Frame Fabrication

The silicon frame supports two metal layers insulated by parylene C. The fabrication steps are shown in Figure 3-4. The fabrication starts with a silicon wafer. The surface of the wafer is roughened by  $\text{XeF}_2$  etching, in order to improve the parylene-to-silicon adhesion. A first layer of parylene C, about 2  $\mu\text{m}$  thick, is deposited by room-temperature LPCVD. A first metal layer (200 Å Cr adhesion layer and 2000 Å Au) is deposited by thermal evaporation and patterned by lift-off. A second deposition of parylene C follows, about 2  $\mu\text{m}$  thick. A second metal layer (200 Å Ti adhesion layer and 2000 Å Pt) is deposited by e-beam evaporation and patterned by lift-off. A final layer of parylene C, about 2  $\mu\text{m}$  thick, is deposited to insulate the second metal layer.

The pads and electrodes are opened by etching the parylene by reactive ion etching (RIE) in  $\text{O}_2$  plasma. The same etching is also used to remove parylene from the device-release outline. The exposed silicon along the outline is then etched by deep reactive ion etching (DRIE), and the devices are released.

The process is slightly different depending on the thickness of the wafer. If the wafer is 500  $\mu\text{m}$  thick, the silicon under the devices must be thinned down to 150-200  $\mu\text{m}$ , preferably at the beginning of the process. DRIE from the back side of the wafer can be used for this purpose. This requires double-side processing of the wafer. Alternatively, a 200  $\mu\text{m}$  thick wafer can be used with no thinning required.

The Ti/Pt metal layer provides the electrodes for electrolysis, while the Cr/Au metal layer provides the electrodes for the neural probe. The Cr/Au openings may be treated or coated (e.g., with platinum black) to improve the performance of the recording electrodes.

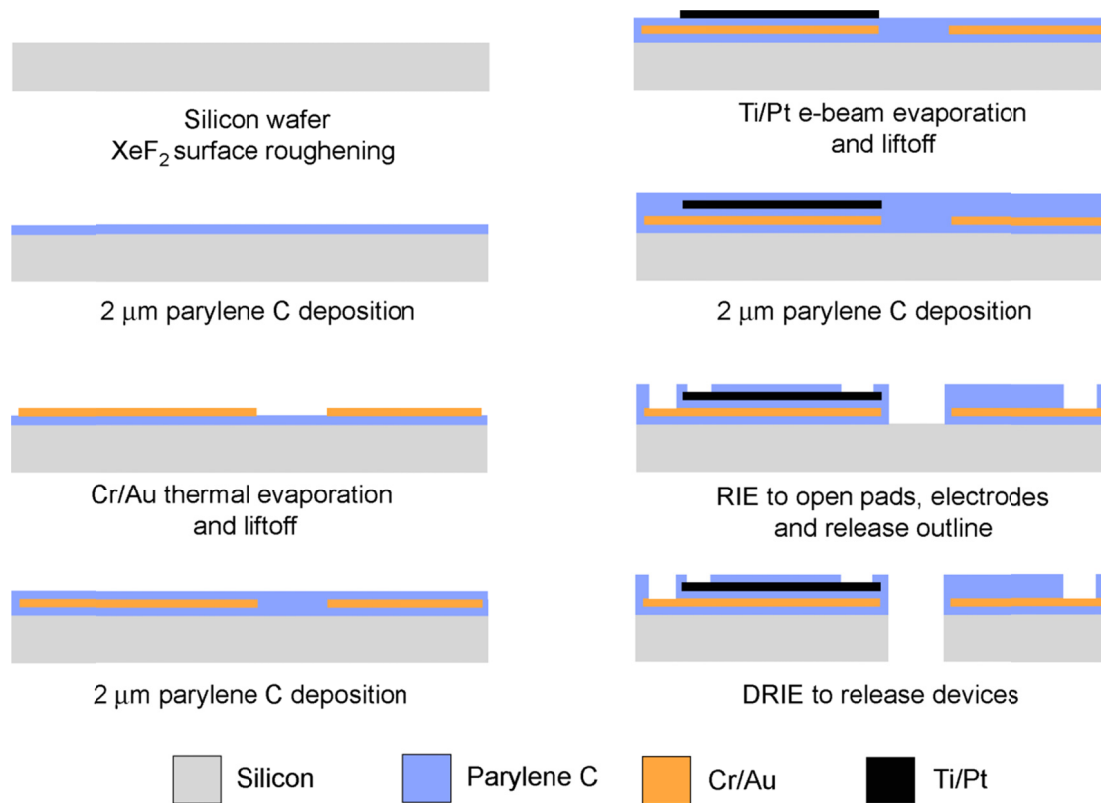


Figure 3-4. Fabrication of the silicon frame.

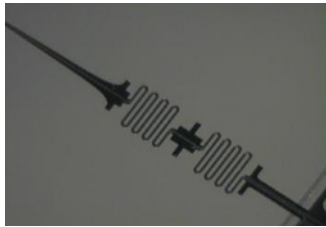
### 3.2.2 Balloon Fabrication

The fabrication steps for the balloons are shown in Figure 3-5. The fabrication steps are the same as described in Section 2.6.2. Sacrificial photoresist (AZ4620) is dispensed around each spring to form a ball. At first, the photoresist was applied manually with a fine brush under a stereoscope. In order to increase the accuracy and the yield, the brush was replaced by a commercial fluid dispenser (EFD 2000XL) equipped with a 33-gauge (180 μm) needle. Photoresist is also dispensed on the probe and the pads, in order to reopen them after the deposition of parylene.

For dual-balloon devices, the section between the two balloons is painted with a very thin layer of photoresist. A less viscous photoresist (AZ1518) is painted with a brush

to obtain a thin layer. This layer defines the connecting channel between the two balloons. If a solid electrolyte is desired in the connecting channel, it should be applied at this moment, in place of the sacrificial photoresist.

After the photoresist is hardened by baking, the devices are coated with parylene C (typically 10  $\mu\text{m}$ ). A hole is opened in the balloon wall using a hot needle. To release the photoresist, the device is immersed in acetone. When the photoresist is fully released, the balloons are filled with an electrolyte (solution of water, acetic acid and methanol in 95:5:0.1 ratio) in vacuum. The hole is finally sealed with epoxy.



1) Fabricated frame



2) PR dispensing and baking



3) Parylene coating



4) Hole opening and PR release



5) Filling with electrolyte in vacuum



6) Sealing of the hole with epoxy

Figure 3-5. Balloon fabrication steps (dual-balloon device).

### 3.3 Results

Displacement of the probe has been experimentally demonstrated both for the single- and dual-balloon devices. This section reports results obtained with dual-balloon devices. For additional experimental results, see [26, 83].

The devices are actuated by applying a voltage to the electrodes to drive electrolysis in the balloons. The displacement of the probe is measured by using a linear variable differential transformer (LVDT). The LVDT is spring-loaded, with a spring constant of  $2.5 \text{ mN}/\mu\text{m}$ . The spring affects the displacement of the probe, because the elastic force of the spring must be overcome to generate displacement. Therefore, the measured displacement is different than it would be in a load-free condition. The knowledge of the spring constant gives us information about the force generated by the device for a certain displacement.

A set of results is shown in Figure 3-6. The device is actuated twice. The first time, a voltage of about 5 V is applied for approximately 5 minutes. The displacement obtained is approximately  $5 \mu\text{m}$ . Electrolysis is then stopped, and relaxation of the balloon occurs. After 30 minutes, the displacement drops by more than half the peak value. The voltage is gradually increased again to about 4 V. As expected, the displacement rate at 4 V is lower than at 5 V, demonstrating that the speed is controllable through the applied voltage. Electrolysis is run until the device fails, as shown by the sudden drop in displacement. Failure occurs at a displacement of about  $27 \mu\text{m}$ , due to the formation of a leak. As observed from the testing of other devices, the sealing of the release/fill hole is the most common failure point, followed by the interface between the parylene of the balloon wall and the parylene on the silicon frame.



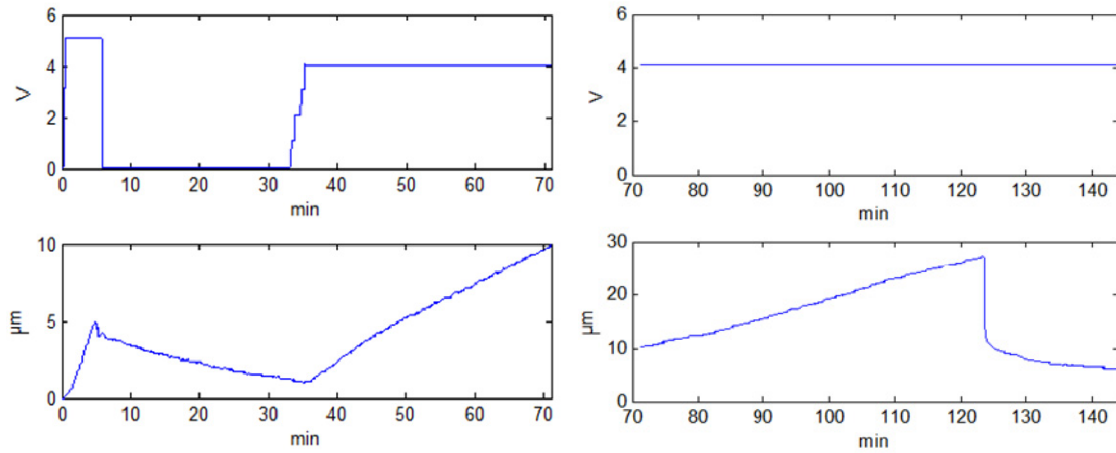


Figure 3-6. Experimental results for the actuation of a dual-balloon monolithic device.

The two sets of plots are part of the same test, and they are separated only for ease of visualization. The applied voltage is at the top, and the resulting displacement is at the bottom.

One problem of the single-balloon design is the relatively fast relaxation time when electrolysis is stopped. As a consequence, power should be continuously supplied to the device to maintain the probe in the same position. Because recombination has been reduced by the dual-balloon design, the relaxation behavior is most probably determined by permeation of gases through the balloon membrane.

At the end of an actuation cycle (i.e., a cycle of expansion and relaxation), a residual gas bubble is always visible inside the balloons, demonstrating that there is a net loss of water. This is another piece of evidence that proves that permeation is a significant phenomenon. Because hydrogen permeates much faster than oxygen through parylene (as the permeability data shows in Table A-2), the residual gas bubble is probably composed mostly of oxygen. The faster permeation of hydrogen also interferes

with the recombination reaction, because hydrogen inside the balloon is relatively quickly depleted, leaving only oxygen behind.

The hypothesis of the dominant role of permeation in the balloons is corroborated by the results obtained with other devices throughout this thesis.

### **3.4 Dealing with Permeation**

Fast relaxation of the balloons is a problem for the monolithic actuators. In order to keep the probe in a specific position, power must be constantly supplied to the device to compensate for recombination and permeation. The latter is found to have a dominant effect. There are two opposite approaches to deal with permeation: preventing it or exploiting it.

To prevent permeation, the balloon membrane should be made of a material with excellent barrier properties. The permeation properties of parylene have been studied by several authors [84-85], and permeation data is generally available from parylene manufacturers. Parylene C has the best gas barrier properties when compared to other members of the parylene family and other common polymers (Table A-2). However, permeation is still much higher than for metals, for example. Also, the effects of permeation are more felt in microdevices like ours, due to the high surface area over volume ratio.

To reduce the permeability of the balloon membrane, a metal layer can be embedded between two parylene layers. Results for such a structure are reported in [86]. In this work, a 20- $\mu\text{m}$  parylene film is compared to a composite film of parylene (10  $\mu\text{m}$ )/aluminum (0.1  $\mu\text{m}$ )/parylene (10  $\mu\text{m}$ ). The inclusion of the aluminum layer causes a

decrease of two orders of magnitude in water vapor permeation and of five orders of magnitude in oxygen permeation.

The embedded metal layer technique could be applied to our balloon devices, but not without complications. First, the balloons are three-dimensional structures, and covering the whole surface in traditional metal evaporation equipment requires the device to be carefully rotated, to ensure uniform deposition everywhere. During the deposition, parts of the device must be protected, for example by coating them with sacrificial photoresist. Second, the balloon membrane must be flexible, in order to allow the expansion of the balloon. Depending on the thickness, a metal layer could stiffen the membrane. A very thin metal layer is sufficient to drastically reduce permeation, probably making the stiffening not serious. However, the thin metal layer cannot sustain the stretching of the parylene without cracking, which would cause the barrier properties of the composite to be degraded.

Coating of the balloon by electroless nickel plating has been tried, using a special process for coating plastic surfaces (Transene RTM process). The results were not satisfactory due to the poor nickel-parylene adhesion and the difficulty in controlling of the deposition thickness for a very thin layer of metal. Manual coating of the balloons with a conductive silver paste has been tried as well, but it was unsuccessful because of the excessive thickness and the insufficient barrier properties. As a matter of fact, the paste is made of silver particles dispersed in a polymer matrix, which do not form a uniform and continuous metal film after curing.

Another possible approach to prevent permeation is to build the balloon completely with silicon. We designed a flexible accordion-like structure with thin silicon

walls, to be fabricated by DRIE. To ensure sufficient flexibility, the silicon walls should be at most 20-30  $\mu\text{m}$  thick, and they should be etched through the thickness of a wafer (500  $\mu\text{m}$ ). Even with this special geometry, it is difficult to obtain large displacement, due to the high elastic modulus of silicon and the low maximum sustainable strain. Excellent control over the sidewall profile of the DRIE etching is required to fabricate these structures, and, after preliminary tests on our DRIE machine, we decided not to follow this approach.

Instead of preventing permeation, the design can be modified to exploit permeation and the relatively fast relaxation it causes. The inchworms illustrated in the following chapters are a product of this approach.

## CHAPTER 4

---

# First-generation Inchworms

In the previous chapter, we found that gas permeation through the wall of a balloon causes it to relax relatively fast. The effect is detrimental to the monolithic actuators, as power has to be constantly supplied to compensate for permeation and to keep the probe in a specific position. The inchworm design presented in this chapter follows a radically different approach, which takes advantage of permeation instead of trying to prevent it.

### 4.1 From Monolithic to Inchworm

The inchworm design has been introduced in Section 1.6. The inchworm has several advantages over the monolithic actuators presented in the previous chapter.

With the monolithic devices, large displacement can only be achieved by operating the balloons at high internal pressure. The maximum displacement achievable is limited by the maximum pressure sustainable by the balloons. The inchworm, on the other hand, is able to provide large displacement in multiple cycles. Proceeding in small steps implies that the balloon internal pressure can be kept low, to the benefit of reliability. The maximum displacement achievable by the inchworm is constrained only by the length of the probe.

Testing of the monolithic devices revealed latchability issues. The balloons relax relatively fast, mostly due to the permeation of gases through the balloon wall. In order to maintain the probe in a certain position, electrolysis must be continuously run to

compensate for the permeation and recombination of the gases. The inchworm, on the other hand, is inherently latchable without power. When the probe is not moved, it stays in the last set position. If the elasticity of the tissue tends to push the probe backward when the inchworm is at rest, the device can be complemented with some passive mechanism to apply friction to the probe and keep it in position.

Due to the inherent latchability of the inchworm, recombination and, most importantly, permeation do not cause problems. The situation is, actually, opposite. In the inchworm, the balloons have to expand and relax cyclically. Therefore, we would like recombination and permeation to be large, in order to reduce the time required to complete one inchworm cycle.

Another very positive aspect of the inchworm is the decoupling of the probe fabrication from the actuator fabrication. This separation dramatically increases the flexibility of the design. The specific issues of the actuator and the probe can be dealt with separately, without the constraints of a common fabrication process. The inchworm can be easily adapted to move different kinds of probes, so that the best probe for a certain application can be selected.

The balloons in the inchworm have another advantage. In the monolithic devices, a spring had to be placed inside the balloons, in order to provide a routing path for the metal traces leading the electrodes on the neural probe. In the inchworm, one spring is still present, but not inside a balloon.

## **4.2 Design**

The inchworm is based on two electrolytic balloon actuators. The balloons are assembled onto a silicon frame, which supports the electrodes and provides a spring

mechanism. The frame with and without the balloons is shown in Figure 4-1. The spring offers a path for the metal traces leading to the clamping balloon electrodes, while preserving the mechanical flexibility required for the operation of the inchworm. The two platinum electrodes to be enclosed in each balloon are  $25\text{ }\mu\text{m}$  wide and  $10\text{ }\mu\text{m}$  from each other. The  $90^\circ$  angles in the frame have been smoothed with a round fillet to reduce stress concentration.

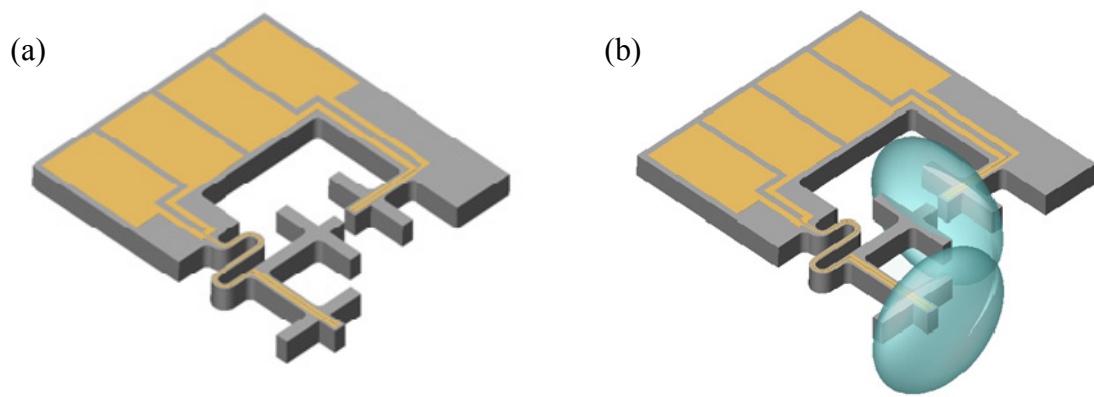


Figure 4-1. 3D model of the inchworm actuator. a) Silicon frame only, without balloons. b) Silicon frame with balloons.

The principle of operation, which follows the steps illustrated in Section 1.6, is illustrated in Figure 4-2. The probe is clamped between the clamping balloon on one side and fixed supports on the other side. The fixed supports have to be provided separately. The friction between the probe and the supports must be lower than the friction between the probe and the clamping balloon; otherwise the inchworm just slips along the probe without moving it. Alternatively, two actuators could be placed side to side, with the probe clamped in between the two.

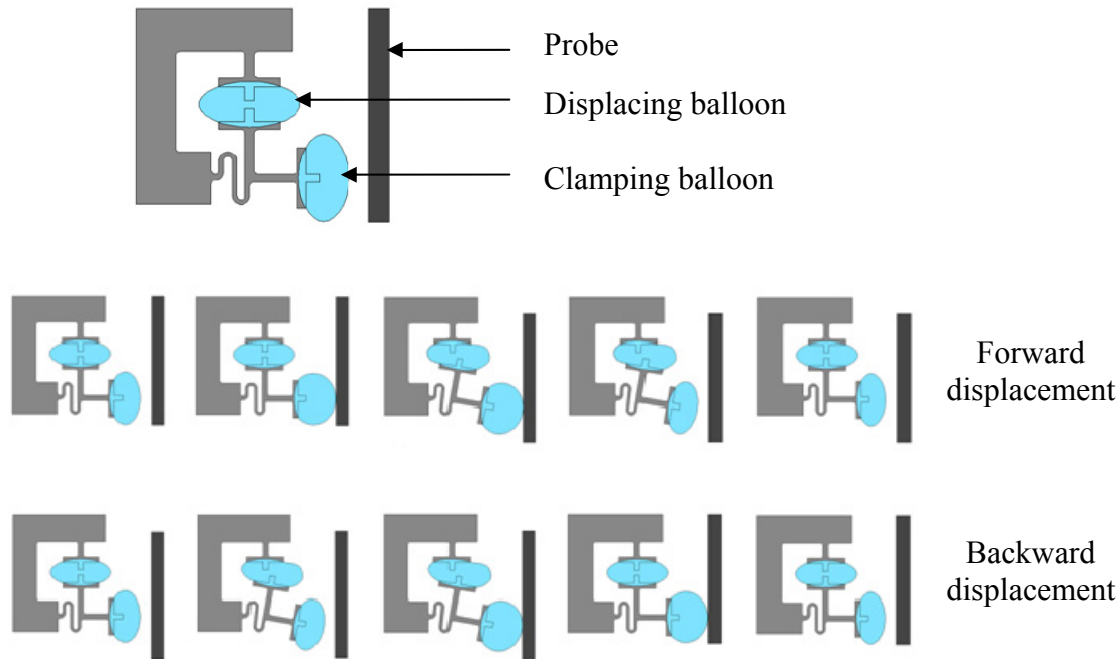


Figure 4-2. Inchworm actuation principle. The steps for forward and backward movement are illustrated.

The position of the spring on the frame was chosen to create a lever effect. As shown in Figure 4-2, the displacing balloon is connected to a point close to the spring. Due to the distance between this point and the probe, the displacement applied by the balloon is amplified at the probe. This is confirmed by a finite element simulation, as presented in the next section. The lever design, however, causes the inchworm arm to move along a curved path during actuation. This is particularly noticeable for large displacement in a single cycle. Placing the spring in-line with the displacing balloon would allow the arm to move along a straight line, but it would not provide any displacement amplification.

A consequence of this design is that the balloon applies force only when pushing the probe forward. When the probe is moved backward, the force is provided only by the



elasticity of the spring and of the displacing balloon wall. If more force is necessary to move the probe backward, an additional displacing balloon should be placed symmetrically on the other side of the spring. In that way, the force of a balloon would be available for both forward and backward displacement.

### 4.3 Simulations

As mentioned in the previous section, the spring mechanism has been designed to provide mechanical amplification of the displacement. The silicon beam forming the spring is 50  $\mu\text{m}$  wide, the whole spring is 600  $\mu\text{m}$  wide from side to side, and the turns have an internal radius of 50  $\mu\text{m}$ . The design is validated through finite-element simulations using COMSOL Multiphysics (Figure 4-3). We compare the displacement obtained when the spring is subject to a side force or an in-line force.

In the first simulation (Figure 4-3a), a force is applied on the side of the spring, in the same position where the displacing balloon applies it. The vertical displacement is measured at the tip of the electrode-supporting shank, even though the displacement at the probe is larger than at that point, due to the clamping balloon extending farther out from there.

In the second simulation (Figure 4-3b), the same force is applied in-line with the spring, and the horizontal displacement is measured. This configuration simulates the behavior of the spring as if it were placed in-line with the displacing balloon. In reality, to place the spring in-line with the displacing balloon, the frame geometry would have to be redesigned. However, this simulation enables us to conveniently examine how the spring would behave in-line without any redesign of the geometry.

For the side-force case, a displacement per unit force of  $0.24 \mu\text{m}/\text{mN}$  is obtained. For the same force, the displacement is five times larger in the case of side force than in the case of in-line force.

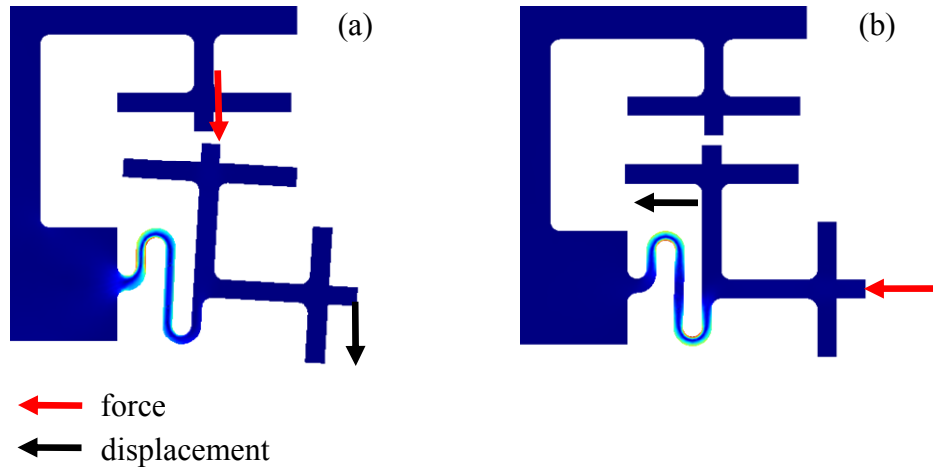


Figure 4-3. Finite-element simulations of the spring mechanism. The colors show the Von Mises stress, to highlight the stress concentrations points. a) The force is applied on the side of the spring. b) The force is applied in-line with the spring.

## 4.4 Fabrication

The fabrication steps are illustrated in Figure 4-4, and they are analogous to the steps illustrated in Section 2.6.1 and 2.6.2. The silicon frame is fabricated first. Thin silicon wafers,  $200 \mu\text{m}$  thick wafers are used as substrates. A first layer of parylene C,  $0.5 \mu\text{m}$  thick, is deposited by LPCVD, and molten at  $350^\circ\text{C}$  in a nitrogen environment. The molten parylene acts as an adhesion layer for a second layer of parylene C,  $1 \mu\text{m}$  thick.

Platinum is deposited by e-beam evaporation, and it is patterned by liftoff. The adhesion of platinum to parylene is sufficient for the fabrication of the devices. The

adhesion of platinum to parylene in different conditions was examined. Platinum adhesion to molten parylene was found to be very poor, which is the reason why the second parylene C layer is deposited on top of the molten parylene. The higher crystalline fraction of molten parylene compared to as-deposited parylene is suspected to be the cause of the scarce adhesion. Furthermore, the thickness of the second parylene layer seems to affect the platinum adhesion, with thicker layers providing better adhesion. The crystalline structure of molten parylene layer may act as a seed for the parylene layer above, causing the crystalline structure to propagate through the second layer. If the second layer is thick enough (1 or 2  $\mu\text{m}$ ), the crystalline structure may be lost, with parylene returning to an amorphous condition that provides better platinum adhesion.

Parylene is patterned by RIE in oxygen plasma. A through-wafer DRIE step releases the devices. Thin wafers (200  $\mu\text{m}$  thick, instead of the conventional 500  $\mu\text{m}$ ) were chosen to shorten the DRIE etching step, without having to thin down the wafers. Figure 4-5a shows a finished frame, with close-ups on the spring and electrodes.

The reflow of the photoresist that acts as a mask for DRIE causes some difficulties. The reflow is caused by the baking step preceding DRIE, which makes the photoresist assume a rounded profile. This is particularly evident for the photoresist that masks narrow features, such as the spring beam (50  $\mu\text{m}$  wide). The photoresist is thinner at the edges of a feature, making it unable to withstand the entire DRIE etch there. As a consequence, the rounded profile is transferred, to a certain extent, to the etched silicon structures. This effect is reduced by making the photoresist thicker.

Processing 200  $\mu\text{m}$  thick 4-inch diameter wafers requires special care, due to the fragility of the substrate. Mounting a backing wafer on the back of a wafer is very

convenient to avoid breaking the wafers during the fabrication process, even though processing without the backing wafers is possible. Photoresist is used as the adhesive between the device wafer and the backing wafer. Photoresist has the advantage of being dissolvable at the end of the process to release the devices from the substrate. The backing wafer can be mounted only after the parylene-melting step, as photoresist cannot be exposed to a temperature of 350 °C. Therefore, the first part of the process must be done without the support of the backing wafer. The backing wafer and the steps required to mount it are not shown in the process steps of Figure 4-4.

After the frame is completed, the balloon fabrication is analogous to the process developed illustrated in Section 2.6.2. The inchworm is based on disc-less balloons with parylene walls, fabricated with a sacrificial photoresist process. The silicon frame is mounted on a glass slide, for ease of handling. Sacrificial photoresist (AZ4620) is dispensed over the frame to define the balloon shape (Figure 4-5d). A commercial fluid dispenser (EFD 2000XL) with a 33-gauge needle is used. Some photoresist is dispensed over the pads as well, so they can be reopened after the parylene deposition. The photoresist is baked on a hotplate at 70 °C. It is important to make sure that no gas bubbles are trapped in the photoresist, as they may burst in vacuum during the following parylene deposition. A layer of parylene is then deposited (typically 10 µm thick). A sharp needle is then used to poke a hole in the parylene of each balloon and over the pads. The device is immersed in acetone for releasing the photoresist. After the photoresist is completely released (Figure 4-5e), and the acetone has completely evaporated, the device is immersed in an electrolyte solution inside a vacuum chamber,

and the balloons are filled. The balloons are finally sealed with a small drop of fast-setting glue and/or epoxy.

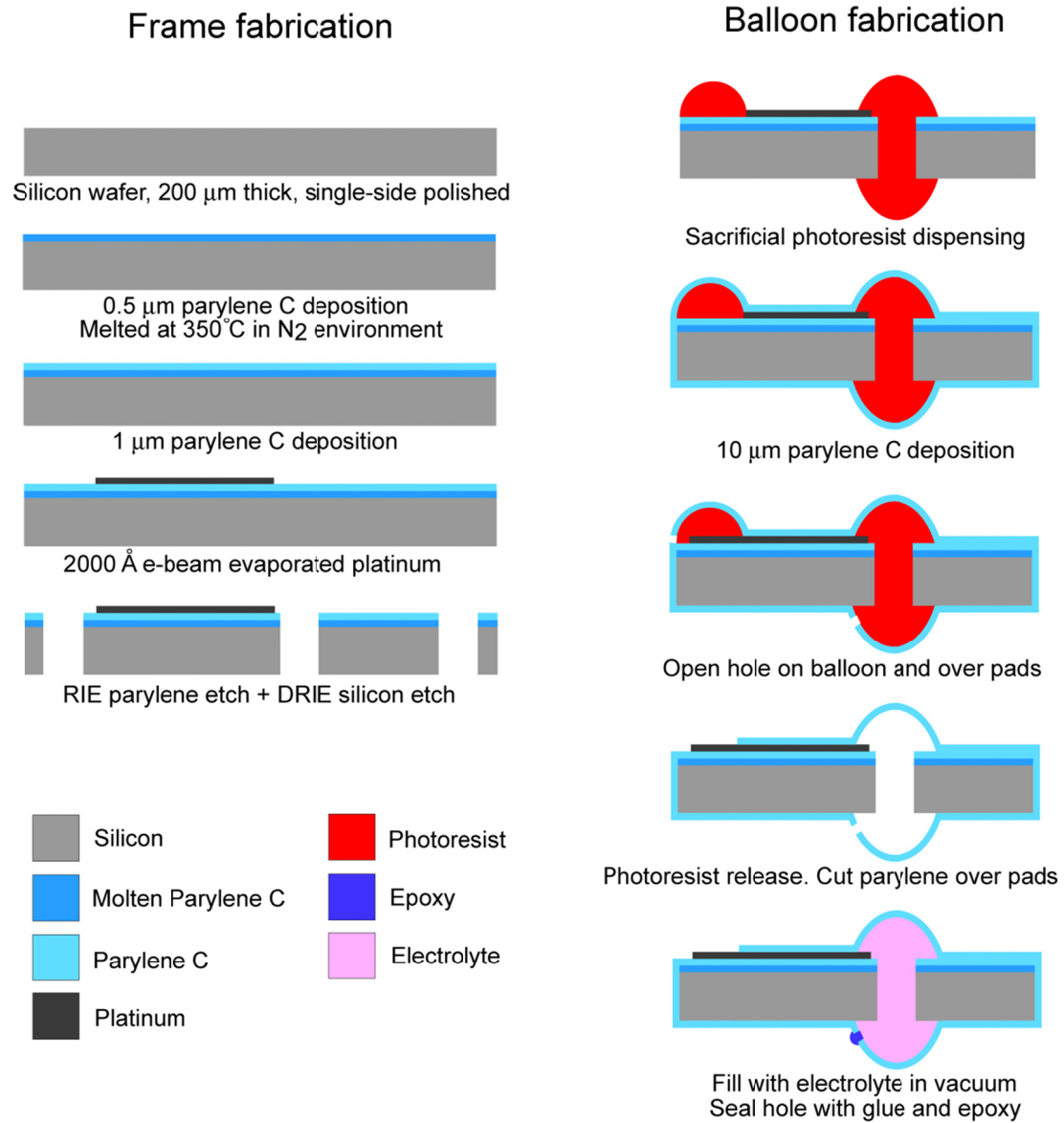


Figure 4-4. Fabrication steps for the inchworm. The process is divided into two parts: frame fabrication and balloon fabrication.

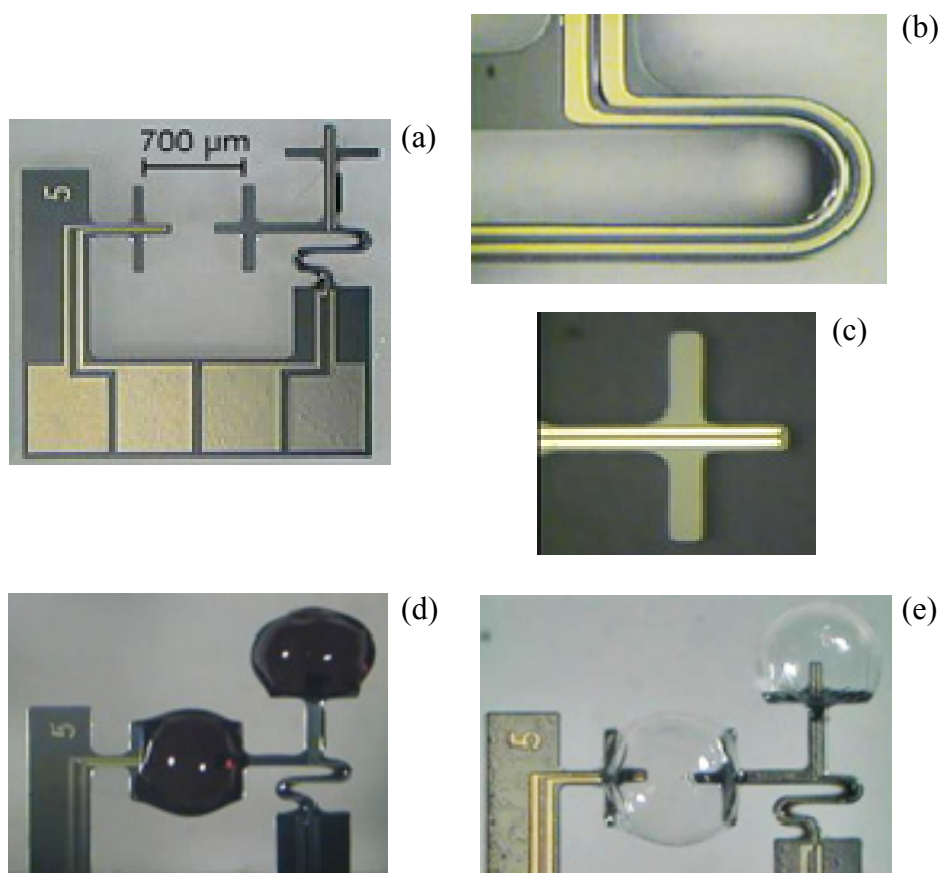


Figure 4-5. Fabricated first-generation inchworm devices. a) Silicon frame. Frames with different dimensions were fabricated, and the number on the frame identifies them. b) Close-up of the spring. c) Close-up of the electrodes. d) Frame with sacrificial photoresist. Due to photoresist reflow, the shape tends to become spherical. e) Frame with parylene balloons, after release of the sacrificial photoresist.

## 4.5 Results

The inchworm was tested by trying to move a piece of thin metal wire. The inchworm was placed horizontally, with the sharp corners of two glass slides acting as the probe supports on the other side of the probe. The sharp corners were used to

minimize the contact area between the probe and the supports, in order to reduce the friction. To further reduce the friction, the corners were covered with Teflon tape. The inchworm was successfully actuated, but the wire could not be displaced reliably, due to the excessive friction of the supports.

The disc-less balloons with parylene walls showed all the problems illustrated in Section 2.6.3. First, there are the reliability issues due to the failure of the release/fill hole seal and to the adhesion between the parylene wall and the parylene and platinum on the frame. Second, the shape of the balloon tends to be almost spherical, due to photoresist reflow. Frame geometries were fabricated that should make the balloon shape more ellipsoidal even after reflow, but the results were not fully satisfactory. Third, the parylene balloons are slow during the relaxation phase, and one inchworm cycle can take more than one hour to complete. Fourth, the parylene balloons provide limited displacement, and the probe must be placed very close to the clamping balloon in order for clamping to occur.





## CHAPTER 5

---

# Second-generation Inchworms

### 5.1 From First to Second Generation

The problems of the first-generation device and the knowledge acquired during the testing of standalone balloon actuators inspired the design of the second-generation inchworm actuators [87]. Table 5-1 is a comparison of the first- and second-generation inchworms, highlighting the new features and technology introduced in the second generation. These improvements are explained in detail in the rest of the chapter.

The research on balloon actuators presented in Chapter 2 offers solutions for improving the inchworm actuators. The first-generation inchworm has balloons with parylene wall and without silicon discs. The introduction of silicon discs and silicone wall is beneficial for the balloon operation and reliability. The silicon discs allow better balloon shape definition, and they improve the sealing of the balloon. Silicone has a lower elastic modulus and higher permeability than parylene. The lower elastic modulus allows operation at lower pressure, while the higher permeability makes the balloon relaxation faster, shortening the duration of each inchworm cycle.

The release/fill hole in the balloons represents a weak point and a reliability concern, as it is one of the main causes of seal failure. The hole can be eliminated by exploiting osmosis to fill and refill the balloon and by using a “sacrificial” material that does not need to be released out of the balloon. With silicone-wall balloons, osmosis was proven to be a viable method to fill the balloon with water and to compensate for water

lost during operation (Section 2.9). Materials that provide the same mechanical support as sacrificial photoresist but that need not be released from the balloon are explored in the second-generation devices. A new hole-less process is introduced where sacrificial photoresist is replaced by magnesium sulfate or hydrogel.

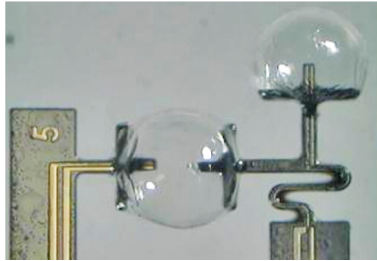
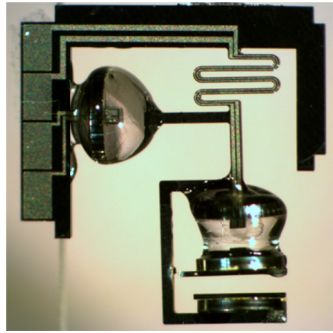
These modifications in the balloon process (silicon discs, silicone walls, and hole-less fabrication) could, in principle, be performed on the frame of the first-generation inchworm devices, but there is another issue that requires a deeper redesign. The single-side clamping of the probe is a serious problem of the first-generation inchworm. As explained in Section 4.2, the clamp has one movable side (the clamping balloon) and one fixed side (the external supports). The friction between the probe and the fixed supports needs to be low for the inchworm to displace the probe. The control of this friction was found to be difficult, and a double-side clamping approach that avoids this problem is followed for the second-generation devices.

## **5.2 Design**

### **5.2.1 Frame Design**

The basic principle of an inchworm with two balloon actuators fabricated on a silicon frame has been preserved in the second generation. The roles of the balloons are the same as in the first generation, with one balloon for clamping the probe and one for displacing it (Figure 5-1b). The silicon frame is still used to support the electrodes and to provide a spring mechanism (Figure 5-1a). The frame has been modified from the first version for two main reasons: making the spring more flexible and introducing double-side clamping of the probe.

Table 5-1: Feature and technology comparison of the first and second generation of inchworms.

First Generation	Second Generation
	
Balloons with no silicon discs	Balloons with silicon discs
Parylene balloons	Silicone balloons
Sacrificial photoresist process	MgSO <sub>4</sub> /Hydrogel process
Vacuum filling through hole	Hole-less (re)filling by osmosis
Single-side probe clamping	Double-side probe clamping

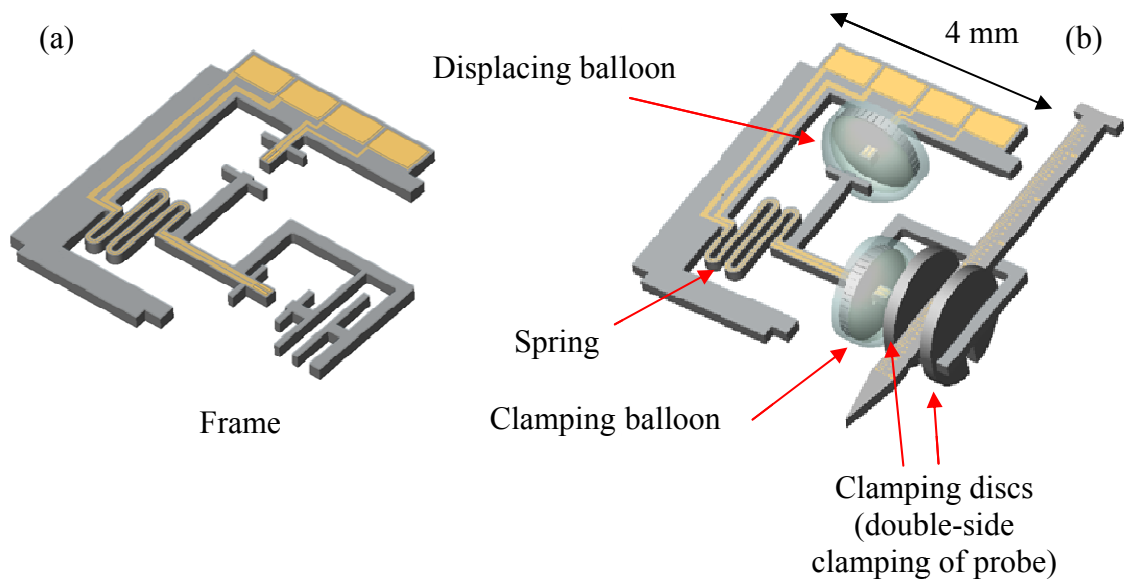


Figure 5-1. Second-generation frame design: a) frame only, b) complete device.

The position of the spring is unchanged from the first generation, to provide the same lever effect and displacement amplification (Section 4.2). The silicon beam forming the spring is 100  $\mu\text{m}$  wide, compared to the 50  $\mu\text{m}$  of the first generation. The larger width provides more space for the metal traces, and it increases the yield of the DRIE process. In fact, reflow of the photoresist that masks DRIE makes it difficult to fabricate narrow beams (Section 4.4). The spring overall width and the number of turns are increased to make the spring more flexible despite the increase in beam width. A more flexible spring allows a more efficient use of the force generated by the displacing balloon, as less force is wasted internally in the device and more is available to displace the probe. The spring is 1.65 mm from side to side, and it has four turns (compared to two in the first generation), each with an internal radius of 50  $\mu\text{m}$ .

The new spring design has been validated by finite-element simulations using COMSOL Multiphysics (COMSOL, Inc.). The simulations are performed in the same way as for the first generation (Section 4.3). For the case of side force, the displacement is measured at the probe location, and a displacement per unit force of 5.7  $\mu\text{m}/\text{mN}$  is obtained. The displacement in the case of side force is about 10 times larger than in the case of in-line force, due to the lever effect.

Similarly to the first-generation inchworm, the lever design produces displacement amplification, but causes the inchworm arm and the probe to move along a curved path during actuation. This is particularly noticeable for large displacement in a single cycle. If this is found to be a problem for the application at hand, the spring can be moved in-line with the displacing balloon. The probe would then move along a straight line at all times, but without any displacement amplification.

Compared to the first generation, the frame has an additional section in front of the clamping balloon, in order to provide for the double-side clamping of the probe. Two special “clamping discs,” which clamp the probe from both sides, are assembled on this part of the frame. The clamping mechanism needs to be released by removing a section of the frame. The fabrication steps in Section 5.3 illustrate the assembly and release of the clamping mechanism more clearly.

The principle of actuation is shown in Figure 5-2, and it is analogous to the first generation’s. One inchworm cycle comprises a number of steps in which the displacing or clamping balloons are expanded or relaxed. The movement direction is reversed just by modifying the order of these steps.

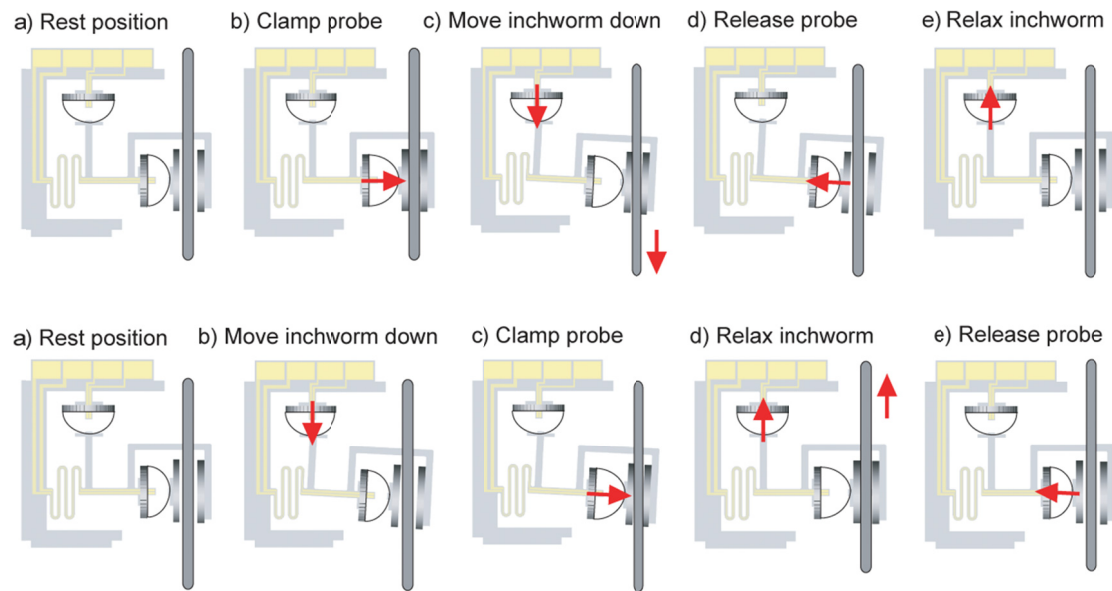


Figure 5-2. Inchworm actuation principle.

### 5.2.2 Balloon Disc Design

The balloon discs have been modified in two ways from the ones introduced in Section 2.7. First, the release/fill hole has been removed because, as it will be explained later, the fabrication process does not require a hole. Second, lateral anchors have been added to reduce the lateral expansion of the balloon (Figure 5-3a). Ideally, the balloon should expand only longitudinally, in order to efficiently exploit the internal pressure. Any lateral expansion of the balloon is not useful for the function of the device, and it is only a wasteful use of the internal pressure. Lateral anchors provide a way to reduce lateral expansion by causing the balloon wall to stick to the sidewall of the discs (Figure 5-3a).

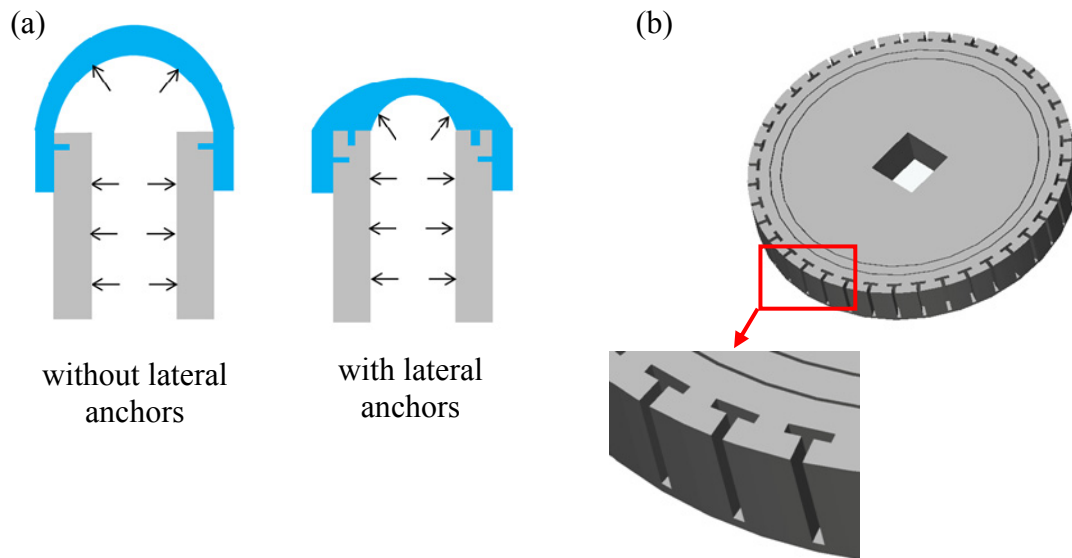


Figure 5-3. a) Effect of the lateral anchors on the lateral expansion of the balloon. b) T-trenches around the edge of the disc to create the lateral anchors.

The introduction of the lateral anchors does not affect the fabrication process. The anchors are obtained by T-shaped features etched at the edge of the disc (Figure 5-3b). The T shape makes the trenches act as lateral anchors even though they are etched from the surface of the disc. Discs are fabricated with radii varying from 500  $\mu\text{m}$  to 750  $\mu\text{m}$ , and discs of different sizes are identified by a notch pattern etched on the surface.

## **5.3 Fabrication**

### **5.3.1 Frame and Ruler Probe**

The fabrication steps for the frame are illustrated in Figure 5-4. The fabrication starts with a 200  $\mu\text{m}$  thick silicon wafer. The wafer is coated with 0.5  $\mu\text{m}$  of parylene C (Specialty Coating Systems), which is then melted at 350  $^{\circ}\text{C}$  in  $\text{N}_2$  atmosphere. The molten layer acts as an adhesion layer for a subsequent 2  $\mu\text{m}$  parylene C deposition. Platinum is then deposited by e-beam evaporation and patterned with a lift-off process. Another layer of parylene C is deposited, completing the insulation of the metal traces. Pads and electrodes are opened in the top parylene layer by RIE in  $\text{O}_2$  plasma. To release the devices, parylene is completely removed by  $\text{O}_2$  RIE around the outline of the frame. The exposed silicon is then etched by DRIE to define and release the frame. A fabricated frame is shown in Figure 5-5a.

Silicon probes with a ruler pattern on the top surface are fabricated on the same wafer as the silicon frames. The ruler pattern is obtained on the platinum layer. The pattern is convenient for measuring the displacement of the probe during testing. One of these probes is shown in Figure 5-5b.

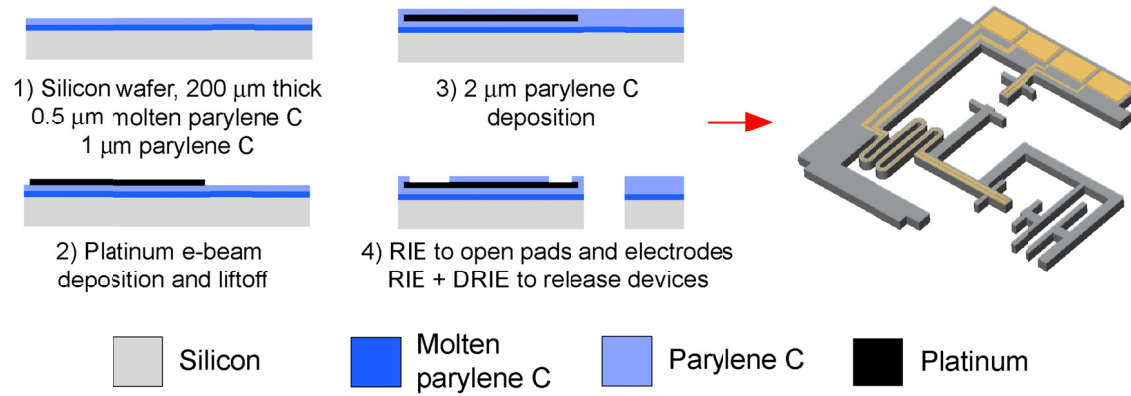


Figure 5-4. Frame fabrication steps.

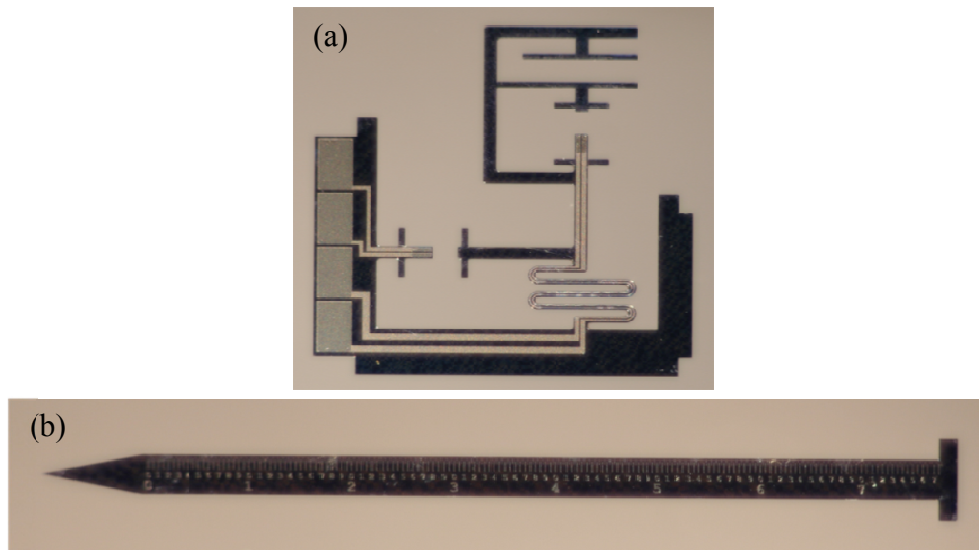


Figure 5-5. a) Fabricated silicon frame. b) Fabricated ruler probe.

### 5.3.2 Balloon and Clamping Discs

The fabrication process for the discs is identical to the one illustrated in Section 2.7. For completeness and convenience, the steps are illustrated again in Figure 5-6a. Two kinds of discs are fabricated: balloon discs and clamping discs. The clamping discs have a notch pattern for geometry identification, but they have no anchors or holes.



A 1.5  $\mu\text{m}$  thick layer of silicon dioxide is grown on thin wafers (200  $\mu\text{m}$  thick) by wet oxidation at 1050  $^{\circ}\text{C}$ . The oxide is then patterned and used as a mask for DRIE. Two kinds of trenches are needed: anchor trenches (5  $\mu\text{m}$  wide) and release trenches (100  $\mu\text{m}$  wide). The DRIE etching rate is lower in narrower trenches (DRIE lag), making it possible to obtain both types of trench with a single-mask process. When the release trenches are etched all the way through the wafer (thus releasing the discs from the wafer), the anchor trenches are only about 80-90% through. Pictures of fabricated balloon and clamping discs are shown in Figure 5-6b.

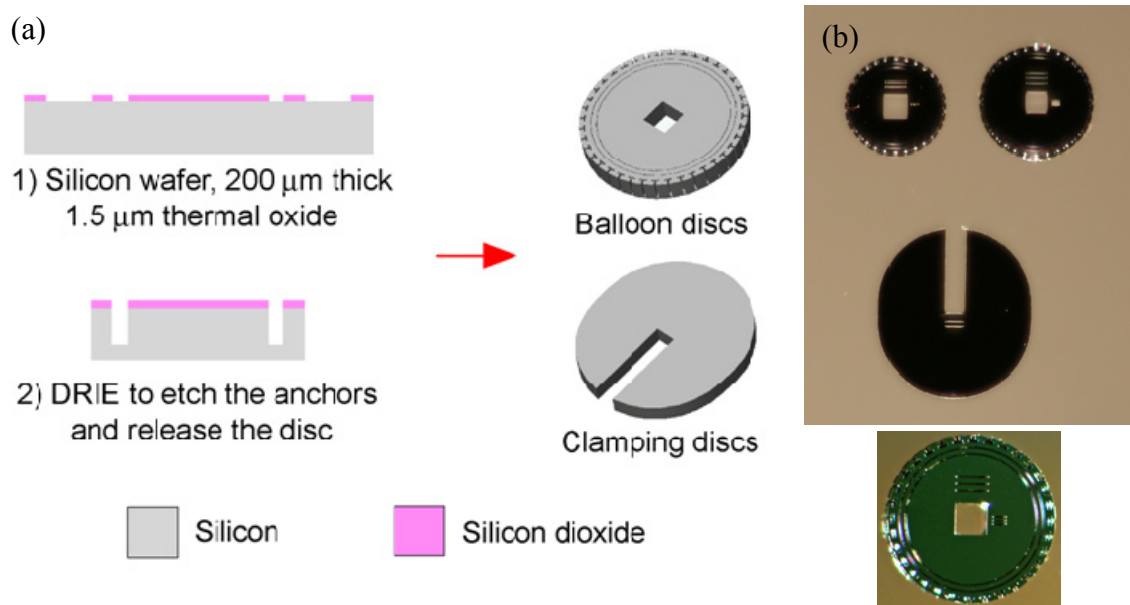


Figure 5-6. a) Fabrication steps for the discs (both balloon discs and clamping discs). b) Fabricated discs.

### 5.3.3 Disc Assembly

For support during assembly and balloon fabrication, the silicon frame is glued to the edge of a glass slide. The silicon discs (balloon discs and clamping discs) are assembled onto the frame using a xyz micrometer stage equipped with tweezers (Figure 5-8). Balloons can be built with one or two discs per balloon. Because balloons with one disc are easier to fabricate, and they are found to have good performance, most devices are built in this way. The balloon discs and the clamping discs have a different assembly procedure. The balloon discs have a central hole that matches the electrode-supporting shank on the frame. A balloon disc is aligned to the side of the shank and then inserted onto it (Figure 5-7a). The clamping discs have a notch, and they are placed onto the frame from above (Figure 5-7b). The discs are secured to the frame using epoxy. The epoxy also has to seal the frame-disc interface of the balloon discs. Initially, a two-part fiberglass-reinforced epoxy (Loctite Fixmaster High Performance Epoxy, Henkel AG & Co.) was used. This was eventually substituted by a biocompatible epoxy (EPO-TEK 301-2, Epoxy Technology). The epoxy is applied using a thin piece of wire manually held by tweezers. The biocompatible epoxy is less viscous than the fiberglass-reinforced one, and more care is required during application. Frames with assembled discs are shown in Figure 5-9.

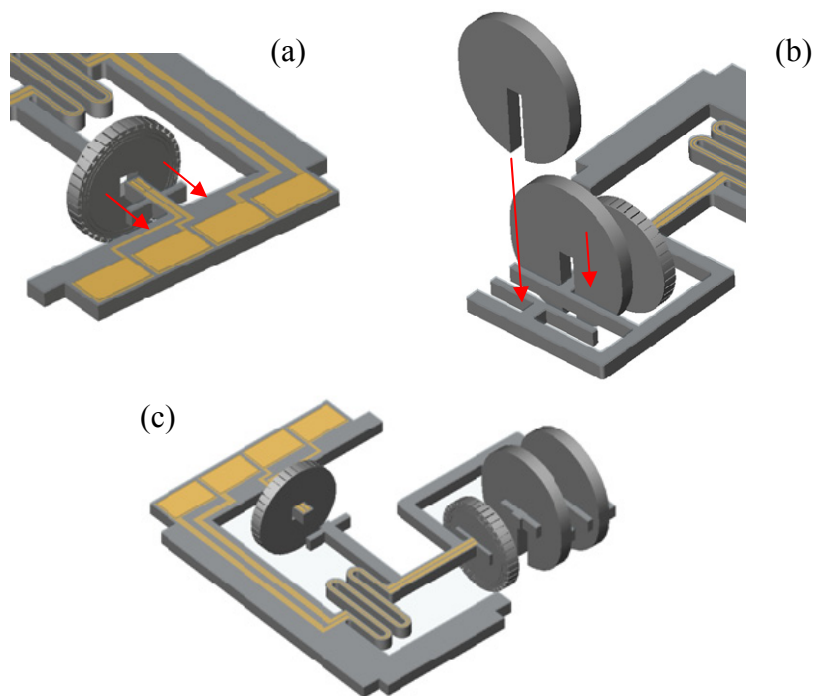


Figure 5-7. a) Assembly of the balloon discs. b) Assembly of the clamping discs. c) Frame with assembled discs (case of balloons with one disc).

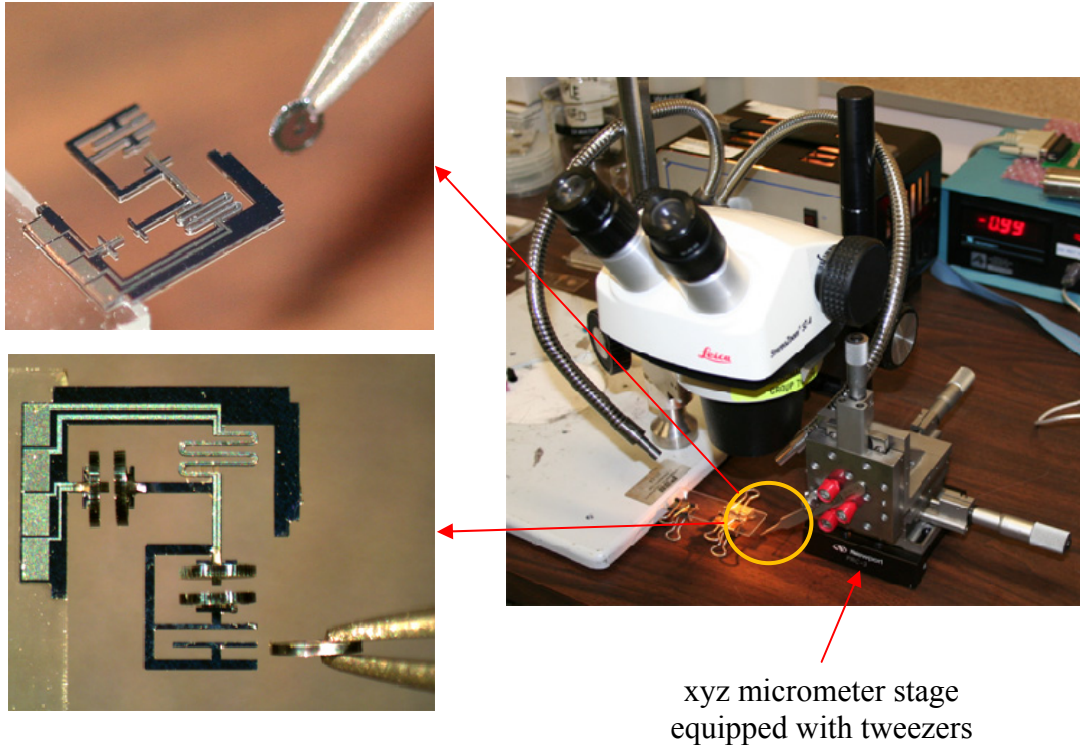


Figure 5-8. Assembly of discs with tweezers mounted on a xyz micrometer stage. The assembly is performed under a stereoscope.

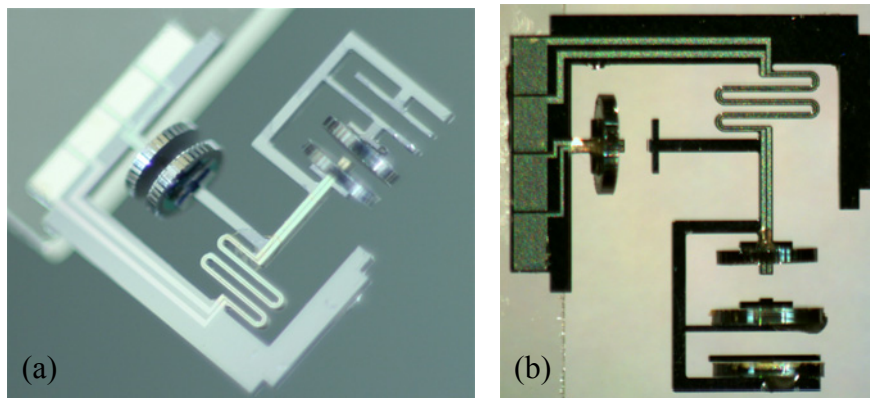


Figure 5-9. a) Frame with assembled balloon discs (case of balloons with two discs). b) Frame with assembled balloon and clamping discs (case of balloons with one disc).

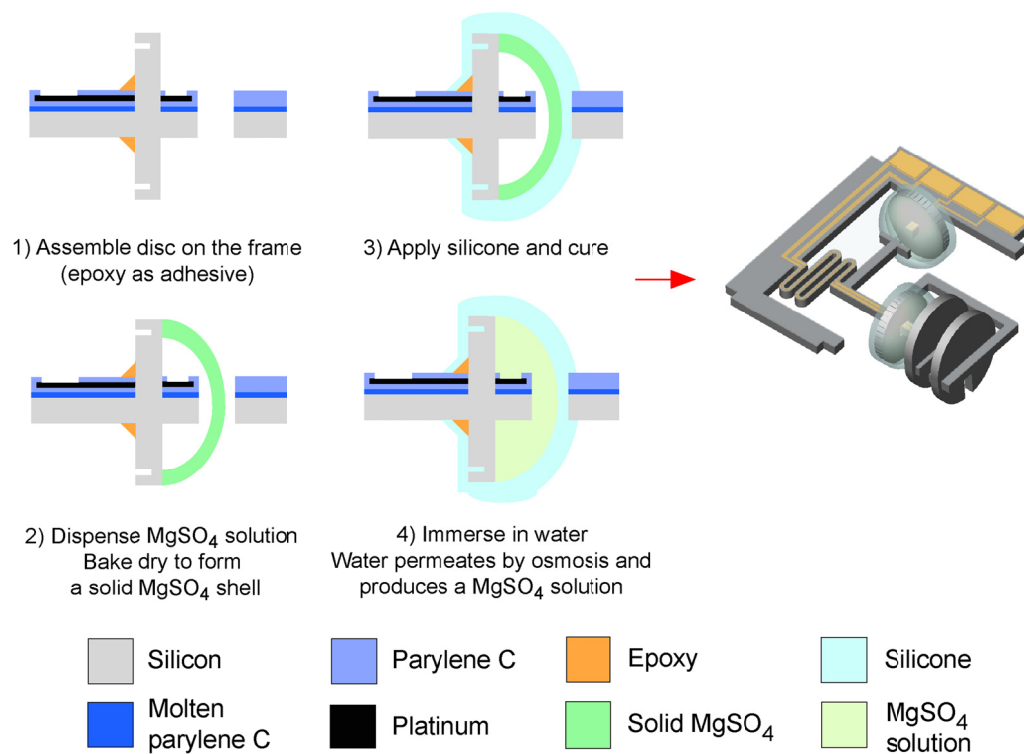


Figure 5-10. Fabrication steps for balloons with one disc.

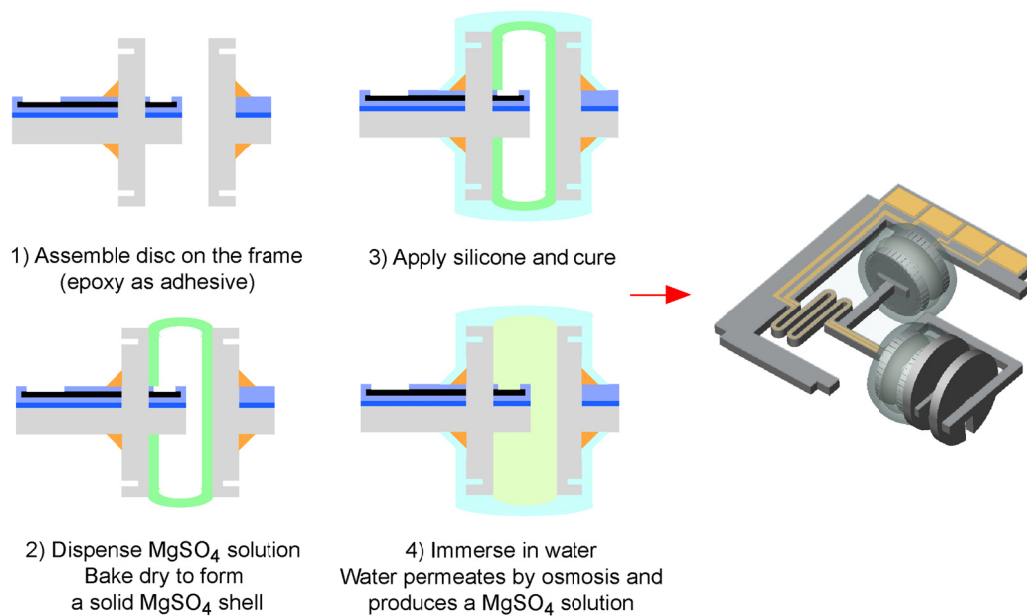


Figure 5-11. Fabrication steps for balloons with two discs.

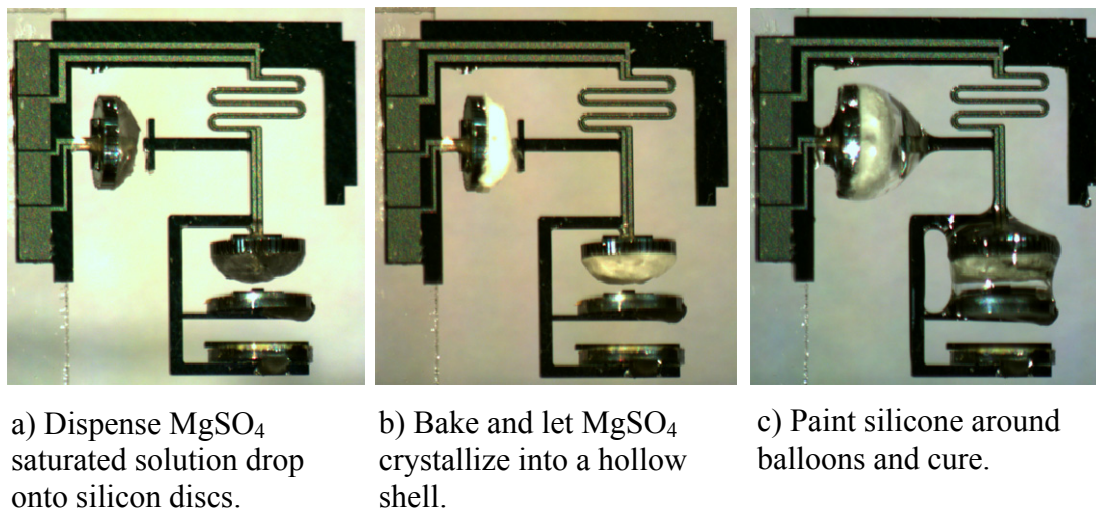


Figure 5-12. Device at different stages of balloon fabrication. The balloons filled with water are shown in Figure 5-14b.

### 5.3.4 $\text{MgSO}_4$ -based Balloon Process

The balloon fabrication steps are illustrated in Figure 5-10 (balloons with one disc) and 5-11 (balloons with two discs). Pictures of a device at different fabrication stages are shown in Figure 5-12. A saturated solution of magnesium sulfate ( $\text{MgSO}_4$ ) is prepared and placed in a syringe.  $\text{MgSO}_4$  saturation in water occurs at a molal concentration of about 2 mol/L. The solution is dispensed on the surface of the discs using a commercial fluid dispenser (EFD 2000XL) with a 33-gauge needle. Due to the high concentration of the solution, the needle is easily clogged by the formation of solid  $\text{MgSO}_4$ , but it is quickly freed by immersing it in deionized water. As water starts to evaporate,  $\text{MgSO}_4$  crystals start forming in the dispensed drop (Figure 5-12a). The device is then baked in a convection oven to make all the water evaporate. When the  $\text{MgSO}_4$  is dried in this way, it crystallizes into a hollow shell shape (Figure 5-12b). The shell shape is probably due to crystallization occurring faster on the surface than in the bulk of the

drop, because of water evaporation from the surface. Once crystallization starts on the surface, it acts as a seed for the rest of the drop. To have a clean shell shape, the temperature of the oven is set to a maximum of 60 °C. If the temperature is too high, bubble formation causes the shell shape to be irregular, with very non-uniform thickness (some sections are very thin and easily broken), or even with holes and cracks. The volume enclosed by the shell is almost equal to the volume of the initial solution drop, even though some shrinking does occur.

Salts other than magnesium sulfate can be used for balloon fabrication. However, it is important to avoid salts containing chlorine ions, as these ions would be converted into chlorine gas during electrolysis. As a matter of fact, electrolysis of salt water is a method of chlorine production in industry. The chlorine gas generated inside the balloon would then permeate out of the balloon wall, with toxic effects on the brain tissue when the actuator is implanted.

In the next step, silicone is painted around the shell and the disc(s) (Figure 5-12c). The magnesium sulfate shell acts as a mechanical support for the silicone before it is cured. Silicone is deaired in vacuum for about 10 minutes, to avoid the presence of gas bubbles in the balloon wall.

The adhesion of the magnesium sulfate shell to the silicon disc is not good, and a small gap between the disc and the shell is often present. We tried to improve the adhesion by oxidizing the surface of the disc, hoping that the increased hydrophilicity of the surface could improve the adhesion. Unfortunately, no satisfactory results were obtained.

If silicone with low viscosity is used, it flows into the gap between the disc and the shell, where it can reach and coat the platinum electrodes, causing the balloon to be defective. To avoid having silicone flowing into the gap, a dual-silicone approach was initially taken. First, a ring of thixotropic silicone (3145, Dow Corning, Inc.) is painted all around the disc-shell interface. After that, a low-viscosity silicone (Sylgard 184, Dow Corning, Inc.) is applied all around the balloon. The presence of the thixotropic silicone (which is a like a paste) at the interface prevents the low-viscosity silicone from flowing into the gap. The use of the low viscosity silicone is necessary because it can flow and provide good coverage all around the balloon, which would be difficult to achieve by only using the thixotropic kind. The chemistries of the two silicones are compatible, and they can be applied and cured together even though the cure mechanism is different (Sylgard 184 is two-part heat-cure, whereas 3145 is one-part moisture-cure). Dow Corning 3145 is basically PDMS, like Sylgard 184, made thixotropic by the addition of silica. The silicone is cured at 60 °C. The silicone can be applied in multiple layers, with a baking step in between. A 15 minute bake produces a partial cure that is sufficient for painting another layer. The partial cure also guarantees excellent bonding between adjacent layers. Usually, two or three layers form a silicone coating about 100  $\mu\text{m}$  thick all over the balloon. A final bake of a few hours completes the cure.

When applying the silicone, it is important to make the coating thick enough at the disc edge. The coating tends to be thin in that region, due to the silicone flow properties. Moreover, the edge constitutes a region of stress concentration during actuation (exacerbated by the presence of the lateral anchors), and a thin layer of silicone is easily torn. The thixotropic silicone helps create a thick layer at the disc edge.



The dual-silicone approach was eventually abandoned for a simpler approach using only one type of silicone. A high-viscosity biocompatible silicone (Silastic MDX4-4210, Dow Corning, Inc.) was chosen. The high viscosity prevents the silicone from flowing into the gap, but the silicone still flows well enough to guarantee good coverage. As a comparison, Sylgard 184 has a viscosity of 4575 cps, while MDX4-4210 has a viscosity of 115000 cps. Similarly to the dual-silicone case, a cure of 15 minutes at 60 °C is done between each layer, with a final cure of a few hours. Typically, the first one or two layers are applied all around the balloon, and then one layer is only applied at the disc edges to thicken the silicone in that region. An additional layer all around the balloon is sometimes applied. The final silicone thickness is typically about 100  $\mu\text{m}$  or more.

After the silicone coating is complete, the device is immersed in deionized water. The high  $\text{MgSO}_4$  concentration inside the balloon causes water to permeate through the balloon wall by osmosis.  $\text{MgSO}_4$  gradually dissolves in the water that permeates into the balloon, forming a concentrated electrolyte with low impedance. During the filling process, only a fraction of the solid  $\text{MgSO}_4$  is in solution, limited by the saturation concentration of  $\text{MgSO}_4$  in water. The solution is, therefore, at saturation during the whole filling process. If the volume enclosed by the crystallized shell is equal to the volume of the saturated solution drop that was dispensed, the  $\text{MgSO}_4$  is completely dissolved in a saturated solution when the balloon is full. If some shrinking occurred during the shell crystallization, the balloon volume is smaller than the initial solution drop, and some  $\text{MgSO}_4$  remains in solid form when the balloon is full. It takes about 2 days to fill the balloon completely by osmosis at room temperature. Filling is faster at higher temperature, taking 12-24 hours at 70 °C and about 6 hours at 85 °C. Permeation

of magnesium and sulfate ions through silicone is slow, and no significant loss of  $\text{MgSO}_4$  from the balloons has been observed when immersing the devices in water. However, more accurate experiments would be needed to assess the ions' permeation rates.

This fabrication process is very convenient because no hole in the balloons is required to release any sacrificial material or to fill the balloons with electrolyte. The magnesium sulfate provides the mechanical support for coating silicone, and it stays inside the balloon in the finished device. Filling of the balloon is obtained by osmosis through the silicone membrane. This is very advantageous compared to our previous photoresist-based process (Section 2.6.2), as eliminating the hole simplifies the process and it improves the reliability of the device. In summary, the magnesium sulfate has three roles: mechanical support for coating silicone, driver for osmosis (by lowering the chemical potential of water), and electrolyte solute. To be noted is that this process would not be possible with parylene balloons, because it is not compatible with a vacuum deposition step.

### **5.3.5 Clamping Balloon Release**

The last step in the inchworm fabrication is the release of the clamping balloon (Figure 5-13). The front side of the clamping balloon must be freely movable, but it has to be physically connected to the rest of the frame for support during fabrication. The connection to the frame is removed in the end by laser ablation of silicon. In this way, the clamping balloon is free to expand and clamp the probe. The laser machine is a frequency-tripled Nd:YAG laser (QuickLaze, New Wave Research) whose UV wavelength is 355 nm.

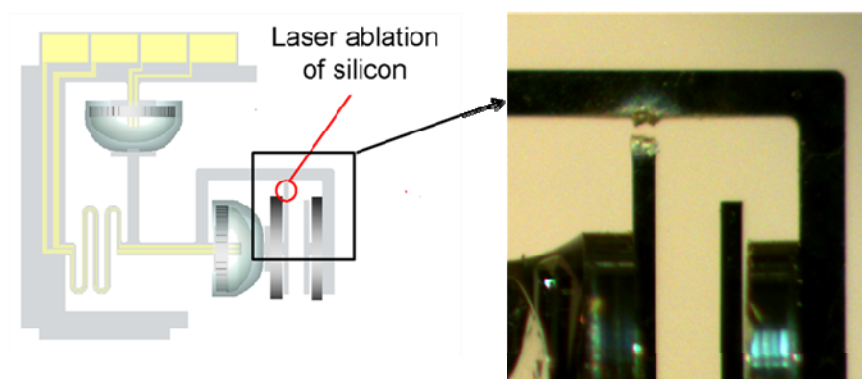


Figure 5-13. Release of the front side of the clamping balloon by laser ablation. A close-up of the ablated section is shown.

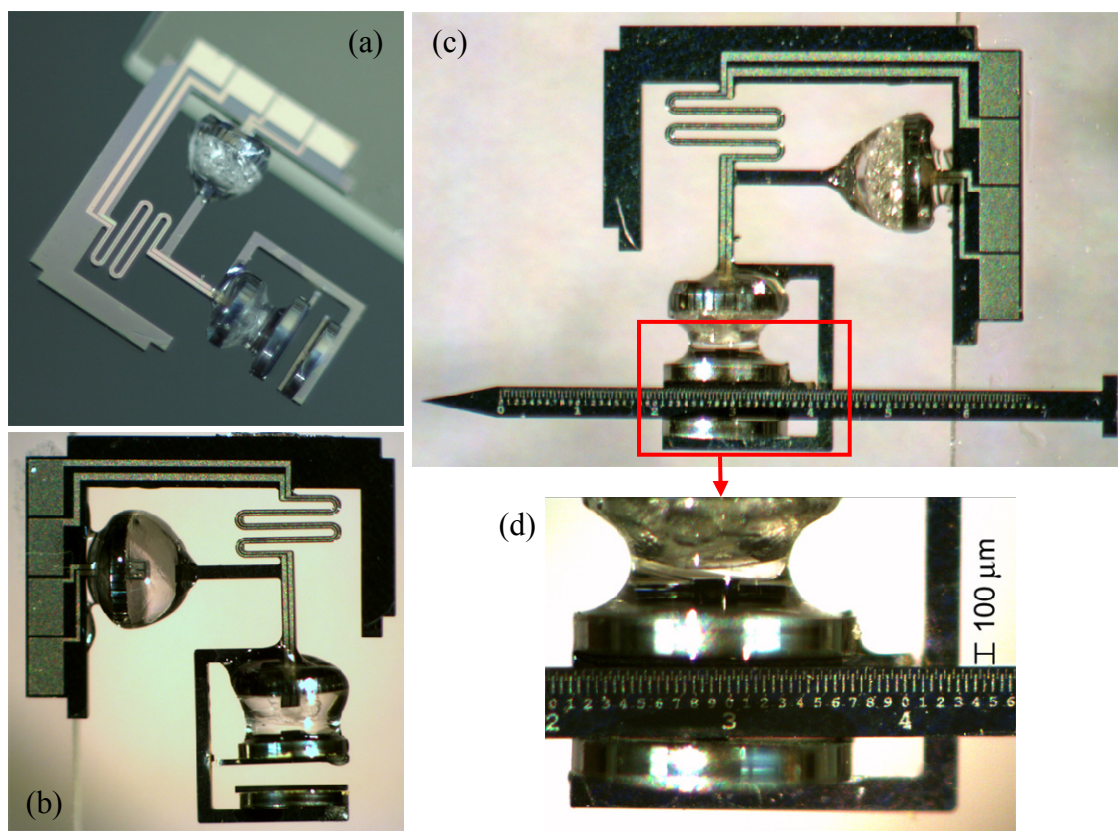


Figure 5-14. a) Inchworm with dry balloons ( $\text{MgSO}_4$  crystals are visible inside). b) Inchworm with balloons full of water (filled by osmosis). c) Inchworm with ruler probe. d) Close-up of the clamping mechanism and ruler probe.

The ruler probe is finally placed between the clamping discs. Pictures of the complete system are shown in Figure 5-14.

## 5.4 MgSO<sub>4</sub>-based Inchworm Results

The devices are tested by actuating the inchworm under a stereoscope. The displacement per cycle is measured by observing the translation of the pattern on the ruler probe relative to the inchworm frame. This method allows the detection of displacements larger than about 10  $\mu\text{m}$ . Movement of the probe in both directions was demonstrated, with displacement per cycle between 20  $\mu\text{m}$  and 75  $\mu\text{m}$ .

Despite some positive results, the MgSO<sub>4</sub>-based devices were found to have some serious problems. Three phenomena negatively affect the performance of the device: balloon overfilling, deposits on the electrodes, and stiction of gas bubbles to the electrode surface.

Balloon overfilling is due to the high concentration of the solution inside the balloon. As explained in Section 5.3.4, when the balloon is completely filled with water, the solution inside the balloon is saturated. The balloon is defined “full” when its internal volume is completely filled with water, and the internal pressure is still equal to the external pressure. If the device remains immersed in deionized water, the chemical potential gradient across the balloon wall is still present even when the balloon is full. Water keeps permeating into the balloon, causing it to overfill. As a consequence, the internal pressure increases, and the balloon expands spontaneously, without running electrolysis. An overfilled device is shown in Figure 5-15a. The large effect of overfilling is not surprising if we consider the osmotic pressure of the saturated MgSO<sub>4</sub> solution inside the balloon. The solution is about 2 M, and we assume that MgSO<sub>4</sub> completely

dissociates in water, giving a Van't Hoff factor of 2. The osmotic pressure, calculated using Equation (B-52), is then about 97 atm, which is extremely high compared to the pressure at which the balloon normally operates (a few tens of psi at most). In conclusion, the large water chemical potential gradient that allows the balloon to fill quickly also causes the overfilling problem. As a possible solution to prevent overfilling, electrolysis can be run to dispose of the excess water that is permeating into the balloon. The electrolysis rate should be low enough not to cause significant expansion of the balloons. This method, however, wastes power and reduces the energy efficiency of the device.

The formation of deposits on the electrodes is also related to the high concentration of the solution inside the balloon. After running electrolysis for some time, especially at a fast rate (current larger than 30  $\mu\text{A}$ ), a solid clear-white deposit appears on the negative electrode. The deposit is most probably magnesium or magnesium hydroxide, produced by a reaction taking place concurrently with electrolysis. The deposit covers the surface of the electrode, increasing the impedance for electrolysis. By inverting the polarity of the electrodes, the deposit is gradually removed from the electrode, but it starts forming on the other one (which is now the negative electrode).

It is difficult to control the bubble dimension and stiction to the electrodes during electrolysis. The topic of electrogenerated bubbles has been investigated by many researchers, for example [88-94]. The behavior of bubbles on gas-evolving electrodes is of great interest because it significantly affects the mass transport. The bubbles are described in terms of nucleation, coalescence, lifetime, motion, average size (when on the electrodes or when leaving the electrode), stiction to the electrode, and so on. The bubble behavior depends on many parameters, such as the characteristics of the electrode

surface, the current density, the type of electrolyte, the presence of dissolved gas in the solution, and the presence of surface-active agents. Lee et al. [95] demonstrated a microbubbler in which a convective flow is used to control the bubble size. On our electrodes, small bubbles form on the electrode and coalesce to form larger bubbles. The larger bubbles tend to stick to the electrodes, causing a dramatic reduction in the surface area available for electrolysis. In some cases, the bubbles eventually grow until they cover the whole electrode surface, preventing further electrolysis (Figure 5-15b). To reduce bubble stiction, we first tried to make the surface more hydrophilic. The device was treated with oxygen plasma before balloon fabrication. Another approach was to add a surfactant to the solution, by adding it to the saturated  $\text{MgSO}_4$  solution drop dispensed during the balloon fabrication. Neither approach was effective in reducing the problem.

These issues have been resolved by employing a hydrogel in place of the  $\text{MgSO}_4$  shell. The new process is illustrated in the next section.

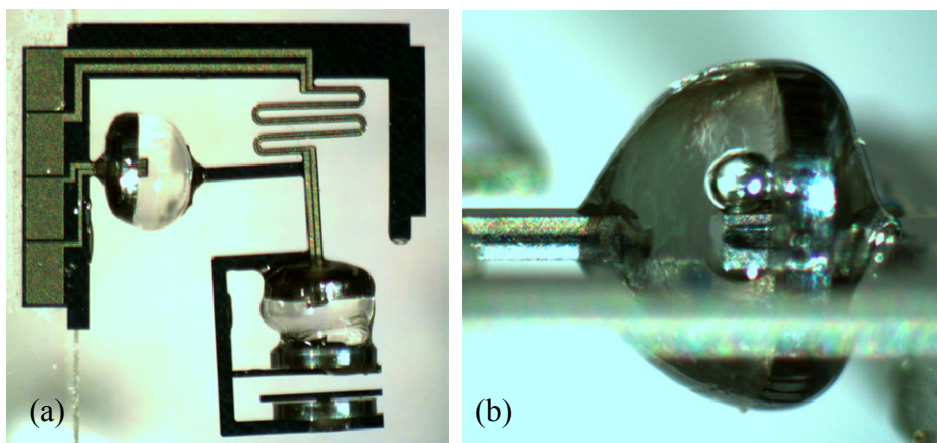


Figure 5-15. a) Balloons overfilled after being immersed in water for 2.5 days (the clamping balloon was not released in this device prior to immersion in water). b) Gas bubble covering the electrodes.

## 5.5 Hydrogel-based Process

Other materials can, in principle, be used in place of the  $\text{MgSO}_4$  shell for the fabrication of the balloons. To qualify as a replacement, a material must satisfy a number of requirements. First, it must provide mechanical support for coating silicone on top of it. Second, it must not need to be released from the balloon. Third, since the material remains inside the balloon, it must promote, or at least be compatible with, the internal operation of the balloon. This means that we must be able to run electrolysis and there must be a chemical potential gradient for water to permeate into the balloon by osmosis.  $\text{MgSO}_4$  satisfies these requirements, because it crystallizes in a hard shell that provides mechanical support, it promotes osmosis by lowering the chemical potential of water, and it provides the ions for the electrolyte when dissolved in water.

In order to solve the overfilling problem, a hydrogel is introduced in place of the  $\text{MgSO}_4$  shell. A hydrogel satisfies the requirements for a balloon fabrication material. In gel form, it provides a surface over which to coat silicone. When inside the balloon, it drives water into the balloon by osmosis, and, because it is able to absorb a large quantity of water, electrolysis can be run in it. Moreover, a hydrogel satisfies these requirements without introducing the large chemical potential gradient that causes the overfilling problem in the  $\text{MgSO}_4$ -based process. Sodium polyacrylate is chosen as the hydrogel, due to the high volume of water it can absorb: it is able to absorb up to 300 times its weight in deionized water while staying in gel form.

The hydrogel process is very similar to the  $\text{MgSO}_4$  process. Some hydrogel is placed on the balloon discs, before or after assembly of the discs on the inchworm frame. Deionized water is dispensed on the hydrogel using a commercial fluid dispenser (EFD

2000XL) with a 33-gauge needle. When the hydrogel is wet, it expands. The amount of hydrogel in each balloon should be the minimum amount that, when expanded to the desired balloon volume, gives a gel that is firm enough to paint silicone on. In this way, the fraction of water in the balloon is maximized, compatibly with the process.

Biocompatible silicone (Dow Corning MDX4-4210) is painted around the hydrogel and the discs using a thin wire handled by tweezers. It is important to keep the hydrogel wet and expanded while the silicone is cured because the hydrogel determines the balloon internal volume. If water permeates out of the hydrogel before the silicone is cured, the shrinking of the hydrogel causes some of the balloon volume to be lost. For this purpose, the curing is done at 60 °C in a humid environment, so there is no net permeation of water from the hydrogel to the outside through the silicone. To create the humid environment, the device is placed in a sealed beaker with water at the bottom, and then put in an oven. Raising the temperature over 60 °C produces some condensation on the silicone during the curing process, resulting in a hazy surface (Figure 5-16). This phenomenon was found to be repeatable over several devices.

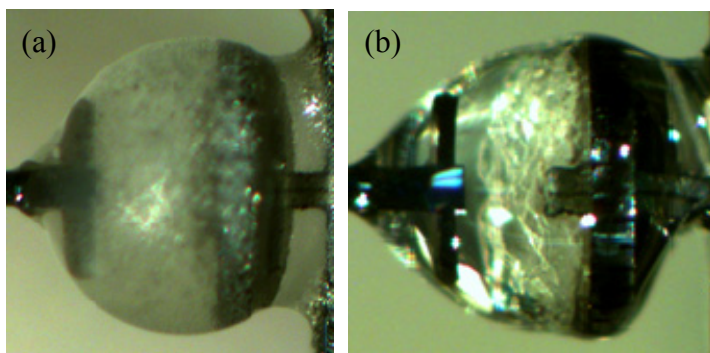


Figure 5-16. a) Balloon with hazy surface. b) Balloon with clear surface.



At the end of the fabrication process, the device is already filled with water, and it is ready for testing. The device is refilled by immersing it in deionized water, so that water is driven into the balloon by osmosis. The osmosis rate is much slower than in the case of the  $\text{MgSO}_4$ -shell process, due to the smaller chemical potential gradient. When starting from a dry balloon, a full refill takes several weeks (around two months). The refill rate is faster in the beginning. While the balloon fills with water, the refill rate decreases, because of the higher dilution inside the balloon. The smaller chemical potential gradient, however, avoids the balloon overfilling problem. There is, therefore, a tradeoff between refill speed and overfill prevention. The loss of hydrogel due to permeation through the silicone is considered negligible, due to the size of the acrylate molecules and crosslinking in the gel. No loss of hydrogel has been observed in any device.

It is possible to mix solutes with the hydrogel (as further discussed in Section 5.6.3) to tailor the chemical potential gradient and, therefore, the refill speed. Using a larger amount of hydrogel inside the balloons is also a viable way to increase the chemical potential gradient, but with a negative effect on the water content of the balloons. To avoid the tradeoff and have fast refill with no overfilling, a substance should be employed that creates a large potential gradient for water during refilling, but which causes the potential gradient to drop dramatically when the balloon is full or almost full.

## 5.6 Hydrogel-based Inchworm Results

### 5.6.1 Results in Air

The device was successfully operated in air, and the probe movement was demonstrated in both directions. The experiments have been video-recorded. Displacement per cycle between 20  $\mu\text{m}$  and 75  $\mu\text{m}$  was demonstrated by measuring with the ruler probe. A minimum displacement of 0.5  $\mu\text{m}$  was demonstrated by using a differential variable reluctance transducer system (illustrated in Section 5.6.4).

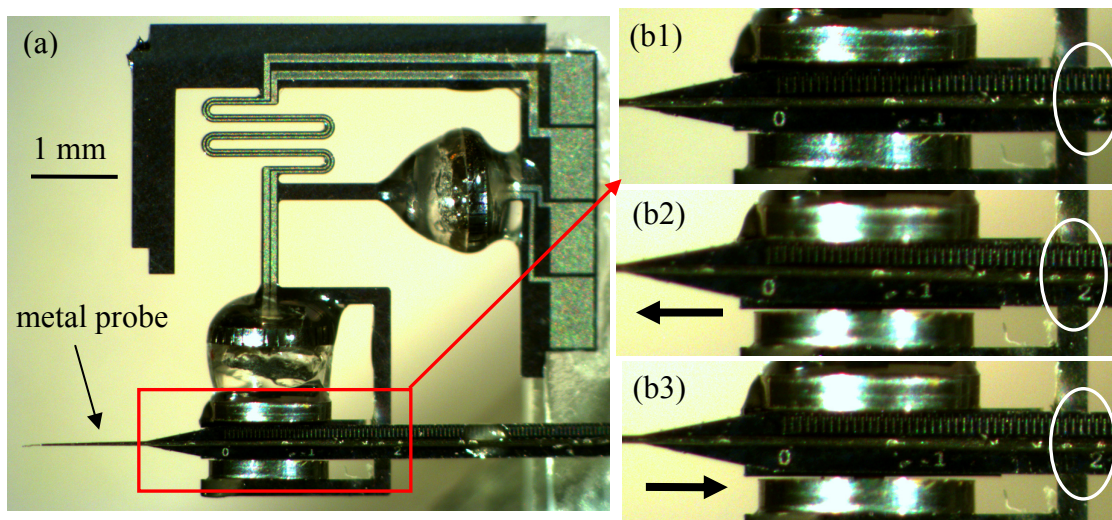


Figure 5-17. a) Complete inchworm system. A commercial metal probe is mounted on top of a silicon ruler probe. b1-b3) Close-ups of the probe, with frames showing the probe displacement (experiment run in air). b1) Initial position of the probe. b2) Probe after 4 cycles of forward displacement (cumulative displacement: about 100  $\mu\text{m}$ ). b3) Probe after 1 cycle of backward displacement from b2 position (displacement: about 75  $\mu\text{m}$ ).

In some experiments, a commercial metal neural probe is mounted on top of the ruler probe, which then acts as a shuttle for the metal probe (Figure 5-17). With this technique, different kinds of neural probes (with different widths) can be handled by the inchworm without redesigning the inchworm clamp.

Electrolysis is run at a voltage between 3 and 5 V, typically around 3.5 V. A current of about 20-30  $\mu\text{A}$  is used to expand a balloon. During an inchworm cycle, the balloons must sometimes be maintained in the expanded state, without producing further expansion. For example, when moving the probe forward, the probe must stay clamped while the displacing balloon is expanded. To maintain the expansion, electrolysis must only compensate for recombination and permeation, and a current of about 10-15  $\mu\text{A}$  is sufficient. These results demonstrate that a maximum power of about 100  $\mu\text{W}$  is typically required during the actuation of a balloon. No power is consumed when the inchworm is at rest.

One inchworm cycle takes about 10 minutes to complete. This is compatible with the duration of a silicone balloon cycle demonstrated in Section 2.8. During an inchworm cycle, it is not necessary to wait for the balloons to fully relax in all cases. For example, the clamping balloon can be considered relaxed as long as the probe is not clamped, and it is not necessary to wait for full relaxation.

The probe needs some friction with a fixed body to be moved correctly; otherwise it is dragged by the inchworm even when unclamped. In some tests, a silicone friction pad was placed under the probe, in the part where it lays on the glass slide the inchworm is glued to. In other tests, the probe was made to penetrate a silicone paste, which provides friction and better simulates the conditions in the brain. For penetration into the

paste, a thin commercial metal probe (like the one shown in Figure 5-17) is always used, in order to have a small cross-section for penetration. To have the probe penetrate into the paste, both balloons must generate more force than in load-free conditions, with consequently higher power and water consumption over each cycle. The displacing balloon must generate enough force to move the probe, and the clamping balloon must apply sufficient clamping force on the probe. As a consequence, electrolysis in the clamping balloon must be run for some time (about 30 seconds) after both clamping discs physically touch the probe, in order to generate sufficient pressure inside the balloon. If the clamping force is not sufficient, the inchworm just slips along the probe without moving it.

Actuation of the inchworm causes a net loss of water from the balloons due to permeation. It was found that using about 10% of water volume is sufficient to obtain a few hundred microns of displacement (200-300  $\mu\text{m}$  was demonstrated). The amount of water consumed is estimated by examining the content of the balloon under a stereoscope. The balloons are refilled by immersing the device in deionized water, to let water permeate into the balloon by osmosis. It takes about one week to refill 10% of the volume. When a large amount of the balloon water (30-50%) is consumed, sometimes the electrodes are not in contact with a sufficient amount of water for electrolysis to proceed, even though the hydrogel helps redistribute the available water around the balloon. It is to be noted that it is not always necessary to wait for a full refill of the balloon, as the amount of water to be replenished depends on the additional displacement required.

One device was left for months in water and no significant overfilling of the balloons was observed. Therefore, the hydrogel does solve the overfilling problem, as it

was supposed to be by design. The problem of deposits on the electrodes is also eliminated, because the gel is wetted with deionized water. The hydrogel is also observed to solve the problem of bubble stiction to the electrodes, probably because it prevents the formation of large bubbles. Large bubbles would have to displace the hydrogel significantly to form, which is not energetically favorable.

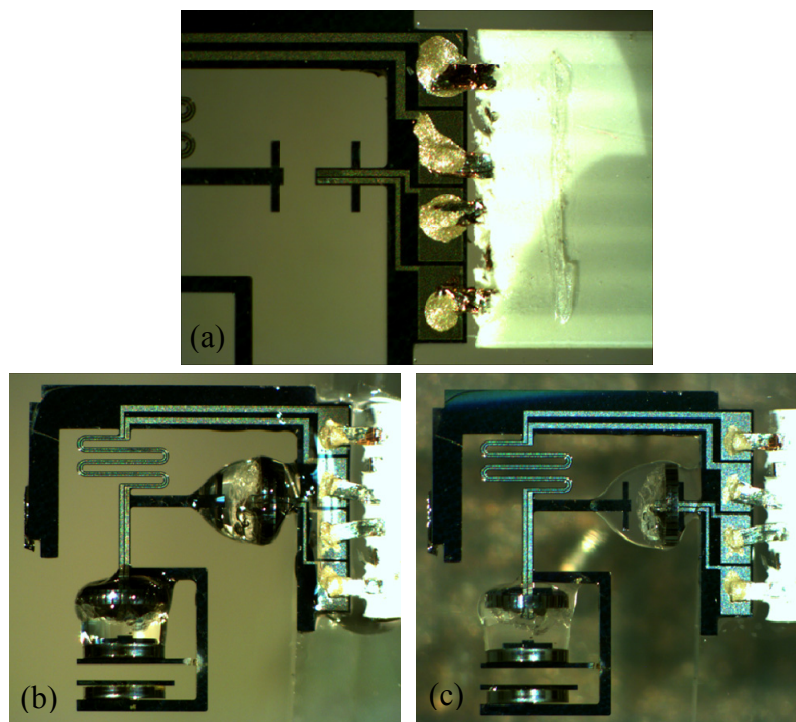


Figure 5-18. a) Connection of the cable to the inchworm by conductive epoxy. b-c) Inchworm with connected and insulated cable b) in air and c) in water.

### 5.6.2 Results in Water

The inchworm was also tested in water, to better simulate the working conditions in the body fluid. When the inchworm is operated in water, the electrical connection to the pads must be isolated from the surrounding environment. A commercial flat cable with 0.5 mm pitch (Parlex Corp.) is electrically connected to the pads by conductive

epoxy (Figure 5-18a). This is done before the balloons are fabricated. The connections are then encapsulated into biocompatible epoxy and biocompatible silicone for insulation (Figures 5-18b and 5-18c). The epoxy and silicone applications are shared with the fabrication of the balloons.

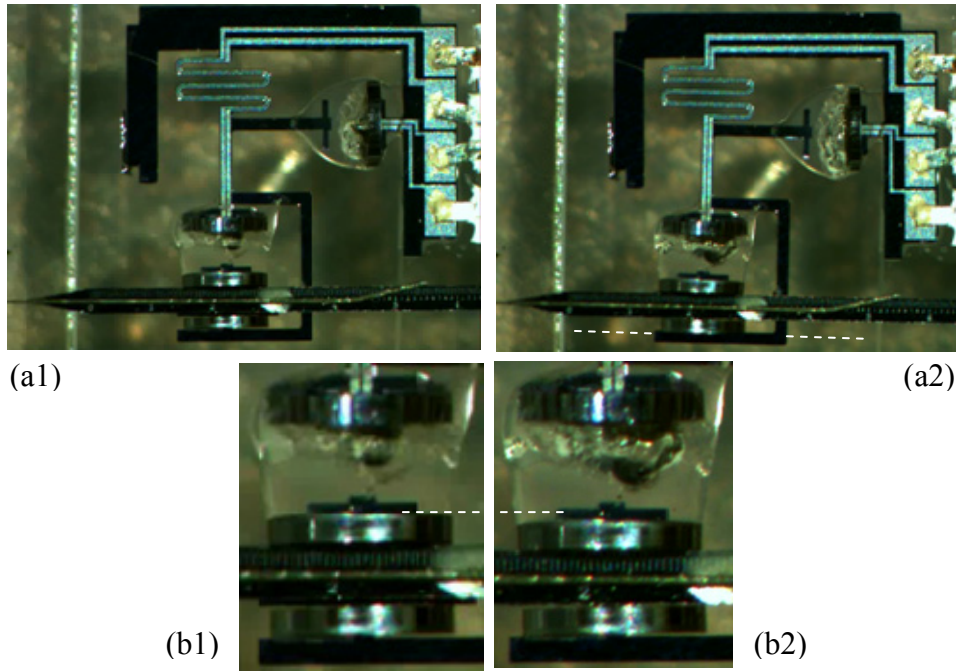


Figure 5-19. Inchworm during an actuation cycle in water. Because the displacements are small compared to the overall size of the device, they are not very visible, and they are highlighted by marker lines. a1) The device is at rest. a2) The same device, with the probe clamped and the displacing balloon expanded. b) Close-ups of the clamping balloon and the probe: b1) unclamped probe, b2) clamped probe.

The performance in water is not different from the performance in air. Osmosis is too slow to provide significant refilling of water over the duration of one cycle. Pauses are needed for the device to refill, similarly to when the device is operated in air. Starting

from fully replenished balloons, cumulative displacement of 600  $\mu\text{m}$  was demonstrated before a pause for refilling was necessary. Around 30% of balloon water was consumed to generate that displacement. Figure 5-19 shows the device during actuation.

During actuation in water, gas bubbles form on the outer surface of the balloons. This is a visible demonstration of gas permeating through the balloon wall. The bubbles tend to stick to the balloon surface, and it takes a long time (more than one week) for them to disappear, as the gas goes slowly into solution. Figure 5-20a shows such bubbles. In Section 5.5, it was mentioned that the silicone surface becomes hazy if the silicone is cured in certain conditions. Figure 5-20b shows the bubbles obtained during the actuation of a balloon with hazy surface. The surface is not smooth, and it provides many nucleation points for the bubbles to form. Instead of the few large bubbles observed in the case of a smooth surface, many smaller bubbles form all over the surface.

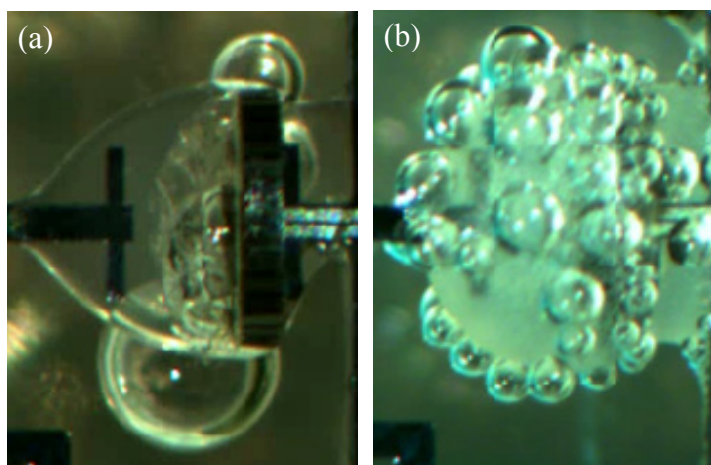


Figure 5-20. Bubbles forming on the surface of the balloons after the inchworm is actuated for several cycles. The bubbles are due to gas permeating through the balloon wall. a) Case of smooth balloon surface: only few large bubbles form. b) Case of hazy balloon surface: many small bubbles form, due to the many nucleation points available.

### 5.6.3 Results in Saline

The device should be tested in saline/body fluid, to make sure it will work correctly when implanted in the body. The previous section reports the results of tests in water, but there is one difference between saline and deionized water that raises concerns for the operation of the device: the chemical potential of water. To refill the balloon by osmosis, a chemical potential gradient across the balloon wall must be maintained, with higher potential outside the balloon. Switching from deionized water to saline causes a reduction in the chemical potential outside balloon. If the chemical potential of water in the hydrogel is not lower than in saline, the osmotic flow does not occur, or it can even occur in reverse (from inside to outside).

Some of the devices that were tested in water have also been tested in saline. A completely dry device has been immersed in saline to test the refilling process. Water does permeate into the balloons by osmosis, proving that the chemical potential gradient is still in the desired direction. However, the refill time is at least 2-3 times longer than in the case of immersion in water, due to the reduction in the chemical potential gradient. The refill experiments are ongoing at the moment of writing.

The operation of the inchworm was also tested in saline. Preliminary results show no visible difference between saline and water environment during an actuation cycle. This is expected, because the time scale of osmosis is much larger than the time scale of an actuation cycle, making the difference in external environment uninfluential as long as gas permeation is not altered.

In order to reduce the refill time, a larger amount of hydrogel can be used inside the balloon or some solute can be added to the hydrogel, in order to lower the chemical



potential of water. For example, instead of wetting the hydrogel with deionized water, a solution of some salt (like  $\text{MgSO}_4$ ) can be used. However, the amount of salt that can be added is limited by two factors. First, a large chemical potential gradient offers fast refill, but it also causes overfilling issues, as illustrated in Section 5.4. Second, the presence of ions negatively affects the water-absorption properties of the hydrogel, which reduces the fraction of water available in the gel. A preliminary test was conducted by mixing a saturated solution of  $\text{MgSO}_4$  with hydrogel. A large amount of hydrogel is needed to start the gelation, but, in the end, it is still possible to run electrolysis through the gel.

Another concern related to a saline environment is the penetration of chlorine ions into the balloon. Once in the balloon, the ions may reach the electrodes and get converted to chlorine gas, which then permeates out of the balloon. Because chlorine is toxic for the brain, this permeation and conversion process is highly undesirable for a brain implant. PDMS is generally a good barrier for ions, but the small size of the chlorine ion may cause non-negligible permeation. Measuring the magnitude of this phenomenon is important to ensure the biocompatibility of the device. Unfortunately, measuring the permeation of chlorine ions and the production of chlorine gas is not an easy task.

#### **5.6.4 DVRT Measurements**

The ruler probe allows the detection of displacements larger than about 10  $\mu\text{m}$ . For measurement of smaller displacements, a differential variable reluctance transducer (DVRT) is used (NANO-DVRT-0.5, MicroStrain, Inc.). The DVRT consists of a metal shaft sliding along a metal guide with integrated readout coils. The DVRT is free-sliding (i.e., not spring-loaded), and it has a range of 500  $\mu\text{m}$  and a resolution of 10 nm.

The DVRT shaft is placed in contact with the silicon frame when the inchworm is at rest. The displacing balloon is then expanded, and the DVRT measures the displacement obtained at the location where the probe would be. During actuation of the balloon, the applied voltage and the resulting current are recorded as well. The DVRT shaft is not spring-loaded, and it is not bonded to the device. Therefore, the shaft does not follow the device during the relaxation phase, and this setup only measures the maximum displacement reached. The experiments are performed in air.

The maximum displacement obtained is plotted as a function of the total charge or power supplied to the balloon. Figure 5-21 shows the results of repeated measurements on a particular device. In order to have comparable conditions across the measurements, the balloon fill level and the current applied are similar in all tests. The applied voltage does not change significantly over the experiments either. Therefore, plotting the supplied charge or power does not change the scatter plot pattern significantly. Data points were obtained over a span of several weeks, with the device immersed in water for refilling when not tested. We notice significant variability of the displacement for the same supplied charge. This variability is explained by two main factors: sensitivity to accumulated gas in the balloon and friction of the DVRT system. The sensitivity to accumulated gas is predicted by our balloon model, as illustrated in Section 2.4.2. The friction between the shaft and the guide tube of the DVRT has been minimized by coating with a silicone-based lubricant and by keeping the shaft aligned with the tube. However, some residual friction remains, which was measured to be in the range of a few hundred micronewtons. This force is not large for the device, but it may account for some variations from measurement to measurement. Also, it is important to take into account

that the probe will most probably experience even wider load variations when operating in the brain. To perform measurements where loading effects are completely eliminated, other measurement techniques (e.g., optical) could be used.

The experiments show that open-loop control is difficult to implement, due to the effects of actuation history and load variations. Dependence on actuation history can in principle be predicted by applying the balloon model, but the accumulation of errors in the long-term makes such predictions inaccurate. Load variations are even harder to model. As a consequence, some form of feedback from the device is necessary to precisely position the probe. Several approaches are possible. One approach is to rely on balloon pressure sensors, which are the subject of the next chapter. Other possible approaches are analyzed in 5.8.

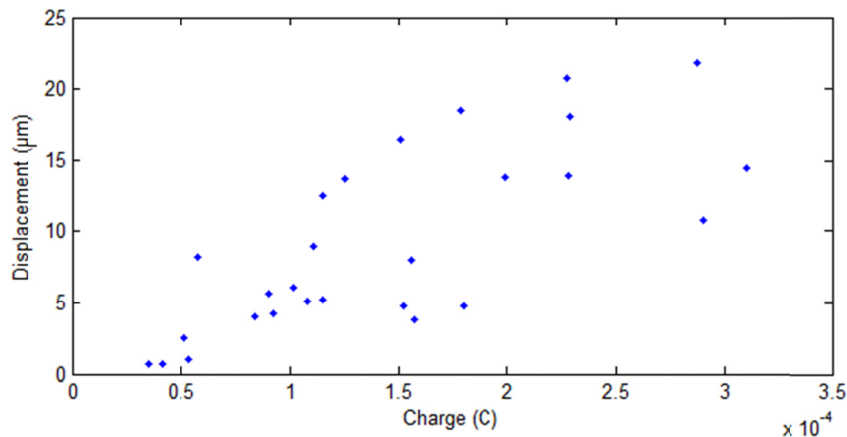


Figure 5-21. Inchworm displacement versus charge supplied to the displacing balloon.

### 5.6.5 Reliability and Failure Modes

Some preliminary experiments have been conducted to evaluate the reliability of the inchworm. A device was left 8.5 months immersed in deionized water, and it was still

fully operational and with no significant visual changes (the experiment is ongoing at the time of writing). Moreover, only very slight overfilling of the balloons was observed, with no significant impact on the device. The same device was also operated for about 200 cycles over several months (with an average displacement per cycle of about 15  $\mu\text{m}$ ), and it was still fully operational after that.

In some instances, failure of a device is observed. The principal failure mode is the formation of a leak in a balloon. In some cases, the leak forms at the disc-frame interface, and it is probably due to the epoxy not completely filling the gap between the disc and the frame. This kind of leak is usually visible only when the balloon reaches a certain pressure, and it is typically small enough that the balloon can still be operated. In other cases, the leak forms at the edge of the disc due to stress concentration in the silicone. This can be prevented by making sure the silicone is thick enough around the edge of the disc, as explained in Section 5.3.4. A leak of this kind is easily repaired by another application of silicone.

Another possible reliability concern is the delamination of platinum from the parylene substrate. To observe the phenomenon, electrolysis was run on a device without balloons. Only the balloon disc was mounted on the frame, and a drop of deionized water was dispensed on the disc and over the electrodes. During electrolysis, the water drop is continuously replenished to keep the electrodes covered. If electrolysis is run at current larger than 100  $\mu\text{A}$  for about 30 minutes, some platinum is observed to delaminate from the center of the electrode. Around the edges of the electrodes, platinum does not come off because it is held in place by the top parylene layer. Electrolysis is not run at such fast rate during regular operation of the device, 10-30  $\mu\text{A}$  being the typical current range.

Moreover, the fact that platinum does not come off around the edges of the electrodes means that electrolysis can continue even if some delamination at the center of the electrodes occurs. Strategies to improve platinum adhesion to parylene may also be devised.

The adhesion of parylene to platinum is another possible cause of concern. After a few months of soaking in deionized water, some delamination of parylene from the platinum traces is visible (Figure 5-22). Adhesion of parylene to platinum is known to be poor. However, this kind of delamination did not affect the performance of the devices.

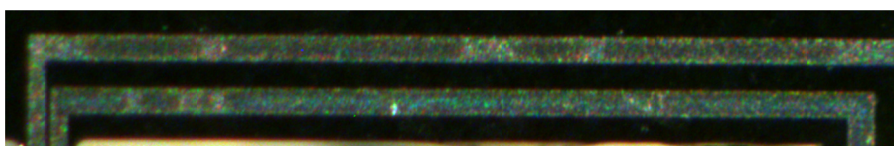


Figure 5-22. Some delamination of parylene from the platinum traces after a few months in deionized water.

## 5.7 Inchworm Array

For neural recordings, it is desirable to have multiple probes next to each other. Recording from neighboring neurons makes it possible, for example, to find correlations between their firing activities. We developed a method to arrange multiple inchworm actuators into an array. The frame of the second-generation inchworms has already been designed to be assembled into the array. At the moment of writing, fabrication of the array components has been completed, but the arrays still have to be assembled and tested.

The array is based on two silicon plates that can host three inchworm actuators and three probes. The array provides electrical connection to the inchworms and guides for the neural probes. Moreover, the array mechanically protects the actuators during implantation and operation in the brain. The plates, the assembly process, and a model of the complete array are shown in Figure 5-23. Pictures of the fabricated plates are shown in Figure 5-24.

The plates have slots in which the inchworm frames are inserted. The components can be secured to each other with epoxy. The top plate has metal pads and traces for the electrical connection of the inchworms. There are pads at the edge of each slot that are matched to those on the inchworm frame. The pads on the plate and the ones on the inchworm are perpendicular to each other, and they can be connected, for example, by conductive epoxy. One possible concern is the insulation between the inchworm pads and the silicon sidewalls of the top plate. Insulation may be provided by a thin layer of the adhesive used to assemble the array.

The plates have guides for the probes, which are aligned with the inchworms' clamps. Each probe, therefore, has to pass through two guides, which keep the probe in place and aligned. The probe guides can also be modified to introduce constant friction on the probe. This may be desirable, for example, if the tissue has an elastic response that pushes the probe backward when it is not clamped.

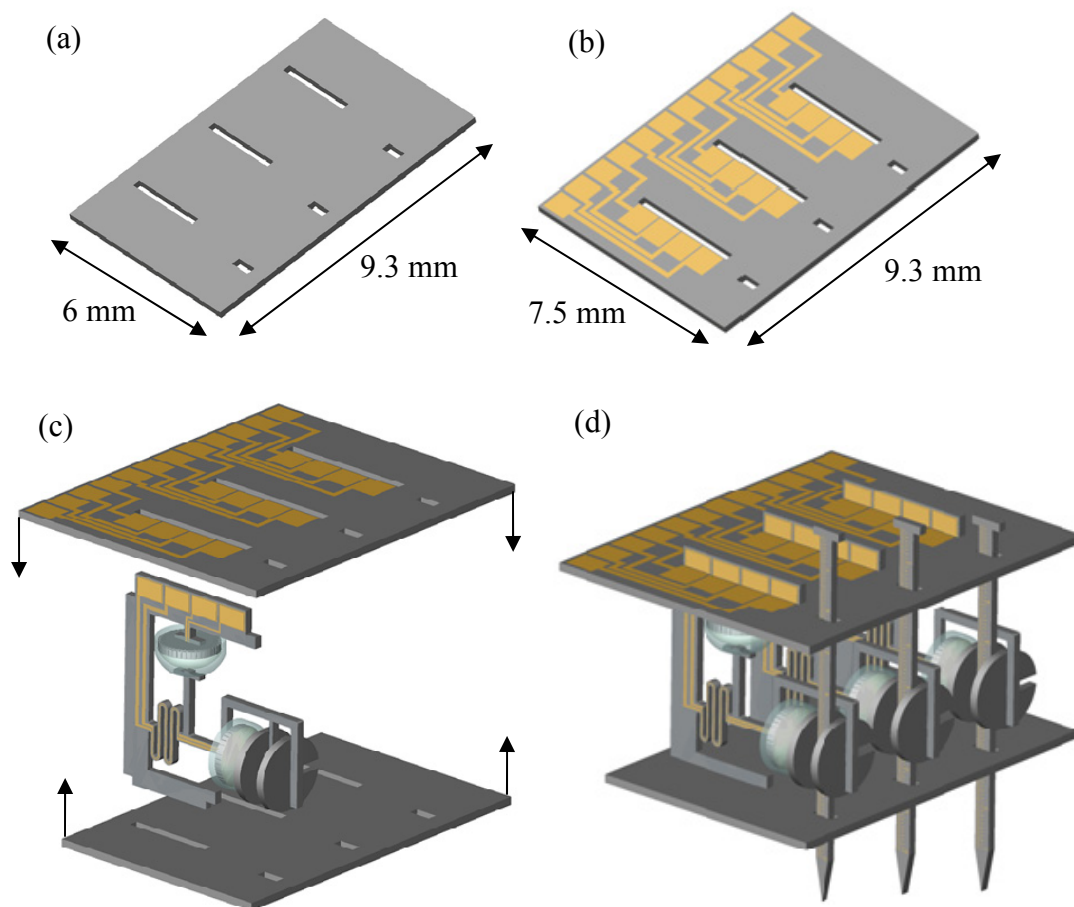


Figure 5-23. a) Array bottom plate. b) Array top plate. c) Assembly of the array (only one inchworm shown for visual convenience). d) Complete array, with three inchworms and probes in their guides.

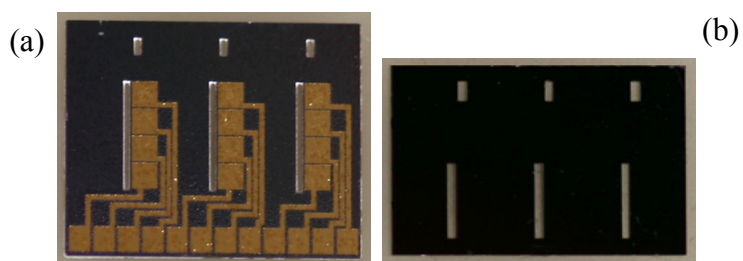


Figure 5-24. Fabricated array components. a) Top plate. b) Bottom plate.

The fabrication process for the top plate is the same as the process for the inchworm frame (Section 5.3.1). The last parylene deposition can be skipped if insulation of the metal traces is provided in another way. For example, after the assembly of the array, the top plate can be completely covered with silicone or epoxy. The process for the bottom plate is the same as the process for the silicon discs (Section 5.3.2).

The array offers several possibilities for the electrical interconnection of the device. A cable can be assembled on the edge pads of the top plate to connect the array to an external power supply. Additional pads for connection to the neural probes can be placed on the top plate, together with additional leads on the cable for their connection to external equipment. It is also possible to mount electronic components on the top plate. Examples of useful circuitry are amplifiers for the neural recordings and multiplexers to reduce the lead count of the cable. If the space on the top plate is not sufficient, the electrical connections and circuitry can be extended to the bottom plate.

The array can be modified and improved in several ways. For instance, each inchworm frame can be modified to handle multiple probes. Each probe would have its own clamping balloon, while one displacing balloon can be shared by multiple probes. In this way, it is possible to save on the total balloon count of the array.

## **5.8 Comments on Feedback Sensors**

The characterization of the inchworms revealed that it is hard to position the probe accurately by open-loop control of the device. There are three main causes: geometric variations from device to device, sensitivity to the actuation history, and load variations. The effect of geometric variations can be compensated for by calibrating each device. The effect of the actuation history (e.g., amount of gas present in the balloon) can



in principle be predicted by applying the balloon model. However, it is difficult to maintain accurate predictions in the long-term, due to accumulation of errors caused by inaccuracies in the model or in the values of its parameters. Load variations are even harder to predict, and they have a major effect on the displacement of the inchworm.

If the load on the balloon is known, information about the displacement can be derived from the internal pressure of the displacing balloon. In this case, a pressure sensor in the balloon (like the ones illustrated in Chapter 6) can be used. If the load is not known, the displacement should be measured directly. Two kinds of displacement sensors can be envisioned: a strain gauge on the inchworm spring and/or a probe position sensor.

The deformation of the inchworm spring is related to the inchworm displacement. Therefore, the output of a strain gauge mounted on the spring can be converted to probe displacement. The conversion can be made accurate by calibration and finite-element simulation. However, the strain gauge cannot detect if the probe is actually being moved. The probe may not be clamped with sufficient force, and it may be slipping between the clamping discs. The inchworm is generating displacement (which is reported by the strain gauge), but no movement is transferred to the probe. This problem is solved by direct measurement of the probe position.

A probe position sensor is the most accurate and reliable way of measuring the displacement of the probe with respect to the inchworm body. Several mechanisms are possible, including capacitive or magnetic. A sensor of this kind has number of requirements. First, it must be easy to integrate on the probe and on the inchworm body. Second, it must be able to measure displacements from a few microns to hundreds of

microns, or even millimeters. Third, it must be low-power, low-voltage, and possibly require only a small number of leads.

The purpose of the feedback sensors is to provide information about the position of the probe with respect to a frame of reference, such as the inchworm body. However, for movable probe applications, the quality of the signal recorded by the probe is the final objective, and it is not strictly necessary to know the exact position of the probe. In other words, we may be able to move a probe close to neurons even without knowing how many microns the probe was moved. The neural signals captured by the electrodes can be used as a feedback mechanism, without requiring any sensor on the inchworm, and algorithms may be developed to move the probe to an optimal position. Of course, having information about the probe position would help, but the integration of feedback sensors may add significant complexity to the devices.

## CHAPTER 6

---

# Balloon Pressure Sensors

## 6.1 Introduction

### 6.1.1 Motivation

The balloon internal pressure is a very important feedback signal during the operation of a balloon. Direct monitoring of the pressure can be used to develop closed-loop control algorithms for balloon actuation. The balloon model presented in Section 2.4 can help make the algorithms more effective. Pressure readings could also work as a leak-detection mechanism. If current is flowing through the balloon, but no pressure increase is observed, a leak has probably formed in the balloon. If the actuator is operating in water, the same behavior can also be caused by failure of the insulation of the metal traces leading to the balloon electrodes, which causes water electrolysis to occur outside the balloon.

Inchworm actuators would benefit from the monitoring of the balloons' internal pressure. The clamping force on the probe can be estimated from the internal pressure of the clamping balloon. The pressure readings can also be used for closed-loop control of the probe position. To convert from pressure to displacement, the load on the probe must be known, and we must also assume that the inchworm is actually moving the probe, and not just sliding along it due to excessive load on the probe (knowing the clamping force on the probe helps in this case). For more accurate probe displacement control, special sensors that directly measure the probe position are desirable, as discussed in Section 5.8.

### **6.1.2 MEMS Pressure Sensors**

Pressure sensors have been one of the first and most successful applications of MEMS technology, and they account for a large part of the MEMS market. It is estimated that the market for MEMS pressure sensors in 2006 has been 1.2 billion dollars [96], with numerous applications in the automotive and biomedical field.

The most common MEMS pressure sensors are based on a silicon diaphragm, typically fabricated by anisotropic wet etching [97]. This normally requires double-side wafer processing. Other sensors are fabricated by surface micromachining, using polysilicon or silicon nitride as membrane materials [98]. Micromachined pressure sensors based on polymers are not as common. A spiral-tube device, which mimics a technique used in macroscale sensors, has been fabricated using parylene [99]. Parylene has also been employed in capacitive pressure sensors [100].

## **6.2 Design**

The design of pressure sensors for integration into balloon actuators must meet two basic requirements. First, the pressure sensor dimensions are limited by the balloon dimensions. The sensor must fit on the silicon shank that supports the electrolysis electrodes. Second, the fabrication of the sensors must be integrated into the inchworm process flow, possibly minimizing the number of additional steps and masks.

In order to satisfy the requirements, a pressure sensor based on a free-standing parylene membrane with embedded metal strain gauges was designed [101] (Figure 6-1). Parylene and metal layers are deposited and patterned during the fabrication of the inchworm, making the sensor fabrication easily integrable in the inchworm process flow.

Furthermore, the fabrication of these sensors requires only single-side wafer processing, which avoids the complications of double-side processing.

Parylene has properties that are desirable for a pressure sensor membrane, in particular flexibility and chemical inertness. On the other hand, parylene shows limitations typical of polymers, such as relatively high permeability to gases compared to materials like silicon or silicon nitride. In addition to that, a parylene-based sensor should only be operated below the glass transition temperature of the polymer, which is in the 80-120 °C range for parylene C.

### **6.2.1 Membrane and Cavity**

The sensors are based on a square parylene membrane, standing over a cavity etched into silicon. Silicon is etched beneath the membrane by  $\text{XeF}_2$ , through an array of holes patterned on the parylene itself (parylene is a good masking material for  $\text{XeF}_2$ ).  $\text{XeF}_2$  etches silicon isotropically, so the etching starts by forming a spherical cavity under each hole. If the etching is carried on deeper than half the distance between the holes, the etched spherical cavities merge and a larger cavity is formed (refer to the fabrication steps in Figure 6-4). The etching holes, and therefore the cavity, are then sealed by a subsequent parylene deposition [102].

The shape of the cavity is determined by parylene-filled trenches, which act as etch stops for  $\text{XeF}_2$  etching. The etch stops also set a limit on the maximum cavity depth. Similar trenches are used to anchor the parylene membrane around the cavity. When pressure is applied to the membrane, tangential stress at the parylene-silicon interface ensues. Even though the use of a promoter already improves the adhesion between the two, the use of anchors for parylene enhances the reliability.

Sensors with different cavity dimensions were designed, ranging from  $100\ \mu\text{m} \times 100\ \mu\text{m}$  to  $200\ \mu\text{m} \times 200\ \mu\text{m}$ . In the fabricated devices, the total membrane thickness is  $21.5\ \mu\text{m}$ , as explained in the fabrication section.

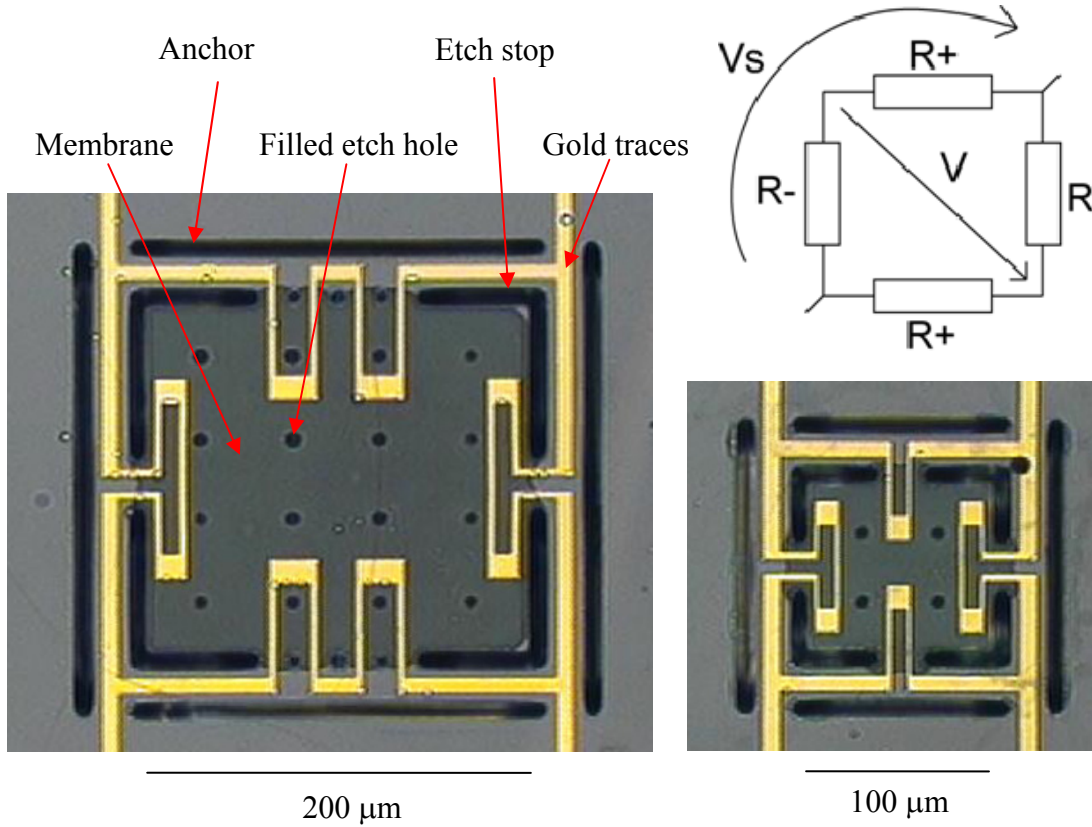


Figure 6-1. Top-view of two fabricated devices with different dimensions. The cavity under the silicon can be clearly seen (dark grey) together with the hole array for  $\text{XeF}_2$  etching (black dots over the cavity). The cavity is surrounded by the etch stops and anchors (black). The Wheatstone bridge arrangement of the strain gauges is also shown.

### 6.2.2 Simulations

A finite-element simulation of the membrane is useful to understand how to design the strain gauges. For the simulation, the case of a square  $200\ \mu\text{m} \times 200\ \mu\text{m}$

membrane with a thickness of  $21.5\ \mu\text{m}$  is considered. For parylene, an elastic modulus of  $2.5\ \text{GPa}$  and a Poisson ratio of  $0.4$  are assumed. Zero-displacement (fixed) boundary conditions are imposed on the four sides of the membrane, and uniform pressure is applied on the top surface. The simulations are run in COMSOL Multiphysics, using a nonlinear solver. The solution reports a deformation of  $6.8\ \text{nm/psi}$  at the center of the membrane. The strain distribution is shown in Figure 6-2.

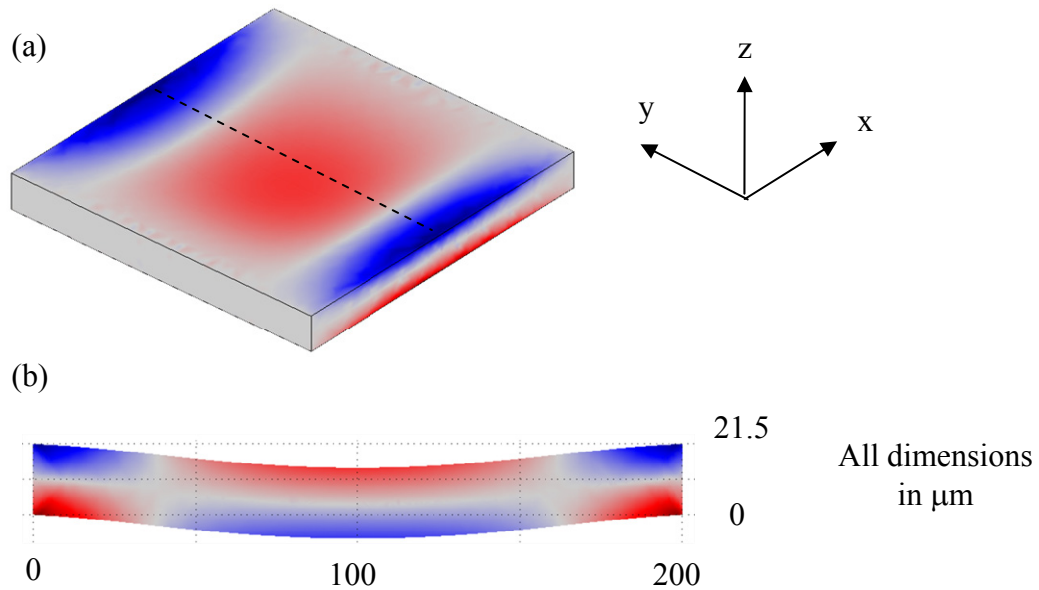


Figure 6-2. a) Distribution of the normal strain the y direction (it is the same for the x direction, due to symmetry). Blue areas correspond to tensile strain, red areas to compressive strain, with the color intensity proportional to the absolute value of the strain. b) Strain distribution along a cross-section passing through the center of the membrane, i.e., along the dashed line in a). The membrane deformation is not to-scale, and it is exaggerated for better visualization.

The modeling of the membrane is simplified for the simulation. Two approximations are particularly important. First, the model does not take into account the presence of the etch-stops at the sides of the membrane, which alter the boundary conditions. Second, the membrane is modeled with uniform thickness, whereas the real membrane has dimples due to the filled etching holes.

Theoretical results are available for the deformation of a clamped rectangular thin plate subject to uniform loading [103-104]. The case of small deformation (deformation much smaller than the membrane thickness) applies. As shown in [104], the deflection  $d$  at the center of the membrane is given by

$$d = 0.00126 \frac{qa^4}{D} \quad (6-1)$$

for a membrane of side  $a$  with an applied pressure  $q$ .  $D$  is the plate stiffness, which is related to the membrane parameters by the formula

$$D = \frac{Eh^3}{12(1-\nu^2)} \quad (6-2)$$

where  $E$  is the elastic modulus,  $\nu$  is the Poisson ratio, and  $h$  is the membrane thickness. Plugging in the numbers for the pressure sensor square membrane with sides of 200  $\mu\text{m}$ , the formula predicts a deflection of 5.64 nm/psi, which is fairly close to the simulation result.



### 6.2.3 Strain Gauges

The deformation of the membrane is sensed by four metal strain gauges embedded in the parylene membrane. The gauges are placed at the four edges of the membrane and arranged in a Wheatstone bridge configuration, in order for common-mode effects on resistance to cancel out. The arrangement is shown in Figure 6-1. When the membrane is deformed by pressure on the top, the gauges on the right and left side of the membrane experience a decrease in resistance, while the ones on the top and bottom side experience an increase in resistance. The strain gauges cannot be placed exactly at the edge of the cavity due to the presence of the etch stops. Some interruptions in the etch stops are required to route the gold traces across the boundary of the cavity.

The strain distribution in the membrane represents the starting point for the design of the strain gauges. Their geometry and position should be designed to maximize their sensitivity to the deformation of the membrane. In the vertical direction (i.e., along the thickness of the membrane), the strain gauges should be placed as close as possible to the top or bottom surface. In fact, the strain is zero at half thickness (Figure 6-2b). Horizontally, the gauges should be placed at the membrane edges, at the center of them, because the strain is maximum there (Figure 6-2a). Moreover, in that location, the strain in the direction perpendicular to the edge dominates over the strain in the other directions, making the gauge design easier. Farther from the edge, the sign of the strain inverts. If a gauge extends past the sign-inversion boundary, it loses sensitivity, due to the summation of opposing effects.

The gauges on the right and left side of the membrane in Figure 6-1 decrease their resistance when the membrane deforms. This is due to the narrow sections of the gauge

(which dominate its resistance) becoming wider with deformation. The gauges on the top and bottom sides increase their resistance when the membrane deforms. This is due to the narrow sections of the gauge becoming longer with deformation. The behavior of the gauges due to the membrane deformation is illustrated in Figure 6-3.

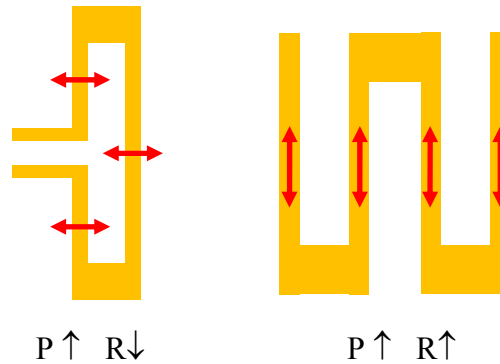


Figure 6-3. Behavior of the strain gauge resistance  $R$  when the pressure  $P$  on the membrane increases and the membrane deforms.

### 6.3 Fabrication

The fabrication steps are illustrated in Figure 6-4. A prime wafer is first cleaned in a piranha solution for 10 minutes. A promoter for parylene-silicon adhesion is then applied, by leaving the wafer for 2 hours in a solution of deionized water, isopropyl alcohol, and A-174 (from Specialty Coating Systems) in 50:50:0.5 proportion. A thin layer of parylene,  $0.8 \mu\text{m}$  thick, is then deposited.

Gold is thermally evaporated on the parylene layer, using chrome as an adhesion layer ( $1000 \text{ \AA}$  Au on  $100 \text{ \AA}$  Cr). The first layer of parylene is needed as a support for the strain gauges. As a result, the metal traces are completely enclosed in parylene.

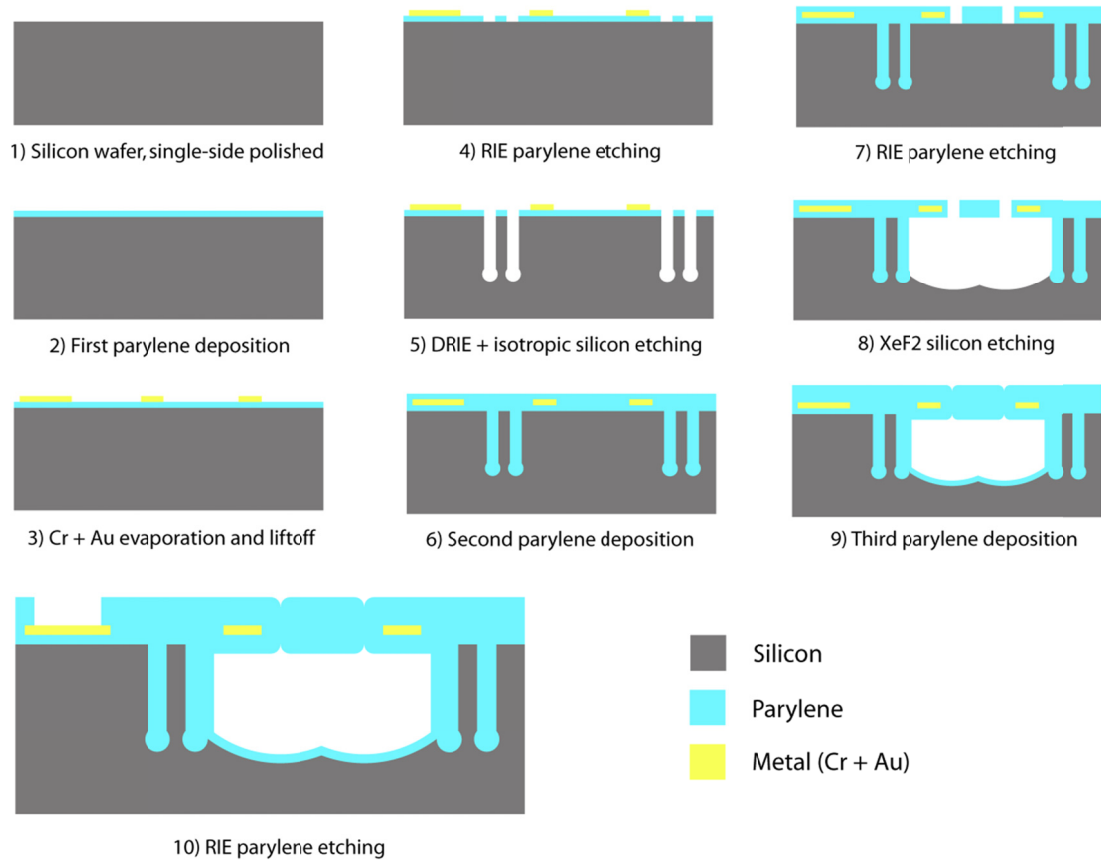


Figure 6-4. Process flow for the fabrication of the pressure sensors.

Parylene is patterned by reactive ion etching (RIE) in O<sub>2</sub> plasma, in order to expose silicon in the areas designated for the anchors and etch stops. Both are etched at the same time by deep reactive ion etching (Bosch process). A final SF<sub>6</sub> isotropic etch creates a larger cavity at the bottom of the trench, improving the anchoring ability [105]. The trenches are 7.5 μm wide and 40 μm deep. A second parylene layer is deposited, 8.5 μm thick, enough to fill the trenches and achieve sufficient planarization over them.

The hole array for XeF<sub>2</sub> etching is then patterned. The holes are 7.5 μm in diameter. An aluminum layer is first deposited by thermal evaporation. The thickness of

the layer is 4000 Å, sufficient to ensure coverage over the anchors and etch stops, where the parylene is not flat. This layer acts as a mask for the parylene patterning, and it allows lithography with a 2-μm photoresist layer, much thinner compared to the 10 μm layer that would be needed to etch parylene with a photoresist mask. Thin photoresist is desirable for accurate patterning of such small holes. After aluminum patterning by wet etching, parylene is etched by reactive ion etching in O<sub>2</sub> plasma. The aluminum mask is then removed.

Before XeF<sub>2</sub> etching, a dip in BHF or 5% diluted HF is mandatory to ensure the thin native oxide is removed from the silicon surface. XeF<sub>2</sub> etches silicon dioxide much more slowly than silicon. If the silicon dioxide is not removed, silicon is reached at different times in each hole, and the etching proceeds very non-uniformly from hole to hole. XeF<sub>2</sub> etching is performed in pulsed mode [106]. Due to the transparency of parylene, it is possible to observe the progress of the etching.

A third parylene layer is then deposited, 8.5 μm thick. Because of the conformal nature of parylene deposition, the etching holes are sealed. A final parylene RIE etch with 20 μm thick photoresist mask is used to open the pads for external connections.

From the process data, the total parylene membrane thickness is estimated to be about 21.5 μm. This is the sum of all the depositions above, with the addition of one etching hole radius. In fact, during the last parylene deposition, before the holes are sealed, parylene is deposited also inside the cavity, and, therefore, on the bottom of the membrane. When a thickness equal to the hole radius is reached, the holes are sealed, and the remaining deposition occurs only on the top of the membrane.

Because of the limited thickness of the first parylene deposition, the gold traces are close to the bottom surface of the membrane, with positive effects on the sensitivity.

Optical microscope pictures of two fabricated devices are shown in Figure 6-1. A surface image obtained with a scanning laser confocal microscope (Keyence Corp.) is shown in Figure 6-5. The filled etching holes are visible as dimples.

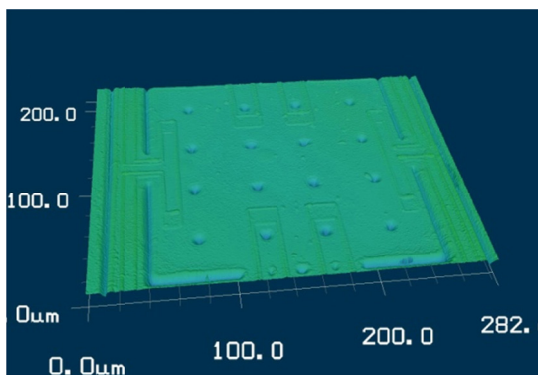


Figure 6-5. Surface scan of a  $200\ \mu\text{m} \times 200\ \mu\text{m}$  sensor. The image was obtained with a scanning laser confocal microscope by Keyence Corporation. The dimples (due to filled etched holes) and grooves (due to the anchors and etch stops) are about  $2\ \mu\text{m}$  deep.

## 6.4 Results

### 6.4.1 Pressure Response

To measure the pressure response, the sensors were placed in a pressure chamber connected to a  $\text{N}_2$  cylinder through a pressure regulator. The chamber is equipped with feed-through wires. Figure 6-6 shows the response of a  $200\ \mu\text{m} \times 200\ \mu\text{m}$  sensor up to 200 psig. The response deviates from linearity, and it is better interpolated by a quadratic

function. The signal at 0 psig can be recovered after the experiment, suggesting that no plastic deformation occurred.

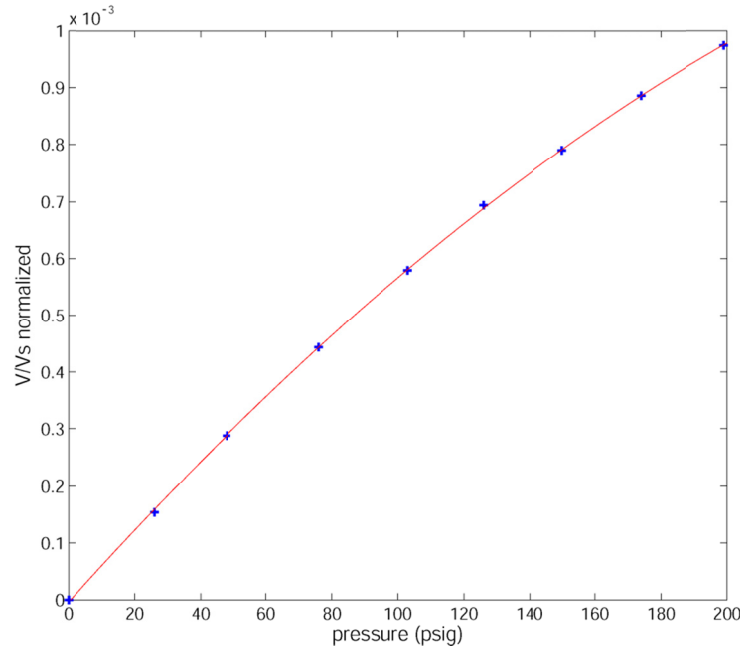


Figure 6-6. Pressure response of the  $200\ \mu\text{m} \times 200\ \mu\text{m}$  sensor.  $V/V_s$  is the ratio of the bridge output and supply voltages. The data point at atmospheric pressure (origin of the plot) is taken as a reference for the data, to eliminate the bridge offset. The data points are fitted to a quadratic function.

### 6.4.2 Membrane Permeability

The effect of gas permeation through parylene was tested by exposing a sensor to constant external pressure. Permeation causes gas to accumulate into the sealed cavity, and the pressure inside the cavity increases until it is equal to the external pressure. As a consequence, the differential pressure on the membrane decreases over time. If the external pressure is then decreased, the pressure inside the cavity will be higher than the

external pressure. Gas will thus gradually permeate out of the cavity, until the pressure inside and outside are again equalized.

This behavior is modeled.  $P_e(t)$  and  $P_c(t)$  are the external and cavity pressure respectively,  $\mu$  is the permeability coefficient of parylene to the gas in the environment ( $N_2$  in this case),  $h$  is the membrane thickness,  $A$  is the membrane area,  $b$  is the cavity depth (the cavity is assumed to have a flat bottom, neglecting the pattern left by  $XeF_2$  etching). The variation in the number of gas moles inside the cavity  $n_c$  is written as

$$\frac{dn_c}{dt} = \mu \frac{A}{h} [P_e(t) - P_c(t)]. \quad (6-3)$$

We assume that the deformation of the membrane causes negligible change in the volume of the cavity, so its value is fixed at  $V = Ab$ . By applying the ideal gas law (temperature is assumed constant), we obtain a differential equation relating  $P_c(t)$  and  $P_e(t)$

$$\frac{dP_c}{dt} = \mu \frac{RT}{hb} [P_e(t) - P_c(t)] \quad (8-4)$$

where  $R$  is the ideal gas constant and  $T$  is the temperature. Given the form of the equation, we can regard the term  $\tau = hb/(\mu RT)$  as the time constant of the system.

Figure 6-7 shows the results of the test on a  $200 \mu m \times 200 \mu m$  sensor. Initially the sensor was left for more than a week at atmospheric pressure, so that the initial pressure inside the cavity became equal to atmospheric pressure. The sensor was then exposed to a pressure of 100 psig in  $N_2$  environment, at a temperature of  $22^\circ C$ .

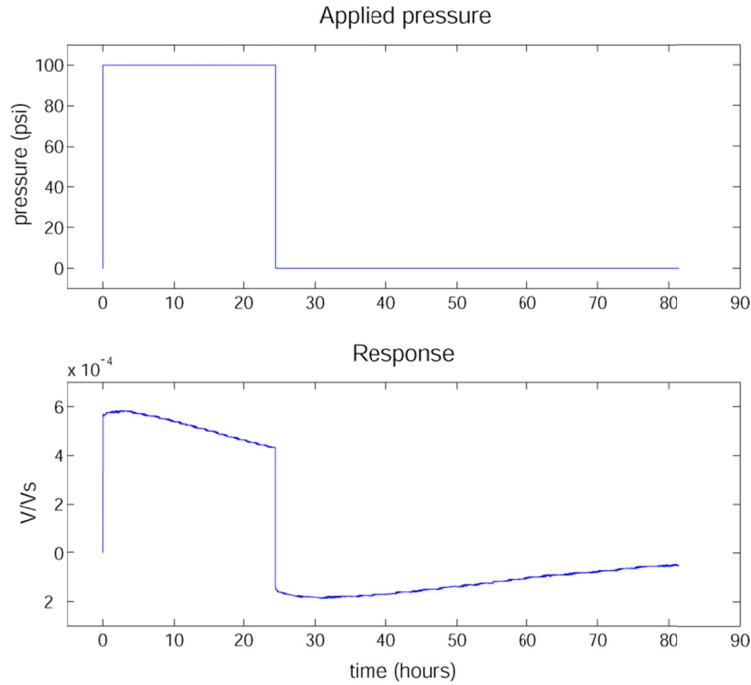


Figure 6-7. Effect of the permeation of  $N_2$  through parylene on the pressure response of the  $200\ \mu m \times 200\ \mu m$  sensor.  $V/V_s$  is the ratio of the bridge output voltage and the supply voltage. The initial data point (at atmospheric pressure) is taken as a reference for the data. Only part of the relaxation after pressure release is shown.

The value of the time constant is extracted from the experimental curve, and it is found to be  $\tau = 85$  hours. From the time constant, we find the experimental value for the permeability coefficient. A correction is applied to take into account that 15% of the membrane area is covered by metal, whose permeability is negligible compared to parylene's. With this information, we find  $\mu = 4.7 \cdot 10^{-15}$  mol/(m·hour·Pa). This can be compared to a value of  $6.79 \cdot 10^{-15}$  mol/(m·hour·Pa) reported by our parylene supplier (Specialty Coating Systems), measured at  $25\ ^\circ C$  following the ASTM D 1434 standard. A possible explanation for the lower measured permeability is the annealing of parylene



during fabrication. During the process, photoresist has to be baked at 100 °C or 120 °C for periods ranging from half an hour to several hours, and the parylene already deposited on the wafer is subject to the same thermal treatment. A decrease in permeability after parylene C annealing has been reported in the literature [107-108].

Techniques are available to drastically reduce the permeability of a parylene film. As reported in [86], a thin aluminum layer (1000 Å) can be used to reduce the permeability by about 5 orders of magnitude. If allowed by the application, a channel can be used to connect the cavity to a reference pressure. The channel can be fabricated in the silicon under the parylene by the same  $\text{XeF}_2$  etching technique.

## 6.5 Modified Design

The pressure sensors illustrated above have been demonstrated to work at pressure up to 200 psi. The pressure inside the balloons of the inchworms is usually much lower, a few tens of psi at most. The design can be modified to have a thinner membrane, which increases the sensitivity at lower pressure.

There are two main design challenges. First, the parylene depositions should be balanced in such a way that the strain gauges are far from the middle section of the membrane, where the strain is theoretically zero. Second, a thin membrane invalidates the assumption that the membrane deformation is much smaller than the membrane thickness. The membrane works in two different regimes, depending on the applied pressure. The small deformation regime holds only in the lower part of the pressure range. For larger deformation, the areas of tensile strain dominate over the areas of compressive strain, and the strain distribution of Figure 6-2 does not hold. When designing the strain gauges, particular attention must be paid to the two different regimes,

as they may cause opposite effects on the resistance changes. Since in the large deformation regime the strain is tensile almost everywhere, we need to place the gauges in an area where the strain is tensile also in the small deformation regime. For this reason, the center part of the membrane near the bottom surface is chosen for the placement of the gauges.

In order to better exploit the tensile strain at the bottom center of the membrane, a rectangular geometry has been chosen (Figure 6-8). The two strain gauges increase their resistance when the membrane deforms. Even though only two gauges are present, a Wheatstone bridge arrangement is still possible by fabricating two fixed resistors outside the membrane. In this way, the temperature compensation offered by the bridge is still available.

### 6.5.1 Simulations

The deformation of the membrane as a function of pressure and the change in strain gauge resistance is simulated by finite-element analysis. Due to the symmetry of the geometry, the simulation is run on only half of the membrane. The simulation is divided in two phases. First, the stress-strain problem is solved, and the deformed geometry is saved. Then the electrostatic problem is solved on the deformed geometry. From the solution of the electrostatic problem, we compute the resistance of the strain gauge on the deformed membrane.

Simulations were run with several different geometric parameters, in order to optimize the design (Figure 6-8):

- dimensions of the cavity (mbx, mby),
- distance between the edges of the strain gauges and the edges of the cavity (dist),

- diameter of the holes used to etch the cavity (hole),
- thickness of the parylene deposition used to seal the cavity (pdep).

The first deposition is assumed to be  $1.5\ \mu\text{m}$  ( $0.5\ \mu\text{m}$  molten parylene, with  $1\ \mu\text{m}$  parylene on top), while the parylene thickness above the metal lines is equal to pdep. The thickness below the metal lines is then equal to  $1.5\ \mu\text{m}$  plus the radius of the etching holes (as explained in Section 6.3).

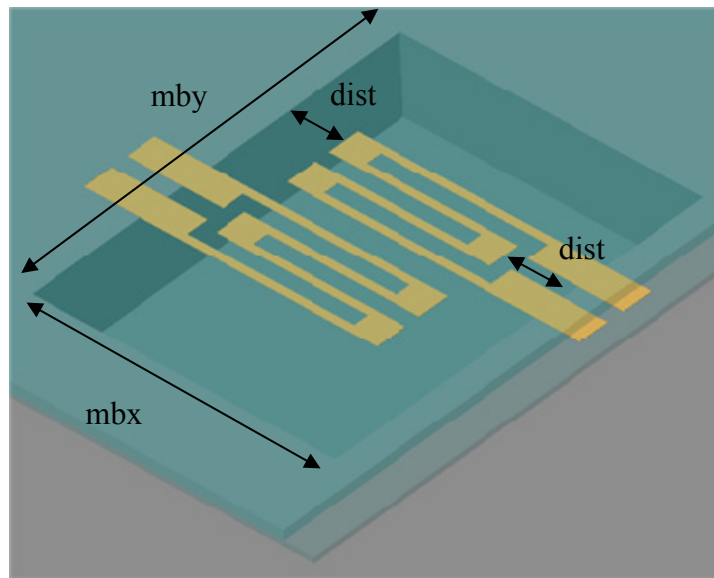


Figure 6-8. Pressure sensor with rectangular cavity. The geometric parameters varied in the simulation are shown.

Figure 6-9 shows the maximum membrane deflection and the relative change in resistance for one strain gauge as a function of the applied pressure. Three sets of parameters are shown. The first set (Figure 6-9a) shows that the strain gauge resistance goes in opposite directions for low and high pressure. This is due to the two different deformation regimes mentioned above. This behavior is undesirable, as it makes the

pressure reading ambiguous. The second set of parameters (Figure 6-9b) shows a monotonic resistance change over the whole pressure range. However, the resistance change in the low pressure range is very small, which reduces the accuracy of the reading there. The third set of parameters (Figure 6-9c) gives a monotonic resistance change as well, and the change is significant for both low and high pressure. This set was found to be the optimum in terms of monotonicity and uniformity over the whole pressure range.

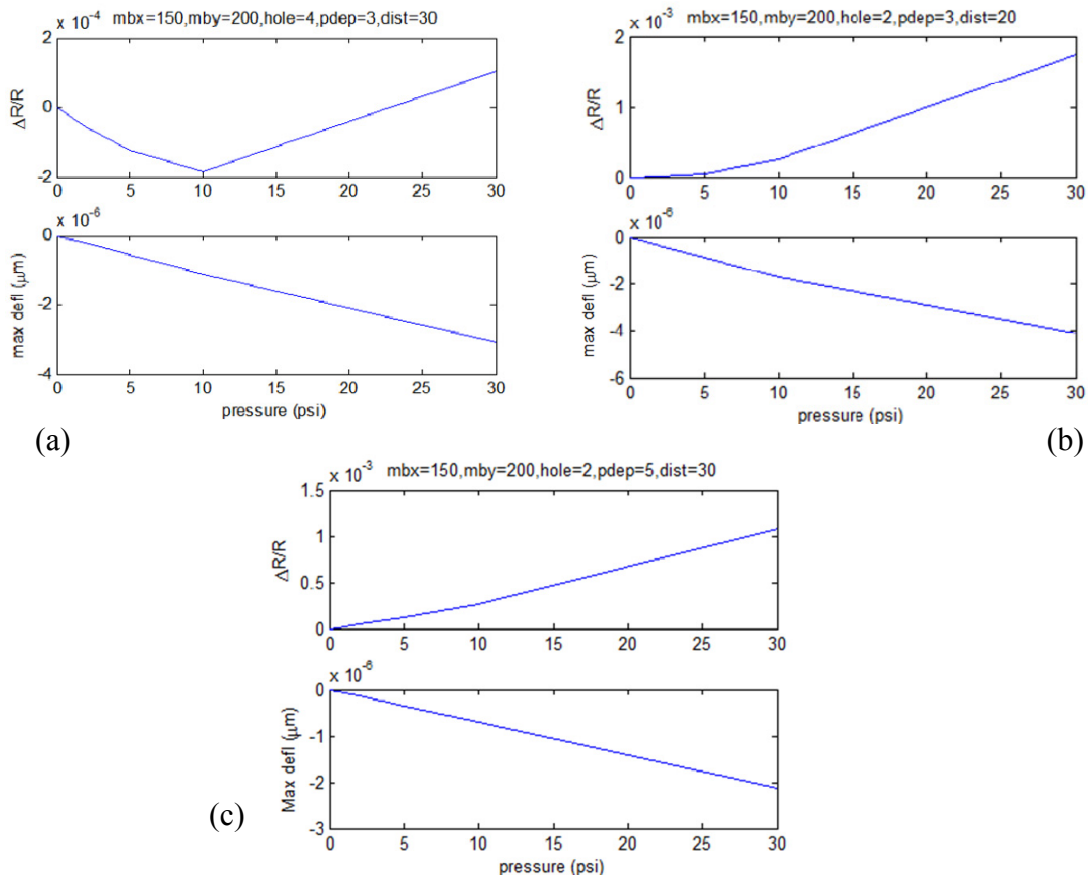


Figure 6-9. Maximum deflection (i.e., deflection at the center of the membrane) and strain gauge relative resistance change as a function of pressure for three different sets of geometric parameters.

### 6.5.2 Process Integration

For better integration in the balloons, the fabrication process is modified too. The steps are illustrated in Figure 6-10. Molten parylene is used to improve the adhesion of parylene to silicon. For this reason, the anchors can be eliminated, making the device more compact.

This process is easily integrated into the process of the second-generation inchworm actuator of Figure 5-4. Only two masks need to be added to the inchworm process: one to pattern the etch-stops and one to pattern the cavity-etching holes. No additional parylene or metal depositions are required, as all the depositions are shared by the inchworm and the pressure sensor processes. It is worth noticing that the layer of molten parylene is left as part of the membrane. The mechanical properties of molten parylene are different from regular parylene, and the previous simulation can be made more accurate by taking this fact into account.

In the inchworm frame, the pressure sensors can be placed next to the electrodes used for electrolysis. The pressure sensor cavity can be left sealed or it can be connected to the external environment. The second approach should be preferred, because a sealed cavity's reading drifts due to permeation through the membrane. To connect the cavity to the external environment, a channel can be etched in the silicon in the same way as the sensor cavity.

The geometry and process design have been completed, but inchworms with integrated pressure sensors still have to be fabricated and demonstrated.

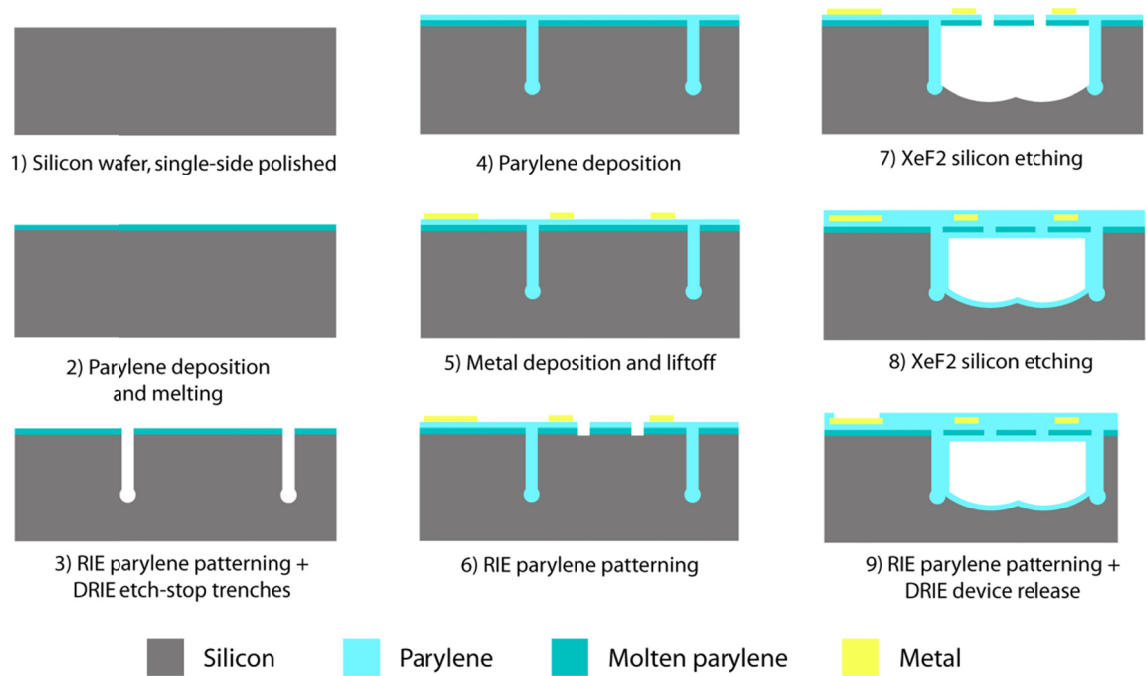


Figure 6-10. Modified pressure sensor fabrication process.

# CHAPTER 7

---

## Conclusion

### 7.1 Conclusions

The field of neural recording and stimulation is rapidly growing, both for research purposes and for medical applications. Single-unit recordings require electrodes to be implanted in the brain. In long-term implants, the recorded signals are observed to degrade over time, due to the relative movement of the electrodes and the tissue and to the encapsulation of the electrodes promoted by the organism's foreign-body response. Movable neural probes offer a viable solution to optimize and maintain the quality of the recordings in chronic implants. Many neural probe microdrives have been previously demonstrated, based on different approaches and technologies. However, these devices are, in general, too bulky for implantation under the skull, or their operation is not compatible with the tissue.

The requirements of an ideal movable neural probe actuator and the challenges faced by the current technology were examined. In terms of size, the device should be small enough to be completely implantable under the skull, making MEMS a suitable fabrication technology. In terms of operation and performance, the device should provide relatively large force and displacement, while operating at low voltage and low power, making electrolysis a convenient actuation method.

The actuator we propose is a MEMS electrolytic inchworm. Each inchworm is based on two balloon actuators. These electrolyte-filled balloons expand when gas is

generated inside of them by electrolysis, and they relax back when electrolysis is stopped, due to the recombination of the gases and their permeation through the balloon wall. The two balloons of the inchworm have specific tasks: one clamps and releases the probe, while the other provides the displacement. By actuating the balloons in specific sequences, a bidirectional inchworm mechanism, with variable displacement per step, is obtained.

Balloon actuators are the building blocks of the inchworms. Standalone balloons were fabricated, characterized, and their behavior was mathematically modeled. The model keeps track of the amount of water, oxygen, hydrogen, and nitrogen (from air) inside the balloon, by considering three phenomena occurring in the balloon: gas generation by electrolysis, gas recombination, and permeation through the balloon wall (including osmosis). The model is able to fit the experimental data very closely.

Initially, balloons with parylene walls were fabricated. The balloon fabrication process underwent several improvements. First, silicon discs were introduced, which allow better shape definition and better sealing of the balloons. Then, silicone (PDMS) replaced parylene as the material for the balloon wall. Compared to parylene, silicone is much more permeable, which makes the relaxation of the balloons faster, and much more flexible, which allows operation at lower pressure. Moreover, silicone does not require a vacuum deposition step, thus easing the constraints for the balloon sacrificial material. The higher permeability of silicone allows osmosis to be exploited to refill the balloons with water, and thus compensate for the water lost through permeation.

Microactuators based on electrolytic balloon actuators were designed, fabricated, tested, and analyzed. The design went through major changes, in order to improve the



performance and reliability of the devices. The first demonstrated device was a monolithic one, in which the actuator and the probe were fabricated on the same device. The limited displacement range, the inadequate latchability, and the lack of flexibility in the choice of the probe are the main drawbacks of this device.

The inchworm design was devised to face the shortcomings of the monolithic devices. The inchworm can generate large displacements in multiple cycles, and it is inherently latchable without power. Moreover, the probe fabrication is decoupled from that of the actuator, offering flexibility in the choice of probes.

A first generation of inchworms was developed. In this version, the balloons are fabricated with sacrificial photoresist coated with parylene, and the probe is clamped between the inchworm and fixed external supports. The minimization of the friction between the probe and the fixed supports was found to be problematic. Moreover, the parylene balloons have unsatisfactory performance, and they are prone to the formation of leaks.

A second generation of inchworms was developed to deal with the drawbacks of the first generation. A double-side clamping mechanism is introduced to eliminate the friction-related problems of the previous version. The parylene balloons of the first generation are replaced by silicone balloons equipped with silicon discs. The balloon fabrication process is further improved to eliminate the need for a hole in the balloon, to the benefit of reliability. The sacrificial photoresist is replaced by a  $\text{MgSO}_4$  shell, which is then coated with silicone. Water permeates by osmosis into the balloon, where it dissolves the salt and form an electrolyte solution. Devices were successfully fabricated and tested using this process. However, the balloons showed issues with water

overflowing, due to the high concentration of the solution inside, and with gas bubbles sticking to the electrodes.

The problems with the salt-shell-based devices were solved by replacing the shell with a hydrogel. Hydrogel-based devices were successfully fabricated and tested. The devices are found to meet the requirements we set in Section 1.5 for movable neural probe actuators. Table 7-1 summarizes the actuator requirements and reports the demonstrated performance of the second-generation inchworm side by side. Preliminary reliability tests gave promising results, with a device still fully operational after 8.5 months of soaking in water and after about 200 actuation cycles. A method to assemble multiple inchworms in an array has been designed, and the components fabricated.

Characterization of the second-generation inchworms revealed the possible need for a feedback mechanism to accurately control the probe position. Several methods can be envisioned to extract feedback signals from the inchworm. The signals can also be used to detect failure of the device. One way to provide feedback is to measure the pressure inside the balloons. For this purpose, pressure sensors based on a parylene membrane and metal strain gauges were designed, fabricated, and tested. The sensor fabrication process can be easily integrated into that of the inchworm. The design methods to tailor the characteristics of the sensors for application in the balloons were also presented.

Table 7-1 (next page): Comparison of actuator requirements and the demonstrated performance of hydrogel-based second-generation inchworms.

Parameter	Desired/acceptable properties	Second-generation inchworm performance
Dimension requirements		
Dimensions	Small, a few millimeters per side	Approximately 5.5 mm by 5.5 mm by 2 mm (single inchworm).
Supply requirements		
Voltage	Low, not higher than a few volts	3-5 V, typically 3.5 V.
Power/heating	Low, with temperature rise less than 1 °C	Typical peak power of 100 $\mu$ W per balloon. Temperature to be determined.
Mechanical requirements		
Displacement	Large (relative to the size of the device), from hundreds of microns to millimeters	Limited by length of the probe (centimeters). Displacement per inchworm cycle between 0.5 and 75 $\mu$ m.
Positioning accuracy	In the micron range	Minimum displacement of 0.5 $\mu$ m demonstrated.
Force	In the millinewton range	Balloons demonstrated to generate force in tens of millinewton range.
Speed	Not a requirement	One inchworm cycle completed typically in 10 minutes. Slow refill of the balloon after water is consumed (around one week for replenishing about 10% of the volume).
Latchability	Latchable without power	Intrinsically latchable. Friction can be added on the probe to compensate for brain elastic response.
Biocompatibility requirements		
Materials	Biocompatible	Parylene. Medical grade PDMS, epoxy, and conductive epoxy. Silicon can be coated with parylene or PDMS if needed.
By-products	Biocompatible	Possible generation of chlorine, because of chlorine ions permeating in from the body fluid (to be verified).
Desirable features		
Choice of probes	Flexible choice	The actuator can be adapted to move different kinds of probes, either by adjusting the clamp width or by mounting a probe on top of a shuttle probe.

## 7.2 Future Work

The future work focuses on further improvement, characterization, and testing of the hydrogel-based balloons and of the second-generation inchworms.

The inchworm body is currently about 5.5 mm by 5.5 mm. Even though the size is adequate for implantation under the skull, further miniaturization is possible and desirable. The miniaturization is limited by the ability to fabricate the balloons. Fabrication of the balloons requires manual steps for the assembly of the silicon discs and for the dispensing of hydrogel, water (to wet the hydrogel), and silicone. It is estimated that the device could be downsized to about 3 mm by 3 mm, while maintaining sufficient space for balloon fabrication. Also, the manual assembly and fabrication steps will have to be streamlined and, where possible, automated if the devices have to be produced in larger numbers.

More thorough characterization of the inchworms is desirable, in particular in terms of reliability, water replenishment time, and operation in saline environment. The design of the balloons should also be optimized, especially in terms of power efficiency. The geometry of the electrodes, for example, can be optimized using the test chamber described in Section 2.10. Also, the temperature of a balloon during actuation should be measured, to verify that the balloons stay cool during operation.

Finally, the devices should be tested in-vivo. Before this test, the inchworms should be assembled into an array (as illustrated in Section 5.7), in order to make the device easy to handle during implantation and to provide guides that keep the probes in place.

# APPENDIX A

---

## MEMS Technology

The term microfabrication, or micromachining, refers to the fabrication of structures with features in the micrometer range. Mechanical structures are combined with electrical ones in microelectromechanical systems (MEMS). This chapter is a brief overview of the most common microfabrication techniques, in particular the ones used for the fabrication of our actuators. For more detailed information, many books are available on the subject, such as [109-110].

Microfabrication process steps can be roughly divided into three categories: patterning, deposition, and etching. Each of these categories will be analyzed in one of the following sections.

### A.1 Bulk and Surface Micromachining

Silicon is the most common substrate for MEMS, due to the large availability of high-quality wafers, the well-developed processing techniques (derived from the integrated circuit industry), the possibility of integrating electronic circuits with mechanical structures on the same device, and the good mechanical properties of silicon. There are two main approaches for the fabrication of micromechanical systems: bulk micromachining and surface micromachining.

With bulk micromachining, mechanical structures are obtained by patterning the silicon substrate itself. The techniques for bulk micromachining are mainly methods to etch silicon isotropically or anisotropically, and they are reviewed in [111-112].

With surface micromachining, layers of materials are deposited and patterned on the substrate. A popular embodiment of surface micromachining is based on polysilicon structural and conductive layers alternated with silicon dioxide sacrificial layers. At the end of the process, the oxide layers are removed, and the polysilicon structures are released. Several foundries offer processes based on this approach, for example the Sandia's Ultraplanar Multi-level MEMS Technology (SUMMiT V) process by Sandia National Labs and the Multi-User MEMS Process (MUMPs) by MEMSCAP. A combination of bulk and surface micromachining techniques is often used in the same device.

## **A.2 Patterning**

Patterning is the transfer of a pattern to some material. The pattern is typically transferred to a resist in a process called lithography. A resist is a polymeric material that is sensitive to exposure to ultraviolet light, electron or ion beams, or x-rays. The resist changes its properties in the regions where it is exposed, and it can subsequently be removed only from those regions (positive resist) or everywhere except for those regions (negative resist) in a process called development. The resist is typically spin-coated onto the substrate.

UV lithography is the most common type of lithography. The light from an ultraviolet source is passed through a mask with a pattern on it. The pattern is defined with a light-blocking material, such as chrome on glass. The photoresist is exposed by having the wafer in direct contact with the mask (contact lithography) or by projecting the pattern through an optical system (projection lithography). Projection lithography

allows the optical reduction of the mask pattern (typically 5 or 10 times), and the minimum patternable feature is determined by the diffraction limit of the optical system.

### **A.3 Deposition**

A large variety of materials (metals, ceramics, and polymers) can be deposited as thin films over a substrate, with thicknesses ranging from a few nanometers to hundreds of microns. Several different techniques have been developed, belonging to two broad categories: chemical deposition and physical deposition.

As the name suggests, chemical deposition involves a chemical reaction. The most common subtype is chemical vapor deposition (CVD). The substrate is placed in a reactor, which is supplied with specific gases. The reaction between the gases causes the deposition of a solid material. CVD is typically run in vacuum (low-pressure CVD, or LPCVD), and the reaction can be enhanced by a plasma (plasma-enhanced CVD, or PECVD). A second type of chemical deposition is electrodeposition, where a redox reaction is exploited. The redox may be caused by the application of a potential (electroplating) or it may happen spontaneously (electroless plating). A third type of chemical deposition is growth, such as that of a silicon dioxide film on a silicon substrate, due to the reaction of silicon with oxygen gas or water vapor at high temperature.

Physical deposition does not involve a chemical reaction. The two most important examples are evaporation and sputtering. These are the standard deposition methods for metal films, but they are not limited to metals. In the case of evaporation, the substrate and a block of the material to be deposited are placed in a vacuum chamber. The material is heated to cause its evaporation and, therefore, deposition on the substrate. The heating is commonly provided by running a current through the material or through a metal

container in contact with it (thermal evaporation), or by an electron beam impinging on the material (e-beam evaporation). In the case of sputtering, a target of material to be deposited is bombarded with ions, which cause atoms to break off from the target and to deposit on the substrate. The ions are generated by plasma, typically an argon one.

## A.4 Etching

Etching is the removal of part of a material from a thin film or from the substrate. To create features on the film or substrate, the removal of the material must occur only in certain regions, while others must be masked. It is therefore important to identify the right masking materials for each type of etch. In some cases, the resist can be used directly as the mask. In other cases, the resist is used to pattern an intermediate layer, which then serves as the mask. The etching techniques are broadly divided into wet and dry. Also, etching can be isotropic (proceeding at the same rate in all directions) or anisotropic (proceeding preferentially along one direction).

In the case of wet etching, the material is removed by a reaction in a liquid solution. Examples of wet etching solutions are

- HF/HNO<sub>3</sub>/Acetic Acid (HNA) for isotropic etching of silicon,
- ethylene diamine pyrocatechol (EDP), tetramethylammonium hydroxide (TMAH), and KOH for anisotropic etching of silicon,
- HF for etching of silicon dioxide.

In the case of dry etching, the material is removed by reaction with a gas or plasma. The isotropic etching of silicon by XeF<sub>2</sub> is an example of gas reaction. When plasma is used, very anisotropic etching can be achieved by accelerating ions perpendicularly to the substrate surface. This technique is called reactive ion etching



(RIE). High-aspect ratio structures with vertical walls are obtained by a variation of the RIE process. One popular process, called deep reactive ion etching (DRIE), was developed by Bosch. The process proceeds in cycles, in which an etching step alternates with a deposition step. The deposited material is teflon-like, and it protects the sidewalls during the etching step. By careful tuning of the recipe, features with high-aspect ratio and vertical walls are obtained.

The etching rates for a number of materials and wet/dry etching combinations can be found in [113-114].

## **A.5 Parylene**

Parylene is a polymer that is widely used in MEMS. Parylene is the trade name for poly(p-xylylene). Several different types of parylene are commercially available. The monomer structures of common parylene types are shown in Figure A-1a.

Parylene is deposited by room-temperature low-pressure chemical vapor deposition (LPCVD). The process is illustrated in Figure A-1b. Parylene is shipped as a dimer powder. The dimer is vaporized and passed through a pyrolysis stage, where it is split into its monomer components at high temperature. The monomer is then allowed in the deposition chamber, where it polymerizes on the substrates. The resulting coating is transparent and conformal.

The different kinds of parylene have different properties (Table A-1). In general, parylene has several desirable properties: it is chemically inert, it is a good electrical and thermal insulator, and it is a good gas and water barrier. The barrier properties of parylene are compared to the ones of other common polymers in Table A-2. Parylene is also biocompatible, being USP class VI and ISO 10993 compliant.

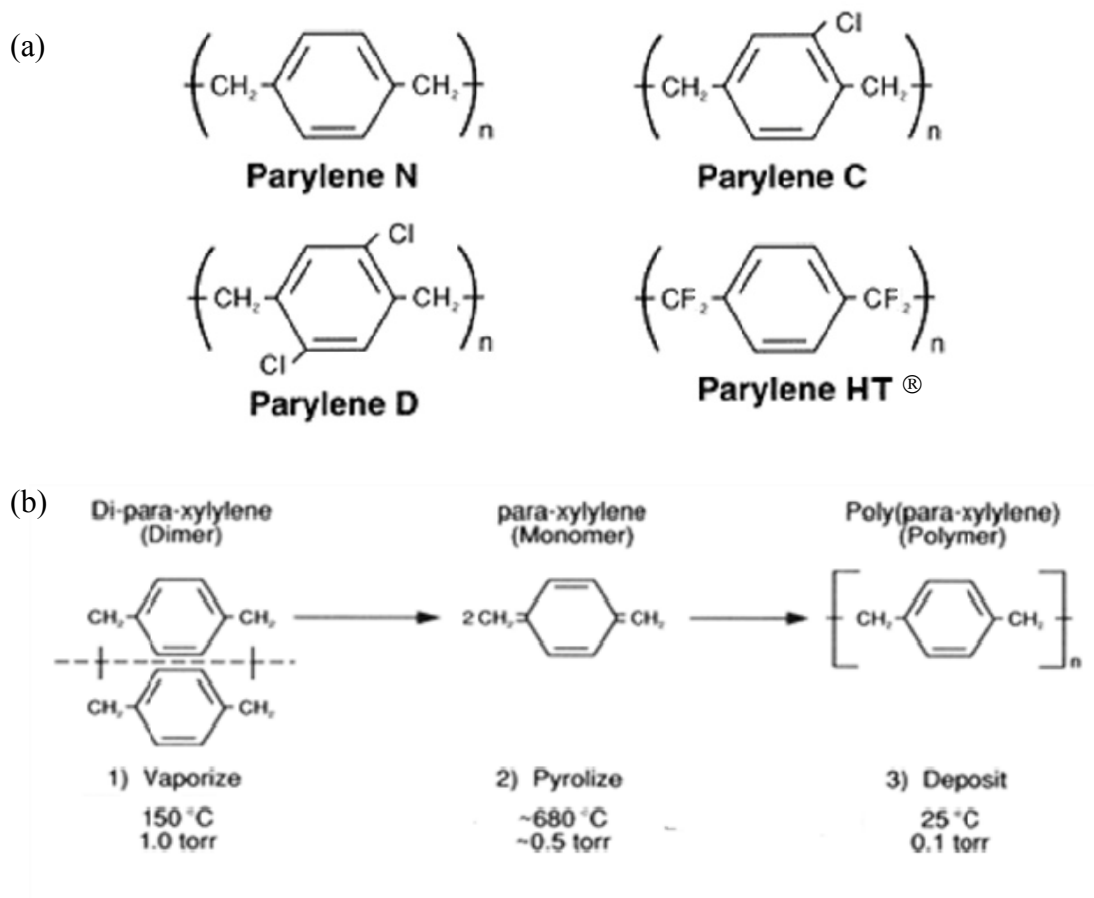


Figure A-1. a) Common types of parylene. b) Parylene deposition process. Images courtesy of Specialty Coating Systems.

Table A-1: Selected properties of parylene (from Specialty Coating Systems).

Parylene	N	C	D	HT
<b>Physical and Mechanical Properties</b>				
Density (g/cm <sup>3</sup> )	1.10–1.12	1.289	1.418	1.32
Young's modulus (GPa)	2.41	2.76	2.62	2.55
Tensile strength (MPa)	48.3	69.0	75.8	51.7
Yield strength (MPa)	42.0	55.2	62.1	34.5
Elongation at break (%)	up to 250	up to 200	up to 200	up to 200
Coefficient of friction (static)	0.25	0.29	0.33	0.15
Coefficient of friction (dynamic)	0.25	0.29	0.31	0.13
Water absorption (% after 24 hr)	< 0.1	< 0.1	< 0.1	< 0.01
<b>Electrical Properties</b>				
Dielectric strength (V/mil)	7000	5600	5500	5400
Volume resistivity, 23 °C, 50% RH (Ω·cm)	$1.4 \times 10^{17}$	$8.8 \times 10^{16}$	$1.2 \times 10^{17}$	$2.0 \times 10^{17}$
Surface resistivity, 23 °C, 50% RH (Ω)	$10^{13}$	$10^{14}$	$10^{16}$	$5 \times 10^{15}$
<b>Thermal Properties</b>				
Melting temperature (°C)	420	290	380	>500
Continuous service temperature (°C)	60	80	100	350
Linear coefficient of expansion at 25 °C (ppm/ °C)	69	35	38	36
Thermal conductivity (W/(m·K))	0.126	0.084	-	0.096

Table A-2: Parylene barrier properties compared to other common polymers (source: Specialty Coating Systems)

Polymer	Gas Permeability at 25°C, (cc·mm)/(m <sup>2</sup> ·day·atm) <sup>a</sup>				Water Vapor Transmission Rate (g·mm)/(m <sup>2</sup> ·day)
	N <sub>2</sub>	O <sub>2</sub>	CO <sub>2</sub>	H <sub>2</sub>	
Parylene N	3.0	15.4	84.3	212.6	0.59 <sup>b</sup>
Parylene C	0.4	2.8	3.0	43.3	0.08 <sup>c</sup>
Parylene D	1.8	12.6	5.1	94.5	0.09 <sup>b</sup>
Parylene HT	4.8	23.5	95.4	–	0.22 <sup>d</sup>
Acrylic (AR)	–	–	–	–	13.9 <sup>e</sup>
Epoxy (ER)	1.6	2.0 – 3.9	3.1	43.3	0.94 <sup>e</sup>
Polyurethane (UR)	31.5	78.7	1,181	–	0.93 – 3.4 <sup>e</sup>
Silicone (SR)	–	19,685	118,110	17,717	1.7 – 47.5 <sup>e</sup>
<sup>a</sup> ASTM D 1434					
<sup>b</sup> ASTM E 96 (at 90% RH, 37°C)					
<sup>c</sup> ASTM F 1249 (at 90% RH, 37°C)					
<sup>d</sup> ASTM F 1249 (at 100% RH, 38°C)					
<sup>e</sup> Coating Materials for Electronic Applications, Licari, J.J., Noyes Publications, New Jersey, 2003.					

# APPENDIX B

---

## Thermodynamics and Electrochemistry

This appendix contains a review of the topics in thermodynamics and electrochemistry that are important for the design and modeling of the actuators, and it introduces the notation we adhere to in this thesis. The review is not meant to be exhaustive, and it is assumed that the reader has at least basic knowledge of subjects. For more in-depth treatments, the reader can refer to [80, 115] for thermodynamics and to [116-117] for electrochemistry.

### B.1 Thermodynamics

#### B.1.1 Energy and Thermodynamic Potentials

We consider a system undergoing a process. The system receives a quantity of heat  $\delta q$  from the surroundings and does a work  $\delta w$  on the surroundings. The first law of thermodynamics expresses the conservation of energy in the system

$$dU = \delta q - \delta w. \quad (\text{B-1})$$

$U$  represents the internal energy of the system, i.e., its energy content. The  $d$  symbol indicates an exact differential, i.e., a differential whose integral depends only on the initial and final points. Quantities associated to exact differentials are state variables, as their values describe the state of the system. The  $\delta$  symbol indicates a non-exact differential, i.e., a differential whose integral depends on the integration path.

The work term is, in general, the sum of several contributions. Only mechanical work due to expansion of the system (pV work) is usually included in classical thermodynamics. For an open system that exchanges matter with the surroundings, we need to account for the energy associated with moving particles in and out of the system. When considering pV work and exchange of matter, Equation (B-1) becomes

$$dU = \delta q - pdV + \sum_i \mu_i dN_i. \quad (\text{B-2})$$

In the mechanical work term,  $p$  is the pressure and  $V$  is the volume of the system. The last term represents the change in energy in the system due to a variation in the number of particles of each species, where  $N_i$  is the number of particles of species  $i$ , and  $\mu_i$  is the chemical potential of the species (examined in the next section). To indicate the number of moles (instead of particles) of species  $i$ , we will use the lowercase symbol  $n_i$ . Changing the units from particles to moles changes the units of the chemical potential.

Forms of energy other than the ones appearing in (B-2) must be included in the analysis when dealing with certain systems. In these cases, we can add a term  $\delta w_o$  to (B-2) to account for other relevant energy contributions

$$dU = \delta q - pdV - \delta w_o + \sum_i \mu_i dN_i. \quad (\text{B-3})$$

Including other forms of energy may require the introduction of additional variables to describe the system, and the  $\delta w_o$  term can be expressed in terms of these variables. Electrochemistry is a case where an additional energy term is required, due to the involvement of charged species and electric potentials.

The second law of thermodynamics introduces the concept of entropy. As explained by statistical mechanics, entropy is related to the “disorder” of the system. One formulation of the second law is

$$dS \geq \frac{\delta q}{T} \quad (\text{B-4})$$

where  $S$  is the entropy and  $T$  is the temperature. The inequality implies that the entropy of an isolated system, for which  $\delta q = 0$ , can only increase, seeking a maximum at equilibrium. The equality in Equation (B-4) holds in case of a reversible process, i.e., process throughout which the system is always at equilibrium. Under the assumption of reversible process, Equation (B-2) can be rewritten in terms of exact differentials

$$dU = TdS - pdV + \sum_i \mu_i dN_i. \quad (\text{B-5})$$

The internal energy  $U$  is one of the thermodynamic potentials. Other potentials are of interest, in particular the enthalpy  $H$  and the Gibbs free energy  $G$ . Their definitions are

$$\begin{aligned} H &= U + pV \\ G &= H - TS. \end{aligned} \quad (\text{B-6})$$

An expression for  $U$  is given by Euler’s relation

$$U = TS - pV + \sum_i \mu_i dN_i. \quad (\text{B-7})$$

From this expression, we can write  $H$  and  $G$  as

$$H = TS + \sum_i \mu_i N_i \quad (\text{B-8})$$

$$G = \sum_i \mu_i N_i. \quad (\text{B-9})$$

The enthalpy and Gibbs free energy do not have a physical interpretation as intuitive as the internal energy has. To better interpret  $H$  and  $G$ , we examine their differentials. From  $dU$  in (B-2), we derive  $dH$

$$dH = dU - d(pV) = dU + pdV - Vdp = \delta q - Vdp + \sum_i \mu_i dN_i. \quad (\text{B-10})$$

A closed system does not exchange particles with the surroundings; therefore  $\sum_i \mu_i dN_i = 0$ . For a closed system and a process at constant pressure, we have

$$\Delta H_p = q \quad (\text{B-11})$$

where variables to be kept constant are listed as subscripts. Therefore, a change in enthalpy in a closed system at constant pressure is equal to the heat transferred to the system. Similarly, we derive  $dG$

$$dG = (\delta q - TdS) + Vdp + \sum_i \mu_i dN_i - SdT. \quad (\text{B-12})$$

For a closed system at constant temperature and pressure,  $dG$  becomes

$$dG_{T,p} = (\delta q - TdS) \leq 0. \quad (\text{B-13})$$



The inequality is given by Equation (B-4), and it shows that  $G$  seeks a minimum at equilibrium. As a consequence, a process at constant temperature and pressure proceeds spontaneously only if the associated  $\Delta G$  is negative. In the case of a reversible process, (B-12) simplifies to

$$dG = Vdp + \sum_i \mu_i dN_i - SdT. \quad (\text{B-14})$$

If we include other forms of energy in a  $w_o$  term, we obtain for a closed system undergoing a reversible process at constant temperature and pressure

$$\Delta G_{T,p} = -w_o. \quad (\text{B-15})$$

This shows that  $\Delta G$  is maximum work that can be obtained from the system. In real situations, the process is never perfectly reversible, and part of the energy is dissipated as heat.

### B.1.2 Chemical and Electrochemical Potential

As Equation (B-2), shows, the chemical potential represents the energy needed to move a new particle into the system (when entropy and volume stay constant). It is usually defined in terms of Gibbs free energy, based on Equation (B-14)

$$\mu_i = \left( \frac{\partial G}{\partial N_i} \right)_{T,p,N_{j \neq i}}. \quad (\text{B-16})$$

The chemical potential is useful in determining the equilibrium conditions in situations where exchange of matter is involved. If two phases exchange matter, the chemical potential of each component is the same in each phase at equilibrium.

When we include electrical energy in our analysis, an energy term must be added to account for the energy of charged particles in an electrical potential. The expression for the Gibbs free energy is analogous to (B-9), with the addition of an extra energy term

$$\overline{G} = \sum_i \mu_i N_i + \sum_i z_i N_i \phi \quad (\text{B-17})$$

where  $z_i$  is the charge of a particle of species  $i$  and  $\phi$  is the electrical potential in the system. Note that when electrical energy is included in the analysis, the affected thermodynamic quantities are marked by an overline. The electrochemical potential of a species is defined similarly to (B-16)

$$\overline{\mu}_i = \left( \frac{\partial \overline{G}}{\partial N_i} \right)_{T, p, N_{j \neq i}} = \mu_i + z_i \phi. \quad (\text{B-18})$$

The amount of species  $i$  is indicated either by the number of particles  $N_i$  or by the number of moles  $n_i$ . To express the electrochemical potential in terms of moles, we replace the charge of a particle  $z_i$  with the charge of a mole of particles  $z_i F$ , where  $F$  is Faraday's constant (96485 C/mol)

$$\overline{\mu}_i = \left( \frac{\partial \overline{G}}{\partial n_i} \right)_{T, p, n_{j \neq i}} = \mu_i + z_i F \phi. \quad (\text{B-19})$$

### B.1.3 Mixtures and Activity

Like any other thermodynamic process, mixing two components has an associated Gibbs free energy change

$$\Delta G_{\text{mix}} = \Delta H_{\text{mix}} - T\Delta S_{\text{mix}}. \quad (\text{B-20})$$

The enthalpy change is determined by the interaction energy of the two species when mixed together. The change in entropy is related to the increase in “disorder” due to mixing. An ideal mixture, or ideal solution, is one where the change in enthalpy is zero, so that

$$\Delta G_{\text{mix}} = -T\Delta S_{\text{mix}}. \quad (\text{B-21})$$

In an ideal solution, the only effect of mixing is increasing the disorder, but the interactions between the molecules do not change with respect to the separate components. An expression for the entropy of mixing can be found using statistical mechanics (starting from Boltzmann’s equation for entropy). For a mixture of several components we have

$$\Delta G_{\text{mix}} = Nk_b T \sum_i \frac{N_i}{N} \ln \frac{N_i}{N} = nRT \sum_i \frac{n_i}{n} \ln \frac{n_i}{n} = nRT \sum_i x_i \ln x_i. \quad (\text{B-22})$$

In this expression,  $N$  is the total number of particles in the mixture,  $k_b$  is Boltzmann constant,  $R$  is the gas constant, and  $x_i$  is the molar fraction of component  $i$  in the solution. For an ideal mixture,  $\Delta G_{\text{mix}}$  is always negative, implying that mixing is always spontaneous. By substituting (B-22) in (B-16), we can compute the chemical potential of each component  $i$  in the mixture

$$\Delta\mu_{i,\text{mix}} = \left( \frac{\partial \Delta G_{\text{mix}}}{\partial N_i} \right)_{p,T,N_{j \neq i}} = RT \ln x_i \quad (\text{B-23})$$

$$\mu_i = \mu_i^0 + \Delta\mu_{i,\text{mix}} = \mu_i^0 + RT \ln x_i. \quad (\text{B-24})$$

The term  $\mu_i^0$  is the chemical potential of the pure substance (for which  $x_i$  is equal to 1). An example of ideal mixture is a mixture of ideal gases, as there are no interactions between the particles by definition. For gas mixtures, the molar fractions can be converted to the partial pressures of the component gases. For liquid solutions, the molar fractions can be converted to the concentrations.

The calculation of the entropy of mixing relies only on the number of particles of each species in the mixture. If a solute separates into multiple units when dissolved (like multi-ionic solutes would do in water), a correction factor, called Van't Hoff factor, must be introduced. The factor indicates the number of units into which the solute separates, and it is a multiplicative factor for the molar fraction.

Equation (B-24) is generalized to non-ideal mixtures by introducing the concept of activity. The activity of species  $i$  is denoted by  $a_i$ , and it is a measure of its “effective concentration” in a mixture. It is defined as

$$\mu_i = \mu_i^0 + RT \ln a_i. \quad (\text{B-25})$$

If a mixture is ideal, the activity of each species is equal to its molar fraction. Deviations from the ideal case are more conveniently represented by the activity coefficient  $\gamma_i$ , defined as

$$a_i = \gamma_i x_i. \quad (\text{B-26})$$

A deviation of the activity coefficient from unity is a measure of the non-ideality of the mixture.

Mixing is related to the concept of solubility. Solubility indicates how much of a substance (solute) can be dissolved into another (solvent). If the solute and solvent form an ideal solution, they can be mixed in any amount, because mixing is thermodynamically favorable for any mixing ratio ( $\Delta G_{\text{mix}}$  is always negative). If the solute and solvent form a non-ideal solution, there may be a maximum amount of solute dissolvable in the solvent. At a certain solute concentration,  $\Delta H_{\text{mix}}$  may become positive and large enough to make  $\Delta G_{\text{mix}}$  positive, making mixing not thermodynamically favorable. The concentration at which  $\Delta G_{\text{mix}} = 0$  represents the maximum concentration the solute can reach in the solvent, and it is known as solubility. A solution at this concentration is called saturated.

Absorption is a special case of mixing. Absorption is the incorporation of a substance into another in a different state. The substance that is absorbed is called absorbate, while the substance that is absorbing is called absorbent. When an absorbate phase is placed in contact with an absorbent phase, absorption occurs until the absorbate has the same chemical potential in the two phases. Several models for absorption have been developed. In the case of a gaseous absorbate and a liquid absorbent, Henry's law is the simplest model. Henry's law states that, at constant temperature, the concentration  $c$  of gas dissolved in a liquid is proportional to the partial pressure  $p$  of the gas above the liquid

$$p = k_H c. \quad (\text{B-27})$$

The proportionality constant  $k_H$  is called Henry's constant.

### B.1.4 Chemical Reactions

We consider a generic chemical reaction

$$\sum_i \alpha_i A_i \rightleftharpoons \sum_i \beta_i B_i \quad (\text{B-28})$$

where  $A_i$  and  $B_i$  are chemical species, and  $\alpha_i$  and  $\beta_i$  are stoichiometric coefficients. The reaction converts a certain amount of reactants into a certain amount of products. The change in Gibbs free energy due to the reaction is

$$\Delta G = \sum_i \Delta n_{B_i} \mu_{B_i} - \sum_i \Delta n_{A_i} \mu_{A_i}. \quad (\text{B-29})$$

The relative amount converted for each species is determined by the stoichiometric coefficients. We consider the  $\Delta G$  associated to the reaction of 1 mole of a reactant with stoichiometric coefficient equal to 1

$$\Delta G = \sum_i \beta_i \mu_{B_i} - \sum_i \alpha_i \mu_{A_i}. \quad (\text{B-30})$$

We now express the chemical potentials in terms of the activities using (B-25), and we find

$$\mu_{A_i} = \mu_{A_i}^0 + RT \ln a_{A_i} \quad \mu_{B_i} = \mu_{B_i}^0 + RT \ln a_{B_i} \quad (\text{B-31})$$

$$\Delta G^0 = \sum_i \beta_i \mu_{B_i}^0 - \sum_i \alpha_i \mu_{A_i}^0 \quad (\text{B-32})$$

$$\Delta G = \Delta G^0 + RT \ln \frac{\prod_i (a_{B_i})^{\beta_i}}{\prod_i (a_{A_i})^{\alpha_i}} = \Delta G^0 + RT \ln K. \quad (\text{B-33})$$

The equilibrium condition is found by setting  $\Delta G = 0$

$$\Delta G^0 + RT \ln K_{eq} = 0 \quad \Rightarrow \quad K_{eq} = \exp\left(-\frac{\Delta G^0}{RT}\right). \quad (\text{B-34})$$

The term  $K_{eq}$  is called the equilibrium constant. In terms of chemical potentials, equilibrium corresponds to the condition where the weighted sum of the chemical potentials on each side of the reaction is the same

$$\sum_i \alpha_i \mu_{A_i} = \sum_i \beta_i \mu_{B_i}. \quad (\text{B-35})$$

In certain cases, the reaction equilibrium theory also offers a method to analyze the dissolution of one substance into another. For example, for the dissolution of magnesium sulfate from solid crystal into ions in water we have



The equilibrium constant for this process is called the solubility product, and it is usually denoted by  $K_{sp}$ . From the solubility product, we can derive the solubility of magnesium sulfate into water.

### B.1.5 Ideal Gases

An ideal gas is a system of non-interacting particles moving in a random manner. Despite the approximation, many gases in common conditions are well described by this model. In thermodynamics, systems are described by relations between the state variables called equations of state. With statistical mechanics considerations, the equation of state of an ideal gas is found to be

$$pV = Nk_B T = nRT \quad (\text{B-37})$$

where  $k_B$  is the Boltzmann constant, and  $R$  is the gas constant (equal to the product of  $k_B$  and Avogadro's number). The internal energy of an ideal monoatomic gas is

$$U = \frac{3}{2} Nk_B T = \frac{3}{2} nRT = \frac{3}{2} pV. \quad (\text{B-38})$$

In case of multiatomic gases, the multiplicative factor is different from 3/2. For each additional degree of freedom of the gas molecules, we add 1 to the constant. For example, the constant is 5/2 for a diatomic gas.

An ideal gas mixture is composed of two or more ideal gases whose particles do not interact with each other. The equation of state for the mixture is the same as for a pure gas, with  $N$  and  $n$  representing the total number or moles of particles respectively

$$pV = Nk_B T = \left( \sum_i N_i \right) k_B T = nRT = \left( \sum_i n_i \right) RT. \quad (\text{B-39})$$

The partial pressure  $p_i$  of each gas is defined as



$$p_i = \frac{n_i RT}{V}. \quad (\text{B-40})$$

It follows that the total pressure of the mixture is simply the sum of the partial pressures of each gas

$$p = \sum_i p_i. \quad (\text{B-41})$$

### B.1.6 Permeation

Permeation is the penetration of a substance (called the permeate) through a solid.

The penetration through the solid occurs in three steps.

- *Sorption (adsorption/absorption)*: the substance accumulates on the first surface of the solid. The substance that accumulates on the surface is called sorbate, while the solid is called sorbent.
- *Diffusion*: the substance diffuses through the solid, and it reaches the second surface.
- *Desorption*: the substance detaches from the second surface of the solid.

The amount of sorbate on the surface is a function of the concentration (or partial pressure) of the substance in the phase in contact with the solid. This function is dependent on temperature. For a given temperature, the relation is called isotherm. There are many empirical models commonly used, derived from different assumptions on the sorption process. The simplest isotherm is Henry's law of absorption (B-27), extended to the case of combined adsorption/absorption. Desorption is treated in the same way as sorption.

There are two main models to describe permeation through a membrane: the solution-diffusion model and the pore-flow model [118]. Both models are based on the fact that permeation is driven by a chemical potential gradient. In the solution-diffusion model, the chemical potential gradient is attributed to a concentration gradient. In the pore-flow model, the chemical potential gradient is attributed to a pressure gradient. In the case of pinhole-free membranes, the main transport mechanism is diffusion, and the solution-diffusion model is usually employed. For membranes having pinholes, bulk flow through the pinholes may dominate over diffusion, making the pore-flow model more appropriate.

A simplified model for permeation is here illustrated. The model is based on Henry's law for sorption/desorption and Fick's law for diffusion. We consider only the case of steady-state diffusion, as expressed by Fick's first law (one-dimensional case)

$$J = -D \frac{\partial c}{\partial x} \quad (\text{B-42})$$

where  $J$  is the flux of substance,  $c$  is the concentration and  $D$  is the diffusion coefficient. If we have a solid slab of thickness  $h$  and area  $A$ , with concentration  $c_1$  on one side and  $c_2$  on the other side, Fick's first law can be solved to find

$$J = -D \frac{A}{h} (c_2 - c_1). \quad (\text{B-43})$$

To understand how permeation is related to sorption, diffusion and desorption, we consider the simplified case of Figure B-1. We assume that Henry's law holds at the two interfaces, which means that the two interfaces are always at equilibrium. This is true if

the sorption and desorption rates are much faster than the diffusion rate through the membrane. We also assume that the phases and interfaces 1 and 2 have similar properties, so the Henry's coefficient for sorption and desorption are the same. This allows us to simplify the final formula, but it is not strictly necessary. The equations at the two interfaces and in the solid are

$$\begin{aligned} \text{phase 1: } p_1 &= k_H c_1 \\ \text{solid: } J &= D \frac{A}{h} (c_1 - c_2) \\ \text{phase 2: } p_2 &= k_H c_2. \end{aligned} \tag{B-44}$$

We want to derive the permeation flux of the substance from phase 1 to phase 2 through the slab

$$J = \frac{D}{k_H} \frac{A}{h} (p_1 - p_2). \tag{B-45}$$

We then define the permeability coefficient  $P$  as

$$P = \frac{D}{k_H}. \tag{B-46}$$

The use of Fick's law for diffusion is inspired by the solution-diffusion model. However, Equation (B-45) is analogous to Darcy's law, which is derived from the pore-flow model. This connection between the two models is determined by the use of Henry's law, which relates pressures and concentrations. The model here presented assumes that the transport is determined by diffusion. In the case of pinholes, bulk flow occurs in addition to diffusion. Bulk flow through a pinhole can be modeled, for example, by the Hagen-Poiseuille equation, which has the same form as Equation (B-45). Therefore, in the case

of pinholes, the form of Equation (B-45) still holds, but the expression for  $P$  will be different from Equation (B-46). This demonstrates that Equation (B-45) can be used for membranes with or without pinholes, with a different coefficient  $P$  in the two cases.

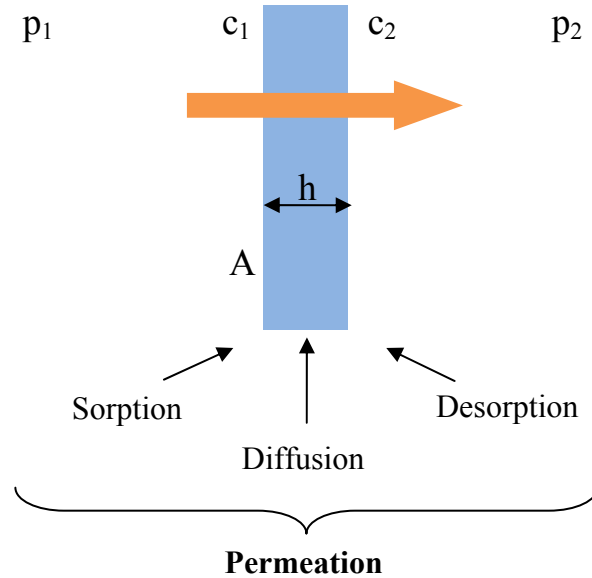


Figure B-1. Schematics of a simplified gas permeation case.

Permeation is an important property of materials for many practical uses. For example, oxygen and water vapor permeation need to be controlled for packaging applications. The time-lag method can be used to measure the permeability [119] of a material. Several methods for measuring permeation have been standardized by ASTM. Some examples follow.

- ASTM D 1434: Standard Test Method for Determining Gas Permeability Characteristics of Plastic Film and Sheetings.
- ASTM F 1249: Standard Test Method for Water Vapor Transmission Rate Through Plastic Films and Sheeting Using a Modulated Infrared Sensor.

- ASTM E 96: Standard Test Methods for Water Vapor Transmission of Materials.

### B.1.7 Osmosis

Osmosis is a special case of permeation. In the case of osmosis, water permeates through a membrane, following a chemical potential gradient. The membrane separates two solutions in which water has different chemical potential. The membrane is semi-permeable, as it allows only water to permeate through, while solutes cannot pass. Due to the chemical potential gradient, water flows from the high potential (low concentration) side to the low potential (high concentration) side. If the system allows it, the accumulation of water on the high concentration side may cause the pressure to increase there. At equilibrium, the pressure balances the chemical potential gradient, and no more water flows. The pressure difference between the two sides at equilibrium is called osmotic pressure.

The osmotic pressure can be calculated if the concentrations of the solutions on the two sides are known [80, 118]. At equilibrium, the chemical potential of water on each side must be the same at equilibrium

$$\mu(c_l, p_l) = \mu(c_h, p_l + \Pi). \quad (\text{B-47})$$

The chemical potential depends on the concentration and pressure. The subscripts  $l$  and  $h$  indicate the low and high concentration side respectively.  $\Pi$  is the osmotic pressure, and  $p_l$  is the pressure on the low-concentration side. We separate the effects of concentration and pressure, and, using (B-24), we write

$$\begin{aligned}\mu(c_l, p_l) &= \mu^0(p_l) + RT \ln x_l \\ \mu(c_h, p_l + \Pi) &= \mu^0(p_l + \Pi) + RT \ln x_h.\end{aligned}\tag{B-48}$$

The dependence on pressure can be derived from the definition of chemical potential [120]. We obtain

$$\mu^0(p_l + \Pi) - \mu^0(p_l) = \Pi v_{\text{H}_2\text{O}}\tag{B-49}$$

where  $v_{\text{H}_2\text{O}}$  is the molar volume of water. To simplify the formulas, we consider the special case of pure water on the low-concentration side, so that  $x_l = 1$ .

$$\begin{aligned}-RT \ln x_h &= \Pi v_{\text{H}_2\text{O}} \\ -RT \ln x_h &= -RT \ln(1 - x_s) \approx RT x_s.\end{aligned}\tag{B-50}$$

where  $x_s$  is the molar fraction of solute on the high-concentration side (assumed much smaller than 1). Finally, we obtain a formula for the osmotic pressure

$$\Pi = \frac{x_s}{v_{\text{H}_2\text{O}}} RT = \frac{x_s n}{v_{\text{H}_2\text{O}} n} RT = \frac{n_s}{V_{\text{H}_2\text{O}}} RT = c_s RT\tag{B-51}$$

where  $c_s$  is the molal concentration of solute on the high-concentration side. Since osmosis depends on the molar fraction of water, the Van't Hoff factor (indicated by  $i$ ) must be added in the case of solute that separates into multiple units when dissolved in water. The expression for the osmotic pressure becomes

$$\Pi = i c_s RT\tag{B-52}$$

For example, if a solute completely separates into two ions when dissolved in water, then  $i = 2$ .

## B.2 Electrochemistry

### B.2.1 Electrochemical Cells

Electrochemistry studies the interrelation of electrical and chemical phenomena. Of particular interest is the interaction between an electronic conductor (electrode) and an ionic conductor (electrolyte). The typical system is an electrochemical cell, consisting of two electrodes immersed in an electrolyte solution. At one electrode, a reduction reaction takes place. This electrode is called cathode, and the electrons are transferred from the electrode to the solution. At the other electrode, an oxidation reaction takes place. This electrode is called anode, and the electrons are transferred from the solution to the electrode. The complete chemical reaction in the system is given by the combination of the two half-reactions occurring at each electrode.

The cell is an electrical circuit. Inside the electrodes the charge is transported by electrons, whereas in the electrolyte it is transported by ions. In some cases, the electrolyte participates in the electrode reactions. In other cases, the electrolyte is added only to decrease the solution resistance (supporting electrolyte).

The reaction in the cell may occur spontaneously or it may require the supply of energy. Depending on which one is the case, the cell has a different name.

- *Galvanic cell*: the reaction proceeds spontaneously when electrodes are connected by a conductor, and chemical energy is converted into electrical energy (like in a battery).
- *Electrolytic cell*: an external potential must be applied to drive the reaction, and electrical energy is consumed and converted into chemical energy.

### B.2.2 Electrode-electrolyte Interface

The phenomena taking place at the electrode-electrolyte interface are the most fundamental aspect of electrochemistry. There are two kinds of phenomena occurring at the electrode-electrolyte interface.

- *Faradaic processes*: they are characterized by the transfer of charge across the interface. These are the processes by which the redox reactions take place at the electrodes.
- *Non-faradaic processes*: they do not involve charge transfer across the interface. They include phenomena like adsorption/desorption and charge accumulation on the sides of the interface.

In the case of non-faradaic processes, the electrode-electrolyte interface behaves like a capacitor. When an electrode is immersed in an electrolyte, charge accumulates on the two sides of the interface, in order to bring the system to equilibrium. The resulting charge distribution produces an electrical potential, which balances the electrochemical potential of the species on the two sides of the interface. On the electrode (a metallic electrode is assumed), charge accumulates in a thin sheet at the surface. The charge distribution inside the electrolyte is more complex, and it takes the form of an electrical double layer (Figure B-2). Close to the electrode surface is a layer of specifically-adsorbed ions. The locus of their electrical centers constitutes the inner Helmholtz plane (IHP). Past this first layer are non-specifically adsorbed ions (mostly solvated ions), which interact with the electrode only through long-range electrostatic forces. These ions are divided into two zones. Some ions are close to the electrode, and the locus of their



electrical centers constitutes the outer Helmholtz plane (OHP). Other ions are part of a diffuse layer that extends farther into the solution.

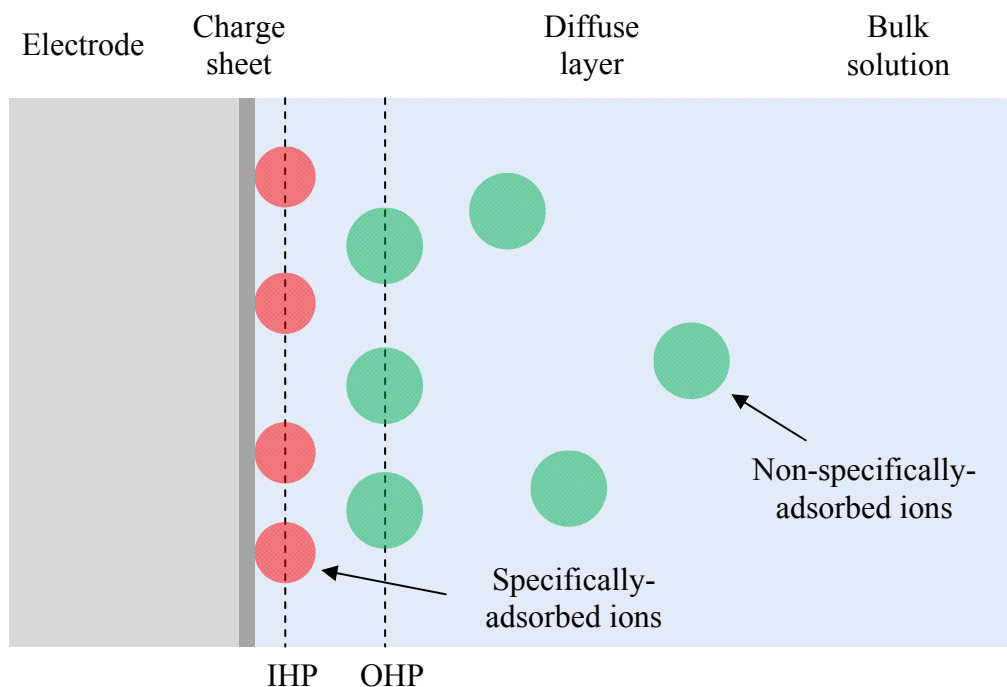


Figure B-2. Electrical double layer at the electrode-electrolyte interface.

Faradaic processes involve charge transfer across the interface, with electrons as the charge carriers. Figure B-3 illustrates a very simplified picture of the physics behind the charge transfer at the interface. Electrons are present at certain energy levels inside the electrode and inside the electrolyte. We assume that electrons inside the electrode have a maximum energy  $E_{el}$ , while the lowest energy level available in the solution is  $E_{sol}$ . If  $E_{el} < E_{sol}$ , the electrons inside the electrode do not have enough energy to pass into the solution. However, we can raise  $E_{el}$  by applying a negative potential to the electrode. When  $E_{el} > E_{sol}$ , electrons can pass into the electrolyte, and a reduction (or cathodic)

current flows. A similar argument applies for the case of electrons passing from the solution into the electrode. If  $E_{el} > E_{sol}$ , we can apply a positive potential to the electrode, in order to lower the first available energy level in the electrode. When this energy is sufficiently low, electrons can pass from the solution to the electrode, and an oxidation (or anodic) current flows.

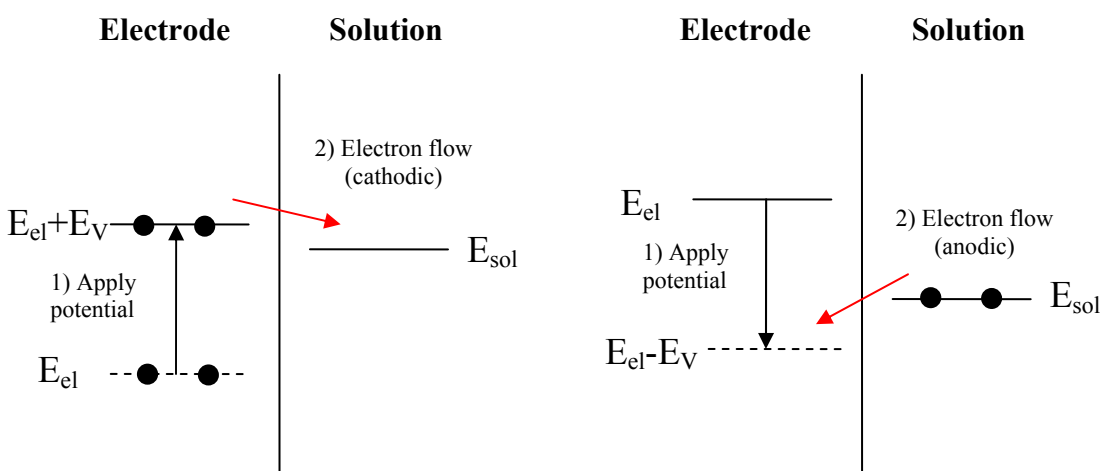


Figure B-3. Electronic energy levels at the electrode-electrolyte interface.

The two types of phenomena, faradaic and non-faradaic, can be combined into an equivalent electrical circuit for the electrode-electrolyte interface. Non-faradaic phenomena are modeled by a capacitor, because charge accumulates on the sides of the interface, but it does not cross it. Faradaic phenomena, on the other hand, are modeled by a resistor. Therefore, the interface is modeled by a capacitor and a resistor in parallel (as it will be shown later in Figure B-4). In general, the circuit components are non-linear, but they can be linearized within certain potential or current ranges.

### B.2.3 Cell and Electrode Potentials

The total cell reaction is associated to a change in Gibbs free energy. We assume that the reaction runs in a thermodynamically reversible way. This means there are no losses to heat, and the whole  $\Delta G$  is exploited to produce net work (the work other than pV work). We can approximate such a condition by running the reaction slowly, i.e., passing the cell current through a load with very high resistance. The work obtained from the cell is all electrical and dissipated to heat on the load. Like we did in Section B.1.4, we consider the  $\Delta G$  associated to the reaction of 1 mole of a reactant with stoichiometric coefficient equal to 1. We denote the stoichiometric coefficient of the electrons in the half-reactions by  $n$ . The amount of charge flowing through the load is  $nF$  (where  $F$  is Faraday's constant). In order to satisfy the energy balance, there must be an electrical potential drop  $E$  across the load. This potential is called cell potential and it satisfies the equation

$$\Delta G = -nFE. \quad (\text{B-53})$$

The minus sign is due to the convention by which the electrical potential is measured. We take the condition in which all components have unit activity as a reference, and call the corresponding potential the standard potential  $E^0$

$$\Delta G^0 = -nFE^0. \quad (\text{B-54})$$

We can write the potential in terms of the reference potential

$$E = E^0 - \frac{\Delta G - \Delta G^0}{nF}. \quad (\text{B-55})$$

By combining Equations (B-33) and (B-55), we obtain Nernst equation, which relates the cell potential to the activities of the species involved

$$E = E^0 + \frac{RT}{nF} \ln \frac{\prod_i (a_{B_i})^{\beta_i}}{\prod_i (a_{A_i})^{\alpha_i}}. \quad (\text{B-56})$$

Nernst equation can also be derived by looking at the redox reaction and considering the electrochemical potentials for all the species (including the electrons), and taking into account that there is a potential difference between the electrode and the solution. The electrochemical potential of electrons in a phase is called the Fermi level. To reach equilibrium between two phases, the Fermi level in the two phases must be the same. When two phases are brought into contact, charge flows and builds a potential difference until the Fermi levels are equalized. This explains the formation of the electrical double layer.

It is very convenient to associate potentials to the electrode half-reactions, so they can be combined to find cell potentials. These are called electrode potentials. The standard potential of each half-reaction is measured against a reference electrode, which is assigned zero potential by convention. The chosen reference is the standard hydrogen electrode (SHE), also called normal hydrogen electrode (NHE). This electrode is written as



This is a common notation to represent electrochemical cells. A slash / indicates a phase boundary. In this case, Pt is in solid form, H<sub>2</sub> is in gas form, and H<sup>+</sup> ions are in solution in water. A comma indicates that two components are in the same phase.

### B.2.4 Overpotential

The potentials examined in the previous section are equilibrium potentials, because the reactions are assumed to occur reversibly. Polarization is the deviation from equilibrium potential upon passage of a faradaic current. It is measured by the overpotential

$$\eta = E - E_{eq} \quad (\text{B-58})$$

where  $E_{eq}$  is the potential as calculated from Nernst equation. For each value of the overpotential, a certain value of the current is observed. The magnitude of the current is affected by several concurrent phenomena, which determine the overall rate of the reaction:

- electron transfer at the electrode surface;
- mass transfer in the solution, both in the bulk and in the diffusion layer in proximity of the electrode surface;
- other processes or reactions preceding or following the electron transfer (such as adsorption/desorption, catalytic phenomena,...).

The rate of each phenomenon is affected by the applied potential. Therefore, the overpotential can be split into several contribution, each one associated to one of the phenomena above. Reaction kinetics and mass transfer are the subjects of the next two sections.

### B.2.5 Reaction Kinetics

Thermodynamics only describes equilibrium conditions, and not how fast the equilibrium is reached. As a consequence, the sign of  $\Delta G$  determines the direction of the reaction, but its value does not give any information about its speed. Even if a reaction has a negative  $\Delta G$  (and it should therefore run spontaneously), its rate may be so slow that almost no current is observed. The reaction kinetics at the electrode surface is a function of the applied potential, and models have been developed to find the relationship between the current  $i$  and the potential  $E$  (the i-E curve).

We consider a redox reaction involving an oxidized species O and a reduced species R



The rate of the forward reaction  $v_f$  and of backward reaction  $v_b$  are written in terms of the rate constants  $k_f$  and  $k_b$  and of the cathodic current  $i_c$  and anodic current  $i_a$

$$v_f = k_f C_O = \frac{i_c}{nFA} \quad v_b = k_b C_R = \frac{i_a}{nFA}. \quad (\text{B-60})$$

$C_O$  and  $C_R$  are the concentrations at the electrode surface of O and R respectively.  $A$  is the surface area of the electrode. The net rate and net current are given by

$$v = v_f - v_b \quad i = i_c - i_a. \quad (\text{B-61})$$

Most rate constants have an Arrhenius dependence on temperature

$$k = D e^{-E_A/RT} = D' e^{-\Delta G_A/RT} \quad (\text{B-62})$$

where  $E_A$  is called the activation energy,  $\Delta G_A$  is the free energy of activation, and  $D$  the frequency factor.  $E_A$  is interpreted as an energy barrier that must be overcome for the reaction to proceed, and  $D$  is related to the frequency of “attempts” to overcome that barrier. Note that the forward and reverse reaction have different activation energies, and we will use the following notation

$$k_f = A_f e^{-\Delta G_c/RT} \quad k_b = A_b e^{-\Delta G_a/RT}. \quad (\text{B-63})$$

By varying the electrode potential, we change the energy of the electrons in the electrode, and, therefore, we change the free energy of activation. As a consequence, the free energies of activation for the forward and reverse reaction are functions of the potential. A commonly used model to express this relationship is the Butler-Volmer model. The reference point for the potential is the standard potential, and the free energy of activation at that potential is denoted by a 0 subscript. We write the free energies of activation

$$\begin{aligned} \Delta G_c &= \Delta G_{0c} + \alpha F (E - E^0) \\ \Delta G_a &= \Delta G_{0a} - (1 - \alpha) F (E - E^0). \end{aligned} \quad (\text{B-64})$$

The parameter  $\alpha$  ranges from 0 to 1, and it is called transfer coefficient. The rate constants are then expressed as

$$\begin{aligned} k_f &= A_f \exp(-\Delta G_{0c}/RT) \exp\left[-\alpha F (E - E^0)/RT\right] \\ k_b &= A_b \exp(-\Delta G_{0a}/RT) \exp\left[(1 - \alpha) F (E - E^0)/RT\right]. \end{aligned} \quad (\text{B-65})$$

To simplify the expression, we take the case in which  $C_O = C_R$  and the electrode is at equilibrium, so  $E = E^0$ . At equilibrium the reaction rates must equalize, and, since we set

$C_O = C_R$ , we also have  $k_f = k_b = k^0$ , where  $k^0$  is called the standard rate. The expressions above can be written in terms of  $k^0$

$$\begin{aligned} k_f &= k^0 \exp\left[-\alpha F(E - E^0)/RT\right] \\ k_b &= k^0 \exp\left[(1 - \alpha)F(E - E^0)/RT\right]. \end{aligned} \quad (\text{B-66})$$

We now have all the results to derive an expression for the i-E curve. To simplify the formulas, we introduce the concept of exchange current, which represents the magnitude of the cathodic or anodic currents that flows at equilibrium. At equilibrium, the two currents balance each other, and the exchange current represents the magnitude of each one of them. The exchange current can be thought of as the “idle” current at equilibrium. At equilibrium, the surface concentrations  $C_O$  and  $C_R$  are equal to the bulk concentrations  $C_{Ob}$  and  $C_{Rb}$  respectively. Using this fact, and combining Equations (B-60) and (B-66), we find an expression for the exchange current

$$i_0 = F A k^0 C_{Ob}^{1-\alpha} C_{Rb}^{\alpha}. \quad (\text{B-67})$$

We are interested in the current as a function of the overpotential, i.e., the potential over the equilibrium one. Substituting Nernst Equation (B-56) inside Equation (B-58) we obtain an expression for the overpotential

$$\eta = E - E_{eq} = E - E^0 + RT \ln \frac{C_{Ob}}{C_{Rb}}. \quad (\text{B-68})$$

We can substitute (B-68) into (B-66), and by using (B-60), (B-61) and (B-67), the i- $\eta$  relation is found to be



$$i = i_0 \left[ \frac{C_O}{C_{Ob}} e^{-\alpha \frac{F}{RT} \eta} - \frac{C_R}{C_{Rb}} e^{(1-\alpha) \frac{F}{RT} \eta} \right]. \quad (\text{B-69})$$

The effect of the overpotential is to increase unbalance  $i_c$  and  $i_a$  from the equilibrium condition, thus giving rise to a net current flow. As an example, we consider the case of a rate-limited reaction, i.e., one for which mass transport is much faster than the reaction. In that case we have  $C_O = C_{Ob}$  and  $C_R = C_{Rb}$ , and (B-69) simplifies to

$$i = i_0 \left[ e^{-\alpha \frac{F}{RT} \eta} - e^{(1-\alpha) \frac{F}{RT} \eta} \right]. \quad (\text{B-70})$$

For small overpotential, the current becomes approximately linear with the overpotential

$$i = -i_0 \frac{F}{RT} \eta. \quad (\text{B-71})$$

For large overpotential, on the other hand we get an exponential dependence

$$i = i_0 e^{-\alpha \frac{F}{RT} \eta}. \quad (\text{B-72})$$

This dependence is called Tafel relation. It holds when the forward reaction is much faster than the reverse reaction, as it is in the case of large overpotential.

## B.2.6 Mass Transfer

For the electrode reaction to occur, reactants have to reach the electrode, and products have to leave it after the reaction. The mass transfer equations determine the flow of each species in the solution. Mass transfer occurs by three different mechanisms:

- *diffusion*: transport of a species under the effect of a chemical potential gradient;

- *migration*: transport of a species under the effect of an electrical potential gradient (i.e., an electric field);
- *convection*: transport of a species due to fluid flow.

The first two mechanisms may be combined to describe mass transport under the effect of an electrochemical potential gradient. We assume a linear relationship between the flux  $\vec{J}_i$  and the electrochemical potential gradient of a species  $i$

$$\vec{J}_i = -\frac{C_i D_i}{RT} \nabla \bar{\mu}_i = -\frac{C_i D_i}{RT} (\nabla \mu_i + z_i F \nabla \phi). \quad (\text{B-73})$$

$C_i$  is the concentration of species  $i$ ,  $D_i$  is the diffusion coefficient, and  $z_i$  is the charge. If we add the convection term and we assume the activity coefficient of species  $i$  to be 1, we obtain Nernst-Planck equation

$$\vec{J}_i = -D_i \nabla C_i - \frac{z_i F}{RT} D_i C_i \nabla \phi + C_i \vec{v}. \quad (\text{B-74})$$

The solution to the mass transfer problem provides a relationship between the bulk concentrations and the electrode surface concentrations.

Mass transfer equations are also used to model the current flow in the bulk of the solution. In the bulk, migration dominates, and the current flows through the movement of ions. The resistance  $R_s$  of a volume of solution of length  $l$  and cross-sectional area  $A$  is related to the conductivity  $\sigma$  of the solution by

$$R_s = \frac{1}{\sigma} \frac{l}{A}. \quad (\text{B-75})$$

When multiple ionic species are present in the solution, they all contribute to the conductivity. For each species  $i$  we define the mobility

$$u_i = \frac{v_i}{E_f} \quad (\text{B-76})$$

where  $v_i$  is the maximum velocity of the ion in the solution when it is subject to the electric field  $E_f$ . If the ions have charge  $z_i$  and concentration  $C_i$ , the total conductivity is

$$\sigma = F \sum_i |z_i| u_i C_i. \quad (\text{B-77})$$

The fraction of the current carried by each species is described by the transference number  $t_i$ , also called transport number,

$$t_i = \frac{|z_i| u_i C_i}{\sum_i |z_i| u_i C_i}. \quad (\text{B-78})$$

Interactions between ions may alter their mobility.

### B.2.7 Equivalent Electrical Model

The electrode reaction kinetics and mass transport of an electrochemical cell can be modeled by an equivalent electric circuit (Figure B-4). We already saw in Section B.2.2 that the phenomena at the electrode are modeled by a capacitor  $C_e$  (for non-Faradaic phenomena) in parallel with a resistor  $R_e$  (for Faradaic phenomena). The potential drop due to mass transfer is split into a resistor  $R_s$  for the bulk solution and a resistor  $R_d$  for the diffusion layer around the electrode. These equivalent electrical components are in general non-linear, but they can be linearized in certain ranges.

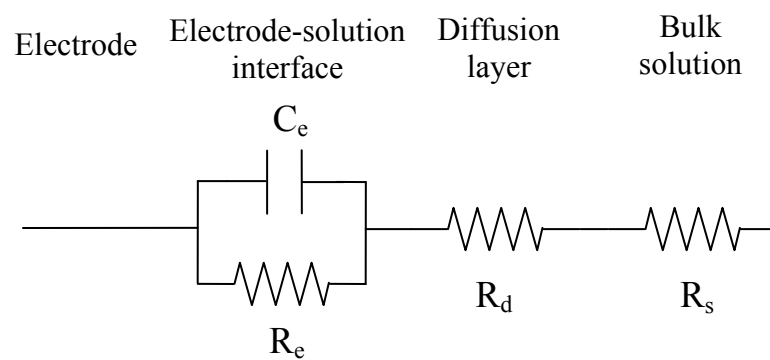


Figure B-4. Electrical model of the electrochemical system, from one electrode the bulk of the solution.

## REFERENCES

---

- [1] V. S. Polikov, P. A. Tresco, and W. M. Reichert, "Response of brain tissue to chronically implanted neural electrodes," *Journal of Neuroscience Methods*, vol. 148, pp. 1-18, 2005.
- [2] A. B. Schwartz, X. Tracy Cui, D. J. Weber, and D. W. Moran, "Brain-Controlled Interfaces: Movement Restoration with Neural Prosthetics," *Neuron*, vol. 52, pp. 205-220, 2006.
- [3] M. A. Lebedev and M. A. L. Nicolelis, "Brain-machine interfaces: past, present and future," *Trends in Neurosciences*, vol. 29, pp. 536-546, 2006.
- [4] A. B. Schwartz, "Cortical Neural Prosthetics," *Annual Review of Neuroscience*, vol. 27, pp. 487-507, 2004.
- [5] E. C. Leuthardt, G. Schalk, D. Moran, and J. G. Ojemann, "The Emerging World of Motor Neuroprosthetics: A Neurosurgical Perspective," *Neurosurgery*, vol. 59, pp. 1-14, 2006.
- [6] M. A. L. Nicolelis, "Brain-machine interfaces to restore motor function and probe neural circuits," *Nature Reviews on Neuroscience*, vol. 4, pp. 417-422, 2003.
- [7] S. Musallam, B. D. Corneil, B. Greger, Scherberger H., and R. A. Andersen, "Cognitive Control Signals for Neural Prosthetics," *Science*, vol. 305, pp. 258-262, 2004.
- [8] R. A. Andersen, S. Musallam, J. W. Burdick, and J. G. Cham, "Cognitive Based Neural Prosthetics," in *The 2005 IEEE International Conference on Robotics and Automation*, Barcelona, Spain, 2005, pp. 1908-1913.

- [9] S. F. Cogan, "Neural Stimulation and Recording Electrodes," *Annual Review of Biomedical Engineering*, vol. 10, pp. 275-309, 2008.
- [10] K. Miller, K. Chinzei, G. Orssengo, and P. Bednarz, "Mechanical properties of brain tissue in-vivo: experiment and computer simulation," *Journal of Biomechanics*, vol. 33, pp. 1369-1376, 2000.
- [11] K. Miller and K. Chinzei, "Mechanical properties of brain tissue in tension," *Journal of Biomechanics*, vol. 35, pp. 483-490, 2002.
- [12] M. A. Howard, B. A. Abkes, M. C. Ollendieck, M. D. Noh, R. C. Ritter, and G. T. Gillies, "Measurement of the Force Required to Move a Neurosurgical Probe Through In vivo Human Brain Tissue," *IEEE Transactions on Biomedical Engineering*, vol. 46, pp. 891-894, 1999.
- [13] D. A. Robinson, "The Electrical Properties of Metal Microelectrodes," *Proceedings of the IEEE*, vol. 56, pp. 1065-1071, 1968.
- [14] B. L. McNaughton, J. O'Keefe, and C. A. Barnes, "The stereotrode: a new technique for simultaneous isolation of several single units in the central nervous system from multiple unit records," *Journal of Neuroscience Methods*, vol. 8, pp. 391-397, 1983.
- [15] C. M. Gray, P. E. Maldonado, M. Wilson, and B. McNaughton, "Tetrodes markedly improve the reliability and yield of multiple single-unit isolation from multi-unit recordings in cat striate cortex," *Journal of Neuroscience Methods*, vol. 63, pp. 43-54, 1995.

- [16] E. M. Schmidt, "Electrodes for Many Single Neuron Recordings," in *Methods for Neural Ensemble Recordings*, M. A. Nicolelis, Ed., First ed: CRC Press, 1999, pp. 1-23.
- [17] MicroProbes. *Company Website*. [www.microprobes.com](http://www.microprobes.com)
- [18] FHC Inc. *Company Website*. [www.fh-co.com](http://www.fh-co.com)
- [19] M. HajjHassan, V. Chodavarapu, and S. Musallam, "NeuroMEMS: Neural Probe Microtechnologies," *Sensors*, vol. 8, pp. 6704-6726, 2009.
- [20] NeuroNexus Technologies. *Company Website*. [www.neuronexustech.com](http://www.neuronexustech.com)
- [21] S. J. Tanghe and K. D. Wise, "A 16-Channel CMOS Neural Stimulating Array," *IEEE Journal of Solid-State Circuits*, vol. 27, pp. 1819-1825, 1992.
- [22] Q. Bai, K. D. Wise, and D. J. Anderson, "High-Yield Microassembly Structure For Three-Dimensional Microelectrode Arrays," *IEEE Transactions on Biomedical Engineering*, vol. 47, pp. 281-289, 2000.
- [23] P. K. Campbell, K. E. Jones, R. J. Huber, K. W. Horch, and R. A. Normann, "A Silicon-Based, Three-Dimensional Neural Interface: Manufacturing Processes for an Intracortical Electrode Array," *IEEE Transactions on Biomedical Engineering*, vol. 38, pp. 758-768, 1991.
- [24] Cyberkinetics. *Company Website*. Available: [www.cyberkinetics.com](http://www.cyberkinetics.com)
- [25] C. Pang, J. G. Cham, S. Musallam, Y.-C. Tai, J. W. Burdick, and R. A. Andersen, "Monolithic Silicon Probes with Flexible Parylene Cables for Neural Prostheses," in *Conference on Nano/Micro Engineered and Molecular Systems*, Zhuhai, China, 2006, pp. 1125-1128.

- [26] C. Pang, "Parylene Technology for Neural Probes Applications," Doctor of Philosophy, Electrical Engineering, California Institute of Technology, Pasadena, 2007.
- [27] R. Huang, C. Pang, Y. C. Tai, J. Emken, C. Ustun, R. Andersen, and J. Burdick, "Integrated Parylene-cabled Silicon Probes for Neural Prosthetics," in *IEEE 21st International Conference on Micro Electro Mechanical Systems (MEMS 2008)*, Tucson, AZ, USA, 2008, pp. 240-243.
- [28] S. Takeuchi, T. Suzuki, K. Mabuchi, and H. Fujita, "3D flexible multichannel neural probe array", *Journal of Micromechanics and Microengineering*, vol. 14, pp. 104-107, 2004.
- [29] D. C. Rodger, A. J. Fong, W. Li, H. Ameri, A. K. Ahuja, C. Gutierrez, I. Lavrov, H. Zhong, P. R. Menon, E. Meng, J. W. Burdick, R. R. Roy, V. Reggie Edgerton, J. D. Weiland, M. S. Humayun, and Y.-C. Tai, "Flexible parylene-based multielectrode array technology for high-density neural stimulation and recording," *Sensors and Actuators B*, vol. 132, pp. 449-460, 2008.
- [30] R. Biran, D. C. Martin, and P. A. Tresco, "Neuronal cell loss accompanies the brain tissue response to chronically implanted silicon microelectrode arrays," *Experimental Neurology*, vol. 195, pp. 115-126, 2005.
- [31] J. N. Turner, W. Shain, D. H. Szarowski, M. Andersen, S. Martins, M. Isaacson, and H. Craighead, "Cerebral Astrocyte Response to Micromachined Silicon Implants," *Experimental Neurology*, vol. 156, pp. 33-49, 1999.



- [32] D. H. Szarowski, M. D. Andersen, S. Retterer, A. J. Spence, M. Isaacson, H. G. Craighead, J. N. Turner, and W. Shain, "Brain responses to micro-machined silicon devices," *Brain Research*, vol. 983, pp. 23-25, 2003.
- [33] R. W. Griffith and D. R. Hymphrey, "Long-term gliosis around chronically implanted platinum electrodes in the Rhesus macaque motor cortex," *Neuroscience Letters* 406, pp. 81-86, 2006.
- [34] G. C. McConnell, R. J. Butera, and R. V. Bellamkonda, "Bioimpedance modeling to monitor astrocytic response to chronically implanted electrodes," *Journal of Neural Engineering*, vol. 6, 2009.
- [35] A. L. Pierce, S. Sommakia, J. L. Rickus, and K. J. Otto, "Thin-film silica sol-gel coatings for neural microelectrodes," *Journal of Neuroscience Methods*, vol. 180, pp. 106-110, 2009.
- [36] P. Stice and J. Muthuswamy, "Assessment of gliosis around moveable implants in the brain," *Journal of Neural Engineering*, vol. 6, 2009.
- [37] A. Jackson and E. E. Fetz, "Compact Movable Microwire Array for Long-Term Chronic Unit Recording in Cerebral Cortex of Primates," *Journal of Neurophysiology*, vol. 98, pp. 3109-3118, 2007.
- [38] B. P. Vos, M. Wijinants, S. Taeymans, and E. D. Schutter, "Miniature carrier with six independently moveable electrodes for recording of multiple single-units in the cerebellar cortex of awake rats," *Journal of Neuroscience Methods*, vol. 94, pp. 19-26, 1999.
- [39] H. A. Swadlow, Y. Bereshpolova, T. Bezdudnaya, M. Cano, and C. R. Stoelzel, "A Multi-Channel, Implantable Microdrive System for Use With Sharp, Ultra-

- Fine "Reitboeck" Microelectrodes," *Journal of Neurophysiology*, vol. 93, pp. 2959-2965, 2005.
- [40] S. Venkatachalam, M. S. Fee, and D. Kleinfeld, "Ultra-miniature headstage with 6-channel drive and vacuum-assisted micro-wire implantation for chronic recording from the neocortex," *Journal of Neuroscience Methods*, vol. 90, pp. 37-46, 1999.
- [41] C. S. Lansink, M. Bakker, W. Buster, J. Lankelma, R. van der Blom, R. Westdorp, R. N. J. M. A. Joosten, B. L. McNaughton, and C. M. A. Pennartz, "A split microdrive for simultaneous multi-electrode recordings from two brain areas in awake small animals," *Journal of Neuroscience Methods*, vol. 162, pp. 129-138, 2007.
- [42] J. D. Kralik, D. F. Dimitrov, D. J. Krupa, D. B. Katz, D. Cohen, and M. A. Nicolelis, "Techniques for long-term multisite neuronal ensemble recordings in behaving animals," *Journal of Neuroscience Methods*, vol. 25, 2001.
- [43] I. Szabo, A. Czurko, J. Csicsvari, H. Hirase, X. Leinekugel, and G. Buzsaki, "The application of printed circuit board technology for fabrication of multi-channel micro-drives," *Journal of Neuroscience Methods*, vol. 105, pp. 105-110, 2001.
- [44] M. S. Fee and A. Leonardo, "Miniature motorized microdrive and commutator system for chronic neural recording in small animals," *Journal of Neuroscience Methods*, vol. 112, pp. 83-94, 2001.
- [45] T. Sato, T. Suzuki, and K. Mabuchi, "A new multi-electrode array design for chronic neural recording, with independent and automatic hydraulic positioning," *Journal of Neuroscience Methods*, vol. 160, pp. 45-51, 2007.

- [46] J. G. Cham, E. A. Branchaud, Z. Nenadic, B. Greger, R. A. Andersen, and J. W. Burdick, "Semi-Chronic Motorized Microdrive and Control Algorithm for Autonomously Isolating and Maintaining Optimal Extracellular Action Potentials," *Journal of Neurophysiology*, vol. 93, pp. 570-579, 2005.
- [47] E. A. Branchaud, J. G. Cham, Z. Nenadic, and J. W. Burdick, "A Miniature Robot for Autonomous Single Neuron Recordings," in *IEEE International Conference On Robotics and Automation*, Barcelona, Spain, 2005, pp. 1920-1926.
- [48] E. A. Branchaud, J. W. Burdick, and R. A. Andersen, "An Algorithm for Autonomous Isolation of Neurons in Extracellular Recordings," presented at the The First IEEE/RAS-EMBS International Conference on Biomedical Robotics and Biomechatronics (BioRob 2006) 2006.
- [49] E. A. Branchaud, "A Control System for Positioning Recording Electrodes to Isolate Neurons in Extracellular Recording," Ph. D. , Mechanical Engineering, California Institute of Technology, 2006.
- [50] J. G. Cham, M. T. Wolf, R. A. Andersen, and J. W. Burdick, "Miniature Neural Interface Microdrive using Parylene-coated Layered Manufacturing," presented at the 2006 IEEE/RAS-EMBS International Conference on Biomedical Robotics and Biomechatronics, 2006.
- [51] M. T. Wolf, J. G. Cham, E. A. Branchaud, G. H. Mulliken, J. W. Burdick, and R. A. Andersen, "A Robotic Neural Interface for Autonomous Positioning of Extracellular Recording Electrodes," *The International Journal of Robotics Research*, vol. 28, pp. 1240-1256, 2009.
- [52] Thomas Recording GmbH. *Company Website*. [www.thomasrecording.com](http://www.thomasrecording.com)

- [53] David Kopf Instruments. *Company Website*. [www.kopfstruments.com](http://www.kopfstruments.com)
- [54] Alpha Omega Ltd. *Company Website*. [www.alphaomega-eng.com](http://www.alphaomega-eng.com)
- [55] Nan Instruments Ltd. *Company Website*. [www.naninstruments.com](http://www.naninstruments.com)
- [56] Narishige. *Company Website*. [narishige-group.com](http://narishige-group.com)
- [57] R. Eckhorn and T. Uwe, "A new method for the insertion of multiple microprobes into neural and muscular tissue, including fiber electrodes, fine wires, needles and microsensors," *Journal of Neuroscience Methods*, vol. 49, pp. 175-179, 1993.
- [58] H. J. Reitboeck, "A 19-channel matrix drive with individually controllable fiber microelectrodes for neurophysiological applications," *IEEE Transactions on Systems, Man and Cybernetics*, vol. 13, pp. 676-683, 1983.
- [59] A. Hernandez, V. Nacher, R. Luna, M. Alvarez, A. Zainos, S. Cordero, L. Camarillo, Y. Vazquez, L. Lemus, and R. Romo, "Procedure for recording the simultaneous activity of single neurons distributed across cortical areas during sensory discrimination," *Proceedings of the National Academy of Sciences*, vol. 105, pp. 16785-16790, 2008.
- [60] S. N. Baker, N. Philbin, R. Spinks, E. M. Pinches, D. M. Wolpert, D. G. MacManus, Q. Pauluis, and R. N. Lemon, "Multiple single unit recording in the cortex of monkeys using independently moveable microelectrodes," *Journal of Neuroscience Methods*, vol. 94, pp. 5-17, 1999.
- [61] R. C. deCharms, D. T. Blake, and M. M. Merzenich, "A multielectrode implant device for the cerebral cortex," *Journal of Neuroscience Methods*, vol. 93, pp. 27-35, 1999.

- [62] J. Muthuswamy, M. Okandan, T. Jain, and A. Gilletti, "Electrostatic Microactuators for Precise Positioning of Neural Microelectrodes," *IEEE Transactions on Biomedical Engineering*, vol. 52, pp. 1748-1755, 2005.
- [63] J. Muthuswamy, M. Okandan, A. Gilletti, M. S. Baker, and T. Jain, "An Array of Microactuated Microelectrodes for Monitoring Single-Neuronal Activity in Rodents," *IEEE Transactions on Biomedical Engineering*, vol. 52, pp. 1470-1477, 2005.
- [64] P. De Moor, "IMEC's ultra-low power actuator suitable for in-vivo biomedical applications," presented at the IMEC Technology Forum Press Gathering, 2009.
- [65] L. Giacchino and Y.-C. Tai, "Electrolysis-based Parylene-balloon Actuators," presented at the The 15th International Conference on Solid-State Sensors, Actuators and Microsystems (Transducers '09), Denver, USA, 2009.
- [66] J. Rossmeisl, A. Logadottir, and J. K. Nørskov, "Electrolysis of Water on (Oxidized) Metal Surfaces," *Chemical Physics*, vol. 319, pp. 178-184, 2005.
- [67] R. B. Dopp, "Hydrogen Generation Via Water Electrolysis Using High-efficiency Nanometal Electrodes," Quantum Sphere Inc. 2007.
- [68] M. J. Joncich and N. H. Hackerman, "The Reaction of Hydrogen and Oxygen on Submerged Platinum Electrode Catalysts. I. Effect of Stirring, Temperature and Electric Polarization," *J. Phys. Chem.*, vol. 57, pp. 674-679, 1953.
- [69] R. Dus and F. C. Tompkins, "Mechanism of the Hydrogen-Oxygen Reaction on Platinum Films from Surface Potential Measurements," *Proceedings of the Royal Society of London. Series A, Mathematical and Physical Sciences*, vol. 343, pp. 477-488, 1975.

- [70] C. G. Cameron and M. S. Freund, "Electrolytic actuators: Alternative, high-performance, material-based devices," *Proceedings of the National Academy of Sciences*, vol. 99, pp. 7827-7831, 2002.
- [71] D.-S. Meng, Y. S. Ju, and C.-J. C. Kim, "A Comparative Study of Electrolysis and Boiling for Bubble-driven Microactuators," presented at the The 13th International Conference on Solid-state Sensors, Actuators and Microsystems, Seoul, Korea, 2005.
- [72] C. Neagu, H. Jansen, H. Gardeniers, and M. Elwenspoek, "The electrolysis of water: an actuation principle for MEMS with a big opportunity," *Mechatronics*, vol. 10, pp. 571-581, 2000.
- [73] A. P. Papavasiliou, D. Liepmann, and A. P. Pisano, "Electrolysis-Bubble Actuated Gate Valve," in *Solid-State Sensor and Actuator Workshop*, Hilton Head, SC, 2000.
- [74] J. Xie, Q. He, Y.-C. Tai, J. Liu, and T. Lee, "Electrolysis-based On-chip Dispensing System for ESI-MS," in *International Conference on Micro Electro Mechanical Systems (MEMS '03)*, 2003.
- [75] C.-M. Cheng and C.-H. Liu, "An Electrolysis-Bubble-Actuated Micropump Based on the Roughness Gradient Design of Hydrophobic Surface," *Journal of Microelectromechanical Systems*, vol. 16, pp. 1095-1105, 2007.
- [76] D.-S. Meng and C.-J. C. Kim, "Micropumping by Directional Growth and Hydrophobic Venting of Bubbles," in *The 18th IEEE Int. Conf. on Micro Electro Mechanical Systems*, Miami, FL, 2005, pp. 423-426.

- [77] D. A. Ateya, A. A. Shah, and S. Z. Hua, "An electrolytically actuated micropump," *Review of Scientific Instruments*, vol. 75, pp. 915-920, 2004.
- [78] C. Pang, Y.-C. Tai, J. W. Burdick, and R. A. Andersen, "Electrolysis-based Diaphragm Actuators," *Nanotechnology*, vol. 17, pp. 64-68, 2006.
- [79] L. M. Kachanov, *Fundamentals of the Theory of Plasticity*: Dover Publications Inc., 2004.
- [80] W. R. Salzman. *Chemical Thermodynamics (Course Notes)*.  
<http://www.chem.arizona.edu/~salzmanr/>
- [81] H. Zhang, "The Permeability Characteristics of Silicone Rubber," in *SAMPE Fall Technical Conference*, Dallas, TX, 2006.
- [82] T. C. Merkel, V. I. Bondar, K. Nagai, B. D. Freeman, and I. Pinnau, "Gas Sorption, Diffusion, and Permeation in Poly(dimethylsiloxane)," *Journal of Polymer Science, part B*, vol. 38, pp. 415-434, 2000.
- [83] C. Pang, Y. C. Tai, J. W. Burdick, and R. A. Andersen, "Electrolysis-based Parylene Balloon Actuators for Movable Neural Probes," presented at the The Second Annual IEEE International Conference on Nano/Micro Engineered and Molecular Systems (NEMS '07), Bangkok, Thailand, 2007.
- [84] A. F. Tanioka, Noriaki, K. Hasegawa, K. Miyasaka, and N. Takahashi, "Permeation of Gases Across the Poly(chloro-p-xylylene) membrane," *Journal of Applied Polymer Science*, vol. 54, pp. 219-229, 1994.
- [85] M. A. Spivack and G. Ferrante, "Determination of the Water Vapor Permeability and Continuity of Ultrathin Parylene Membranes," *J. Electrochem. Soc.*, vol. 116, pp. 1592-1594, 1969.

- [86] H.-S. Noh, C. Bonner, P. J. Hesketh, and G. C. Frye-Mason, "Fabrication of Parylene Column for Micro Gas Chromatograph," presented at the The 7th Mechatronics Forum International Conference, 2000.
- [87] L. Giacchino and Y.-C. Tai, "Electrolysis-based Inchworm Actuators," presented at the The 14th Hilton Head Workshops on the science and technology of solid-state sensors, actuators, and microsystems (Hilton Head 2010), Hilton Head Island, SC, USA, 2010.
- [88] N. P. Brandon and G. H. Kelsall, "Growth kinetics of bubbles electrogenerated at microelectrodes," *Journal of Applied Electrochemistry*, vol. 15, pp. 475-484, 1985.
- [89] S. Lubetkin, "The motion of electrolytic gas bubbles near electrodes," *Electrochimica Acta*, vol. 48, pp. 357-375, 2002.
- [90] J. L. Trompette and H. Vergnes, "Characteristic Aspects of Bubble Coalescence during Electrolysis of Ammonium Salt Solutions," *Journal of Physical Chemistry C*, vol. 111, pp. 5236-5243, 2007.
- [91] R. L. Stover, "Bubble Coalescence Dynamics and Supersaturation in Electrolytic Gas Evolution," Ph.D., Energy and Environment Division, Ernest Orlando Lawrence Berkeley National Laboratory, 1996.
- [92] H. K. Christenson, R. E. Bowen, J. A. Carlton, J. R. M. Denne, and Y. Lu, "Electrolytes that Show a Transition to Bubble Coalescence Inhibition at High Concentrations," *Journal of Physical Chemistry C*, vol. 112, pp. 794-796, 2008.



- [93] M. El-Batouti, "Effect of sodium dodecyl sulfate on the rate of hydrogen evolution at a cathode," *Journal of Colloid and Interface Science*, vol. 268, pp. 425-428, 2003.
- [94] H. Matsushima, T. Nishida, Y. Konishi, Y. Fukunaka, Y. Ito, and K. Kuribayashi, "Water Electrolysis Under Microgravity Part 1. Experimental Technique," *Electrochimica Acta*, pp. 4119-4125, 2003.
- [95] S. Lee, W. Sutomo, C. Liu, and E. Loth, "Micro-fabricated electrolytic micro-bubblers," *International Journal of Multiphase Flow*, vol. 31, pp. 706-722, 2005.
- [96] J. Bouchaud, "MEMS industry and market overview," WTC, Munich 2008.
- [97] S. Beeby, G. Ensell, M. Kraft, and N. White, *MEMS Mechanical Sensors*: Artech House, 2004.
- [98] W. P. Eaton and J. H. Smith, "Micromachined Pressure Sensors: Review and Recent Developments," *Smart Materials and Structures*, vol. 6, pp. 530-539, 1997.
- [99] P. J. Chen, D. C. Rodger, M. S. Humayun, and Y. C. Tai, "Unpowered Spiral-Tuved Parylene Pressure Sensor for Intraocular Pressure Sensing," *Sensors and Actuators A*, vol. 127, pp. 276-282, 2006.
- [100] P. J. Chen, D. C. Rodger, M. S. Humayun, and Y. C. Tai, "Implantable Parylene-based Wireless Intraocular Pressure Sensor," presented at the IEEE 21st International Conference on Micro Electro Mechanical Systems (MEMS '08), Tucson, 2008.

- [101] L. Giacchino and Y.-C. Tai, "Parylene-membrane Piezoresistive Pressure Sensors with XeF<sub>2</sub>-etched Cavity," presented at the The 7th IEEE Conference on Sensors (IEEE Sensors 2008), Lecce, Italy, 2008.
- [102] P. J. Chen, C. Y. Shih, and Y. C. Tai, "Design, Fabrication and Characterization of Monolithic Embedded Parylene Microchannels in Silicon Substrate," *Lab on a Chip*, vol. 6, pp. 803-810, 2006.
- [103] R. L. Taylor and S. Govindjee, "Solution of clamped rectangular plate problems," *Communications in numerical methods in engineering*, vol. 20, pp. 757-765, 2004.
- [104] S. Timoshenko and S. Woinowsky-Krieger, *Theory of Plates and Shells*, Second Edition ed.: McGraw-Hill, 1959.
- [105] M. Liger, D. C. Rodger, and Y. C. Tai, "Robust Parylene-to-Silicon Mechanical Anchoring," presented at the IEEE 16th Annual International Conference on Micro Electro Mechanical Systems (MEMS '03), Kyoto, Japan, 2003.
- [106] P. B. Chu, J. T. Chen, R. Yeht, G. Lin, J. C. P. Huang, B. A. Warneket, and K. S. J. Pister, "Controlled Pulse-Etching with Xenon Difluoride," presented at the International Conference on Solid State Sensors and Actuators (Transducers '97), Chicago, 1997.
- [107] Y.-C. Tai, D. C. Rodger, W. Li, and A. Tooker, "Method for Decreasing Chemical Diffusion in Parylene and Trapping at Parylene-to-Parylene Interfaces," United States Patent, 2006.

- [108] Y. S. Yeh, W. J. James, and H. Y. Yasuda, "Polymerization of Paraxylylene Derivatives. VI. Morphology of Parylene N and Parylene C Films Investigated by Gas Transport Characteristics," *Journal of Polymer Science, part B*, vol. 28, 1990.
- [109] M. J. Madou, *Fundamentals of Microfabrication: The Science of Miniaturization*, Second Edition ed.: CRC Press, 2002.
- [110] M. Gad-el-Hak, *The MEMS Handbook*, Second Edition ed.: CRC Press, 2005.
- [111] K. E. Petersen, "Silicon as a Mechanical Material," *Proceedings of the IEEE*, vol. 70, pp. 420-455, 1982.
- [112] G. T. A. Kovacs, N. I. Maluf, and K. E. Petersen, "Bulk Micromachining of Silicon," *Proceedings of the IEEE*, vol. 86, pp. 1536-1551, 1998.
- [113] K. R. Williams and R. S. Muller, "Etch Rates for Micromachining Processing," *Journal of Microelectromechanical Systems*, vol. 5, pp. 256-269, 1996.
- [114] K. R. Williams, K. Gupta, and M. Wasilik, "Etch Rates for Micromachining Processing - Part II," *Journal of Microelectromechanical Systems*, vol. 12, pp. 761-777, 2003.
- [115] G. Lebon, D. Jou, and J. Casas-Vázquez, *Understanding Non-Equilibrium Thermodynamics*: Springer-Verlag, 2008.
- [116] A. J. Bard and L. R. Faulkner, *Electrochemical Methods: Fundamentals and Applications*, Second Edition ed.: Wiley, 2000.
- [117] C. M. A. Brett and A. M. O. Brett, *Electrochemistry. Principles, Methods, and Applications*: Oxford University Press, 1993.
- [118] J. G. Wijmans and R. W. Baker, "The solution-diffusion model: a review," *Journal of Membrane Science*, vol. 107, pp. 1-21, 1995.

- [119] S. W. Rutherford and D. D. Do, "Review of Time Lag Permeation Technique as a Method for Characterisation of Porous Media and Membranes," *Adsorption*, vol. 3, pp. 283-312, 1997.
- [120] R. Chang, *Physical Chemistry for the Chemical and Biological Sciences*, 3rd ed.: University Science Books, 2000.